

INDIUM NITRIDE GROWTH BY METAL-ORGANIC VAPOR PHASE EPITAXY

By

TAEWOONG KIM

A DISSERTATION PRESENTED TO THE GRADUATE SCHOOL  
OF THE UNIVERSITY OF FLORIDA IN PARTIAL FULFILLMENT  
OF THE REQUIREMENTS FOR THE DEGREE OF  
DOCTOR OF PHILOSOPHY

UNIVERSITY OF FLORIDA

2006

Copyright 2006

by

Taewoong Kim

## ACKNOWLEDGMENTS

The author wishes first to thank his advisor, Dr. Timothy J. Anderson, for providing five years of valuable advice and guidance. Dr. Anderson always encouraged the author to approach his research from the highest scientific level. He is deeply thankful to his co-advisor, Dr. Olga Kryliouk, for her valuable guidance, sincere advice, and consistent support for the past five years.

Secondly, the author wishes to thank the remaining committee members of Dr. Steve Pearton and Dr. Fan Ren for their advice and guidance

The author is grateful to Scott Gapinski, the staff at Microfabritech, and Eric Lambers, the staff at the Major Analytical Instrumentation Center, especially for Auger characterization.

Acknowledgement needs to be given to Sangwon Kang who worked with the author for the past year and provided valuable assistance.

Thanks go to Youngsun Won for his useful discussion of quantum calculation and SEM characterization, and to Dr. Jianyun Shen for her assistance about how to use the ThermoCalc.

The author wishes to thank Hyunjong Park for useful discussion and Youngseok Kim for his kindness and friendship.

Most importantly, the author is grateful to Moonhee Choi, his beloved wife, for her endless support, trust, love, sacrifice and encouragement. Without her help, he would have not finished the Ph.D. course.

The author is grateful to his mother, father, mother-in-law, father-in-law, sisters, and brother for providing love, support and guidance throughout his life.

## TABLE OF CONTENTS

	<u>page</u>
ACKNOWLEDGMENTS .....	iii
LIST OF TABLES .....	viii
LIST OF FIGURES .....	x
ABSTRACT .....	xvii
CHAPTER	
1 INTRODUCTION .....	1
2 LITERATURE REVIEW .....	3
2.1 Indium Nitride (InN) and Indium Gallium Nitride ( $\text{In}_x\text{Ga}_{1-x}\text{N}$ ) Properties .....	4
2.1.1 Structural Properties .....	4
2.1.2 Physical Properties .....	7
2.1.3 Electrical Properties of InN .....	9
2.1.3.1 Background Defects .....	9
2.1.3.2 Hall mobility and Electron Concentration in Undoped InN .....	10
2.1.4 Optical Properties of InN .....	14
2.1.5. Indium Nitride (InN) and Indium Gallium Nitride ( $\text{In}_x\text{Ga}_{1-x}\text{N}$ ) Applications .....	16
2.2 Thermodynamic Analysis and Phase Separation in the $\text{In}_x\text{Ga}_{1-x}\text{N}$ System .....	18
2.2.1 Thermodynamic Models in Solid Solution .....	19
2.2.1.1 Regular Solution Model .....	19
2.2.1.2 Bonding in Semiconductor Solid Solutions Model .....	19
2.2.1.3 Delta Lattice Parameter (DLP) Model for Enthalpy of Mixing .....	21
2.2.1.4 Strain Energy Model .....	22
2.2.1.5 First-Principal Models .....	23
2.2.2 Thermodynamic Analysis of InN .....	24
2.2.3 Phase Separation in $\text{In}_x\text{Ga}_{1-x}\text{N}$ .....	26
2.3 Indium Nitride (InN) and Indium Gallium Nitride ( $\text{In}_x\text{Ga}_{1-x}\text{N}$ ) Growth Challenges .....	32
2.3.1 Growth Temperature and V/III Ratio .....	32
2.3.2 Nitrogen Source .....	34
2.3.3 Carrier Gas .....	36

2.4	Indium Nitride (InN) Growth Techniques.....	37
2.4.1	Chemical Vapor Deposition (CVD).....	37
2.4.1.1	Metal-Organic Vapor Phase Epitaxy (MOVPE).....	38
2.4.1.2	Hydride Vapor Phase Epitaxy (HVPE).....	41
2.4.1.3	Plasma Enhanced Chemical Vapor Deposition (PECVD).....	42
2.4.2	Molecular Beam Epitaxy (MBE) and Metalorganic Molecular Beam Epitaxy (MOMBE).....	44
2.4.3	Atomic Layer Deposition (ALD).....	45
2.5	Substrate Materials.....	46
2.5.1	Sapphire Substrate ( $\text{Al}_2\text{O}_3$ ) (0001).....	47
2.5.2	Silicon (Si) Substrate.....	49
2.5.3	Gallium Nitride (GaN) and Aluminium Nitride (AlN) Substrate.....	50
2.5.4	Other Substrates.....	51
2.5.5	Buffer Layer.....	52
2.6	Summary for Growth of InN on Different Substrate.....	53
2.6.1	Growth on Sapphire ( $\text{Al}_2\text{O}_3$ ) Substrate.....	53
2.6.2	Growth on Silicon (Si) Substrate.....	55
2.6.3	Growth on Gallium Arsenide (GaAs) Substrate.....	56
2.6.4	Growth on Gallium Phosphorus (GaP) Substrate.....	57
2.6.5	Growth on Gallium Nitride (GaN) and Alumimum Nitride (AlN) Substrate.....	58
2.7	Overview.....	59
3	THERMODYNAMIC ANALYSIS OF InN AND $\text{In}_x\text{Ga}_{1-x}\text{N}$ MOVPE GROWTH ..	60
3.1	Thermodynamic Analysis of InN and $\text{In}_x\text{Ga}_{1-x}\text{N}$ .....	60
3.1.1	Reaction Mechanism and Kinetics of InN MOVPE.....	60
3.1.2	Pressur-Temperature (P-T) Phase Diagram of $\text{In}_x\text{Ga}_{1-x}\text{N}$ and Phase Separation in $\text{In}_x\text{Ga}_{1-x}\text{N}$ .....	65
3.2	Quantum Calculation of Phase Separation in $\text{In}_x\text{Ga}_{1-x}\text{N}$ .....	70
3.2.1	Boundary Passivation Method with Hydrogen.....	70
4	CALCULATION OF THE CRITICAL THICKNESS OF InN ON GaN, AlN, Si, AND $\text{Al}_2\text{O}_3$ .....	76
4.1	Calculation of Critical Thickness of InN by Matthews' Method.....	77
4.2	Calculation of Critical Thickness of InN by van der Merwe's Method.....	80
4.3	Calculation of Critical Thickness of InN by the Methods of Shen, Jesser, and Wilsdorf.....	86
5	Indium Nitride (InN) GROWTH BY METAL-ORGANIC VAPOR PHASE EPITAXY (MOVPE).....	93
5.1	Indium Nitride (InN) Growth Optimization.....	93
5.1.1	Substrate Selection.....	94
5.1.1.1	Sapphire (c- $\text{Al}_2\text{O}_3$ (0001)).....	96
5.1.1.2	Gallium Nitride (GaN/c- $\text{Al}_2\text{O}_3$ (0001)).....	97

5.1.1.3. Silicon (Si (111)).....	97
5.1.2. Substrate Preparation Procedure.....	98
5.1.3. Metal-Organic Vapor Phase Epitaxy (MOVPE) Reactor.....	98
5.1.4. Growth Chemistry and Conditions for InN Growth.....	99
5.1.5. Indium Nitride (InN) Growth and Optimization .....	102
5.1.5.1. Influence of Growth Temperature.....	102
5.1.5.2. Influence of Substrate Nitridation .....	110
5.1.5.3. Influence of N/In Ratio .....	115
5.1.5.4. Influence of Buffer Layer and Morphological Study.....	118
5.1.5.5. Influence of Pressure.....	125
5.1.5.6. Optical and Electrical Properties.....	127
5.1.5.7. Summary .....	129
5.1.6. Indium Nitride (InN) Droplet Formation .....	130
5.1.7. Annealing Effect.....	136
5.2. Computational Fluid Dynamic Analysis of the Flow of NH <sub>3</sub> and Proposed Inlet Tube Modification to Improve Flow Pattern of NH <sub>3</sub> .....	138
5.3. Inlet Tube Modification and Growth Results.....	145
6 CONCLUSIONS .....	154
LIST OF REFERENCES .....	158
BIOGRAPHICAL SKETCH .....	179

## LIST OF TABLES

<u>Table</u>	<u>page</u>
2-1. Lattice constants of InN.....	5
2-2. Properties of GaN and InN. ....	6
2-3. Elastic constants of wurtzite InN at room temperature. ....	7
2-4. Physical properties of InN. ....	7
2-5. Carrier concentration and Hall mobility for the different growth methods.....	14
2-6. Comparison of interaction parameters calculated using various models with experimental data. ....	22
2-7. Interaction parameters for various III-V ternary alloy systems.....	30
2-8. Properties of nitrogen precursors for MOVPE. ....	36
2-9. Structural properties of substrates. ....	47
3-1. Reported reaction rate constants for TMIn decomposition. ....	62
3-2. Species, phases, and thermodynamic properties included in the analysis of MOVPE of InN. ....	64
3-3. Phases and species included in the analysis of MOVPE of $\text{In}_x\text{Ga}_{1-x}\text{N}$ .....	67
3-4. Bond lengths for the calculation using HF-SCF.....	74
3-5. Calculated total energy for three types of different bond length.....	74
3-6. Calculated energies of $\text{In}_x\text{Ga}_{1-x}\text{N}$ with the phase separation and without phase separation. ....	75
4-1. Physical properties required for the calculation of the critical thickness of InN on GaN, AlN, $\text{Al}_2\text{O}_3$ , and Si substrates. ....	79
4-2. Calculated critical thickness of InN on GaN, AlN, $\text{Al}_2\text{O}_3$ , and Si substrates using Matthews' method.....	79

4-3. Physical properties required for the calculation of critical thickness of InN on GaN, AlN, Al <sub>2</sub> O <sub>3</sub> , and Si substrates. ....	82
4-4. Calculated shear moduli for InN, GaN, AlN, Al <sub>2</sub> O <sub>3</sub> , and Si materials. ....	82
4-5. Calculated critical thickness of InN using van der Merwe's method. ....	85
4-6. Lattice constant (Å) of InN, GaN, AlN. ....	88
4-7. Elastic constants $c_{ij}$ and compliances $s_{ij}$ of InN. ....	89
4-8. Critical thickness ( $h_c$ ) calculated of InN using three different models. ....	92
5-1. Structural properties of InN, GaN, Al <sub>2</sub> O <sub>3</sub> , Si, and AlN substrates. ....	95
5-2. Range of growth conditions examined for growth of InN. ....	101
5-3. Optimum growth temperature of InN on LT-GaN and LT-InN buffer layers on various substrates. ....	110
5-4. Comparison by ESCA of Si anneals. ....	115
5-5. Optimum growth temperature of LT-InN buffer layer depending on Al <sub>2</sub> O <sub>3</sub> (0001). ....	122
5-6. Root Mean Square (RMS) roughness for as-grown buffer layers and InN films. ....	124
5-7. Growth conditions for InN. ....	129
5-8. Optimum growth condition of InN for Al <sub>2</sub> O <sub>3</sub> (0001), GaN/Al <sub>2</sub> O <sub>3</sub> (0001), Si (111). ....	130
5-9. Density and velocity of NH <sub>3</sub> at reactor wall and substrate. ....	139
5-10. Reynolds number ( $Re$ ) calculated in the inlet tube and in the reactor depending on temperature. ....	139
5-11. Typical values of FWHM depending on different reactor systems. ....	153
5-12. Reference data available for FWHM for MOVPE reactor. ....	153

## LIST OF FIGURES

<u>Figure</u>	<u>page</u>
1-1. Bandgap energies $E_g$ of the semiconductor materials.....	2
2-1. Lattice parameter for polycrystalline and single crystalline InN reported by different groups. ....	5
2-2. Carrier concentration and hall mobility reported for undoped InN film grown in a variety of technique is plotted against the calendar year.....	12
2-3. Room-temperature Hall mobility as a function of InN thickness in InN films grown by MBE, MOVPE, and MEE.....	13
2-4. Photoluminescence spectra for MBE grown InN.....	15
2-5. Band gap energy for InN films as a function of carrier concentration.....	16
2-6. Tetrahedral cells in a ternary III-V alloy semiconductor. ....	20
2-7. Calculated phase diagram for the MBE deposition of InN using atomic N and $NH_3$ gases. There are three deposition modes: etching, droplet and growth..	26
2-8. Free energy versus solid composition for a hypothetical semiconductor alloy having a large positive enthalpy of mixing. Point A and B are the bimodal points, and points C and D represent the spinodal points. ....	27
2-9. Schematic liquid-solid pseudobinary phase diagram. ....	27
2-10. Binodal (solid) and spinodal (dashed) curves for the $In_xGa_{1-x}N$ system, calculated assuming a constant average value for the solid phase interaction parameter.....	28
2-11. Schematic illustration of the key CVD steps during deposition.....	38
2-12. Schematic of horizontal cold-wall MOVPE system.....	39
2-13. Schematics of horizontal hot-wall hydride vapor phase epitaxy chamber. ....	42
2-14. Schematics of PECVD.....	43

2-15. Perspective views in ( $2 \times 2 \times 1$ ) unit cell: (a) along [0001] direction in a rhombohedral unit cell; (b) along the (0001) direction in hexagonal unit cell. ....	48
2-16. Common facets of sapphire crystals: (a) view down $c$ -axis; (b) surface planes.....	48
2-17. Perspective views of Si along various directions: (a) [001]; (b) [011]; (c) [111]. ...	49
2-18. Perspective views of wurtzite GaN along various directions: (a) [0001]; (b) $[11\bar{2}0]$ ; (c) $[10\bar{1}0]$ . ....	50
2-19. Perspective views of zincblende GaN along various directions: (a) [100] ( $1 \times 1 \times 1$ unit); (b) [110] ( $2 \times 2 \times 2$ units); (c) [111] ( $2 \times 2 \times 2$ units). ....	51
3-1. Calculated P-T phase diagram for InN at $X(\text{In}) = 5.31212 \times 10^{-6}$ , $X(\text{N}) = 0.24998$ , $X(\text{H}) = 0.75000$ , $X(\text{C}) = 1.59364 \times 10^{-5}$ and $V/\text{III} = X(\text{N})/X(\text{In}) = 50,000$ . .	65
3-2. Relation between indium mole fraction ( $x$ ) of $\text{In}_x\text{Ga}_{1-x}\text{N}$ and the flow rate ratio of the sum of group III source of TMI and TEG. ....	68
3-3. Calculated P-T phase diagram for $\text{In}_{0.3}\text{Ga}_{0.7}\text{N}$ at $X(\text{In})=1.87328 \times 10^{-5}$ , $X(\text{Ga})=3.05276 \times 10^{-5}$ , $X(\text{N})=0.111$ , $X(\text{H})=0.8887$ , $X(\text{C})=2.39364 \times 10^{-4}$ and the data points (■) are from the measurements observed by Matsuoka. .	68
3-4. Thermodynamically calculated miscibility gap of $\text{In}_x\text{Ga}_{1-x}\text{N}$ grown by MOVPE and the data points (▲■) are from the measurements observed by Piner <i>et al.</i> .....	70
3-5. Flow chart of the HF-SCF procedure. ....	72
3-6. Structures used to compute the total energy for the $\text{In}_x\text{Ga}_{1-x}\text{N}$ vs. indium mole fraction. ....	73
4-1. Schematic representation of the formation of misfit dislocations: (a) unstrained lattice; (b) thickness of the film is less than $h_c$ ; (c) thickness of the film is greater than $h_c$ misfit dislocations are generated. ....	77
4-2. Model of epitaxial interface between two semi-infinite crystals resolved in a sequence of misfit dislocations spaced at an average distance $p$ . ....	81
4-3. Homogeneous strain energy, $E_{hs}$ for the 1 <sup>st</sup> InN epilayer and dislocation energy, $E_d$ vs. the misfit, $f$ on GaN substrate. ....	83
4-4. Homogeneous strain energy, $E_{hs}$ for the 1 <sup>st</sup> InN epilayer and dislocation energy, $E_d$ vs. the misfit, $f$ on AlN substrate. ....	84

4-5. Homogeneous strain energy, $E_{hs}$ for the 1 <sup>st</sup> InN epilayer and dislocation energy, $E_d$ vs. the misfit, $f$ on Al <sub>2</sub> O <sub>3</sub> substrate. ....	84
4-6. Homogeneous strain energy, $E_{hs}$ for the 1 <sup>st</sup> InN epilayer and dislocation energy, $E_d$ vs. the misfit, $f$ on Si substrate.....	85
4-7. Total energy $E_t$ , strain energy $E_s$ , interfacial energy $E_i$ vs. lattice constant of InN for 1 <sup>st</sup> epilayer InN on GaN substrate.....	89
4-8. Total energy $E_t$ , strain energy $E_s$ , interfacial energy $E_i$ vs. lattice constant of InN for 1 <sup>st</sup> epilayer InN on AlN substrate. ....	90
4-9. Total energy $E_t$ , strain energy $E_s$ , interfacial energy $E_i$ vs. lattice constant of InN for 1 <sup>st</sup> epilayer InN on Al <sub>2</sub> O <sub>3</sub> substrate.....	90
4-10. Total energy $E_t$ , strain energy $E_s$ , interfacial energy $E_i$ vs. lattice constant of InN for 1 <sup>st</sup> epilayer InN on Si substrate.....	91
5-1. Schematic for the deposition of the (0001)//(0001), [ $\bar{1}010$ ]/[ $\bar{1}210$ ] GaN/Al <sub>2</sub> O <sub>3</sub> system.....	96
5-2. Planes of Si (111) substrate. ....	96
5-3. Image and schematic of horizontal, cold-wall MOVPE reactor system.....	99
5-4. Indium Nitride (InN) growth sequence for each of the three substrates. ....	101
5-5. X-ray Diffraction (XRD) $\theta$ -2 $\theta$ scans for InN/LT-GaN on (a) Al <sub>2</sub> O <sub>3</sub> (0001) at N/In = 3000, T = 450, 550, 650, and 750 °C.....	102
5-6. X-ray Diffraction (XRD) $\theta$ -2 $\theta$ scan for InN/LT-GaN on (a) Al <sub>2</sub> O <sub>3</sub> (0001) at N/In = 3000, T = 450, 550, 650, and 750 °C. Pure In was removed by etching with HCl. ....	104
5-7. X-ray Diffraction (XRD) $\theta$ -2 $\theta$ scan for InN/LT-GaN on Al <sub>2</sub> O <sub>3</sub> (0001) at N/In = 50,000, T = 530, 550, and 570 °C. ....	105
5-8. X-ray Diffraction (XRD) $\theta$ -2 $\theta$ scan for InN/LT-InN on Al <sub>2</sub> O <sub>3</sub> (0001) at N/In = 50,000 and T = 500, 530, and 550 °C.....	105
5-9. Full Width Half Maximum (FWHM) of XRC for InN/LT-InN on Al <sub>2</sub> O <sub>3</sub> (0001) at N/In = 50,000 and T = 500, 530, and 550 °C. ....	106
5-10. X-ray Diffraction (XRD) $\theta$ -2 $\theta$ scan for InN/LT-InN on GaN/Al <sub>2</sub> O <sub>3</sub> (0001) at N/In = 50,000, T = 500, 530, and 550 °C.....	106
5-11. Full Width Half Maximum (FWHM) of XRC for InN/LT-InN on GaN/Al <sub>2</sub> O <sub>3</sub> (0001) at N/In = 50,000, T = 500, 530, and 550 °C. ....	107

5-12. X-ray Diffraction (XRD) $\theta$ - $2\theta$ scan for InN/LT-GaN on Si (111), at N/In = 50,000, T = 500, 530, 550, and 570 °C. ....	108
5-14. Growth rate of InN on various substrates (a) InN/LT-GaN on Al <sub>2</sub> O <sub>3</sub> (0001) at N/In = 3000, (b) for InN/LT-GaN on Al <sub>2</sub> O <sub>3</sub> (0001) at N/In = 50,000, (c) InN/LT-InN on GaN/Al <sub>2</sub> O <sub>3</sub> (0001) at N/In = 50,000, and (d) InN/LT-InN on Si (111) at N/In = 50,000 .....	109
5-15. Cross-sectional SEM micrographs of InN for 60 min growth at 530, 550, and 570 °C, and N/In = 50,000 with LT-GaN buffer. ....	110
5-16. X-ray Diffraction (XRD) $\theta$ - $2\theta$ scan for InN/LT-InN (T <sub>LT-InN</sub> = 450 °C) on Al <sub>2</sub> O <sub>3</sub> (0001) at N/In = 50,000, and T <sub>LT-InN</sub> = 450 °C without and with nitridation. ....	111
5-17. X-ray Diffraction (XRD) $\theta$ - $2\theta$ scan for InN/LT-InN GaN/Al <sub>2</sub> O <sub>3</sub> (0001) at N/In = 50,000, T = 530 °C, and T <sub>LT-InN</sub> = 450, 500 °C with and without nitridation. ....	112
5-18. X-ray Diffraction (XRD) $\theta$ - $2\theta$ scan for (a) InN/LT-InN on Si (111), at N/In = 50,000, T = 530 °C, and T <sub>LT-InN</sub> = 450, 500 °C with the nitridation and without the nitridation. ....	113
5-19. Electron Spectroscopy of Chemical Analysis (ESCA) spectra of Si 2p <sub>3</sub> peak for Si annealed at 850 °C in 1.0 slm N <sub>2</sub> (a) with 100% NH <sub>3</sub> at 1.0 slm (b) without NH <sub>3</sub> .....	114
5-20. X-ray Diffraction (XRD) $\theta$ - $2\theta$ scan at N/In=20,000, 30,000, and 50,000, T = 550 °C for InN/LT-GaN on Al <sub>2</sub> O <sub>3</sub> (0001) at N/In of 50,000.....	115
5-21. Full Width Half Maximum (FWHM) of XRC for InN/LT-GaN on Al <sub>2</sub> O <sub>3</sub> (0001) at N/In of 50,000. ....	116
5-22. X-ray Diffraction (XRD) $\theta$ - $2\theta$ scan for InN/LT-InN on GaN/Al <sub>2</sub> O <sub>3</sub> (0001) at, T = 530 °C, T <sub>LT-InN</sub> = 400 °C, and N/In = 30,000 and 50,000.....	116
5-23. X-ray Diffraction (XRD) $\theta$ - $2\theta$ scan for InN/LT-GaN on Si (111) at N/In = 20,000, 30,000 and 50,000, T = 530 °C. ....	117
5-24. Growth rate vs. N/In ratio for InN/LT-GaN on Al <sub>2</sub> O <sub>3</sub> (0001), GaN/Al <sub>2</sub> O <sub>3</sub> (0001), and Si (111) at N/In = 6000, 9000, 12,000, and 15,000 with T = 550 °C, TMI = 0.26 sccm and NH <sub>3</sub> = 1600-4000 sccm.....	118
5-25. X-ray Diffraction (XRD) $\theta$ - $2\theta$ scan for InN/LT-InN on Al <sub>2</sub> O <sub>3</sub> (0001) at N/In = 50,000, T = 530 °C, and T <sub>LT-InN</sub> = 400, 450, and 500 °C.....	119
5-26. X-ray Diffraction (XRD) $\theta$ - $2\theta$ scan for InN/LT-InN on GaN/Al <sub>2</sub> O <sub>3</sub> (0001) at T = 530 °C, T <sub>LT-InN</sub> = 350, 400, 450, and 500 °C, and N/In = 50,000.....	120

5-27. Full Width Half Maximum (FWHM) of XRC for InN/LT-InN on GaN/Al <sub>2</sub> O <sub>3</sub> (0001) at T = 530 °C, T <sub>LT-InN</sub> = 350, 400, 450, and 500 °C, and N/In = 50,000.....	120
5-28. X-ray Diffraction (XRD) $\theta$ -2 $\theta$ scan for InN/LT-InN on Si (111) at N/In = 50,000, T = 530 °C, and T <sub>LT-InN</sub> = 400, 450, and 500 °C.....	121
5-29. X-ray Diffraction (XRD) $\theta$ -2 $\theta$ scan for InN/LT-InN on Si (111) at N/In = 50,000, T = 530 °C, T <sub>LT-InN</sub> = 450 °C, and t = 5, 15, and 30 min. ....	121
5-30. X-ray Diffraction (XRD) $\theta$ -2 $\theta$ scan for InN/LT-InN (T <sub>LT-InN</sub> = 450 °C) and LT-GaN (T <sub>LT-GaN</sub> = 560 °C) on Al <sub>2</sub> O <sub>3</sub> (0001) at N/In = 50,000, T = 530 °C (LT-InN buffer) and T = 550 °C (LT-GaN buffer). ....	122
5-31. Full Width Half Maximum (FWHM) of XRC for InN/LT-InN (T <sub>LT-InN</sub> = 450 °C) and LT-GaN (T <sub>LT-GaN</sub> = 560 °C) on Al <sub>2</sub> O <sub>3</sub> (0001) at N/In = 50,000, T = 530 °C (LT-InN buffer) and T = 550 °C (LT-GaN buffer).....	123
5-32. Root Mean Square (RMS) roughness by ATM for (a) InN/LT-InN (T = 530 °C, T <sub>LT-InN</sub> = 450 °C), (b) InN/LT-GaN (T = 550 °C, T <sub>LT-GaN</sub> = 560 °C), (c) as-grown LT-InN (450 °C), and (d) as-grown LT-GaN (560 °C) on Al <sub>2</sub> O <sub>3</sub> (0001) at N/In=50,000.....	124
5-33. X-ray Diffraction (XRD) $\theta$ -2 $\theta$ scan for InN/LT-InN and InN/LT-GaN on Si (111) at N/In = 50,000, T = 530 °C, T <sub>LT-InN</sub> = 450 °C, and T <sub>LT-InN</sub> = 560 °C.....	125
5-34. X-ray Diffraction (XRD) $\theta$ -2 $\theta$ scan for InN/LT-InN on GaN/Al <sub>2</sub> O <sub>3</sub> (0001) at N/In = 50,000, T <sub>LT-InN</sub> = 450 and 500 °C and T = 530 °C with the different growth pressure of LT-InN. ....	126
5-35. X-ray Diffraction (XRD) $\theta$ -2 $\theta$ scan for InN/LT-InN on Si (111) at N/In = 50,000, T <sub>LT-InN</sub> = 450 and 500 °C and T = 530 °C with two different growth pressures for LT-InN.....	126
5-36. Photoluminescence for (a) InN grown on Al <sub>2</sub> O <sub>3</sub> (0001) at T = 530 °C, T <sub>LT-InN</sub> = 500 °C, (b) InN grown on GaN/Al <sub>2</sub> O <sub>3</sub> (0001) at T = 530 °C, T <sub>LT-InN</sub> = 400 °C, (c) InN grown on Si (111) substrate at T <sub>LT-GaN</sub> = 560 °C, T = 550 °C and N/In = 50,000.....	128
5-37. Carrier concentrations and mobilities of InN films grown with different growth conditions at different characterization temperature using Hall measurement.....	128
5-38. Carrier concentration and mobility of InN on Si (111) at different characterization temperature using Hall measurement. ....	129

5-39. Scanning Electron Microscopy (SEM) and EDS for the surface of InN/LT-GaN on Al <sub>2</sub> O <sub>3</sub> (0001) at N/In = 3000, 6000, 9000, 20,000, 30,000, and 50,000.	131
5-40. Number density of indium droplets vs. N/In ratio depending on different N/In, when InN was grown on Al <sub>2</sub> O <sub>3</sub> (0001) at T = 550 °C and N/In = 3000, 6000, 9000.	132
5-41. Percent (%) vs. indium droplet size depending on different N/In, when InN was grown on Al <sub>2</sub> O <sub>3</sub> (0001) at T = 550 °C and N/In = 3000, 6000, 9000.	132
5-42. X-ray Diffraction (XRD) $\theta$ -2 $\theta$ scans for InN/LT-GaN on Al <sub>2</sub> O <sub>3</sub> (0001) at N/In = 3000, T = 450, 550, 650, and 750 °C before HCl wet etching.	133
5-43. X-ray Diffraction (XRD) $\theta$ -2 $\theta$ scans for InN/LT-GaN on Al <sub>2</sub> O <sub>3</sub> (0001) at N/In = 3000, T = 450, 550, 650, and 750 °C after HCl wet etching.	133
5-44. X-ray Diffraction (XRD) $\theta$ -2 $\theta$ scan for InN/LT-GaN on Si (111) at N/In = 3000, T = 450, 550, 650, and 750 °C before HCl wet.	134
5-45. X-ray Diffraction (XRD) $\theta$ -2 $\theta$ scan for InN/LT-GaN on Si (111) at N/In = 3000, T = 450, 550, 650, and 750 °C after HCl wet etching.	134
5-46. Characterization result by AES for In droplets formed during the growth of InN on Al <sub>2</sub> O <sub>3</sub> (0001) with LT-GaN buffer layer before the HCl wet etching after the HCl wet etching at N/In = 3000.	135
5-47. Full Width Half Maximum (FWHM) of XRC of InN/LT-InN (450 °C) on Al <sub>2</sub> O <sub>3</sub> (0001) at T = 450 °C in N <sub>2</sub> flow with different annealing time (0, 10, 30, 60 and 90 min).	137
5-48. Full Width Half Maximum (FWHM) of XRC of InN/LT-InN (400 °C) on GaN/Al <sub>2</sub> O <sub>3</sub> (0001) at T = 450 °C in N <sub>2</sub> flow with different annealing time (0, 10, 30, and 60 min).	137
5-49. Schematic for three types of inlet tubes used for the Fluent simulation.	141
5-50. Flow of NH <sub>3</sub> in the reactor with the current inlet tube.	142
5-51. Flow of NH <sub>3</sub> 1 mm above the surface of substrate with the current inlet tube.	142
5-52. Flow of NH <sub>3</sub> in the reactor with the horizontally extended inlet tube.	142
5-53. Flow in the reactor with the vertical inlet tube.	143
5-54. Flow of NH <sub>3</sub> 1 mm above the surface of substrate with the vertical inlet tube.	143
5-55. X-ray Diffraction (XRD) $\theta$ -2 $\theta$ scan for InN/LT-InN on Al <sub>2</sub> O <sub>3</sub> (0001) at N/In = 50,000, T = 530 °C and T <sub>LT-InN</sub> = 450 °C with different inlet tubes.	146

5-56. Full Width Half Maximum (FWHM) of XRC for InN/LT-InN on Al <sub>2</sub> O <sub>3</sub> (0001) at N/In = 50,000, T = 530 °C and T <sub>LT-InN</sub> = 450 °C with different inlet tubes. ....	146
5-57. Cross-sectional SEM for InN/LT-InN on Al <sub>2</sub> O <sub>3</sub> (0001) at N/In = 50,000, T = 530 °C, and T <sub>LT-InN</sub> = 450 °C with the horizontal and vertical inlet tubes..	147
5-58. X-ray Diffraction (XRD) $\theta$ -2 $\theta$ scan for InN/LT-InN on GaN/Al <sub>2</sub> O <sub>3</sub> (0001) at N/In = 50,000, T = 530 °C and T <sub>LT-InN</sub> = 450 °C with different inlet tubes.	147
5-59. Full Width Half Maximum (FWHM) of XRC for InN/LT-InN on GaN/Al <sub>2</sub> O <sub>3</sub> (0001) at N/In = 50,000, T = 530 °C and T <sub>LT-InN</sub> = 450 °C with different inlet tubes. ....	148
5-60. Cross-sectional SEM for InN/LT-InN on GaN/Al <sub>2</sub> O <sub>3</sub> (0001) at N/In = 50,000, T = 530 °C and T <sub>LT-InN</sub> = 400 °C with the horizontal and the vertical inlet tubes. ....	148
5-61. Grazing Angle Incident X-ray Diffraction (GIXD) for InN grown on Al <sub>2</sub> O <sub>3</sub> (0002) with the incident angle of 1 degree when the horizontal inlet tube was used. ....	149
5-62. Grazing Angle Incident X-ray Diffraction (GIXD) for InN grown on GaN/Al <sub>2</sub> O <sub>3</sub> (0002) with the incident angle of 1 degree when the horizontal inlet tube was used. ....	150
5-63. Grazing Angle Incident X-ray Diffraction (GIXD) for InN grown on (a) Al <sub>2</sub> O <sub>3</sub> (0002) and (b) GaN/Al <sub>2</sub> O <sub>3</sub> (0002) with the incident angle of 1 degree when the vertical inlet tube was used.....	151
5-64. X-ray Diffraction (XRD) $\theta$ -2 $\theta$ scan of InN/LT-InN/GaN/LT-GaN on Si (111) at N/In = 50,000, T = 530 °C and T <sub>LT-InN</sub> = 400 °C for both horizontal and vertical inlet tubes. ....	151
5-65. Full Width Half Maximum (FWHM) of XRC of InN/LT-InN on Al <sub>2</sub> O <sub>3</sub> (0001) at N/In = 50,000, T = 530 °C for both horizontal and vertical inlet tubes. The annealing test is performed at T = 450 °C for 30 min.....	152
5-66. Full Width Half Maximum (FWHM) of XRC of InN/LT-InN on GaN/Al <sub>2</sub> O <sub>3</sub> (0001) at N/In = 50,000, T = 530 °C for both horizontal and vertical inlet tubes. The annealing test is performed at T = 450 °C for 30 min. ....	152

Abstract of Dissertation Presented to the Graduate School  
of the University of Florida in Partial Fulfillment of the  
Requirements for the Degree of Doctor of Philosophy

INDIUM NITRIDE GROWTH BY METAL-ORGANIC VAPOR PHASE EPITAXY

By

Taewoong Kim

August 2006

Chair: Timothy J. Anderson

Major Department: Chemical Engineering

InN and In-rich compositions of  $\text{In}_x\text{Ga}_{1-x}\text{N}$ , have potential for a variety of device applications including solar cells. This work addresses the growth of high quality InN by metalorganic vapor phase epitaxy. To better understand the material a thermodynamic assessment of the In-N-C-H system was performed to yield the In-N P-T diagram. In addition, the InN critical thickness was calculated for several candidate substrates to guide substrate selection. Furthermore, computational fluid dynamics was used to design an improved reactor. A vertical  $\text{NH}_3$  tube design produced the lowest reported  $\Omega$ -2 $\theta$  rocking curve FWHM value of (574 arcsec) for InN grown on GaN/ $\text{Al}_2\text{O}_3$  (0001). The film surface was also mirror-like as judged by AFM (RMS roughness = 4.2 nm). The PL peak energy of 0.82 eV was obtained for InN grown on Si, consistent with recent reports of a considerably lower of bandgap energy.

## CHAPTER 1 INTRODUCTION

During the last few years the interest in indium nitride (InN) has brought remarkable attention due to its highly attractive inherent properties, such as high mobility and high saturation velocity [Yam02 and Yam04b].

Epitaxial growth of InN films by metal-organic vapor phase epitaxy (MOVPE), was first reported by Matsuoka *et al.* and Wakahara *et al.* in 1989 independently [Mat89, Wak89]. In the 1990s, epitaxial growth of InN films was performed by several scientists [Wak90, Yam94a, Yam94b, Guo95a, Guo95b, Uch96, Che97, Yam97a, Sat97a, Yam98a, Yan99, Tsu99, Pan99, Yam99a]. These studies included the growth by MOVPE and MBE on different substrates such as Si, GaAs, GaAsB, Al<sub>2</sub>O<sub>3</sub> and GaP over a wide range of growth conditions but had not shown any good results, however, no high quality films were produced.

Because of the low decomposition temperature of InN (~ 650 °C), poor lattice matched substrate, high equilibrium pressure of nitrogen, and the low cracking efficiency of NH<sub>3</sub> at the growth temperature, the growth of high quality InN film is challenging.

Since the bandgap energy of InN has recently been discovered to be ~ 0.7 eV,[Wu02] the use of InN with GaN and AlN make it possible to extend the emission of nitrided-based LEDs from ultraviolet to infrared regions. The bandgap energies of the semiconductor materials are shown in Fig.1.1. Alloying InN with GaN creates an In<sub>x</sub>Ga<sub>1-x</sub>N active layer that is suitable for light emitting devices because In<sub>x</sub>Ga<sub>1-x</sub>N considerably

increases luminescence efficiency due to the localized energy states formed by alloy composition fluctuations of the  $\text{In}_x\text{Ga}_{1-x}\text{N}$  [Nak92].

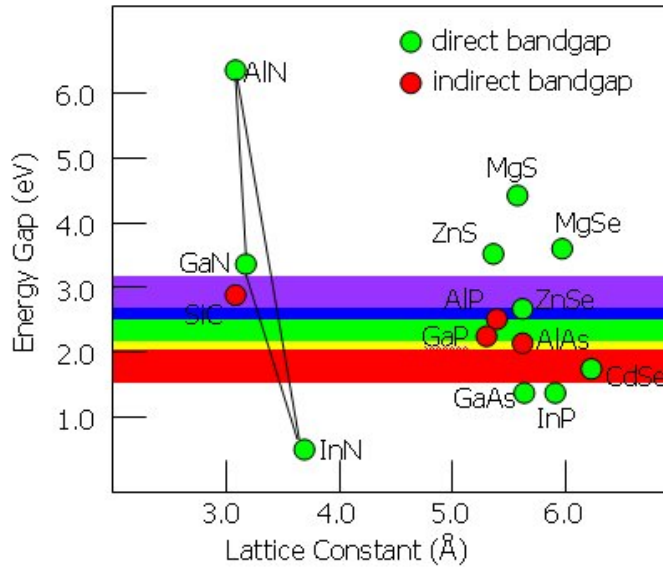


Figure 1-1. Bandgap energies  $E_g$  of the semiconductor materials.

InN was predicted to have the lowest effective mass for electrons among all III-nitride semiconductors, which leads to high mobility and high saturation (drift) velocity.

The theoretical maximum mobility calculated in InN at 300K is  $4400 \text{ cm}^2 \text{ V}^{-1} \text{ S}^{-1}$  ( $\text{GaN} \sim 1000 \text{ cm}^2 \text{ V}^{-1} \text{ S}^{-1}$ ) [Chi94]. It was found that InN exhibits an extremely high peak drift velocity of  $4.2 \times 10^7 \text{ cm/s}$  [Bel99]. Thus, InN is promising as a highly potential material for the fabrication of high-speed high-performance heterojunction field-effect transistors (FETs). The use of wurtzite InN would permit photonic devices in infrared and much faster electronic devices, because it could induce higher mobility and high peak (saturation) velocity than most other III-nitride based materials.

Single crystalline epitaxial InN films by MOVPE were first reported in [Mat98 and Wak89]. The typical FWHM of single crystalline InN grown by MOVPE is 4000 - 5500 arcsec [Che97]. Significant improvement in the growth of InN film has been made by

MOVPE during the last few years. The average reported data on FWHM of the X-ray Rocking Curve (XRC) is ~2000 arcsec for single crystal InN [Yam01b, Yan02a, and Yam04a] which may indicate that the highest crystalline quality of this material has not been achieved yet. The high crystalline quality InN can reduce the leakage current and extend the lifetime of the laser diodes (LDs) due to reduced dislocations. Therefore, the growth of high quality crystalline InN is essential to obtain high performance devices.

The highest mobility and lowest background carrier concentration of InN by MOVPE are reported to be  $900 \text{ cm}^2/\text{Vs}$  and  $5 \times 10^{18} \text{ cm}^{-3}$ , [Yam04b]. Better results were achieved using molecular beam epitaxy (MBE), and the highest reported data on mobility and lowest background carrier concentration of InN are  $2050 \text{ cm}^2/\text{Vs}$  and  $3.49 \times 10^{17} \text{ cm}^{-3}$ , respectively [Lu02a].

In addition, InN has potential for highly efficient low cost solar cell. Yamamoto *et al.* proposed InN for a top cell material of a two-junction tandem solar cell [Yam94a].

In summary, InN is a very attractive material for semiconductor device applications and high structural quality, low defect density material with high mobility and low carrier concentration has not been achieved to date. Therefore, more research is needed for the improvement of crystalline quality, transport and optical properties of InN epitaxial films by MOVPE.

## CHAPTER 2 LITERATURE REVIEW

### 2.1 Indium Nitride (InN) and Indium Gallium Nitride (In<sub>x</sub>Ga<sub>1-x</sub>N) Properties

In this section, the fundamental properties of InN and In<sub>x</sub>Ga<sub>1-x</sub>N such as structural, physical, electrical, and optical properties will be discussed. The understandings of these properties are important when selecting a suitable substrate and buffer layer for obtaining high quality InN and In<sub>x</sub>Ga<sub>1-x</sub>N films. Also, possible applications of InN and In<sub>x</sub>Ga<sub>1-x</sub>N will be assessed.

#### 2.1.1 Structural Properties

Lattice parameters of the wurtzite crystalline structure of InN was first reported as  $a = 3.53 \text{ \AA}$  and  $c = 5.69 \text{ \AA}$  [Juz38]. However, the lattice parameter in the rf-sputtered InN film measured by Tansley and Folsey,  $a = 3.548 \text{ \AA}$  and  $c = 5.760 \text{ \AA}$  [Tan86a], showing a slight increase in the lattice parameter values, which also differs from the lattice parameter measured in the rf-sputtered InN film by Kubota *et al.*,  $a = 3.540 \text{ \AA}$  and  $c = 5.705 \text{ \AA}$  [Kub89]. The crystalline quality of InN obtained by Kubota *et al.* was higher than the other previously reported InN films and the lattice parameter is much closer with the lattice parameter measured in the single crystalline InN film. Based on the recent results reported by Davydov, the lattice parameter in the high quality single crystal hexagonal InN film was reported to be  $a = 3.5365 \text{ \AA}$  and  $c = 5.7039 \text{ \AA}$  [Dav02a]. The lattice parameters for polycrystalline and single crystalline InN reported by several groups are plotted in Fig. 2.1 [Bhu03b]. Probable reasons for the variation in lattice parameter are different crystalline quality and oxygen incorporation [Yam03].

pattern [Lim99]. At 2002, Bhattacharya *et al.* reported the observation of zincblende phase in InN thin film grown by pulsed laser deposition (PLD) and measured a lattice constant of  $5.09 \pm 0.04 \text{ \AA}$  [Bha02]. The different lattice constants of InN were summarized in Table 2-1.

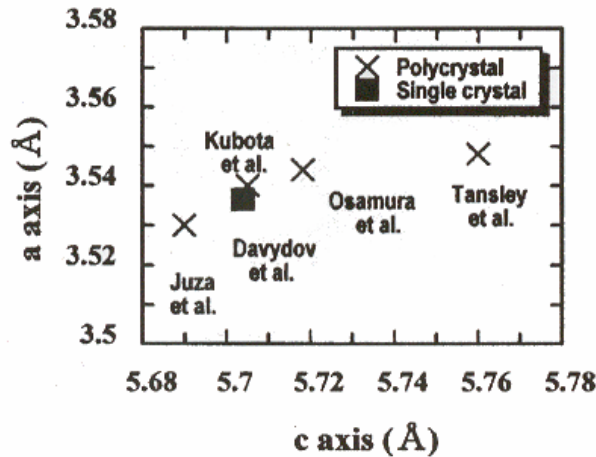


Figure 2-1. Lattice parameter for polycrystalline and single crystalline InN reported by different groups.

Table 2-1. Lattice constants of InN.

Structure	a (Å)	c (Å)	References
Wurtzite	3.53	5.69	Zuda and Hahn [Juz38]
Wurtzite	3.548	5.760	Tansley and Foley [Tan86a]
Wurtzite	3.540	5.705	Kubota [Kub89]
Wurtzite	3.5365	5.7039	Davydov [Dav02a]
Zincblende	4.98		Strite [Str93]
Zincblende	4.98-5.04		Lima [Lim99]
Zincblende	$5.09 \pm 0.04$		Bhattacharya [Bha02]

$\text{In}_x\text{Ga}_x\text{N}$  films were usually deposited on GaN buffer layers, because the lattice constant of  $\text{In}_x\text{Ga}_x\text{N}$  is closer to that of GaN than sapphire when the mole fraction of indium (x) in  $\text{In}_x\text{Ga}_x\text{N}$  is less than 0.3.

The indium mole fraction of  $\text{In}_x\text{Ga}_{1-x}\text{N}$  films is estimated from the lattice constant along with the *c* axis measured by x-ray diffraction, assuming that the lattice constant

changes linearly with the indium mole fraction given (Eq. 2-1). In the calculation,  $a_{\text{GaN}} = 3.189 \text{ \AA}$ ,  $c_{\text{GaN}} = 5.178 \text{ \AA}$ ,  $a_{\text{InN}} = 3.548 \text{ \AA}$  and  $c_{\text{InN}} = 5.7034 \text{ \AA}$  [Nak02, Qia02, Yos91]. The fundamental properties of GaN and InN are listed below in Table 2-2.

$$a_{\text{In}_x\text{Ga}_{1-x}\text{N}} = x a_{\text{InN}} + (1-x) a_{\text{GaN}}$$

$$c_{\text{In}_x\text{Ga}_{1-x}\text{N}} = x c_{\text{InN}} + (1-x) c_{\text{GaN}} \quad (2-1)$$

Table 2-2. Properties of GaN and InN.

Fundamental properties of GaN		Fundamental properties of InN	
Wurtzite type:		Wurtzite type:	
Band gap energy	$E_g(300\text{K})= 3.39 \text{ eV}$ $E_g(1.6\text{K})= 3.50 \text{ eV}$	Band gap energy	$E_g(300\text{K})= 0.6\text{-}0.9 \text{ eV}$
Temperature coeff.	$dE_g/dT=-6.0 \times 10^{-4} \text{ eV/K}$	Temperature coeff.	$dE_g/dT=-1.8 \times 10^{-4} \text{ eV/K}$
Pressure coefficient	$dE_g/dT= 4.2 \times 10^{-3} \text{ eV/kbar}$	Lattice constants <sup>a</sup>	$a=3.537 \text{ \AA}$ $c=5.704 \text{ \AA}$
Lattice constants	$a=3.189 \text{ \AA}$ $c=5.185 \text{ \AA}$	Thermal expansion	$\Delta a/a \approx 4 \times 10^{-6} \text{ K}$ $\Delta c/c \approx 3 \times 10^{-6} \text{ K}$
Thermal expansion	$\Delta a/a= 5.59 \times 10^{-6} \text{ K}$ $\Delta c/c= 3.17 \times 10^{-6} \text{ K}$	Thermal conductivity	$\kappa=0.8 \pm 0.2 \text{ W/cm K}$
Thermal conductivity	$\kappa=1.3 \text{ W/cmK}$	Index of refraction	$n=2.9\text{-}3.05$
Index of refraction	$n(1 \text{ eV}) = 2.33$ $n(3.38 \text{ eV}) = 2.67$	Zincblende polytype:	
Zincblende polytype:		Band gap energy	$E_g(300\text{K})= 2.2 \text{ eV}$
Band gap energy	$E_g(300\text{K})= 3.2\text{-}3.3 \text{ eV}$	Lattice constant <sup>b</sup>	$a=5.09 \text{ \AA}$
Lattice constants	$a= 4.52 \text{ \AA}$		
Index of refraction	$n(3 \text{ eV ?})= 2.9$		

[<sup>b</sup>Bha02, <sup>a</sup>Dav02a, Mor94]

In summary, the different lattice constants of InN obtained by several scientists were discussed. The difference of lattice constants is thought to be caused by the difference in the crystalline quality of InN. The lattice constant of  $\text{In}_x\text{Ga}_x\text{N}$  can be calculated by using the Vegard's law with the lattice constants of InN and GaN.

### 2.1.2 Physical Properties

Directly measured density of wurtzite InN is  $6.89 \times 10^3 \text{ kg m}^{-3}$  at 25 °C [Hah40]. A comparable value of  $6.81 \times 10^3 \text{ kg m}^{-3}$  has been estimated from X-ray data [Pea67]. The cell volume, taken in conjunction with a molar mass of  $128.827 \text{ g mol}^{-1}$ , yields densities of  $(6.81 \pm 0.05) \times 10^3 \text{ kg m}^{-3}$  and  $6.97 \times 10 \text{ kg m}^{-3}$  for the wurtzite and zinc blende polytypes, respectively. Bulk modulus has been calculated from first principles by a local-density approximation [Cam90] and by a linear muffin-tin orbital method [Kub89], suggesting a value of  $B = 165 \text{ GPa}$ .

The five distinguishable second-order elastic moduli in a hexagonal crystal are  $c_{11}$ ,  $c_{12}$ ,  $c_{13}$ ,  $c_{33}$  and  $c_{44}$ . Other researchers have utilized empirical and theoretical approaches to calculate the thermoelastic properties of the wurtzite structure InN [She91, Kim96a, Wri97, Mar98, Chi99]. Table 2-3 summarizes the room-temperature elastic constants from both experimental and theoretical results. Estimates of the principal transverse and longitudinal elastic constants  $c_t$  and  $c_l$  are given in Table 2-4.

Table 2-3. Elastic constants of wurtzite InN at room temperature.

Elastic constants	Sheleg and Savastenko [She79]	Kim et al. [Kim96a]	Wright [Wri97]	Marmalyuk et al. [Mar98]	Chisholm et al. [Chi99]
$C_{11}$ (GPa)	190	271	223	257	297.5
$C_{12}$ (GPa)	104	124	115	92	107.4
$C_{13}$ (GPa)	121	94	92	70	108.7
$C_{33}$ (GPa)	182	200	224	278	25.05
$C_{44}$ (GPa)	9.9	46	48	68	89.4

[Wan01]

Table 2-4. Physical properties of InN.

Property	Value	Ref.	Comments
----------	-------	------	----------

Density (wurtzite)	$6.89 \times 10^3 \text{ kg m}^{-3}$ $(6.81 \pm 0.05) \times 10^3 \text{ kg m}^{-3}$	H. Hahn -	Meas. by displacement Various X-ray data
Density (zinc blende)	$6.97 \times 10^3 \text{ kg m}^{-3}$	S. Strite	X-ray data
Molar mass	$128.827 \text{ g mol}^{-1}$		
Mol. Vol. (wurtzite)	$31.2 \text{ \AA}^3$		From lattice constants
Mol. Vol. (zinc blende)	$30.9 \text{ \AA}^3$		From lattice constants
$c_t$	$4.42 \times 10^{11} \text{ dyn cm}^{-2}$	V. W. Chin	Estimate
$c_l$	$2.65 \times 10^{12} \text{ dyn cm}^{-2}$	V. W. Chin	Estimate
Deformation potential	$7.1 \text{ eV}$	V. W. Chin	Estimate
$\hbar\omega_{\text{TO}}$	$59.3 \text{ meV (478 cm}^{-1}\text{)}$	K. Osamura	Reflectance meas.
	$57.1 \text{ meV (460 cm}^{-1}\text{)}$	T. L. Tansley	Transmission meas.
	$86.2 \text{ meV (694 cm}^{-1}\text{)}$	K. Osamura	Est.-Brout sum rule
$\hbar\omega_{\text{LO}}$	$89.2 \text{ meV (719 cm}^{-1}\text{)}$	T. L. Tansley	Est.-Brout sum rule

[Edg94], (reprinted from the Institute of Electrical Engineers with the permission of INSPEC)

The piezoelectric constant has not been reported, but its dependence on the dielectric constants  $\epsilon_r$  and  $\epsilon_{14}$  [Wol89] allows values of about 50 % of those found in AlN to be inferred [Chi94].

Indium nitride has twelve phonon modes at the zone centre (symmetry group  $C_{6v}$ ), three acoustic and nine optical with the acoustic branches essentially zero at  $k = 0$ . The IR active modes are  $E_1(\text{LO})$ ,  $E_1(\text{TO})$ ,  $A_1(\text{LO})$  and  $A_1(\text{TO})$ . A transverse optical mode has been identified at  $478 \text{ cm}^{-1}$  (59.3 meV) by reflectance and  $460 \text{ cm}^{-1}$  (57.1 meV) by transmission [Tan88]. In both reports the location of a longitudinal optical mode is inferred from the Brout sum rule, giving respective values of  $694 \text{ cm}^{-1}$  (86.1 meV) and  $719 \text{ cm}^{-1}$  (89.2 meV).

In summary, the physical properties of InN films were briefly discussed, especially the elastic constants used to calculate the strain energy and thus estimate the critical thickness of InN film.

### 2.1.3 Electrical Properties of InN

#### 2.1.3.1 Background Defects

As-grown InN is always n-type with a very high background carrier concentration. There has been much speculation as to what species is responsible for the high background donor concentration in InN. Potential candidates for such high background donors are native defects, such as N vacancy or nitrogen antisite, and impurities, such as  $O_N$ ,  $Si_{In}$ , and possibly interstitial H.

According to the oldest and most common view, the nitrogen vacancy is the most probable reason for *n*-type conductivity of InN. Tansley and Foley [Tan84b] had speculated that the *n*-type behavior is caused by an antisite defect: N on an In site ( $N_{In}$ ), which they had suggested might be a double donor. Jenkins and Dow [Jen89] showed that the native defect responsible for naturally occurring *n*-type InN is a nitrogen vacancy. Another defect possibly responsible for the *n*-type character of InN is oxygen on an N site, which is not a native defect but is nevertheless likely to be present in significant concentration. It is most likely that every nitrogen vacancy donates a single donor but possibly donates three electrons to the conduction band [Jen89]. Tansley and Egan [Tan92a, Tan92b] have also speculated that the N vacancy might be the defect responsible for natural *n*-type character of InN. There is a simple approach to how the nitrogen vacancy contributes a donor in the as-grown InN film. The donor nature of the N vacancy is constructed as a missing N atom surrounded by four indium atoms that provide three valence electrons to complete the bonding octet with the five missing electrons of nitrogen. Two of these three electrons would be donated to the conduction band. Therefore, it has been believed that nitrogen vacancy is the dominant donor in the as-grown InN film [Yam01, Yam02].

In contrast with the above views, there are also some theoretical and experimental evidence, which argues against the nitrogen vacancy being responsible for the background n-type conductivity. Stampfl *et al.* [Sta00] performed first-principles density-functional calculation to investigate the electronic and atomic structure and formation energies of native defects and selected impurities (O, Si, and Mg) in InN. Their calculation showed that oxygen and silicon impurities act as donors and that they can easily be incorporated during growth.

At 2002, Look *et al.* [Loo02] presented a rule to determine donor and acceptor concentrations in degenerate InN. From a comparison with glow discharge mass spectroscopy measurement and the developed theory, they suggested that a potential candidate for the dominant donor in InN is H. However, the native defects also cannot be completely ruled out.

As discussed above both theoretical calculation and experimental result give conflicting views and opinions regarding the major reasons responsible for high n-type conductivity of as-grown InN film. However, on the basis of the data available in the literature, two major reasons can be concluded. One is native defects, mainly nitrogen vacancy, and one is impurities, mainly oxygen.

### **2.1.3.2 Hall mobility and Electron Concentration in Undoped InN**

The carrier concentrations and Hall mobilities reported for undoped InN films grown by a variety of techniques are plotted against the calendar year in Fig. 2.2 [Bhu03b].

The growth methods are divided into five categories: molecular beam epitaxy (MBE), metal-organic chemical vapor phase epitaxy (MOVPE), hydride vapor phase epitaxy (HVPE), sputtering, and others, including electron beam plasma method, reactive

evaporation and pulsed laser deposition. Until the 1980s most of the InN films were deposited using sputtering. The grown films were polycrystalline with a carrier concentration scattered from  $10^{18}$  to  $10^{21}$   $\text{cm}^{-3}$  and Hall mobility from 20 to 250  $\text{cm}^2/\text{Vs}$  with the exception of the results obtained by Tansley and Foley [Tan84a].

Tansley and Foley [Tan84a] attained a dramatic reduction of the carrier concentration with very high electron mobility. A room temperature electron mobility of 2700  $\text{cm}^2/\text{V s}$ , which reached a maximum value of 5000  $\text{cm}^2/\text{V s}$  at 150 K, was measured. These are the best electrical properties ever reported in InN. It should be noted that the InN was a polycrystalline. Unfortunately, the InN film prepared by reactive sputtering in other laboratories has not met these results of Tansley and Foley and has universally high carrier concentration near  $10^{20}$   $\text{cm}^{-3}$  and constantly low electron mobility of less than 100  $\text{cm}^2/\text{Vs}$ . The InN film grown by different techniques also showed the high carrier concentrations and low electron mobility.

Sato [Sat97b] achieved a carrier concentration of  $4 \times 10^{19}$   $\text{cm}^{-3}$  in the InN epitaxial layer grown on sapphire substrate by plasma-assisted MOVPE in 1997. However, there is no further improvement or report on the electrical properties of InN by plasma-assisted MOVPE.

The significant improvements in conventional MOVPE grown InN films started with the work of Yamamoto *et al.* and Pan *et al.* [Yam98a, Pan99] in which they reported an electron concentration of  $5 \times 10^{19}$   $\text{cm}^{-3}$  with a Hall mobility of about 300  $\text{cm}^2/\text{V s}$  in the InN film grown on sapphire substrate.

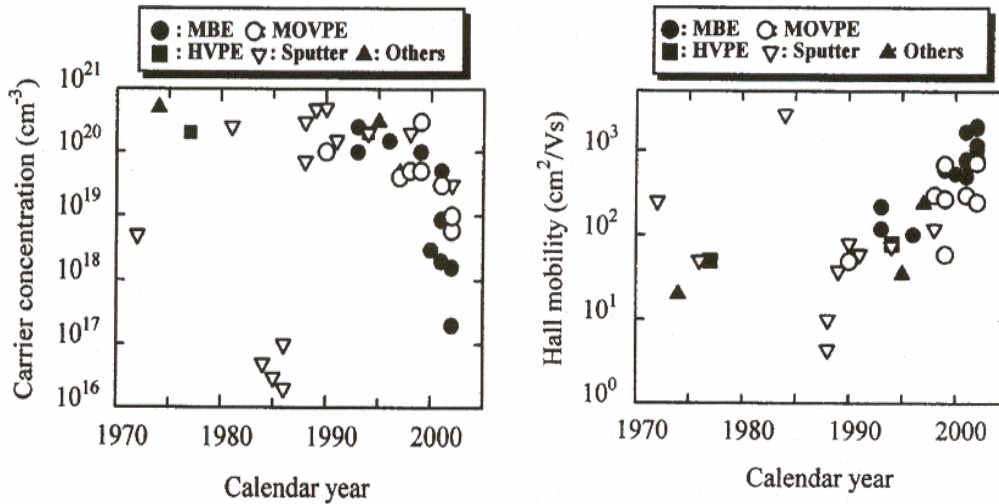


Figure 2-2. Carrier concentration and hall mobility reported for undoped InN film grown in a variety of technique is plotted against the calendar year.

Yamaguchi *et al.* [Yam99a] showed that using a GaN underlying layer increased InN film thickness and significantly improve the Hall mobility. A Hall mobility of about  $700 \text{ cm}^2/\text{V s}$  was obtained in the InN film grown on GaN even at an electron concentration of  $5 \times 10^{19} \text{ cm}^{-3}$ . Yamamoto *et al.* [Yam98a, Yam01, Yam02] showed a high  $\text{NH}_3/\text{TMI}$  molar ratio and enhanced  $\text{NH}_3$  decomposition (by growth temperature, atmospheric pressure growth, reduced flow velocity, etc.) significantly improved the electrical properties of MOVPE grown InN film.

As a result, a carrier concentration in the order of  $10^{18} \text{ cm}^{-3}$  and the electron mobility of  $730 \text{ cm}^2/\text{Vs}$  were reported. Recently, Yamamoto *et al.* [Yam04b] also reported a carrier concentration of  $5 \times 10^{18} \text{ cm}^{-3}$  and the electron mobility of  $900 \text{ cm}^2/\text{V s}$  for the MOVPE grown InN film.

Laser-assisted MOVPE has the potential to decompose  $\text{NH}_3$  photolytically independent of the substrate temperature [Bhu02a].

Lu *et al.* [Lu00] have obtained an electron concentration of  $3 \times 10^{18} \text{ cm}^{-3}$  with a Hall mobility of  $542 \text{ cm}^2/\text{V s}$  in the InN film grown by MEE (Migration Enhanced Epitaxy). They also showed that the Hall mobility for both growth methods, MEE and MBE, increases with film thickness. Similar thickness dependence in Hall mobility was also observed in the MOVPE grown InN film [Yam99a]. The thickness dependence of the Hall mobility is presumed to be caused by the reduced defect density away from the lattice-mismatched substrate. Higashiwaki and Matsui [Hig02] found that there was an immediate sharp increase in mobility up to a film thickness of 150 nm, beyond which it almost leveled out. The room-temperature Hall mobility as a function of InN thickness in the InN film grown by MBE, MPVPE, and MEE is shown in Fig. 2.3 [Hig02a].

Lu *et al.* [Lu02a] have achieved a carrier concentration in the order of  $10^{17} \text{ cm}^{-3}$  and a mobility of more than  $2000 \text{ cm}^2/\text{V s}$  for the thick InN film grown on HVPE grown on bulk GaN template. The use of a buffer layer of AlN, GaN or InN seems to contribute to the improvement of structural and electrical properties of MBE grown InN. The better electrical properties in the MBE InN film compared with the MOVPE are believed to be because the active nitrogen can be supplied independently of the growth temperature and reduced impurity incorporation in the MBE growth.

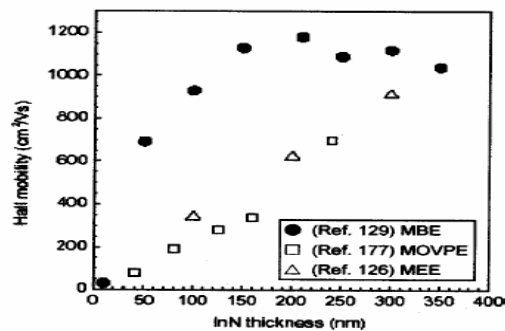


Figure 2-3. Room-temperature Hall mobility as a function of InN thickness in InN films grown by MBE, MOVPE, and MEE.

Table 2-5. Carrier concentration and Hall mobility for the different growth methods.

Growth methods	Carrier concentration (cm <sup>-3</sup> )	Hall mobility (cm <sup>2</sup> /V s)	References
MOVPE	$\sim 5 \times 10^{18}$	$\sim 900$	Yamamoto [Yam04b]
PA-MOVPE	$\sim 4 \times 10^{19}$	-	Sato [Sat97b]
HVPE	$\sim 10^{17}$	$\sim 2000$	Lu [Lu02a]
MBE	$10^{17}$ - $10^{20}$	600-1200	Bhuiyan [Bhu02a]
MEE	$\sim 3 \times 10^{18}$	$\sim 542$	Lu [Lu00]
Sputtering	$10^{18}$ - $10^{21}$	20-250	Bhuiyan [Bhu02a]

The typical range of carrier concentrations and mobilities for the different growth methods including MOVPE, PA-MOVPE, HVPE, MBE, MEE, and sputtering was discussed in detail and summarized in Table 2-5.

#### 2.1.4 Optical Properties of InN

Until 2001, the measured bandgap of 1.89 eV has been commonly accepted for InN [Tan86a]. However, a few groups recently showed by PL measurements that the band gap energy of InN is in between 0.65 and 0.90 eV, [Dav02a, Dav02b, Dav02c, Wu02, Tat02, Hor02, Sai02, Miy02] which is much smaller than 1.89 eV.

Evidence of a narrower band gap for InN was reported in 2001. Inushima *et al.* insisted that the fundamental absorption edge of MBE grown InN layer lies around 1.1 eV, which is much lower than the previously reported values [Inu01]. Davydov *et al.* reported a band gap value of 0.9 eV for high quality MBE grown InN, studied by means of optical absorption, PL, photoluminescence excitation (PLE) spectroscopy, as well as by *ab initio* calculation [Dav02a]. Figure 2-4 shows photoluminescence spectra for MBE grown InN sample which showed that the band gap of InN was much less than the previously reported value (around 1.9 eV) [Dav02a]. They further studied in detail with different high quality hexagonal InN films grown by different epitaxy methods. Analysis of optical absorption, PL, PLE, and photorefectivity data obtained on single crystalline hexagonal

InN film leads to the conclusion that the true band gap of InN is  $E_g \sim 0.7$  eV [Dav02b, Dav02c].

The larger band gap ( $\sim 1.89$  eV) cited in the literature may be due to the formation of oxynitrides, which have much larger band gaps than that of InN. As can be seen in Fig. 2.5, the energy gap data less than 1 eV were obtained for single crystalline InN film with a relatively low carrier concentration, while the larger values were mostly for polycrystalline InN film [Bhu03a]. It should also be pointed out that the band gap obtained from epitaxial films shows a remarkable dependence of carrier concentration, which is different from the larger one obtained from polycrystalline films. Polycrystalline films show a similar band gap ( $\sim 2$  eV) in spite of the wide range variation of carrier concentration  $10^{16}$ - $10^{21}$   $\text{cm}^{-3}$ .

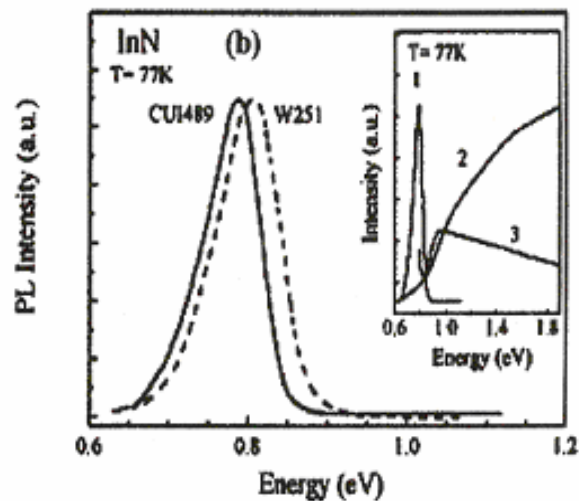


Figure 2-4. Photoluminescence spectra for MBE grown InN.

As Motlan *et al.* [Mol02] reported, oxygen incorporation is one of the causes for the large band gap energy. Therefore, the larger values may be related to oxygen incorporation into grown InN because polycrystalline films can contain a high density of oxygen atoms at their grain boundaries.

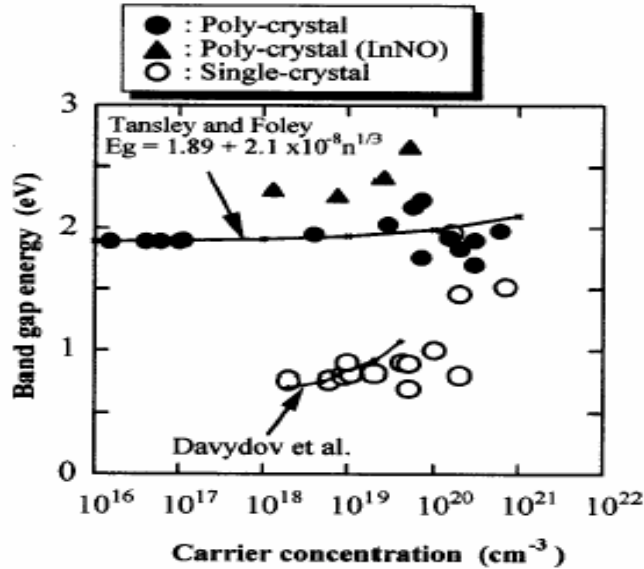


Figure 2-5. Band gap energy for InN films as a function of carrier concentration.

Davydov *et al.* [Dav02c] showed that the sample with band gap in the region of 1.8-2.1 eV contained up to 20 % of oxygen, much higher than for samples with narrow band gap. It can be assumed that oxygen is responsible for a high concentration of defects. Therefore, this increase of the band gap energy can be caused by formation of oxynitrides, which have a much larger band gap than that of InN.

### 2.1.5. Indium Nitride (InN) and Indium Gallium Nitride ( $\text{In}_x\text{Ga}_{1-x}\text{N}$ ) Applications

The latest progress in improving the InN film quality indicates that the InN film almost meets the requirements for application to practical devices. Nowadays, the bandgap energy of InN is known as 0.7 eV and thus  $\text{In}_x\text{Ga}_{1-x}\text{N}$  layers can be used as absorber layers in tandem solar cells where the mole fraction of indium ( $x$ ) is varied from 0 to 1 which tunes the bandgap from 0.7 to 3.4 eV. This energy range covers the majority of the solar spectrum, therefore improving efficiency.

In addition to the tandem solar cells, InN can also be applied to LED and LD similar to other III-V nitride compounds. Because the reported band gap value of InN is about 0.7 eV, which is compatible with the wavelength of the optical fiber, another very

important potential application of InN, fabrication of high-speed LD and PD in the optical communication system, is expected.

It is expected to be a highly promising material for the fabrication of high performance high electron mobility transistor (HEMT). InN as a HEMT channel requires a larger band gap barrier to induce and confine electrons. The significant lattice mismatch between InN and GaN or AlN can result in a large piezo-electric charge, which is very advantageous for HEMT applications. The strained  $\text{In}_x\text{Ga}_{1-x}\text{N}$  or  $\text{In}_x\text{Al}_{1-x}\text{N}$  is also a good choice as a barrier layer.

$\text{In}_x\text{Ga}_{1-x}\text{N}$  is a very important compound semiconductor among III-V nitride compounds because the  $\text{In}_x\text{Ga}_{1-x}\text{N}$  active layer emits light by the recombination of the injected electrons and holes into this active layer. The addition of a small amount of indium into the GaN was very important in obtaining a strong band-to-band emission because GaN without the indium could not emit a strong band-to-band emission at RT. This reason is considered to be related to deep localized energy states.

Currently,  $\text{In}_x\text{Ga}_{1-x}\text{N}$  is usually applied for the active layer in LEDs and LDs for this characteristic of the deep localized energy states, which can facilitate the efficiency of the band-to-band emission. For  $\text{In}_x\text{Ga}_{1-x}\text{N}$ -based LDs, however, the TDs (threading dislocations) density had to be decreased to lengthen the lifetime by using the ELOG (Epitaxial Lateral Overgrowth). For  $\text{In}_x\text{Ga}_{1-x}\text{N}$ -based LEDs, the lifetime of the LEDs is more than 100,000 hours in spite of the large number of dislocations. This difference in lifetime-behavior between LDs and LEDs is probably caused by the difference in the operating current density in the two devices. The operating current density of LDs is about one order higher than that of LEDs. Numerous studies have investigated the origin

of these defects, and their effects on the structural, optical, electronic, and morphological properties of heteroepitaxial  $\text{In}_x\text{Ga}_{1-x}\text{N}$  layers [Chen06, Cho04, Jin06, Lil06].

## **2.2 Thermodynamic Analysis and Phase Separation in the $\text{In}_x\text{Ga}_{1-x}\text{N}$ System**

Thermodynamics give the guideline for the epitaxial growth process for all techniques, including MOVPE, since epitaxial growth is simply a highly controlled phase transition. A thermodynamic understanding of epitaxy allows the determination of alloy composition as well as the solid stoichiometry.

The thermodynamics of mixing of semiconductor alloys (III/V, II/VI, and IV/IV) determines many characteristics of the growth process as well as the properties of the resultant materials. For example, Thermodynamic factors may limit the mutual solubility of the two (or more) components of an alloy. When the sizes of the constituent atoms are sufficiently different, miscibility gap exist. In addition to solid-phase immiscibility in important alloys systems such as GaInAsP and  $\text{In}_x\text{Ga}_{1-x}\text{N}$ , this size difference also leads to microscopic structures far different than the random, totally disordered state normally expected for alloys. Both miscibility gaps and deviations from a random distribution of the atoms constituting the lattice affect the electrical and optical properties of semiconductor alloys in ways that are extremely important for many types of devices.

The thermodynamics of the surface must also be considered in any effort to understand the growth processes as well as the characteristics of the materials produced epitaxially.

The basic goal of thermodynamics, as applied to epitaxy, is to define the relationship between the compositions of the various phases in an equilibrium system at constant temperature and pressure.

## 2.2.1 Thermodynamic Models in Solid Solution

### 2.2.1.1 Regular Solution Model

The term regular solution was first used by Hilderbrand to describe a class of solutions that are nonideal but consist of a random arrangement of the constituents. The term has since come to designate a more restricted, semiquantative model for the calculation of the free energy of mixing of multicomponent systems. Two additional assumptions are (1) interactions between the constituent atoms occur only pair-wise- that is, only between nearest neighbor pairs, and (2) the atoms reside on a lattice with each atom surrounded by  $Z$  neighbors. The bond energies are commonly thought of as being the sum of “chemical” energies, frequently related to charge transfer due to differences in electronegativity, and “strain” energies related to distortions in the lattice due to differences in the sizes of the constituent atoms. The enthalpy of mixing is obtained by summing nearest-neighbor bond energies

$$\Delta H^M = x(1-x) \cdot \Omega \quad (2-2)$$

where interaction parameter ( $\Omega$ ) is

$$\Omega = ZN^o \cdot \left[ H_{AC} - \frac{1}{2} \cdot (H_{AA} + H_{CC}) \right] \quad (2-3)$$

where  $N^o$  is Avogadro’s number.

### 2.2.1.2 Bonding in Semiconductor Solid Solutions Model

Traditionally, semiconductor alloys have been described in terms of the virtual crystal approximation (VCA), where the lattice on which the atoms are situated is uniform; that is, the individual bonds are dislocated to form a microscopically uniform solid solution. This was believed to be dictated by the accuracy with which Vegard’s law describes the linear dependence of lattice constant on solid solution. However, it has been

recently found that the virtual crystal model for semiconductor solid solution is in fact not a good description of the solid. The bond lengths in the alloy more nearly resemble the bond lengths in the pure binary compounds than the average values anticipated from the virtual crystal model [Ega02]. The valence force field (VFF) model can be used to explain this behavior [Pos02]. The interactions between atoms are considered to be due to entirely to strain (i.e., the stretching and bending of the bonds). The simplest form of the VFF calculation for an alloy AC-BC assumes that the lattice is composed of five types of tetrahedra shown in Fig.2.6 [Ich86, Kea66]. It is known that the bonding in a semiconductor is due to long-range effects, particularly the distributed electron energy states in the solid. The same valence electrons that determine the optical and electrical properties of the semiconductor also determine the bonding, as well as the elastic constant. This is contrary to the basic assumptions of the regular solution model, which cannot be expected to provide a physically accurate, predictive description of the enthalpy of mixing in semiconductor alloys.

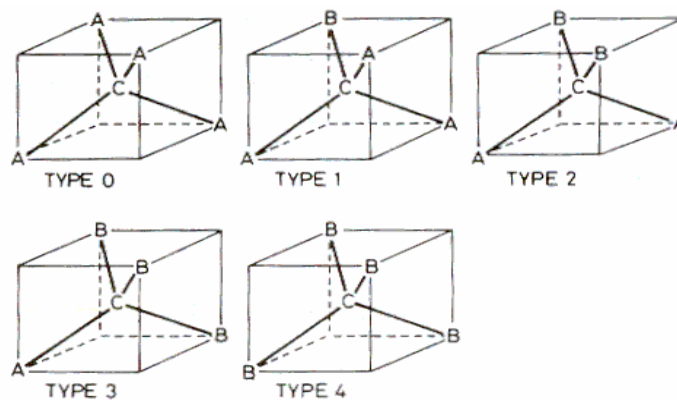


Figure 2-6. Tetrahedral cells in a ternary III-V alloy semiconductor.

### 2.2.1.3 Delta Lattice Parameter (DLP) Model for Enthalpy of Mixing

Important information needed for the calculation of solid-solid, solid-liquid, and solid-vapor phase equilibriums is the heat of mixing in the solid,  $\Delta H^M$ . This coupled with the assumption of a random distribution of constituents on their respective sublattices allows the calculation of the free energy of mixing of the solid alloy. Several researchers have suggested that the bonding energy in semiconductors is linearly related to the bandgap [May90, Pan98, Sun94, and Ho96]. The work of Phillips and Van Vechten suggested that the average band gap should be used in this relationship. Since it varies as  $a_o^{-2.5}$  in semiconductors that are nearly covalent such as the III-V compounds,  $\Delta H^{at}$ , which is used as a measure of bonding energy, might be written

$$\Delta H^{at} = K \cdot a_o^{-2.5} \quad (2-4)$$

Considering the zero of enthalpy to be infinitely separated atoms, the interaction parameter can be calculated from the enthalpy of mixing at  $x = 1/2$ , yielding

$$\Omega^s = 4K \cdot \left[ -\left(\frac{a_A + a_B}{2}\right)^{-2.5} + \frac{1}{2}(a_A^{-2.5} + a_B^{-2.5}) \right] \approx 99K \frac{(a_A - a_B)^2}{(a_A + a_B)^{4.5}} \quad (2-5)$$

Using Vegard's law to obtain the lattice constant at  $x=0.5$ . The value of  $K$  was obtained by making a least-square fit of Equation (Eqn.2-5) to available experimental values of  $\Omega^s$  that are listed in Table 2-6. The DLP calculation also appears to be quite accurate for the III/V nitride alloys. A striking feature of the DLP model is that the interaction parameter, hence the enthalpy of mixing, is always positive.

Table 2-6. Comparison of interaction parameters calculated using various models with experimental data.

Alloy	$\Omega^s$ (exp) <sup>a</sup> (kcal/mol)	$\Omega^s$ (DLP) (kcal/mol)	$\Omega^s$ (VFF) (kcal/mol)	$\Omega^s$ (Mod VFF) (kcal/mol)	Phase Separation
AlGaN		1.19	1.34	0.87	
AlInN		17.45	18.10	11.44	
GaInN		9.60	9.62	5.98	Yes
AlPN		19.68	60.79	36.56	
AlAsN		57.93	85.33	53.42	
GaPN	23	28.90	42.43	27.38	Yes
GaAsN		42.78	59.09	36.84	Yes
InPN		19.68	29.09	16.33	Yes
InAsN		26.71	39.14	21.87	Yes

[Str99]

#### 2.2.1.4 Strain Energy Model

In the traditional regular solution model, the uniformly positive values of enthalpy of mixing strongly suggest that the enthalpy of mixing is due to strain, rather than chemical factors. The mixing enthalpy can also be estimated using the simplified VFF model. The solid is considered to be made up to identical tetrahedra (Fig.2.6) with the position of the central atoms, located on the sub-lattice with no mixing, allowed to relax to the position giving the lowest strain energy, considering both stretching and bending distortions. The strain energy due to the stretching and bending of the bonds in each type of tetrahedron is summed over the five types of tetrahedral weighted by the distribution probability (random arrangement was not assumed in reference [Ich86]). The two terms are coupled and must be solved simultaneously [Ich86]. This approach allows a calculation of the free energy of mixing. There are two major drawbacks to the simple forms of the VFF model described here. First, when the lattice is assumed to be made up of tetrahedral where the corner atoms take the VCA positions, one of the sublattices is not relaxed. This causes a significant overestimation of the total strain energy. Second, the

difference in energy between the several tetrahedral types is much greater than  $kT$  for many types of tetrahedrals. Taking into account the effects of the resulting short-range order (SRO) makes the calculation of the mixing enthalpy difficult, since it couples the two factors [Ich86]. These problems can be surmounted by considering a large ensemble of several hundred atoms with the positions of each allowed to relax while maintaining a relatively simple calculation by considering only the dilute limit, where the effect of the SRO is negligible [Sch91, Ho96]. This approach was developed specifically for dealing with systems with very low solubility limits, in particular for the solubility of the very small N atom in conventional III/V semiconductors such as GaAs, InP, GaP, and so forth.

#### **2.2.1.5 First-Principal Models**

Advances in fundamental insight for the energy of a semiconductor lattice and the methodology of solving mathematical problems of large matrices have been achieved recently due to the availability of high-powered computers.

These achievements can make possible the first-principle local density self-consistent total energy minimization calculations in semiconductor alloy systems [Zun94]. Using these quantum mechanical calculations, the thermodynamics of semiconductor solid solutions can be calculated without any of the extreme simplifying approximations necessary to obtain simple analytic models.

The total energy minimization calculations are based on the entire complex band structures. The results from such calculations are included in Table 2-4. The mixing enthalpies have also been calculated for  $\text{In}_x\text{Ga}_{1-x}\text{N}$ ,  $\text{InAlN}$ , and  $\text{AlGaIn}$  alloys using a pseudopotential perturbation approach [Ito97].

### 2.2.2 Thermodynamic Analysis of InN

Koukitu and Seki have performed a thermodynamic analysis of the MBE growth of III-nitrides [Kou97a]. The equilibrium partial pressure and the growth rate were calculated for input V/III ratio, input partial pressure of group III elements and growth temperature. A summary of their calculation results as a phase diagram for the deposition, indicating etching, droplet formation and growth regions are shown in the Fig. 2.6. The chemical reaction, which connects all species at the substrate surface, is



The equilibrium equation for the reaction is as follows:

$$K_1 = 1/(P_{\text{In}} + P_{\text{N}}). \quad (2-7)$$

From the conservation constraint we have

$$P_{\text{In}}^0 - P_{\text{In}} = P_{\text{N}}^0 - P_{\text{N}}, \quad (2-8)$$

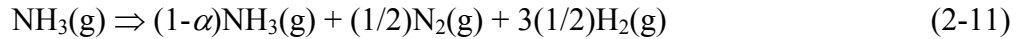
where  $P_{\text{In}}^0$  and  $P_{\text{N}}^0$  are the input partial pressures, which are obtained from the incident beam flux, and  $P_{\text{In}}$  and  $P_{\text{N}}$  are the equilibrium partial pressures. Equation (2-8) expresses that the deposition occurs in the ratio of 1: 1 for In and N. The equilibrium partial pressures at the substrate surface can be obtained from the solution of the above simultaneous equations. The value of the equilibrium constant was obtained from the literature [Kou97a]. The corresponding free energy to the chemical reaction (Eq.2-6) used in the analysis is as follows:

$$\begin{aligned} \Delta G^0(\text{kcal/mol}) = & (-1.764 \times 10^2) + 3.067 \times 10^2/T \\ & + (-1.451 \times 10^{-3}) \times T \times \ln(T) + 7.909 \times 10^{-2} \times T \\ & + 3.883 \times 10^{-11} \times T \times T. \end{aligned} \quad (2-9)$$

The calculation for the MBE growth technique using an  $\text{NH}_3$  source was performed in a similar manner, using atomic nitrogen. The chemical reaction is



In  $\text{NH}_3$  case, they introduce  $\alpha$ , the molar fraction of decomposed  $\text{NH}_3$ , into the calculation as follows:



The value of  $\alpha$  is assumed appropriately as that of MOVPE growth [Kou96], because it is difficult to know the exact value. The equilibrium partial pressure and the growth rate were calculated for input V/III ratio, input partial pressure of In, and growth temperature. In the growth of InN, they conclude that three deposition modes, i.e., etching, droplet formation and growth regions, appear in the temperature range from 500 to 900 °C. The temperature suitable for the InN growth is predicted to be from 600 to 700 °C with  $V/\text{III} \geq 1$ , which is essential in the MBE growth. However, the experimental growth temperature is much lower than this theoretical prediction, and almost experiments have been done in the temperature range from 450 to 550 °C. They also reported that there is a difference between the atomic nitrogen and the  $\text{NH}_3$  source as shown in the corner of diagram (Fig. 2.7) where the etching region appears [Kou97a]. In the case of the atomic nitrogen source, the etching region appears constantly at the region where the input V/III ratio and the input  $P_{\text{In}}^0$  are low value. On the other hand, in the case of the  $\text{NH}_3$  source, it appears at the region where the V/III ratio is high and the input  $P_{\text{In}}^0$  is low. They concluded that this is due to the decomposition of  $\text{NH}_3$ : when  $\text{NH}_3$  is decomposed,  $\text{H}_2$  gas is produced, and the produced  $\text{H}_2$  drives Eqn. (2-10) to the left hand. Consequently, the deposition moves into the etching mode due to the increase in  $\text{H}_2$ .

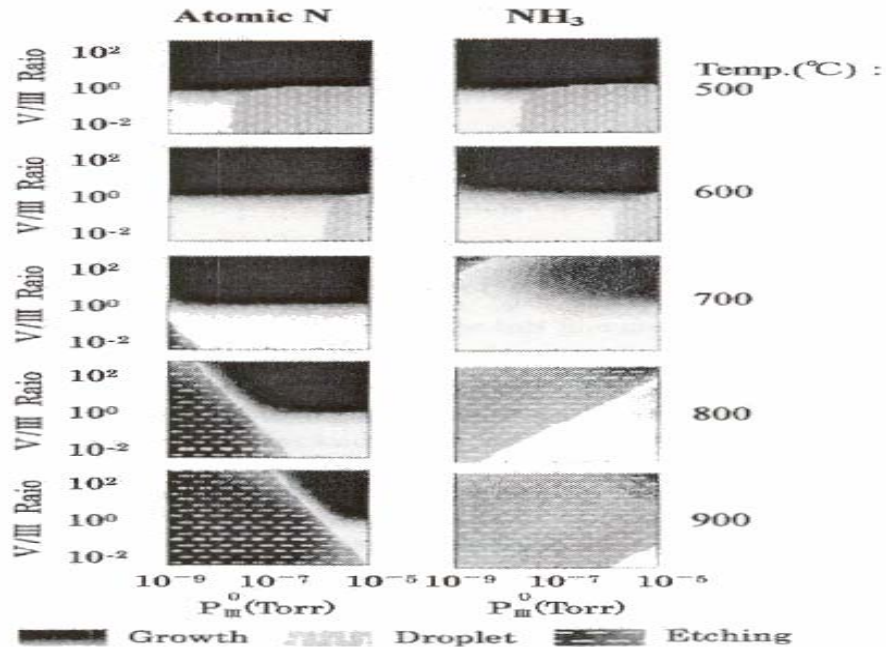


Figure 2-7. Calculated phase diagram for the MBE deposition of InN using atomic N and  $\text{NH}_3$  gases. There are three deposition modes: etching, droplet and growth.

### 2.2.3 Phase Separation in $\text{In}_x\text{Ga}_{1-x}\text{N}$

The large positive enthalpy of mixing for systems with a large lattice mismatch can overwhelm the negative entropy of mixing for temperatures below the critical temperature. This results in a free energy versus composition curve shown schematically in Fig. 2.8, with an upward bowing in the center [Str99]. This dictates that at equilibrium, a random alloy with composition between points A and B will decompose into a mixture of two phases. Two other important points in the  $G$  versus energy curve shown in Fig. 2.8 are the inflection points lying between A and B. Between these two points the solid solution is unstable against an infinitesimal fluctuation of composition. The spinodal appears on the  $T$ - $x$  phase diagram, as indicated in Fig. 2.9 [Str99]. In the pseudobinary phase diagram, the boundary of the unstable region is defined by the locus of  $(d^2G/dx^2)_{T,P} = 0$  [25], called the *spinode*. Inside this region, the solid can decompose “spoinodally,” with no energy barrier.

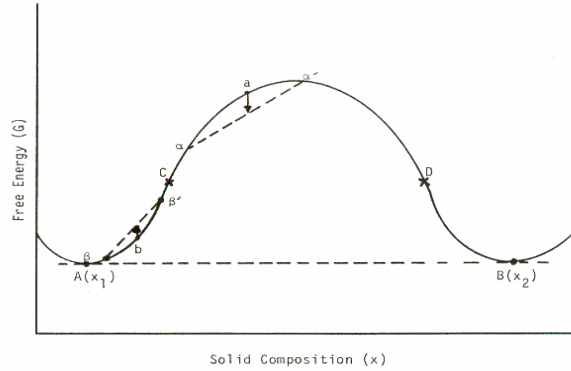


Figure 2-8. Free energy versus solid composition for a hypothetical semiconductor alloy having a large positive enthalpy of mixing. Point A and B are the bimodal points, and points C and D represent the spinodal points.

The growth of  $\text{In}_x\text{Ga}_{1-x}\text{N}$  alloys has proven to be extremely challenging, mostly due to the trade-off between the epilayer quality and the amount of InN incorporation into the alloy as the growth temperature is changed. Growth using high temperatures of approximately  $800^\circ\text{C}$ , typically results in high crystalline quality but the amount of InN in the solid is limited to low values because of the high volatility of N over InN. Ho and Stringfellow performed a theoretical calculation of the enthalpy of mixing, the solid phase interaction parameter, and the extent of the miscibility gap for  $\text{In}_x\text{Ga}_{1-x}\text{N}$  alloy system using a modified valence-force-field (VFF) model calculation where the lattice is allowed to relax beyond the first nearest neighbor [Str97].

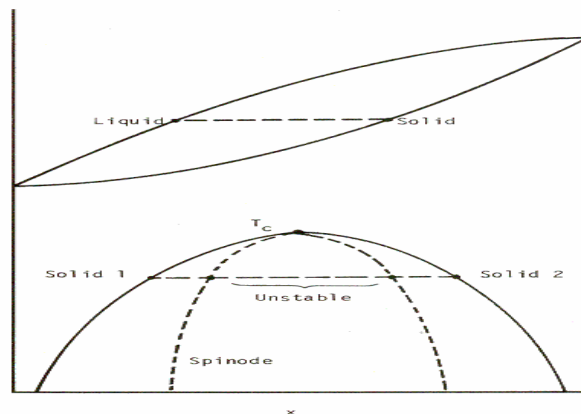


Figure 2-9. Schematic liquid-solid pseudobinary phase diagram.

The VFF model, itself, is found to overestimate the total strain energy of a ternary system due to the constraint that only one of the two sublattices is allowed to relax. The calculation of the enthalpy of mixing or the interaction parameter in III-V system has been a topic of interest for nearly twenty-five years. In 1972 Stringfellow developed the semi-empirical delta-lattice-parameter (DLP) model, which is found to yield surprisingly accurate interaction parameters for a wide range of III-V alloys knowing only the lattice constants of the binary constituents. The temperature dependence of the bimodal and spinodal lines in the  $\text{In}_x\text{Ga}_{1-x}\text{N}$  system was calculated using a modified VFF model. The strain energy is found to decrease until approximately the sixth nearest neighbor, but this approximation is suitable only in the dilute limit. Assuming a symmetric, regular solution-like composition dependence of the enthalpy of mixing yields an interaction parameter of 5.98 kcal/mole and a critical temperature for the phase separation of 1250 °C (Fig. 2.10) [Ho96]. At a typical growth temperature of 800 °C, the solubility of indium in GaN calculated to be less than 6 %. The miscibility gap is expected to represent a significant problem for the epitaxial growth of these alloys [Ho96].

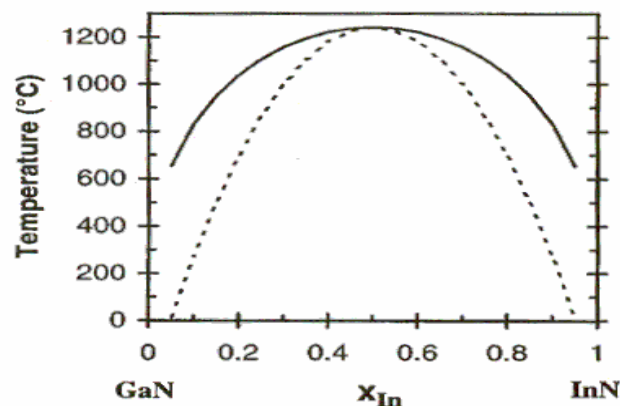


Figure 2-10. Binodal (solid) and spinodal (dashed) curves for the  $\text{In}_x\text{Ga}_{1-x}\text{N}$  system, calculated assuming a constant average value for the solid phase interaction parameter.

Singh *et al.* reported the growth of InGaN thick (0.3~0.4  $\mu\text{m}$ ) films and  $\text{In}_x\text{Ga}_{1-x}\text{N}$  /GaN double heterostructures by MBE at the substrate temperatures 700-800°C. X-ray diffraction and optical absorption studies showed that the phase separation of InN of  $\text{In}_x\text{Ga}_{1-x}\text{N}$  thick films occurred with  $x > 0.3$ . On the other hand,  $\text{In}_x\text{Ga}_{1-x}\text{N}$ /GaN double heterostructures showed no evidence of phase separation. These observations were accounted for using Stringfellow's model (DLP model) on phase separation, which gives a critical temperature for miscibility of the GaN-InGaN system equal to 2457 K. The maximum value of the critical temperature ( $T_c$ ) above which the InN-GaN system is completely miscible can be computed from Stringfellow's equation for a binary system (Eq.2-12) [Sin97].

$$T_c = \frac{8.75 K}{4 R} \cdot \frac{(\Delta a)^2}{(\bar{a})^{4.5}} \quad (2-12)$$

Where  $\Delta a$  is the difference in the lattice constants of GaN and InN,  $\bar{a}$  is the average lattice of GaN and InN, and R is the gas constant. K is the proportionality constant between atomization enthalpy (bonding energy). Phase separation in any alloy requires long-range diffusion and thus a correlation should exist between phase separation and a time required for the growth of the film. They believed this is one of the reasons for the non-observable phase separation in GaN/  $\text{In}_x\text{Ga}_{1-x}\text{N}$  /GaN double heterostructures with thin  $\text{In}_x\text{Ga}_{1-x}\text{N}$  layers. Strain associated with thin  $\text{In}_x\text{Ga}_{1-x}\text{N}$  quantum wells could also stabilize alloys against phase separation.

Wakahara *et al.* calculated the compositional inhomogeneity in  $\text{In}_x\text{Ga}_{1-x}\text{N}$  by using a theoretical estimation of the interaction parameter based on DLP model [Wak97]. Table 2-7 summarize the lattice mismatching, the interaction parameter ( $\alpha$ ) and the critical

temperature of spinodal decomposition, which is denoted as  $T_c = \alpha / 2R$ , for the III-V ternary alloy system.

It can clearly be seen that the nitride alloys including the InN have a very large interaction parameter thus, the critical temperature of the spinodal decomposition also becomes very high. It is expected that the immiscibility of the  $\text{In}_x\text{Ga}_{1-x}\text{N}$  alloy is very strong. The critical temperature of the spinodal decomposition defined at the composition  $x = 0.5$  is much higher than the typically used growth temperature of 800 °C. The evidence of the phase separation in the InN containing nitride alloys was resulted in [Mor94]. Recently, Koukitsu and Seki [Zun94] reported compositional inhomogeneity based on a thermodynamic analysis of the vapor-solid interface. They predicted that the compositional inhomogeneity of  $\text{In}_x\text{Ga}_{1-x}\text{N}$  increases with an increase of the growth temperature and in the partial pressure of the hydrogen but decreases with V/III ratio.

Table 2-7. Interaction parameters for various III-V ternary alloy systems.

III-V ternary alloy system	Lattice mismatch $\Delta a/a$ (%)	Interaction parameter $\alpha$ (DLP model) (cal/mol)	Critical temperature $T_c$ (K)
AlAs-GaAs	0.159	0	0
GaAs-InAs	6.92	2815	709
AlP-GaP	0.239	0	0
GaP-InP	7.39	3630	914
GaP-GaN	18.9	28900	7276
AlN-GaN	2.93	931	233
AlN-InN	13.38	17300	4338
GaN-InN	10.46	10300	2583

[Wak97]

The resulting strain in the layers could lead to deviations from homogeneity of the sublattice. Zunger and Mahajan have reviewed several observations, which indicate that when the tetrahedral radii are different, two types of structural variations are observed: phase separation and atomic ordering. The difficulties in  $\text{In}_x\text{Ga}_{1-x}\text{N}$  growth are mainly

due to (a) very high equilibrium vapor pressure (EVPs) of nitrogen over InN and (b) a large lattice mismatch (11 %) between InN and GaN. The lattice mismatch between InN and GaN (due to the very different tetrahedral radii) results in highly strained  $\text{In}_x\text{Ga}_{1-x}\text{N}$  alloys. Therefore, at relatively low growth temperature (650-800 °C), phase separation is a major concern. The majorities of the III-V ternary and quaternary alloys are predicted to be thermodynamically unstable and show a tendency towards clustering and phase separation. The phase separation and ordering phenomena in  $\text{In}_x\text{Ga}_{1-x}\text{N}$  alloys with MBE was studied by Doppalapudi *et al.* [Kel98]. The ordering parameter was found to increase with the growth rates of the films, a result which is consistent with the notion that ordering is induced at the surface of the growing films where it is thermodynamically stable and is then subsequently “frozen in“ during further growth. Phase separation was found to be essential for films with high indium content (> 25 %), while ordering was noticeable for films with small indium content (< 10 %). This competition between the two phenomena is consistent with the proposal that lattice strain is the driving force for both. The effect of elastic strain in epitaxial  $\text{In}_x\text{Ga}_{1-x}\text{N}$  layers coherently grown on GaN wafers on spinodal decomposition of the ternary compound was examined. The effect results in considerable suppression of phase separation in the strained  $\text{In}_x\text{Ga}_{1-x}\text{N}$  layers. The elastic strain effect is predicted to lower the critical temperature. This effect does work only if the relaxation of strain in the epitaxial layer is not yet started.

In summary, the results obtained by the several models used in the thermodynamic analysis about InN and  $\text{In}_x\text{Ga}_{1-x}\text{N}$  were reviewed. For InN, the thermodynamic result showed that the growth region is and the stable InN growth can be achieved at high V/III ratio. For  $\text{In}_x\text{Ga}_{1-x}\text{N}$ , it was found that phase separation commonly occurs and that the

critical temperatures could be calculated through the interaction parameter and these critical values depend on the chosen model. The maximum mole fraction of indium incorporated into  $\text{In}_x\text{Ga}_{1-x}\text{N}$ , which depends on the value of elastic strain of  $\text{In}_x\text{Ga}_{1-x}\text{N}$  was studied. From this result, it can be suggested that the maximum mole fraction of indium incorporated into  $\text{In}_x\text{Ga}_{1-x}\text{N}$  can be increased by decreasing the strain energy of  $\text{In}_x\text{Ga}_{1-x}\text{N}$ .

### **2.3 Indium Nitride (InN) and Indium Gallium Nitride ( $\text{In}_x\text{Ga}_{1-x}\text{N}$ ) Growth Challenges**

There are several problems to be overcome for high crystalline InN and  $\text{In}_x\text{Ga}_{1-x}\text{N}$  film growth. These problems are narrow region of growth temperature due to the low decomposition temperature, low cracking efficiency of  $\text{NH}_3$ , no suitable nitrogen precursors to improve the decomposition efficiency of  $\text{NH}_3$ , and carrier gas. These problems which occur during the growth of InN and  $\text{In}_x\text{Ga}_{1-x}\text{N}$  are briefly discussed in this part.

#### **2.3.1 Growth Temperature and V/III Ratio**

The growth of InN is the most difficult among the III-nitrides because the equilibrium vapor pressure of nitrogen over the InN is several orders higher than AlN and GaN [Amb96]. Because of the low InN dissociation temperature and high equilibrium  $\text{N}_2$  vapor pressure over the InN film [McC70], the growth of InN requires a low growth temperature. Due to the low ( $\sim 550$  °C) growth temperature, the MOVPE growth of InN is thought to be restricted by a low decomposition rate of  $\text{NH}_3$ . Although a higher growth temperature is expected to result in a higher decomposition rate of  $\text{NH}_3$ , it can also result in thermal decomposition (thermal etching) of the grown InN. On the other hand, the growth at a low temperature (lower than 400 °C) is dominated by the formation of

metallic indium droplets due to the shortage of reactive nitrogen. Epitaxial growth at low temperature becomes impossible due to reduced migration of the deposited materials. Therefore, the region suitable for the deposition of InN is very narrow.

Koukitu *et al.* carried out a thermodynamic study on the MOVPE growth of III-nitrides [Kou97b]. They pointed out that a high input V/III ratio, the use of an inert carrier gas, and a low mole fraction of the decomposed  $\text{NH}_3$  are required for the growth of InN. Experimental results also match well with the first two points (high input V/III ratio and the use of inert carrier gas) but are not clear on the last point (a low mole fraction of the decomposed  $\text{NH}_3$ ).

High input V/III provides sufficient amount of reactive nitrogen, since the  $\text{NH}_3$  decomposition rate is low at low growth temperature.  $\text{NH}_3$  is decomposed thermodynamically into  $\text{H}_2$  and  $\text{N}_2$  with low decomposition efficiency at temperature higher than  $300\text{ }^\circ\text{C}$ , which results in the increase of  $\text{H}_2$  partial pressure [this sentence does not make sense, there is low decomposition efficiency at  $T < 300\text{ }^\circ\text{C}$ , and at higher temperatures the  $\text{H}_2$  partial pressure increases]. Thus too high ratio of V/III significantly prevents the growth of InN and leads to the etching of InN due to the increase of  $\text{H}_2$  partial pressure (Eq. (2-10)). A suitable region of V/III ratio and growth temperature is required for the high quality InN growth without indium droplets formation during the growth.

The main problem in growing  $\text{In}_x\text{Ga}_{1-x}\text{N}$  has been the phase separation at high indium incorporation ( $x(\text{In}) > 0.3$ ) due to the very high equilibrium vapor pressure of nitrogen over InN. The compositional control has only been achieved for relatively low growth temperature, up to  $650\text{ }^\circ\text{C}$ . However, crystal quality is not good because the

decomposition rate of  $\text{NH}_3$  is very low below 1000 °C. Yoshimoto *et al.* [Yos91] obtained the relatively high-quality  $\text{In}_x\text{Ga}_{1-x}\text{N}$  using a high temperature (800 °C) and a high indium flow rate. In that case of the temperature growth (650-800 °C), the phase separation may occur because of the large mismatch (11 %) between InN and GaN. The lattice mismatch between InN and GaN (due to the very different tetrahedral radii) results in highly strained  $\text{In}_x\text{Ga}_{1-x}\text{N}$ . Therefore at the growth temperature of 650-850 °C, phase separation is still a major concern.

### 2.3.2 Nitrogen Source

InN and  $\text{In}_x\text{Ga}_{1-x}\text{N}$  are typically grown by MOVPE using conventional group III precursors such as tri-methyl indium and tri-ethyl indium with  $\text{NH}_3$  as the active nitrogen source. However, InN and  $\text{In}_x\text{Ga}_{1-x}\text{N}$  are relatively difficult to produce with the high quality required for minority carrier devices due to high equilibrium  $\text{N}_2$  vapor pressure and the low decomposition efficiency of  $\text{NH}_3$  as discussed earlier.

$\text{NH}_3$  is almost stable even at 1000 °C and decomposes only 15 % at 950 °C, even when catalyzed by GaN [Che91]. The combination of high growth temperatures and high nitrogen volatility leads to high concentrations of N vacancies in GaN and InN. This is often cited as the reason that the GaN and InN epitaxial layers are n-type.

Solution of this problem will probably require N precursor to give the high active nitrogen reduction at the low growth temperature. Hydrazine ( $\text{N}_2\text{H}_4$ ) is an attractive N precursor because it contains no carbon atoms to be incorporated into the solid, and the hydrogen atoms are potentially beneficial for removal of the alkyl radicals (from the group III precursors) from the surface. It decomposes at temperatures as low as 400° C, considerably lower than temperatures required for  $\text{NH}_3$  because of the weaker N-N bond [Gas86], thus making it suitable for growth at temperatures well at the current growth

temperature ( $\sim 550$  °C) and at low V/III ratio as low as 10 which prevents the waste of N precursor. It also has a favorable vapor pressure of approximately 10 Torr at 18°C, as indicated in Table 2-8. However, hydrazine is a toxic material, a rocket fuel, and explosive. When hydrazine is used in III-V nitride growth with the trimethyl-group III alkyls, the adduct formation between hydrazine and the group III precursors was observed. The layers were found to be contaminated with both oxygen and carbon. The hazard associated with the toxicity and explosiveness of hydrazine makes its use in a production environment unlikely.

Unsymmetrical dimethylhydrazine ( $\text{H}_2\text{N}_2(\text{CH}_3)_2$ , 1,1 DMHy) is a considerably safer alternative to hydrazine. It has a vapor pressure of 157 Torr at 25 °C and pyrolyzes at temperatures considerable lower than for  $\text{NH}_3$ . However, relatively high ( $>10^{19}$   $\text{cm}^{-3}$ ) levels of oxygen and carbon were observed, both of which are associated with the use of DMHy.

A potentially less hazardous precursor, phenyl hydrazine, has also been explored [Jon95]. However, the vapor pressure of 0.03 Torr at room temperature is far too low to be acceptable.

Hydrogen azide, or hydrazoic acid ( $\text{HN}_3$ ) has also been successfully used for MOVPE growth in a low-pressure reactor [Cht97]. This precursor is attractive because it has a high vapor pressure (the boiling temperature is 37 °C) and decomposes at approximately 300 °C to yield HN radicals with two dangling bonds, a potentially good source of atomic nitrogen, and N. However, it is highly toxic and potentially explosive.

The N precursor tertiary-butylamine ( $(\text{C}_4\text{H}_9)\text{NH}_2$  or TBAm) has a convenient vapor pressure of 340 Torr at 25 °C, a low toxicity, and is stable. However, the use of TBAm

for the growth of GaN has proven unsuccessful [Rus96, Bea97]. They observed no GaN deposition but rather deposition of a layer consisting mostly of carbon [Bea97].

In summary, several candidates for nitrogen sources were reviewed and all of them have some problems such as toxicity, explosion, low decomposition efficiency, and contamination.  $\text{NH}_3$  has been still widely used as a nitrogen source in spite of low decomposition efficiency. The design of the optimum nitrogen source for the growth of III/V nitrides is still required even though it is tricky.

Table 2-8. Properties of nitrogen precursors for MOVPE.

Precursor	Melting Point (°C)	Boiling Point (°C)	Vapor Pressure		P (Torr)/T(°C)
			a	b, K	
$\text{NH}_3$	-77.7		9.9974	31.211	
$\text{N}_2\text{H}_4$	1.3				10/18
MMHy		113			49.7/25
1,1 DMHy					157/25
$\text{N}_2\text{H}_3(\text{C}_6\text{H}_5)$ (phenyl hydrazine)		37	8.749	3.014	0.03/23
$\text{HN}_3$ (hydrogen azide)	-67	45.2	7.61	1,509.8	288/20
TBAm					

[Str99]

### 2.3.3 Carrier Gas

Carrier gas is used as the medium to give the uniform flow pattern of precursors in MOVPE reactor.  $\text{H}_2$  and  $\text{N}_2$  carrier gas have been usually used in InN growth. Koukitu *et al.* carried out a detailed thermodynamic study on the role of hydrogen during the MOVPE growth of III-nitrides [Kou99a]. They showed that increase of hydrogen in the growth system results in a decrease of InN deposition rate (called etching), which they suggested was due to the decrease of driving force for the deposition.

Thus the reaction for the growth of InN proceeds more effectively in the inert gas system and is prevented with the increase of  $\text{H}_2$ . Therefore it is necessary to use inert

carrier gas in the growth of InN. These theoretical and experimental results confirm that using a N<sub>2</sub> carrier gas is preferred (and widely used) for successful InN growth.

## **2.4 Indium Nitride (InN) Growth Techniques**

In this part, we review the several growth techniques commonly used for InN growth each of which deals briefly with the characteristics of the reaction system, the precursors, the chemistry, the applications, the disadvantages and advantage of each growth technique.

### **2.4.1 Chemical Vapor Deposition (CVD)**

CVD involves the dissociation and/or chemical reactions of gaseous reactants in an activated (heated, plasma etc.) environment, followed by the formation of a solid film. The deposition involves homogeneous gas phase reactions, which occur in the gas phase, and heterogeneous chemical reactions which occur on a heated surface leading to the formation of epitaxial films.

In general, the CVD process involves the following key steps as shown in Fig. 2.11 [Cho00b, Cho03].

- (1) Generation of active gaseous reactant species.
- (2) Transport of the gaseous species into the reaction chamber.
- (3) Gaseous reactants undergo gas phase reactions forming intermediate species:
- (4) Absorption of gaseous reactants onto the heated substrate, and the heterogeneous reaction occurs at the gas—solid interface (i.e. heated substrate) which produces the deposit and by-product species.
- (5) The deposits will diffuse along the heated substrate surface forming the crystallization centre and growth of the film.

(6) Gaseous by-products are removed from the boundary layer through diffusion or convection,

(7) The unreacted gaseous precursors and by-products will be transported away from the deposition chamber.

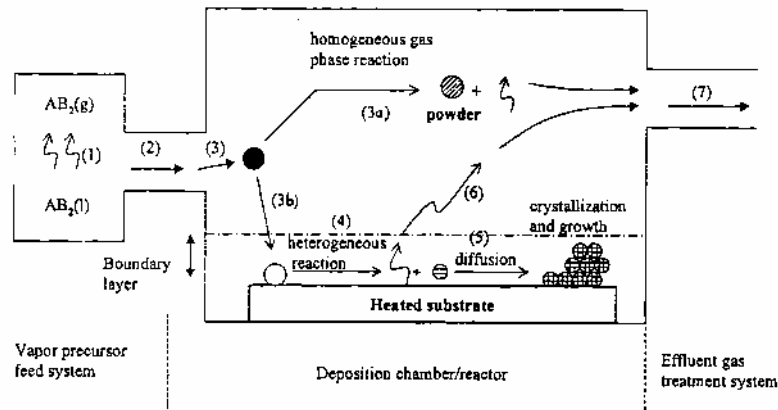


Figure 2-11. Schematic illustration of the key CVD steps during deposition.

#### 2.4.1.1 Metal-Organic Vapor Phase Epitaxy (MOVPE)

Metalorganic Vapor Phase Epitaxy (MOVPE) is one growth method among CVD, which has been classified according to the use of metalorganics as precursors. Compounds containing metal atoms bonded to organic radicals are known as “Metalorganics”. MOVPE can be used to deposit a wide range of materials in the form of amorphous, epitaxial, and polycrystalline films.

The schematic of MOVPE was shown in Fig. 2.12 where TMI is delivered by  $N_2$  carrier gas and  $NH_3$  is also delivered directly into MOVPE reactor and the thermal environment for the decomposition and/or deposition reaction of the precursors can be supplied using resistance heating, radio-frequency or infrared lamp heating. MOVPE tend to involve endothermic reactions, thus cold-wall reactors with a single temperature zone can be used.

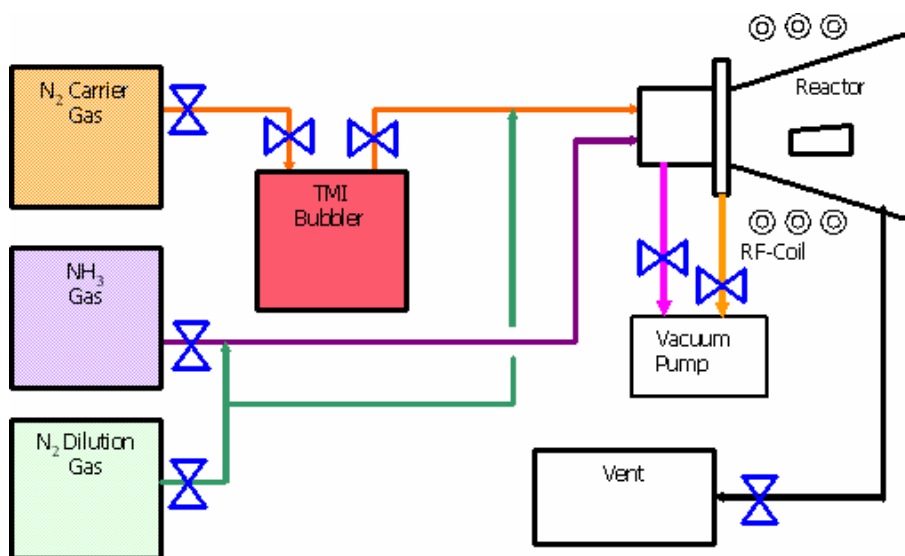


Figure 2-12. Schematic of horizontal cold-wall MOVPE system.

The metalorganic precursors generally undergo decomposition or pyrolysis reactions. In general, metalorganics precursors have lower decomposition or pyrolysis temperatures than halides, hydrides or halohydrides. Thus, metalorganic precursors enable MOVPE process to perform at a lower deposition temperature than conventional CVD, which generally uses halides or hydrides.

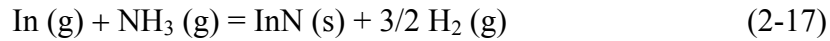
The source materials generally used for the MOVPE growth of InN, are trimethylindium (TMI) as In source, and ammonia (NH<sub>3</sub>) as N source.

The pyrolysis of TMI in MOVPE was first studied by Jacko and Price who founded that the decomposition occurred in three steps as each of the In-CH<sub>3</sub> bonds were broken at the temperature above 400 °C [ Jac64]. The methyl radicals thus formed were then found to recombine to yield ethane (C<sub>2</sub>H<sub>6</sub>). This mechanism is given by Eq. (2-13) to (2-16).

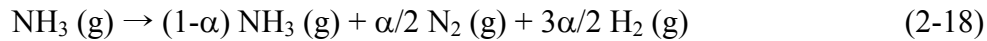




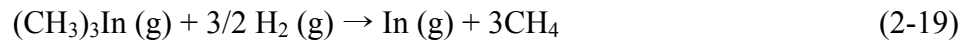
The indium reacts with  $\text{NH}_3$  at the substrate surface in high temperature ( $> 500^\circ\text{C}$ ) to form  $\text{InN}$  (Eq. (2-17)).



The other method was suggested by Koukitu and the reaction procedure is given as follows [Kou97b]. First, thermodynamically, almost all the  $\text{NH}_3$  is decomposed into  $\text{N}_2$  and  $\text{H}_2$  at temperatures higher than  $300^\circ\text{C}$ . However, it is well known that the decomposition rate of  $\text{NH}_3$  under typical growth conditions is slow without a catalyst and the extent of the decomposition strongly depends on the growth conditions. The mole fraction of decomposed  $\text{NH}_3$ , into the calculation as follows (Eq. (2-18)).



The metal-organic precursors TMI are decomposed irreversibly, according to the following homogeneous reaction, near the vapor-solid interface (Eq. (2-19)).



The chemical reaction which occurs at the substrate surface to form  $\text{InN}$  is the same as the former method given in Eq.(2-17).

MOVPE can be performed at atmospheric pressure and low pressure (about 2.7-26.7 kPa). For a typical MOVPE process, the deposition is entirely kinetically controlled at very low deposition pressure ( $< 1$  kPa), even though the deposition temperature is relatively high. At pressures above 1 kPa, the growth rate is predominantly controlled by diffusion-rate limited mechanism [Dup95].

Despite the high cost of precursors, MOVPE have been developed especially for the growth of epitaxy of III-V as well as II-VI and IV-VI semiconducting material for optoelectronic applications (e.g. light-emitting diode, heterojunction bipolar transistor, solar cells, photocathode advanced laser designs such as quantum well and double heterostructures, etc.).

#### **2.4.1.2 Hydride Vapor Phase Epitaxy (HVPE)**

Hydride vapor phase epitaxy (HVPE) has been important in the development of a variety of semiconductors including the III-arsenides, the III-phosphides and the III nitrides such as InN. HVPE occurs usually at atmospheric pressure (horizontal or vertical).

Generally, HVPE using chloride sources provides a high growth rate ( $> 30\mu\text{m}$ ) compared with that of MOVPE and MBE. Because of the group III element is transported to the substrate as a volatile compound (usually a chloride), this technique is often referred to as chloride-transported vapor phase epitaxy.

The source material generally used for the HVPE growth of InN is liquid indium as indium source, which will react with HCl and form indium monochloride (InCl) or indium trichloride (InCl<sub>3</sub>) and ammonia (NH<sub>3</sub>) or monomethylhydrazine (MMHy) as nitrogen source. The source of InCl is formed by the reaction between metallic In and HCl at 780 °C and the InCl<sub>3</sub> is presynthesized and is evaporated from the source boat in the temperature range from 325 to 375 °C (Fig. 2.13) [Tak97a]. The reaction chemistry for InN growth was given



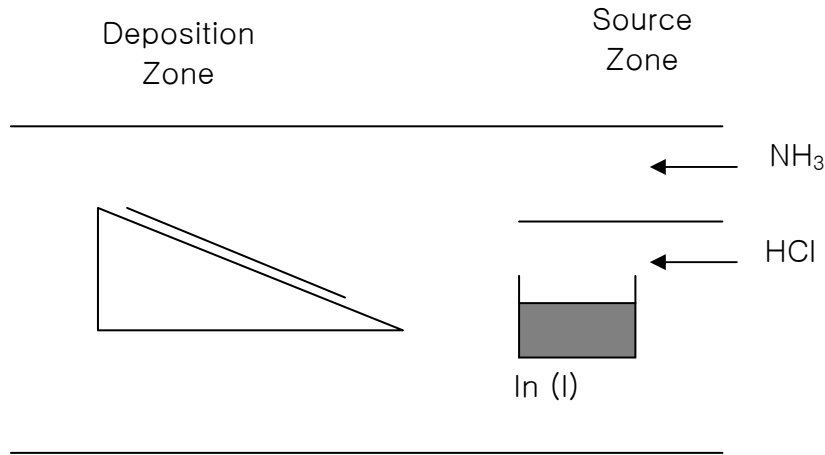


Figure 2-13. Schematics of horizontal hot-wall hydride vapor phase epitaxy chamber.

Theoretically, the chlorine in the HVPE chemistry should reduce the amount of impurities from the system due to the formation of highly volatile species, producing films with low carrier concentrations. However, Si and O impurities from the quartz tube can cause highly n-type films.

#### 2.4.1.3 Plasma Enhanced Chemical Vapor Deposition (PECVD)

Plasma Enhanced Chemical Vapor Deposition (PECVD) is also known as glow discharge chemical vapor deposition. It uses electron energy (plasma) as the activation method to enable deposition to occur at a low temperature and at a reasonable rate. Supplying electrical power at a sufficiently high voltage to a gas at reduced pressures (<1.3 kPa) results in the breaking down of the gas and generates a glow discharge plasma consisting of electrons, ions and electronically excited species.

Uncracked trimethylindium (TEI) carried by Ar or H<sub>2</sub> as In source and uncracked N<sub>2</sub> as N source are ionized and dissociated by electron impact, and hence generating chemically active ions (radicals). These radicals undergo the heterogeneous chemical reaction at or near the heated substrate surface and deposit the thin film (Fig.2.14) [Cho03].

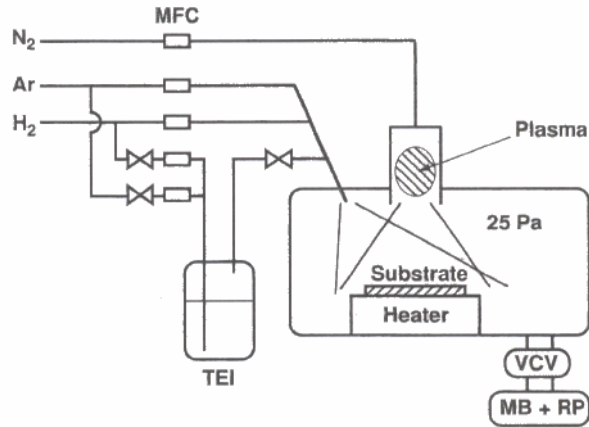


Figure 2-14. Schematics of PECVD.

The disadvantage of PECVD is that it requires the use of a vacuum system to generate the plasma, and a more sophisticated reactor to contain the plasma. PECVD is often more expensive and in general has difficulty in depositing high purity films. This is mostly due to the incomplete desorption of by-product and unreacted precursor at low temperatures, especially hydrogen which remains incorporated into the films.

However, PECVD can find applications where technology will balance the cost of fabrication and also where low deposition temperatures are required on temperature sensitive substrates, which can not be met by the conventional CVD.

The main advantage of PECVD over other CVD methods is that the deposition can occur at relatively low temperatures on large areas. It also offers flexibility for the microstructure of the film and deposition to be controlled separately. The ion bombardment can be substituted for deposition temperature to obtain the required film density. Such low temperature deposition is important for applications that involve the use of temperature sensitive substrates.

### **2.4.2 Molecular Beam Epitaxy (MBE) and Metalorganic Molecular Beam Epitaxy (MOMBE)**

MBE is a common technique for thin epitaxial growth of semiconductors, metals and insulators. MBE has the capability of growing device quality layers of semiconductors with atomic resolution. The low growth temperature (300-600 °C) ensures negligible dopant diffusion. The apparatus consists of an UHV cold-wall chamber, independently controlled thermal or e-beam cells to supply the sources, in situ heating and cleaning, and in-situ monitors of growth and chemical analysis.

The simplest method for generating molecular beams is from heated Knudsen cells containing Ga, In, Al or dopant material. Shutters open to allow the molecular beams to leave the cells and the beams are directed at a heated substrate. Thermal beams of atoms or molecules react on a clean substrate surface to grow an epitaxial film under UHV conditions. The atomic species undergo adsorption and migration on the surface. MBE can be also equipped with a number of in-situ probes that monitor the growth real time including RHEED where high-energy electrons are diffracted off the growing surface and imaged to describe the nature of the epitaxy.

In the MBE growth of III-nitrides, the solid sources of the group III elements such as Ga, In, and Al are used in general, but the nitrogen is supplied by the gas source such as N<sub>2</sub> and NH<sub>3</sub>. In general, this type of MBE system is called gas source MBE [Dav97].

When organometallic sources replace the group-III elemental source, it is called metalorganic molecular beam epitaxy (MOMBE) or chemical beam epitaxy [Abe97]. In both types of MBE, the key issue in the growth is the nitrogen source. The dissociation energy of N<sub>2</sub> molecules is as high as 9.5 eV, therefore, the supply of N<sub>2</sub> gas to the substrate surface with the group-III elemental beams can not induce any growth of the

nitrides. For obtaining atomic reactive nitrogen, the  $N_2$  molecules are dissociated by the radio-frequency (rf)-plasma or the electron cyclotron resonance (ECR) method. Although the rf-plasma source is the most popular and the rf-radical source produces considerably fewer ions than an ECR source due to the higher plasma pressures [Hug95], it is well known that ion damage can still induce during the epitaxy [Pow93]. Some techniques to avoid such ion damage by an ion tapping system using the static electric field, have been tried [Bot95, Mol94, Iwa96]. The other serious problems induced by the plasma may be some contamination such as oxygen or carbon dioxide.

MOMBE is also one of the potential growth techniques where the advantages of both MOVPE and MBE can be utilized. Film can be grown relatively at low temperature by MOMBE and premature reaction of the precursors, a serious problem in MOVPE, is minimized due to the large mean free path of gaseous molecules.

### **2.4.3 Atomic Layer Deposition (ALD)**

Atomic Layer Deposition (ALD) can be considered as a special mode of CVD. It is a surface deposition process that can be used for the controlled growth of epitaxial films, and the fabrication of tailored molecular structures on the surfaces of solid substrates. 'Monatomic layers' can be grown in sequence which is a characteristic feature of ALD. Therefore, the desired coating thickness can be produced simply by counting the number of reaction sequences in the process. The surface reconstruction of the monolayer formed in the reaction sequence will influence the saturation mechanism and the saturation density of the precursor.

The ALD reaction sequences are normally performed in an 'effective overdosing' condition to ensure a complete saturation of the surface reaction to form the monoatomic layer. Furthermore, such 'effective overdosing' condition also provides good conformal

coverage that allows uniform coatings onto complex shaped substrates. The sequencing in ALD also eliminates the gas phase reactions, and enables a wider choice of reactants (e.g. halides, metalorganics, elemental metal, etc.).

The ALD process has the potential to be scaled up for the deposition of high quality thin films with excellent uniformity and reproducibility onto large area substrate [Nii96, Lau98].

The ALD process can be performed at atmosphere pressure or in a vacuum system as in molecular beam epitaxy. The use of vacuum enables a variety of in-situ surface analysis methods to be incorporated into the ALD equipment for the in-situ analysis of the growth mechanism and the deposited surface structures [Bac97, Kou97c, Her99].

The distinctive sequencing feature in ALD makes it an attractive method for the precise growth of crystalline compound layers, complex layered structures [Cha98] superlattices [Tor00, Har98] and layered alloys with precise interfaces.

Currently, a wide range of thin films have been synthesized using ALD methods. These include semiconductor III-V, II-VI, oxides, nitrides, phosphides, and metallic films [Gup98, Hsu98, Utr99, Mar99, Ish97b, Utr00].

The ALD process can produce films with good conformal coverage and it has the ability to control film thickness accurately at the sub-nanometer level. Such distinctive advantages have made it a potentially valuable tool for nanotechnology.

## **2.5 Substrate Materials**

The important properties of substrate are the lattice constant which causes the lattice mismatch for the epitaxial InN film and thermal expansion coefficient which also can create dislocations during cooling when there is a large thermal coefficient mismatch

between the film and substrate. The properties of the substrate commonly used in III-V nitrided film growth are summarized based on InN film in Table 2-9.

Table 2-9. Structural properties of substrates.

Substrates	Lattice constant	Lattice constant	Lattice mismatch	TEC ( $10^{-6} \text{ K}^{-1}$ )		TEC mismatch
	a (Å)	c (Å)	(%)	a	c	(%)
InN-Wurtzite	0.537 <sup>b</sup>	5.704 <sup>b</sup>		5.70 <sup>b</sup>	3.70 <sup>b</sup>	0
GaN-Wurtzite	3.189 <sup>a</sup> (5.524 when rotated 30 °C)	5.18 <sup>a</sup>	-10.9	5.59 <sup>a</sup>	3.17 <sup>a</sup>	-30.9
AlN – wurtzite	3.112 <sup>b</sup>	4.98 <sup>b</sup>	-13.7	4.2 <sup>b</sup>	5.3 <sup>b</sup>	-8.1
6H-SiC – wurtzite	3.08 <sup>b</sup>	15.1 <sup>b</sup>	14.8	4.2 <sup>b</sup>	4.7 <sup>b</sup>	-8.1
Al <sub>2</sub> O <sub>3</sub> – rhombohedral	4.758 <sup>b</sup>	12.991 <sup>b</sup>	25.7	7.5 <sup>b</sup>	8.5 <sup>b</sup>	-48.5
ZnO - wurtzite	3.252 <sup>b</sup>	5.213	-8.8 <sup>b</sup>	2.9 <sup>b</sup>	4.8 <sup>b</sup>	33.1
LiAlO <sub>2</sub> – tetragonal	5.17 <sup>b</sup> (3.134 as a wurtzite)	5.1687 <sup>b</sup>	-12.9 (wurtzite)	7.1 <sup>b</sup>	7.5 <sup>b</sup>	-45.6
LiGaO <sub>2</sub> – orthorhombic	5.40 <sup>b</sup> (3.186 as a wurtzite)	5.007 <sup>b</sup>	-11 (wurtzite)	6 <sup>b</sup>	7 <sup>b</sup>	-35.7
GaN – zincblende	4.53 <sup>b</sup>		21.9	5.2 <sup>b</sup>		-25.8
Si (111) – cubic	5.43 <sup>b</sup> ( 3.84 as a hexagonal)		7.9 (hexagonal)	6.2 <sup>b</sup>		-37.7
3C-SiC – zincblende	4.36 <sup>b</sup>		18.9	2.7 <sup>b</sup>		43
GaAs - zincblende	5.65 <sup>b</sup>		37.4	6.0 <sup>b</sup>		-35.7

[<sup>a</sup>Mor94, <sup>b</sup>Dav02a]

### 2.5.1 Sapphire Substrate (Al<sub>2</sub>O<sub>3</sub>) (0001)

Sapphire is the most extensively used substrate material for the epitaxial growth of III-V nitride materials. Large area good quality crystals of sapphire are easily available at relatively low cost. They are transparent and stable at high temperature. The large lattice mismatch (25.7%) and thermal expansion coefficient difference (48.5 %) for InN can result in an extremely high density of structural defects of InN film. However, researchers have revealed that the substrate surface pretreatment and insert of an



### 2.5.2 Silicon (Si) Substrate

Si (111) substrate is usually spotlighted as an attractive substrate because of the high quality and low cost of Si. The availability of the either *n* or *p*-type substrate is advantageous. The doped substrates can significantly simplify device structures.

The bulk Si crystal is a diamond structure and has lattice constant  $a = 5.43 \text{ \AA}$  at room temperature. However, Si (111) surface has hexagonal surface and lattice parameter of  $a = 3.84 \text{ \AA}$ . Therefore, Si has the small lattice mismatch (7.9 %) for InN.

The unit cell is outlined as a diamond shape with seven atoms along each edge, for two different orientations. Si has a diamond-lattice structure with the space group of  $Fd\bar{3}m$  (no.227), which belongs to the cubic-crystal family. It can be represented as two interpenetrating fcc sublattices with one sublattice displaced from the other by one quarter of the distance along a body diagonal of the cube (i.e. the displacement of a  $\sqrt{3} a/4$ , where  $a = 0.543 \text{ nm}$ ). Each atom in the lattice is surrounded by four equidistant nearest neighbors that lie at the corners of a tetrahedron. Figure 2-17 illustrates the perspective views along the [001], [011] and [111] directions of a Si unit cell [Liu02]. There are several methods for Si substrate preparation (Table 4) [Yan96, Gru91, Dad01a, Wat93].

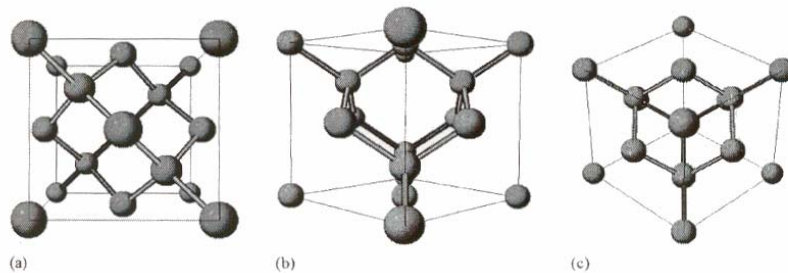


Figure 2-17. Perspective views of Si along various directions: (a) [001]; (b) [011]; (c) [111].

### 2.5.3 Gallium Nitride (GaN) and Aluminium Nitride (AlN) Substrate

Gallium nitride substrate has a small lattice mismatch of 10.9 % with InN compared with sapphire substrate (25.7 %) and AlN substrate (13.7 %) even if it is greater than that of silicon of 7.9 %. Gallium nitride normally has a wurtzite structure, with the space group of  $P6_3mc$  (no.186). The wurtzite structure consists of alternating biatomic close-packed (0001) planes of Ga and N pairs stacked in an ABABAB sequence. Atoms in the first and third layers are directly aligned with each other. Figure 2-18 displays the perspective views of wurtzite GaN along  $[0001]$ ,  $[11\bar{2}0]$  and  $[10\bar{1}0]$  directions, where the large circles represent gallium atoms and the small circles nitrogen [Liu02]. The close-packed planes are the (0001) planes. The group III nitrides lack an inversion plane perpendicular to the  $c$ -axis, thus, crystals surfaces have either a group III element (Al, Ga, or In) polarity (designated (0001) or (0001)A) or a N-polarity (designated  $(000\bar{1})$  or (0001)B). An excellent review on crystal polarity is given by Hellman [Hel98]. The zincblende structure (space group  $F\bar{4}3m$ ) of GaN can be stabilized in epitaxial films. The stacking sequence for the (111) close-packed planes in this structure is ABCABC. Perspective views of the zincblende structure are shown in Fig. 2.19 [Liu02].

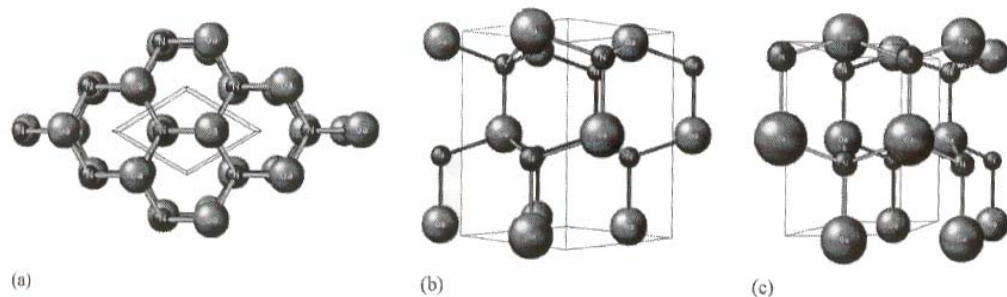


Figure 2-18. Perspective views of wurtzite GaN along various directions: (a)  $[0001]$ ; (b)  $[11\bar{2}0]$ ; (c)  $[10\bar{1}0]$ .

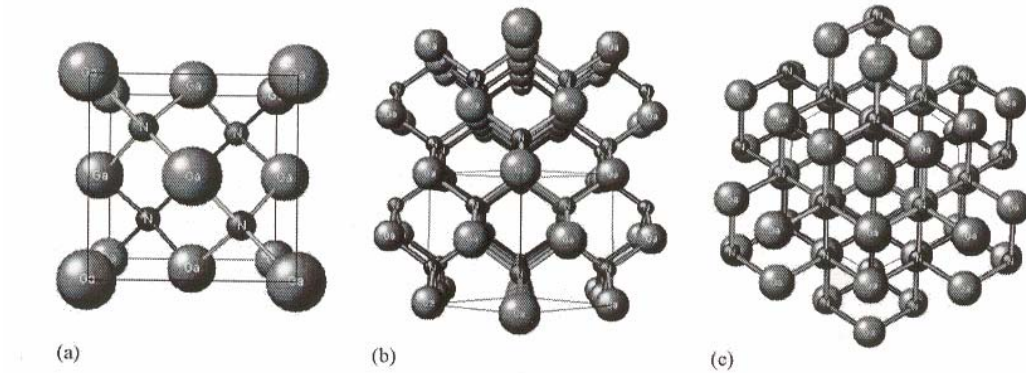


Figure 2-19. Perspective views of zincblende GaN along various directions: (a) [100] ( $1 \times 1 \times 1$  unit); (b) [110] ( $2 \times 2 \times 2$  units); (c) [111] ( $2 \times 2 \times 2$  units).

AlN normally has the wurtzite structure, although epitaxial layers of zincblende structure AlN have been made [Oku98a, Oku98b]. Wurtzite AlN has the space group of  $P6_3mc$  (no. 186) as same as wurtzite GaN. The (0001) surfaces of AlN are polar, which has an important effect on its etching, bulk crystal growth and GaN epitaxy. AlN has the properties such as high thermal conductivity, low thermal expansion coefficient, high electrical resistivity, good dielectric properties, and excellent oxidation resistance.

#### 2.5.4 Other Substrates

GaAs has the same structure as zincblende GaN. GaAs is less stable than SiC or sapphire. Above 800 °C its decomposition rate to liquid gallium and arsenic vapor is considerable. GaAs has the large lattice mismatch of 37.4 % for InN film.

Zinc oxide (ZnO) has a wurtzite structure and its stacking order match with lattice constants closely matched to GaN ( $a=3.249 \text{ \AA}$ ,  $c= 5.205 \text{ \AA}$ ). The small lattice mismatch of 8.8 % for InN makes ZnO attractive substrate for InN growth. Lithium gallate ( $\text{LiGaO}_2$ ) also has the small lattice mismatch of 11 % for InN film. Therefore,  $\text{LiGaO}_2$  is another candidate for the suitable substrate for InN growth.

### 2.5.5 Buffer Layer

There is no lattice matched substrate available for InN so far. For example, the InN has a lattice mismatch of 25 % with sapphire, 8% with Si (111), 37.4 % with GaAs, and 11 % with GaN. High quality single crystalline InN is very difficult to be obtained because of these problems.

The two-step growth method or growth using buffer layer has now become a standard method for the heteroepitaxial growth of thin films. This method is commonly used to alleviate lattice mismatch and thermal expansion coefficient difference the substrate and epilayer. In this method, a thin buffer layer is grown at a low temperature in the first step. The main epilayer is grown in the second step at a high temperature. The buffer layer provides the high density of nucleation centers and promotes the lateral growth of the main epilayer. The two-step growth of InN is not well studied, especially in the MOVPE growth.

There are very few studies about the MOVPE growth of InN using buffer layer such as GaN, AlN, and InN. There is no significant report that use of low temperature InN buffer layers in the growth InN gives improvement. Pan *et al.* studied two-step growth of InN using conventional MOVPE [Pan99]. Based on their findings, they concluded that the two-step growth is not adequate for InN, which may correlate to the unstable nature of the InN film. Guo *et al.* reported that if a single crystalline InN film is heated above 550 °C in a N<sub>2</sub> flow, the surface undergoes a considerable change, owing to the decomposition and desorption of nitrogen [Guo93].

## 2.6 Summary for Growth of InN on Different Substrate

### 2.6.1 Growth on Sapphire ( $\text{Al}_2\text{O}_3$ ) Substrate

The growth of InN in horizontal MOVPE reactor has been studied using  $\alpha\text{-Al}_2\text{O}_3$  (0001) substrate by Yamamoto [Yam94b]. A single-crystalline InN film was obtained on  $\alpha\text{-Al}_2\text{O}_3$  substrate at 500 °C, in spite of the larger lattice mismatch for InN (0001)/ $\alpha\text{-Al}_2\text{O}_3$  (0001) by the nitridation of the  $\text{Al}_2\text{O}_3$  (0001) substrate prior to the growth. Nitridation of  $\alpha\text{-Al}_2\text{O}_3$  surface occurs at the temperature region from 800 °C to 1000 °C. AlN is formed during the nitridation and the lattice mismatch is reduced from 25 % for InN/  $\alpha\text{-Al}_2\text{O}_3$  to about 13 % for InN/AlN [Yam94b, Pan99].

Chen found that the InN film quality is strongly dependent on the growth temperature and V/III ratio [Che97]. He reported the best quality of InN film was grown at 375 °C under a high V/III ratio of 146000 and the flow rate of  $\text{NH}_3$  of 2000 sccm. InN film growth was carried out in the atmospheric-pressure horizontal MOVPE reactor with a cross-section of  $30 \times 14 \text{ mm}^2$ . The FWHM of the best quality of InN (0002) was 96 arcsec with InN (10-11) existing while the typical FWHM of XRC of MOVPE-grown InN is from 4000 to 5500 arcsec [Che97].

Surface morphology study of InN grown in MOVPE was carried out by AFM with different growth condition by Yamamoto [Yam01a]. A continuous InN film with enhanced two-dimensional growth was obtained at 630-650 °C. It was reported that growth rate was increased with increasing growth temperature in the range of 500-630 °C, while it is independent of growth temperature at a temperature higher than 630 °C. It was suggested that when the growth is performed at 630-650 °C, growth rate is proportional to TMI supply. The increase in growth rate with increasing growth temperature at a temperature less than 630 °C can be explained by taking account that

growth rate is limited by  $\text{NH}_3$  decomposition rate. Yamamoto studied the effect of GaN buffer layer on InN and found that uniformity for grown InN film is markedly improved by employing a GaN buffer layer and this improvement is due to the uniform nucleation of InN [Yam04a].

The growth of InN in vertical resistive heated MOVPE reactor was performed by Hwang [Hwa01] where InN was grown at 360-540 °C; high V/III ratio was used to prevent indium droplet formation. The best InN was obtained at 540 °C and there was no reported about the value of FWHM.

Takahashi carried out the growth of InN by HVPE at V/III = 10-100 using InCl and  $\text{InCl}_3$  as In sources and  $\text{NH}_3$  and MMHy as N sources where the source of InCl was formed by the reaction between metallic In and HCl at 780 °C and  $\text{InCl}_3$  was evaporated from the source boat in temperature range 325-375 °C. The  $\text{InCl}_3$ - $\text{NH}_3$  system showed an appreciable growth rate of InN ( $\sim 0.3 \mu\text{m/hr}$ ) and the growth rate initially increases with increasing growth temperature up to 550 °C and then gradually decreases to 700 °C. The other systems such as  $\text{InCl}_3$ -MMHy, InCl- $\text{NH}_3$ , and InCl-MMHy showed the very small growth rate ( $< 0.05 \mu\text{m}$ ) [Tak97a].

The hydride vapor phase epitaxy growth of InN was performed by Yuichi Sato where HCl (diluted with  $\text{N}_2$  to 1 %) gas was passed over the indium metal source, which was kept in a quartz boat and the indium source was maintained at 900 °C in order to form InCl. The growth rate of the film gradually increases with increasing growth temperature and reaches the maximum growth rate of  $0.3 \mu\text{m/h}$  at 510 °C [Sat94a].

In addition to MOVPE and HVPE, atomic layer deposition (ALD) and molecular beam epitaxy (MBE) were also used for InN growth on sapphire substrate by several researchers [Bed 97, Hig20, and Mam99].

In summary, the growth conditions of InN on sapphire substrate for the different growth methods such as MOVPE, HVPE, and ALD were discussed. The MOVPE is the commonly used growth method for InN and the high quality single crystalline InN growth by MOVPE is still required because the typical range of FWHM of XRC is higher than 1000 arcsec.

### **2.6.2 Growth on Silicon (Si) Substrate**

The growth of InN on Si in horizontal MOVPE reactor was carried out by Yamamoto [Yam94b]. For Si substrate, relatively well oriented InN films are grown at about 400 °C. Polycrystalline InN films are grown both at 350 °C and at 500 °C on Si substrate. Polycrystalline InN growth below 350 °C is believed to be due to reduced migration of deposited materials on Si or decomposition rate of raw materials. The growth at a temperature higher than 450 °C results in serious deterioration of InN films grown on Si substrates. It was shown that the nitridation occurs at a temperature as low as 500 °C by exposing to NH<sub>3</sub> [Yam94b]. The cause for poorly-oriented or polycrystalline InN film growth on Si at a temperature above 400 °C was due to the formation of amorphous silicon nitride (SiN<sub>x</sub>) on Si substrates before the growth.

He suggested that epitaxial growth of InN on Si without a buffer layer is found to be difficult owing to the nitridation of Si substrate. The application of InN on Si to a tandem solar cell was suggested by Yamamoto [Yam94a, Yam94b].

Yang *et al.* improved the growth rate of InN on Si with a double-zone MOVPE system consisting of a high temperature NH<sub>3</sub> pre-cracking zone and a low temperature

deposition zone [Yan02c]. A maximum growth rate of 6  $\mu\text{m}/\text{h}$  was achieved due to the high cracking efficiency of  $\text{NH}_3$ . In this experiment, he used  $\text{N}_2$  as a carrier gas, the flow rate of  $\text{NH}_3$  at 800-1600 sccm, and V/III ratio of several hundreds. The optimal growth temperature was 450  $^\circ\text{C}$  [Yan02c].

In summary, single crystalline InN growth on Si was obtained but no reports on crystalline quality (FWHM of XRC) have been reported. Therefore, the growth conditions for high quality single crystalline InN should to be studied and optimized.

### **2.6.3 Growth on Gallium Arsenide (GaAs) Substrate**

InN films was obtained on GaAs(111) at 500  $^\circ\text{C}$ , 1.3 Torr, and  $\text{N}_2$  flow rate of 200 sccm, using microwave-excited MOVPE by Guo *et al.*[Guo95b]. Yamamoto *et al.* studied thermal nitridation of GaAs (111) in flowing  $\text{NH}_3$  and horizontal MOVPE growth of InN on the nitrated GaAs (111) as a result of the thermal nitridation [Yam97a].

In the case of GaAs(111) substrates, crystal structure of a GaN layer formed by the nitridation before the InN growth was found to be dependent on nitridation temperature  $T_N$ ; zincblende structure for  $T_N < 700$   $^\circ\text{C}$  and wurtzite for  $T_N > 800$   $^\circ\text{C}$ .

For an InN film grown on a GaAs (111) substrate with a zincblende GaN layer, its crystalline structure is changed from zincblende to wurtzite when the thickness exceeds about 0.2  $\mu\text{m}$ . On a GaAs (111) with a wurtzite GaN layer, on the other hand, growth of zincblende InN is not found [Yam98a].

Using an atmospheric HVPE system, InN growth was carried out on a GaN layer which was formed on a GaAs (100) substrate inclined 10  $^\circ$  toward the  $\langle 111 \rangle_B$  direction of GaAs substrate. An important requirement for growth was to keep low temperatures of less than 750  $^\circ\text{C}$  in the upstream region of the reactor to raise the amount of  $\text{InCl}_3$ , where

indium chloride is formed at the temperature higher than 750 °C. Furthermore, it was necessary to exclude H<sub>2</sub> from the reaction system for deposition to occur because the high partial pressure of H<sub>2</sub> increases the amount of InCl. These results indicate that the effective chemical substance of indium chlorides for the growth is InCl<sub>3</sub>. Growth rate of 1.5 μm/h was obtained at 570 °C and single crystalline InN growth was confirmed by X-ray diffraction measurement [Sun96].

The growth of InN using MOVPE and HVPE was discussed in terms of growth conditions. For MOVPE, the structure of InN depends on the nitridation temperature for GaAs(111)B substrates. For HVPE, InCl<sub>3</sub> forms InN film more effectively than InCl does.

#### **2.6.4 Growth on Gallium Phosphorus (GaP) Substrate**

Guo *et al.* reported that InN films had been grown on GaP (111) substrate at 500 °C using microwave-excited MOVPE and TMI and nitrogen were used as the source materials. The epitaxial InN film was obtained on GaP (111) by exposing the substrate to the nitrogen plasma for 60min before growth [Guo95b]. InN films have a wurtzite structure [Guo95b].

Bhuiyan *et al.* obtained InN on GaP(111)B by the horizontal MOVPE reactor where single crystalline InN films can be obtained on GaP(111)B only when the nitridation of the substrate is not made intentionally. InN films grown on nitrided GaP(111)B are found to be polycrystalline. XPS analysis shows the formation of PN<sub>x</sub> as well as GaN after the nitridation of GaP (111)B substrate surfaces by flowing NH<sub>3</sub> above 500 °C. Formation of PN<sub>x</sub> is responsible for the poor crystalline structure for InN. A single crystalline InN film with an excellent surface morphology can be grown on

GaP(111)B at high temperature (600-650 °C) using a low temperature InN buffer layer [Bhu00a,Bhu01,Bhu02b].

The growth of InN on GaP substrate using MOVPE was briefly discussed. When the growth of InN is performed on GaP substrate, the nitridation step should not be required in order to obtain the single crystalline InN.

### **2.6.5 Growth on Gallium Nitride (GaN) and Aluminum Nitride (AlN) Substrate**

Yamaguchi *et al.* presented the result of the InN film grown on GaN substrate with AlN buffer layer using atmospheric MOVPE. Growth temperature was 450 °C and V/III ratio was  $10^5$ . The FWHM of XRC decreases with increasing the thickness of InN film [Yam99a].

The effects of reactant-gas velocity on the growth of InN on GaN/sapphire by MOVPE were studied by Yang *et al.* With a high-speed reactant gas, the thickness of the stagnant layer is reduced so that the reactant species can reach the surface effectively. A layer like growth of InN was achieved, resulting in a significant improvement of the film quality. In addition, significant enhancement of the growth rate up to 2  $\mu\text{m/h}$  was obtained. The FWHM of XRC decreased with increasing gas velocity. FWHM of XRC for InN (0002) with 476 arcsec was reported but there was no report about whether the InN is single or poly crystalline [Yan02a].

The possibility that high quality single crystalline InN can be grown on GaN/sapphire substrate using MOVPE is studied and it is found that the flow pattern of source materials can have an effect on the InN film quality.

## 2.7 Overview

The latest lattice constant of single crystal InN with wurtzite was reported to be  $a = 3.537 \text{ \AA}$  and  $c = 5.704 \text{ \AA}$  [Dav02a]. The band-gap energy of InN is nowadays accepted to  $\sim 0.7 \text{ eV}$  instead of  $1.89 \text{ eV}$ .

Thermodynamic analysis helped us to understand at which growth condition the growth and etching happen and therefore help us to predict where InN film can be grown before the epitaxial growth is performed.

The possible candidates as N precursor were reviewed due to low decomposition efficiency of  $\text{NH}_3$  at low growth temperature of InN ( $\sim 550 \text{ }^\circ\text{C}$ ). Because all of other candidates for nitrogen source have the several problems such as toxicity, explosion and contamination,  $\text{NH}_3$  is still widely used N precursor and  $\text{N}_2$  carrier gas is better than  $\text{H}_2$  as carrier gas.

MOVPE is still the most widely used growth technique for InN for the industry and academy to date.

Based on available published data, the typical range of FWHM of XRC for single crystalline InN grown by MOVPE is higher than  $2000 \text{ arcsec}$  [Yam04a]. For Si substrate, it is still very difficult to have the high crystalline InN because of the bad coverage of InN on Si substrate despite of a small lattice mismatch [this topic was not reviewed in the InN growth on Si substrates section]. Therefore the study for the growth high quality single crystalline InN has been still required.

It is found that some factors such as growth temperature, V/III ratio, substrate, nitridation treatment, buffer layer, and flow pattern of source gases can have an effect on the structural quality of InN film. Based on the results of this review, these factors will be analyzed in detail to conduct our experiments of InN growth by MOVPE.

CHAPTER 3  
THERMODYNAMIC ANALYSIS OF InN AND In<sub>x</sub>Ga<sub>1-x</sub>N MOVPE GROWTH

**3.1 Thermodynamic Analysis of InN and In<sub>x</sub>Ga<sub>1-x</sub>N**

The results of a study on the effect of pressure and temperature on the equilibrium growth of InN and In<sub>x</sub>Ga<sub>1-x</sub>N are presented in this chapter. Specifically, equilibrium in IN-Ga-N-C-H system is studied to clarify the impact of process variables on film composition and to estimate a suitable growth condition for InN and In<sub>x</sub>Ga<sub>1-x</sub>N to support the experimental studies. For example, it is interesting to know the maximum content of indium that can be incorporated into the In<sub>x</sub>Ga<sub>1-x</sub>N phase without the phase separation.

The Gibbs energy functions for InN and GaN from the Scientific Group Thermodata Europe (SGTE) and the ThermoCalc software package were used for these calculations.

**3.1.1 Reaction Mechanism and Kinetics of InN MOVPE**

Growth of InN by MOVPE typically uses trimethylindium (TMI) and NH<sub>3</sub> precursors in a N<sub>2</sub> carrier gas. The pyrolysis of TMI was studied by Jacko *et al.* [Jac64, Tra78, and Lar85] and they proposed the sequential hemolytic fission of the In-C bond along methyl radical recombination described by Eq. (3-1a) to (3-1d).



It is reported that reactions 3.1a and 3.1c are slow steps, thus producing  $\text{In}(\text{CH}_3)$  into the vapor phase.

Stepwise hemolytic fission of the In-C bond in TMI was first proposed as in Eq. 3-1 [Jac64] and recently mono-methyl indium (MMIn) and atomic indiums were experimentally observed in the gas phase [Par02]. New reaction intermediates are proposed based on experimental evidence using *in situ* Raman and computational chemistry supports by Hwang [Hwa04]. It has been suggested from Hwang's experimental results [Hwa04] that MMIn and/or dimethyl indium (DMIn) seem to hide from Raman detection by forming another intermediate, presence of which in contrast to MMIn is evident. A new intermediate ( $\text{HInCH}_3$ ) was found to exist during TMI decomposition in a nitrogen carrier. It has some of its characteristic vibrations at 416 [ $\nu(\text{H-In-C})$ ], 464 [ $\nu(\text{In-C})$ ], and  $1560 \text{ cm}^{-1}$  [ $\nu(\text{H-In})$ ]. The new intermediate was experimentally observed to decompose very quickly in a high temperature region of the reactor. In addition, it was considered highly probable that  $(\text{DMIn})_2$  and DMIn-MMIn would form during TMI decomposition, as shown in Eq. (3-2) [Hwa04].



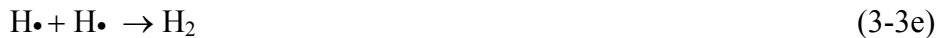
In terms of the kinetics of TMI decomposition (Eq. (3-1)), several experimental results are summarized in Table 3-1. Reaction rate constant and activation energies of TMI decomposition are shown in Table 3-1.

Table 3-1. Reported reaction rate constants for TMIn decomposition.

	$k_0$ ( $s^{-1}$ )	$E_a$ (kcal/mol)	Carrier
Hwang [Hwa04]	$10^{17.9}$	56.1	$N_2$
Jacko & Price [jac64]	$10^{15.7}$	47.2	Toluene
Larsen & Stringfellow [Lar86]	$10^{12.6}$ $10^{12.0}$	40.5 35.9	$N_2$ $H_2$
Buchan et al. [Buc88]	$10^{17.9}$ $10^{13.4}$ $10^{15.0}$	54.0 39.8 42.6	He $D_2$ $H_2$

Ammonia is the most widespread precursor for III-Nitrides growth by MOVPE. Complex chemical equilibrium analysis by Koukitu suggested that most of the  $NH_3$  should be decomposed into  $N_2$  and  $H_2$  at temperatures greater than 300 °C [Kou97b].

It is well known, however, that the decomposition rate of  $NH_3$  under typical growth conditions is slow without a catalyst and the extent of the decomposition strongly depends on the growth conditions. The decomposition reactions of  $NH_3$  are presented by Eq. (3a-3c).



Based on the aforementioned consideration, the several possible reactions for InN formation are suggested (Eq. (3-4)).





This complex chemical equilibrium analysis of the growth of InN requires computing the equilibrium state in the In-N-C-H system. The growth conditions of InN were calculated as a function of deposition temperature, pressure, and composition. It is assumed that the vapor phase follows an ideal gas mixture and the vapor species whose equilibrium mole fractions are negligible (below  $10^{-30}$ ) are not taken into account in this calculation because the same result for P-T diagram was obtained in either case when the species with the mole fraction less than  $10^{-30}$  ( $\text{C}_4\text{H}_{10}$ ,  $\text{C}_4\text{H}_2$ ,  $\text{C}_4$ , and  $\text{N}_3$  *etc.*) were included or excluded in the calculation. Therefore, the species with the mole fraction less than  $10^{-30}$  are thought to be insignificant in the calculation. The equilibrium mole fractions of each component can be obtained from the equilibrium result data of ThermoCalc. With this assumption, species, phase, and thermodynamic properties included in this analysis are summarized in Table 3-2. Diamond was not considered in the calculation as the phase of graphite is taken as a stable one.

The equilibrium state for the growth of InN without indium formation of 2-phase (In (*l*) + InN) was computed in the range of  $P = 1$  to  $101.3$  kPa ( $7.5$  to  $760$  Torr),  $T = 400$  to  $1000$  °C, and  $V/\text{III}$  ( $\text{NH}_3/\text{TMI}$ ) =  $50,000$ .

The P-T diagram is shown in Fig. 3.1 and the results indicate that the etching temperature (decomposition temperature) is  $810$  °C at  $P = 13.3$  kPa ( $100$  Torr) and  $V/\text{III} = 50,000$ . Pressure and  $V/\text{III}$  ratio were chosen based on our current operation conditions of the MOVPE system used in this study.

Table 3-2. Species, phases, and thermodynamic properties included in the analysis of MOVPE of InN.

Phase	Species	Parameter (J/mol)
Solid (s)	C, InN, In	$G_{C(s)} = -17368.4408 + 170.730318T - 24.3TLN(T) - 4.723 \times 10^{-4} T^2 + 2562600T^{-1} - 2.643 \times 10^8 T^{-2} + 1.2 \times 10^{10} T^{-3}$ $G_{InN(s)} = -149963.181 + 215.110609T - 38.0744TLN(T) - 0.0060668T^2$ $G_{In(s)} = -6978.89011 + 92.3381153T - 21.8386TLN(T) - 0.00572566T^2 - 2.12032167 \times 10^{-6} T^3 - 22906T^{-1}$
Liquid (l)	In, N	$G_{In(l)} = -6978.89011 + 92.3381153T - 21.8386TLN(T) - 0.00572566T^2 - 2.12032167 \times 10^{-6} T^3 - 22906T^{-1} + 3283.7 - 7.6402121T$ $G_{N(l)} = -4461.675 + 60.74575T - 12.7819TLN(T) - 0.00176686T^2 + 2.680735 \times 10^{-9} T^3 - 32374T^{-1}$
Gas (g)	C, CH <sub>4</sub> , H <sub>2</sub> , NH <sub>3</sub> , In, In <sub>2</sub> , N, N <sub>2</sub>	$G_{C(g)} = 710430.933 - 17.7062915T - 20.97529TLN(T) + 1.998237 \times 10^{-4} T^2 - 3.34617167 \times 10^{-8} T^3 + 1680.6515T^{-1} + RTLN(10^{-5}P)$ $G_{CH_4(g)} = -77295.5632 - 147.095196T - 2.234656TLN(T) - 0.048463265T^2 + 4.33754333 \times 10^{-6} T^3 - 305431.45T^{-1} + RTLN(10^{-5}P)$ $G_{H(g)} = 211801.621 + 24.4989821T - 20.78611TLN(T) + RTLN(10^{-5}P)$ $G_{H_2(g)} = 9522.9741 + 78.5273879T - 31.35707TLN(T) + 0.0027589925T^2 - 7.46390667 \times 10^{-7} T^3 + 56582.3T^{-1} + RTLN(10^{-5}P)$ $G_{NH_3(g)} = -53688.8736 - 38.3667407T - 21.21774TLN(T) - 0.022871695T^2 + 1.80809167 \times 10^{-6} T^3 - 76698.65T^{-1} + RTLN(10^{-5}P)$ $G_{In(g)} = 236267.082 - 68.7705731T - 15.35206TLN(T) - 0.00527185T^2 - 3.98269833 \times 10^{-7} T^3 - 94519.9T^{-1} + RTLN(10^{-5}P)$ $G_{In_2(g)} = 407673.852 - 41.5349376T - 35.82134TLN(T) - 0.00654889T^2 + 2.03928167 \times 10^{-8} T^3 - 20133.605T^{-1} + RTLN(10^{-5}P)$ $G_{N(g)} = 466446.153 - 13.3752574T - 20.89393TLN(T) + 8.45521 \times 10^{-5} T^2 - 1.0018685 \times 10^{-8} T^3 + 2788.7865T^{-1} + RTLN(10^{-5}P)$ $G_{N_2(g)} = -8000.12556 - 8.81620364T - 27.22332TLN(T) - 0.0012599175T^2 - 5.39381 \times 10^{-7} T^3 - 38326.695T^{-1} + RTLN(10^{-5}P)$

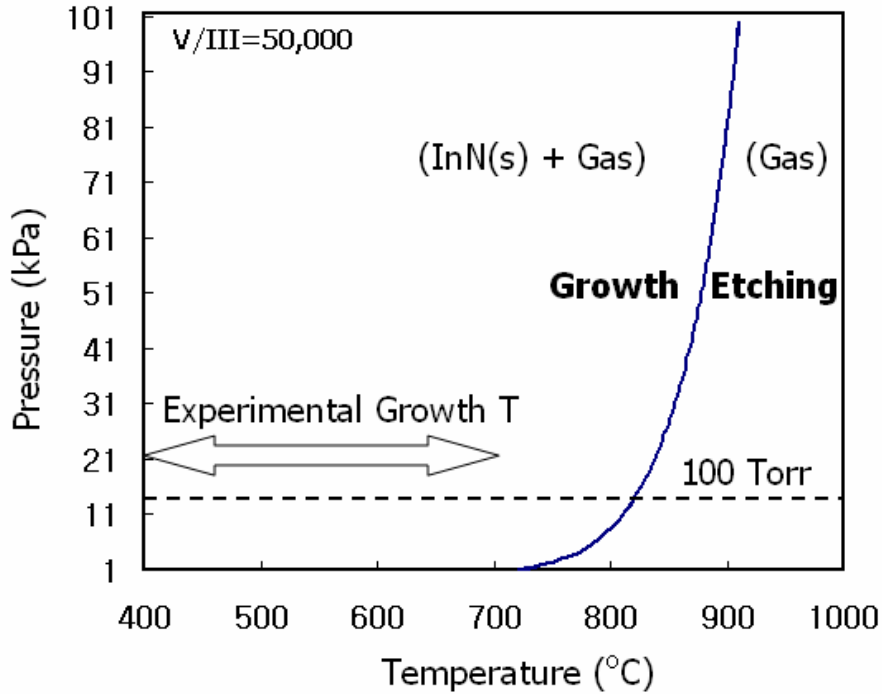


Figure 3-1. Calculated P-T phase diagram for InN at  $X(\text{In}) = 5.31212 \times 10^{-6}$ ,  $X(\text{N}) = 0.24998$ ,  $X(\text{H}) = 0.75000$ ,  $X(\text{C}) = 1.59364 \times 10^{-5}$  and  $V/\text{III} = X(\text{N})/X(\text{In}) = 50,000$ .

In summary, the InN P-T diagram was computed and the maximum growth temperature was estimated at the condition used in this study ( $P = 13.3 \text{ kPa}$  (100 Torr) for  $V/\text{III} = 50,000$ ) using ThermoCalc software. It is known that the typical MOVPE growth temperature of InN is in the range of 400 to 700°C depending on  $V/\text{III}$  ratio, pressure, residence time, and probing methods [Bhu03b].

In terms of the growth temperature region of InN, the difference between thermodynamic calculation and the experimental result is thought to be caused by the fact that the MOVPE growth of InN is non-equilibrium reaction.

### 3.1.2 Pressur-Temperature (P-T) Phase Diagram of $\text{In}_x\text{Ga}_{1-x}\text{N}$ and Phase Separation in $\text{In}_x\text{Ga}_{1-x}\text{N}$

For MOVPE growth of  $\text{In}_x\text{Ga}_{1-x}\text{N}$  in this study, trimethylindium (TMI) was used as In precursor, triethylgallium (TEG) as Ga precursor,  $\text{NH}_3$  as the reactive N source, and

$N_2$  as a carrier gas. Thus chemical equilibrium state was computed in the In-Ga-N-C-H system.

The growth condition for the growth of InN was calculated as a function of deposition temperature, pressure, and composition. In the thermodynamic analysis, the calculation procedures for  $In_xGa_{1-x}N$  are the same as that of InN, which was already discussed 3.1.1. The species, phases and thermodynamic properties included in this analysis are summarized in Table 3-3. The Redlich-Kister equation was used and the interaction parameters ( $L_0$  and  $L_1$ ) of liquid indium and liquid gallium are presented in Table 3-3.

The input mole fraction ratio of TMI to TEG which leads to the growth of  $In_{0.3}Ga_{0.7}N$  was calculated to show the relation of the input ratio of indium with the indium content in  $In_xGa_{1-x}N$ , which is obtained experimentally (Fig. 3.2) [Mat92]. The indium content of 0.3 in  $In_{0.3}Ga_{0.7}N$  is chosen in this calculation because the maximum indium mole fraction is reported to be about 0.3 [Elm98, Sin97, Nak94, Shi94, Nak93, Mat92]. The flow rate of TEG of 0.44 sccm, the flow rate of  $H_2$  of 4 slm, the flow rate of TMI of 0.27 sccm and the flow rate of  $NH_3$  of 1.6 slm were chosen in this study. This condition corresponds to  $X(In) = 1.87328 \times 10^{-5}$ ,  $X(Ga) = 3.05276 \times 10^{-5}$ ,  $X(N) = 0.111$ ,  $X(H) = 0.8887$ ,  $X(C) = 2.39364 \times 10^{-4}$ . The P-T phase diagram (Fig. 3.3) shows that the stable  $In_{0.3}Ga_{0.7}N$  can be obtained below the growth temperature of 730 °C and at  $P = 13.3$  kPa (100 Torr), which is the operating pressure of our MOVPE system [Mat92]. From these results, it is also clear that  $In_{0.3}Ga_{0.7}N$  is decomposed at  $T > 800$  °C. Experimentally, the growth of  $In_{0.3}Ga_{0.7}N$  is very difficult at the temperature above 800 °C [Mat92]. These calculated results are in the good agreement with the data obtained by Matsuoka [Mat92].

Table 3-3. Phases and species included in the analysis of MOVPE of  $\text{In}_x\text{Ga}_{1-x}\text{N}$ .

Phase	Species	Parameter (J/mol)
Solid (s)	C, InN, GaN, InGaN	$G_{\text{C(s)}} = -17368.4408 + 170.730318T - 24.3\text{TLN}(T) - 4.723 \times 10^{-4} T^2 + 2562600T^{-1} - 2.643 \times 10^8 T^{-2} + 1.2 \times 10^{10} T^{-3}$ $G_{\text{InN(s)}} = -149963.181 + 215.110609T - 38.0744\text{TLN}(T) - 0.0060668T^2$ $G_{\text{GaN(s)}} = -137112 + 272.388T - 44.3769\text{TLN}(T) - 0.0063011T^2 + 586387T^{-1}$ $L_{\text{InGaN(s)}} = 40320$
Liquid (l)	In, Ga, N	$G_{\text{In(l)}} = -6978.89011 + 92.3381153T - 21.8386\text{TLN}(T) - 0.00572566T^2 - 2.12032167 \times 10^{-6} T^3 - 22906T^{-1} + 3283.7 - 7.6402121T$ $G_{\text{Ga(l)}} = 5491.298 - 18.073995T - 7.017 \times 10^{-17} T^7 - 7055.643 + 132.73019T - 26.0692906\text{TLN}(T) + 1.506 \times 10^{-4} T^2 - 4.0173 \times 10^{-8} T^3 - 118332T^{-1} + 1.645 \times 10^{23} T^{-9}$ $G_{\text{N(l)}} = -4461.675 + 60.74575T - 12.7819\text{TLN}(T) - 0.00176686T^2 + 2.680735 \times 10^{-9} T^3 - 32374T^{-1}$ $L_0(\text{Ga, In}) = 4450 + 1.19185T$ $L_1(\text{Ga, In}) = 0.25943 T$
Gas (g)	C, C1H4, H, H2, N1H3, Ga1, Ga2, In, In2, N, N2	$G_{\text{C(g)}} = 710430.933 - 17.7062915T - 20.97529\text{TLN}(T) + 1.998237 \times 10^{-4} T^2 - 3.34617167 \times 10^{-8} T^3 + 1680.6515T^{-1} + \text{RTLN}(10^{-5}\text{P})$ $G_{\text{C1H4(g)}} = -77295.5632 - 147.095196T - 2.234656\text{TLN}(T) - 0.048463265T^2 + 4.33754333 \times 10^{-6} T^3 - 305431.45T^{-1} + \text{RTLN}(10^{-5}\text{P})$ $G_{\text{H(g)}} = 211801.621 + 24.4989821T - 20.78611\text{TLN}(T) + \text{RTLN}(10^{-5}\text{P})$ $G_{\text{H2(g)}} = 9522.9741 + 78.5273879T - 31.35707\text{TLN}(T) + 0.0027589925T^2 - 7.46390667 \times 10^{-7} T^3 + 56582.3T^{-1} + \text{RTLN}(10^{-5}\text{P})$ $G_{\text{NH3(g)}} = -53688.8736 - 38.3667407T - 21.21774\text{TLN}(T) - 0.022871695T^2 + 1.80809167 \times 10^{-6} T^3 - 76698.65T^{-1} + \text{RTLN}(10^{-5}\text{P})$ $G_{\text{Ga(g)}} = 259072.279 + 88.0130701T - 38.71057\text{TLN}(T) + 0.01053784T^2 - 9.86907833 \times 10^{-7} T^3 (298.13 \text{ K} \leq T \leq 600 \text{ K})$ $263812.519 + 33.4871429T - 30.75007\text{TLN}(T) + 0.00537745T^2 - 5.46534 \times 10^{-7} T^3 - 150942.65T^{-1} (600 \text{ K} \leq T \leq 1400 \text{ K})$ $G_{\text{Ga2(g)}} = 422882.385 - 36.0787973T - 33.72863\text{TLN}(T) - 0.009368525T^2 + 7.62775167 \times 10^{-7} T^3 - 19520.385T^{-1}$ $G_{\text{In(g)}} = 236267.082 - 68.7705731 * T - 15.35206\text{TLN}(T) - 0.00527185T^2 - 3.98269833 \times 10^{-7} T^3 - 94519.9T^{-1} + \text{RTLN}(10^{-5}\text{P})$ $G_{\text{In2(g)}} = 407673.852 - 41.5349376T - 35.82134\text{TLN}(T) - 0.00654889T^2 + 2.03928167 \times 10^{-8} T^3 - 20133.605T^{-1} + \text{RTLN}(10^{-5}\text{P})$ $G_{\text{N(g)}} = 466446.153 - 13.3752574T - 20.89393\text{TLN}(T) + 8.45521 \times 10^{-5} T^2 - 1.0018685 \times 10^{-8} T^3 + 2788.7865T^{-1} + \text{RTLN}(10^{-5}\text{P})$ $G_{\text{N2(g)}} = -8000.12556 - 8.81620364T - 27.22332\text{TLN}(T) - 0.0012599175T^2 - 5.39381 \times 10^{-7} T^3 - 38326.695T^{-1} + \text{RTLN}(10^{-5}\text{P})$

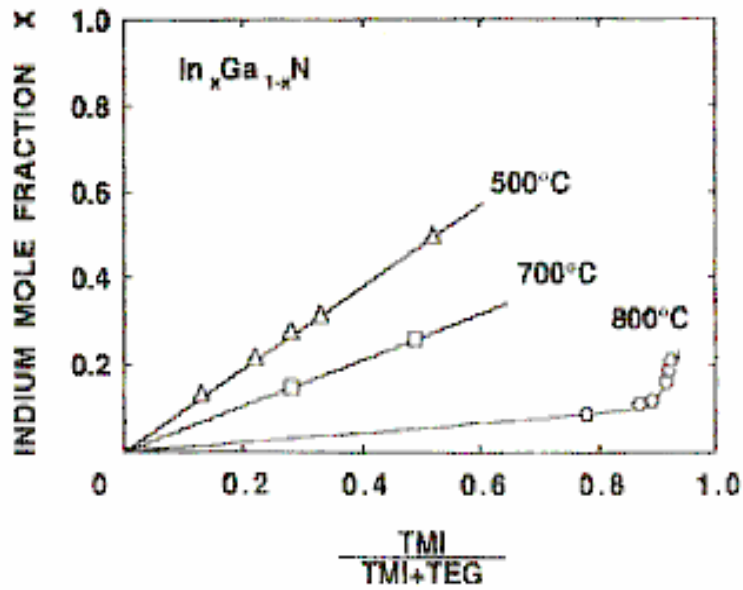


Figure 3-2. Relation between indium mole fraction ( $x$ ) of  $\text{In}_x\text{Ga}_{1-x}\text{N}$  and the flow rate ratio of the sum of group III source of TMI and TEG.

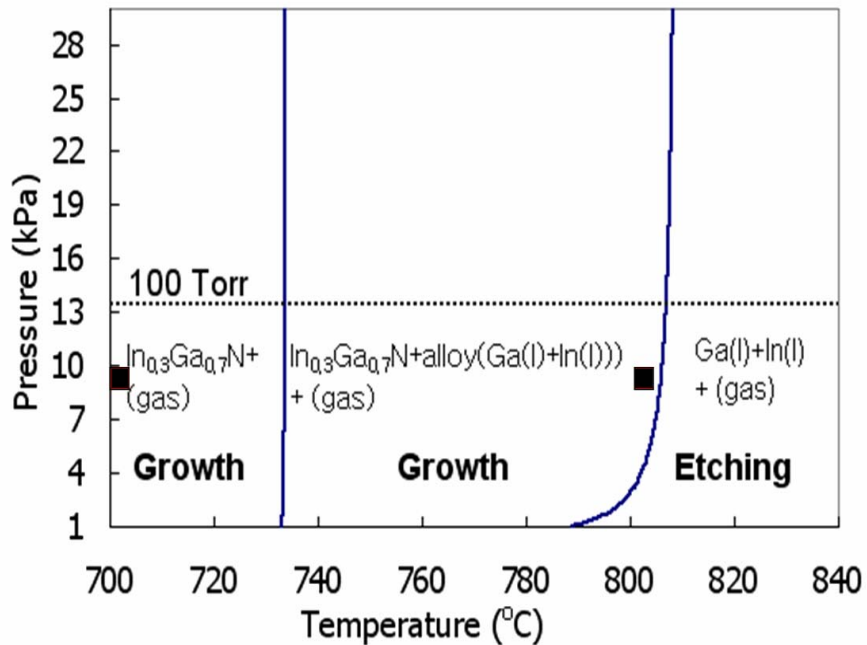


Figure 3-3. Calculated P-T phase diagram for  $\text{In}_{0.3}\text{Ga}_{0.7}\text{N}$  at  $X(\text{In})=1.87328 \times 10^{-5}$ ,  $X(\text{Ga})=3.05276 \times 10^{-5}$ ,  $X(\text{N})=0.111$ ,  $X(\text{H})=0.8887$ ,  $X(\text{C})=2.39364 \times 10^{-4}$  and the data points (■) are from the measurements observed by Matsuoka.

The main problem in growing  $\text{In}_x\text{Ga}_{1-x}\text{N}$  has been the phase separation at high indium content ( $X(\text{In}) > 0.3$ ) due to the very high equilibrium vapor pressure of nitrogen over  $\text{InN}$ . This phase separation leads to the miscibility gap in  $\text{In}_x\text{Ga}_{1-x}\text{N}$  [Ho96].

In the calculation of the miscibility gap in  $\text{In}_x\text{Ga}_{1-x}\text{N}$ , the 2-sublattice regular solution model was used for solid phase which consists of  $\text{InN}$  and  $\text{GaN}$  sub-lattices and the interaction parameter ( $L$ ) of 5.98 kcal/mol [Ho96] and the Redlich-Kister model was used for liquid phase where the interaction parameter of  $L_0$  and  $L_1$  are given in Table 3-2. The regular solution model for the Gibbs excess energy of mixing for  $\text{In}_x\text{Ga}_{1-x}\text{N}$  is given by

$$\Delta G_{mix}^{xs}(\text{In}_x\text{Ga}_{1-x}\text{N}) = x_{\text{InN}}x_{\text{GaN}}L \quad (3-5)$$

The Redlich-Kister model for the Gibbs excess energy of mixing for  $\text{In}(l)$  and  $\text{Ga}(l)$  is given by

$$\Delta G_{mix}^{xs}(\text{In}(l) - \text{Ga}(l)) = x_{\text{In}(l)}x_{\text{Ga}(l)}(L_0 + L_1(x_{\text{In}(l)} - x_{\text{Ga}(l)})) \quad (3-6)$$

The existence of a miscibility gap and phase separation of  $\text{In}_x\text{Ga}_{1-x}\text{N}$  grown by MOPVE was confirmed by using ThermoCalc Software (Fig.3.4) [Pin98].

The maximum calculated indium content in  $\text{In}_x\text{Ga}_{1-x}\text{N}$  grown by MOVPE is  $\sim 0.1$  at 780 °C, and the experimental data were used from the paper of E.L. Piner [Pin99]. Our calculations of the maximum indium content in  $\text{In}_x\text{Ga}_{1-x}\text{N}$  and the critical temperature are in the good agreement with results presented in [Str99]. However, based on experimental data the maximum indium content in  $\text{In}_x\text{Ga}_{1-x}\text{N}$  is  $\sim 0.3$  [Elm98].

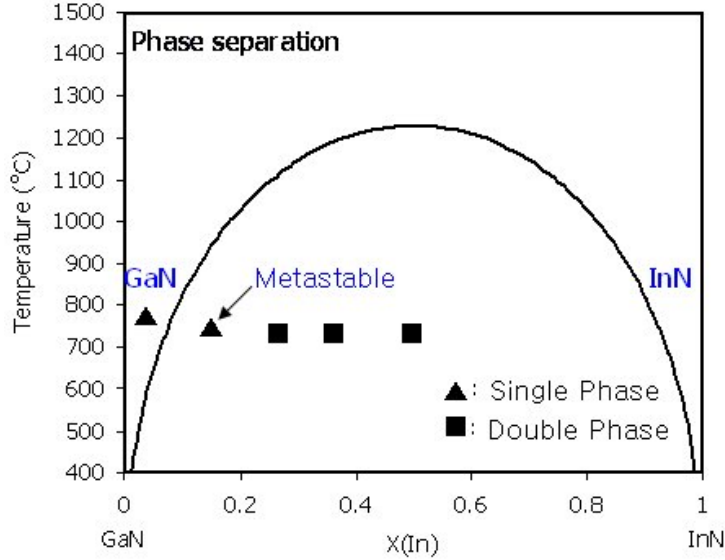


Figure 3-4. Thermodynamically calculated miscibility gap of  $\text{In}_x\text{Ga}_{1-x}\text{N}$  grown by MOVPE and the data points (▲■) are from the measurements observed by Piner.

This gap between the experimental result and theoretical one is caused by the fact that MOVPE growth of  $\text{In}_x\text{Ga}_{1-x}\text{N}$  is non-equilibrium reaction and this thermodynamic results show the binodal curve which corresponds to the stable region but not show the spinodal curve corresponding to the meta-stable region which can be achieved experimentally.

### 3.2 Quantum Calculation of Phase Separation in $\text{In}_x\text{Ga}_{1-x}\text{N}$

#### 3.2.1 Boundary Passivation Method with Hydrogen

The phase separation in  $\text{In}_x\text{Ga}_{1-x}\text{N}$  was studied using Quantum calculation method (also called the first-principle method or *ab-initio* method). For this calculation, the Hatree-Fock Self-Consistent-Field (HF-SCF) method was used and the total energy of the system was calculated by the Schrödinger equation (Eq.3-7).

$$\hat{H}\Psi_{HP} = E\Psi_{HP} \quad (3-7)$$

where  $\hat{H}$  is the Hamiltonian operator,  $E$  is the energy of system, and  $\Psi_{HP}$  is the Hatree product (the wave function of the system);

$$\Psi_{HP} = \psi_1 \psi_2 \cdots \psi_N \quad (3-8)$$

$$h_i \psi_i = \varepsilon_i \psi_i \quad (3-9)$$

Therefore,

$$H\Psi_{HP} = \left( \sum_{i=1}^N h_i \right) \Psi_{HP} = \left( \sum_{i=1}^N h_i \right) \psi_1 \psi_2 \cdots \psi_N = \left( \sum_{i=1}^N \varepsilon_i \right) \Psi_{HP} \quad (3-10)$$

$$h_i = -\frac{1}{2} \nabla_i^2 - \sum_{k=1}^M \frac{Z_k}{r_{ik}} + V_i\{j\} \quad (3-11)$$

$$V_i\{j\} = \sum_{j \neq i} \frac{|\psi_j|^2}{r_{ij}} dr = \sum_{j \neq i} \left\langle \psi_j \left| \frac{1}{r_{ij}} \right| \psi_j \right\rangle \quad (3-12)$$

where  $V_i\{j\}$  represents an interaction potential with all of the other electrons occupying orbitals  $\{j\}$  and  $i, j$  represent the electron and  $k$  the nucleus.

In the first step of the SCF, one guesses the wave function  $\psi$  for all of the occupied molecular orbitals (MOs) and uses these to construct the necessary one-electron operator,  $h$ . Solution of each differential equation (Eq. 3-11) provides a new set of  $\psi$ , presumably different from the initial guess. The one-electron Hamiltonians are formed anew using these presumably more accurate  $\psi$ . At some point, the difference between a newly determined set and the immediately preceding set falls some threshold criterion and the final set of  $\psi$  is referred to as the ‘converged’ SCF orbitals. The computational process is shown in Fig. 3.5.

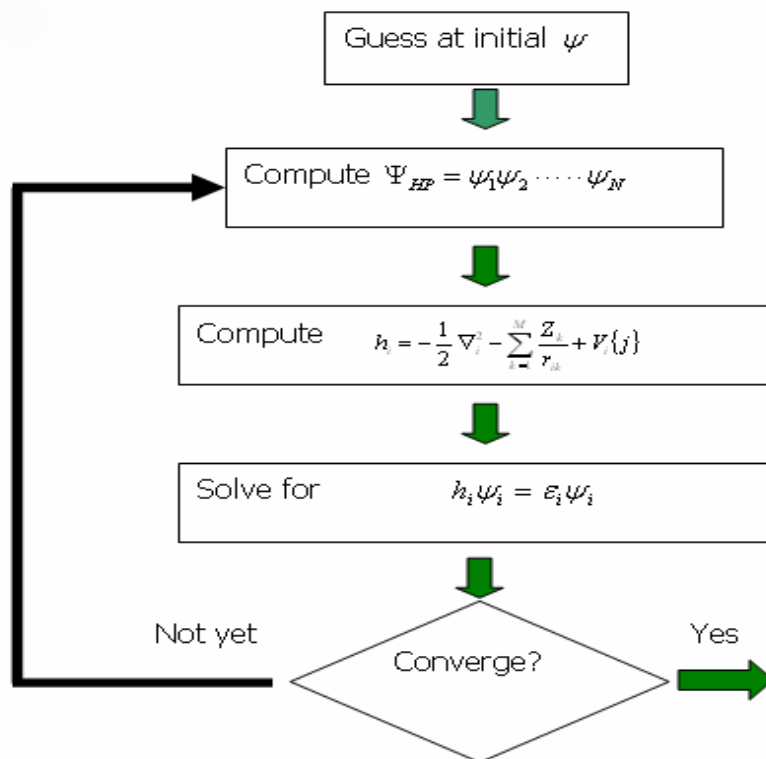


Figure 3-5. Flow chart of the HF-SCF procedure.

For the calculation of phase separation in  $\text{In}_x\text{Ga}_{1-x}\text{N}$ , the structure of the unit cell was set up, which contains In, Ga, N, and H with different indium composition and all nitrogens at the wall sides were passivated by hydrogen to calculate the total energy (see Fig. 3.6). As the indium content increases, the site of Ga is exchanged with In atom.

Three sets of bond lengths for In-H, Ga-H, and N-H were used for HF-SCF/3-21G calculation. The first one is derived from the calculation of the software of Molden, the second one from that of Hiraoka [Hir94], and the third one is obtained using PM3 method, one of semi-empirical methods with Hyperchem software (Table 3-4). The other bond lengths were obtained from the data of Inaba, who calculated these bond lengths using the Cambridge serial Total Energy Package (CASTEP) code [Ina01]. The energies were

calculated using three different calculation methods with Gaussian software (Table 3-5) where Hartree energy is equal to 627.51kcal/mol.

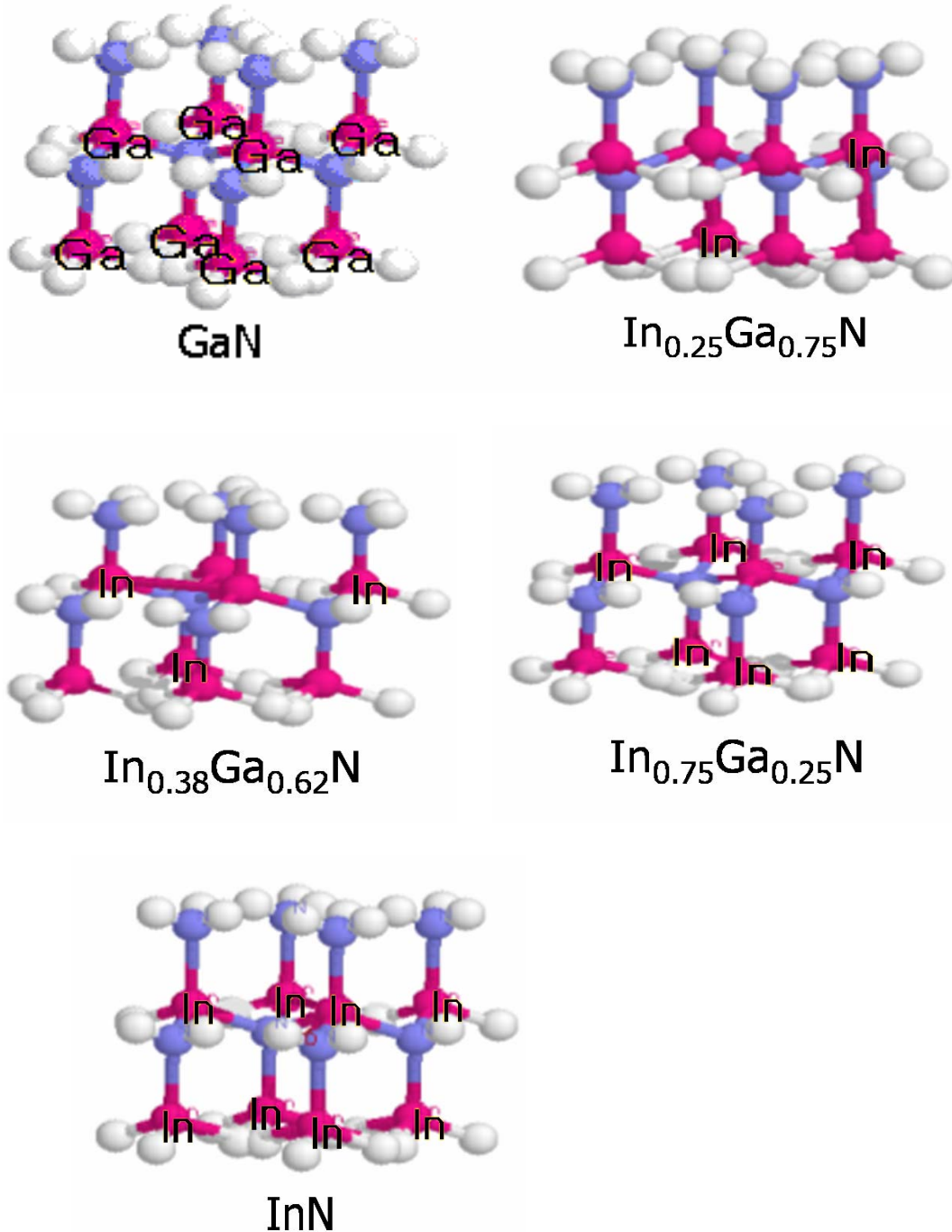


Figure 3-6. Structures used to compute the total energy for the In<sub>x</sub>Ga<sub>1-x</sub>N vs. indium mole fraction.

Table 3-4. Bond lengths for the calculation using HF-SCF.

	In-H	Ga-H	N-H	Ga-N (x=0)	In <sub>0.25</sub> Ga <sub>0.75</sub> N In-N	Ga-N	In <sub>0.38</sub> Ga <sub>0.62</sub> N In-N	Ga-N	In <sub>0.75</sub> Ga <sub>0.25</sub> N In-N	Ga-N	InN (x=1)
1	1.813	1.813	1.008	1.96	2.17	1.968	2.174	1.969	2.187	1.971	2.188
2	1.588	1.588	0.991	1.96	2.17	1.968	2.174	1.969	2.187	1.971	2.188
3	1.694	1.624	0.991	1.96	2.17	1.968	2.174	1.969	2.187	1.971	2.188

Table 3-5. Calculated total energy for three types of different bond length.

Energy (Hartree)	HF/3-21G (1)	HF/3-21G (2)	HF/3-21G (3)
GaN	-15758	-15763	-15762
In <sub>0.25</sub> Ga <sub>0.75</sub> N	-23365	-23366	-23366
In <sub>0.38</sub> Ga <sub>0.62</sub> N	-27166	-27167	-27167
In <sub>0.75</sub> Ga <sub>0.62</sub> N	-38558	-38570	-38570
InN	-46173	-46173	-46173

In the method of HF/3-21G, the 3 signifies that three core expanded Gaussian basis function are used as the core function and the 21G indicates that the valence functions are split into one basis function with two Gaussian type orbitals and one with only one Gaussian type orbital.

When these energies were compared, all three showed a similar value for each mole fraction of In. After the first one was selected, the energy in the state without phase-separation and the energy in the state with phase separation were compared. The energy in the state with phase separation was calculated from the summation of the energy of GaN and the energy of InN according to the lever rule. It is found out that the energy with phase separation is less than the energy without phase separation when the indium mole fraction (X(In)) is changed from 0.25 to 0.38 (Table 3-6).

Table 3-6. Calculated energies of  $\text{In}_x\text{Ga}_{1-x}\text{N}$  with the phase separation and without phase separation.

Energy (Hartree)	Energy for $\text{In}_x\text{Ga}_{1-x}\text{N}$ (HF/3-21G (1))	Energy for $(1-x)\text{GaN} + x \text{InN}$ (Phase separation)
GaN	-15758	-15758
$\text{In}_{0.25}\text{Ga}_{0.75}\text{N}$	-23365	-23361
$\text{In}_{0.38}\text{Ga}_{0.62}\text{N}$	-27166	-27315
$\text{In}_{0.75}\text{Ga}_{0.25}\text{N}$	-38558	-38569
InN	-46173	-46173

Based on presented data, the phase separation in  $\text{In}_x\text{Ga}_{1-x}\text{N}$  started to occur at  $0.25 \leq X(\text{In}) \leq 0.38$ . This result is in good agreement with the reported value of  $X(\text{In}) = 0.28$  [Elm98].

In summary, the phase separation in  $\text{In}_x\text{Ga}_{1-x}\text{N}$  was studied using quantum calculation method and 2-sublattice regular solution model. Calculated values of the maximum indium mole fraction,  $X(\text{In})$ , in  $\text{In}_x\text{Ga}_{1-x}\text{N}$  by quantum calculation method are in a good agreement with the reported experimental data.

CHAPTER 4  
CALCULATION OF THE CRITICAL THICKNESS OF InN ON GaN, AlN, Si, AND  
Al<sub>2</sub>O<sub>3</sub>

As the lattice mismatch between an epitaxial film and substrate increases, high-quality epitaxial growth can not continue indefinitely because the strain energy of the layer is eventually completely or partially relieved (or relaxed) by the generation of dislocations at the interface (misfit dislocations).

When a film with an unstrained lattice constant,  $a_f$  is deposited on a substrate with a different lattice constant,  $a_s$  (Fig. 4.1a), it initially grows with a lattice constant equal to that of the substrate. The mismatch is accommodated by strain in the layer. This is known as a pseudomorphic film. This continues until the film reaches some critical thickness  $h_c$  (Fig. 4.1b). The critical thickness is the thickness of the overgrown film at which misfit dislocation begins to occur. When the film thickness exceeds  $h_c$ , the misfit is accommodated by the formation of misfit dislocations which emanate from the interface between the film and substrate, and the lattice constant of the film relaxes toward the unstrained value (Fig. 4.1c) [Woo83].

The critical thickness for pseudomorphous growth is very important from a technological point of view. First, the misfit dislocations deteriorate the performance of the heterostructure devices due to the increased leakage current. Second, in uniformly strained epilayers, the interatomic spacing differs from that in the unstrained (relaxed) ones, thus changing the bandgap energy. Sapphire traditionally has been the most commonly used substrate for III-Nitride growth. Unfortunately, in case of InN the lattice

mismatch is significant – 25.7%. Several alternative substrates are considered, such as GaN, AlN, and Si with the lattice mismatch of 10.9 %, 13.7 %, and 7.9 % respectively. These values are much smaller compare to In/Al<sub>2</sub>O<sub>3</sub> case. The values of critical thickness of InN on grown on GaN, AlN, Al<sub>2</sub>O<sub>3</sub>, and Si substrates were calculated using different models and results are presented in this chapter.

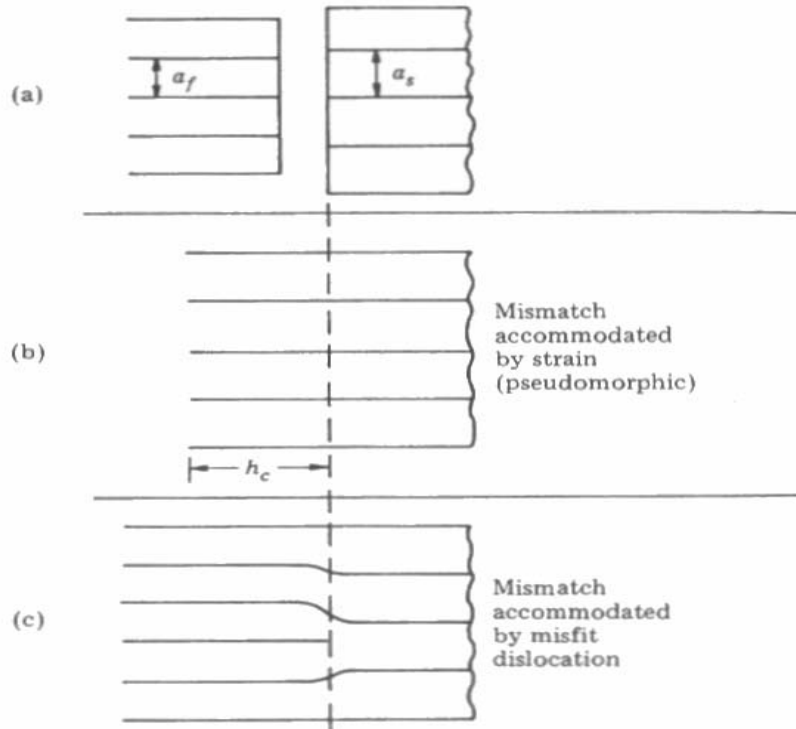


Figure 4-1. Schematic representation of the formation of misfit dislocations: (a) unstrained lattice; (b) thickness of the film is less than  $h_c$ ; (c) thickness of the film is greater than  $h_c$  misfit dislocations are generated.

#### 4.1 Calculation of Critical Thickness of InN by Matthews' Method.

In the simple model of Matthews (Mat75, Tu92), the critical thickness ( $h_c$ ) for pseudomorphic epitaxy is derived by minimizing the total energy, as the sum of the stored energy as strain and the net energy which film releases from dislocation formation.

It is assumed that film and substrate are cubic and prepared from elastically isotropic material. The elastic constants of the two crystals are assumed equal. The misfit

dislocations are considered to be arranged in a square network, to be in edge orientation, and to have Burgers vectors in the interface plane. The energy of a square grid made up of two perpendicular and non-interacting arrays of edge dislocation is therefore given by Eq. (4-1). The energy associated with the elastic strain in the film is given by Eq. (4-2).

$$E_{dislocation} = \frac{G_f b}{2\pi(1-\nu)} (f - \varepsilon) \left[ \ln\left(\frac{h}{b}\right) + 1 \right] \quad (4-1)$$

$$E_{strain} = \varepsilon^2 2G_f \frac{(1+\nu)}{(1-\nu)} h \quad (4-2)$$

$$E_{total} = \varepsilon^2 2G_f \frac{(1+\nu)}{(1-\nu)} h + \frac{G_f b}{2\pi(1-\nu)} (f - \varepsilon) \left[ \ln\left(\frac{h}{b}\right) + 1 \right] \quad (4-3)$$

where the in-plane strain  $\varepsilon$  is defined as

$$\varepsilon = \frac{a_{fl} - a_f}{a_f} \quad (4-4)$$

$$f = \frac{a_f - a_s}{a_f} \quad (4-5)$$

$$b = \frac{2(a_f \times a_s)}{a_f + a_s} \quad (4-6)$$

where  $a_{fl}$  is the parallel-to- the-interface or in-plane lattice constant of the deposited film material,  $a_f$  is the lattice constant of film material in the bulk or unstrained state,  $a_s$  is the lattice constant of substrate,  $f$  is the misfit between film and substrate,  $G_f$  is the shear modulus of the film,  $b$  is the Burger vector of the dislocation, and  $\nu$  is Poisson's ratio for the film.

The strain that minimizes the total energy is obtained by setting  $dE_{total}/d\varepsilon = 0$  to give the critical strain ( $\varepsilon^*$ ).

$$\varepsilon^* = \frac{b}{8\pi(1+\nu)h} \left[ \ln\left(\frac{h}{b}\right) + 1 \right] \quad (4-7)$$

The critical thickness ( $h_c$ ) is obtained by iteration with  $\varepsilon^* = f$ .

$$h_c = \frac{b}{8\pi(1+\nu)f} \left[ \ln\left(\frac{h_c}{b}\right) + 1 \right] \quad (4-8)$$

According to Eq. (4-7), the critical thickness of the overgrown film depends on the misfit  $f$ , Burger vector  $b$  and the Poisson's ratio  $\nu$  for the film.

For the calculation of the critical thickness of InN film on GaN and AlN substrates, selected physical properties of these materials are needed including the lattice constants of InN, GaN, and AlN. These property values are summarized in Table 4-1, where the Burger vector is calculated using Eq. (4-6) and Misfit dislocation is calculated using Eq. (4-5).

Table 4-1. Physical properties required for the calculation of the critical thickness of InN on GaN, AlN, Al<sub>2</sub>O<sub>3</sub>, and Si substrates.

	GaN (0001) substrate	AlN (0001) substrate	Al <sub>2</sub> O <sub>3</sub> (0001) substrate	Si (111) substrate
Burger vector ( $b$ )	3.354Å	3.311Å	4.758Å	3.840Å
Poisson's ratio of InN ( $\nu$ )	0.3 <sup>a</sup> (300K)	0.3 <sup>a</sup> (300K)	0.3 <sup>b</sup> (300K)	0.3 <sup>b</sup> (300K)
Misfit dislocation ( $f$ )	-0.098	-0.120	0.345	0.086

[<sup>a</sup>Bel04, <sup>b</sup>Liu02]

Table 4-2. Calculated critical thickness of InN on GaN, AlN, Al<sub>2</sub>O<sub>3</sub>, and Si substrates using Matthews' method.

	GaN (0001) substrate	AlN (0001) substrate	Al <sub>2</sub> O <sub>3</sub> (0001) substrate	Si (111) substrate
Critical thickness ( Å )	0.658	0.599	0.440	0.760

All these calculated values of critical thickness of InN lead to the conclusion that the misfit dislocations are formed during the growth of the first monolayer on all considered substrates.

#### 4.2 Calculation of Critical Thickness of InN by van der Merwe's Method.

When the square atomic meshes of the adjoining crystal planes are considered, the energy of the interface due to the lattice misfit will be equal to the energy of the homogeneous strain  $E_{hs}$  given by

$$E_{hs} = 2G_f h f^2 \frac{1 + \nu_b}{1 - \nu_b} \quad (4-9)$$

Beyond the critical thickness, misfit dislocations are introduced at the interface so that initially homogeneous strain and misfit dislocation energy coexist. According to the theory of van der Merwe, the energy of the misfit dislocations (the homogeneous strain is absent) is naturally divided into two parts. The first is the energy of intersection between the atoms of the two crystal halves (Eq. 4-10) [Mar03].

$$E_i = \frac{G_i b^2}{4\pi^2 d} \left( 1 + \lambda - \sqrt{1 + \lambda^2} \right) \quad (4-10)$$

where  $d \cong b$  is the separation of the atoms of the adjoining crystal planes.

The second is the energy of the periodic elastic strain energy which is distributed in the two crystal halves. This second energy is the total strain energy per atom of the misfit dislocations (Eq. 4-11).

$$E_e = -\frac{G_i b^2}{4\pi^2 d} \lambda \ln \left( 2\lambda \sqrt{1 + \lambda^2} - 2\lambda^2 \right) \quad (4-11)$$

The misfit dislocation energy  $E_d$  is then given by van der Merwe (Eq. (4-10)) through the sum of (Eq. 4-10) and (Eq. 4-11) [Mar03].

$$E_d = \frac{G_i b}{4\pi^2 d} \left[ 1 + \lambda - \sqrt{1 + \lambda^2} - \lambda \ln \left( 2\lambda \sqrt{1 + \lambda^2} - 2\lambda^2 \right) \right] \quad (4-12)$$

$$\lambda = 2\pi \frac{G' b}{G_i p}$$

$$\frac{1}{G'} = \frac{1 - \nu_a}{G_a} + \frac{1 - \nu_b}{G_b}$$

$$G_i = \sqrt{G_f G_s}$$

$$b = \frac{2a_f a_s}{(a_f + a_s)}$$

$$p = \frac{a_f a_s}{|a_f - a_s|}$$

where  $G'$  is the shear modulus at the interface,  $G_f$  is the shear modulus of the film,  $G_s$  is the shear modulus of the substrate,  $b$  is Burger vector, and  $p$  is the vernier of misfit or the dislocation spacing as shown in Fig. 4.2 [Mar03]. The dashed lines located at a distance  $p/2$  from the contact plane show the boundary beyond which the periodic strains originating from the dislocations practically vanish. The physical properties for the calculation of critical thickness of InN on GaN, AlN, Al<sub>2</sub>O<sub>3</sub>, and Si substrates are summarized in Table 4-3.

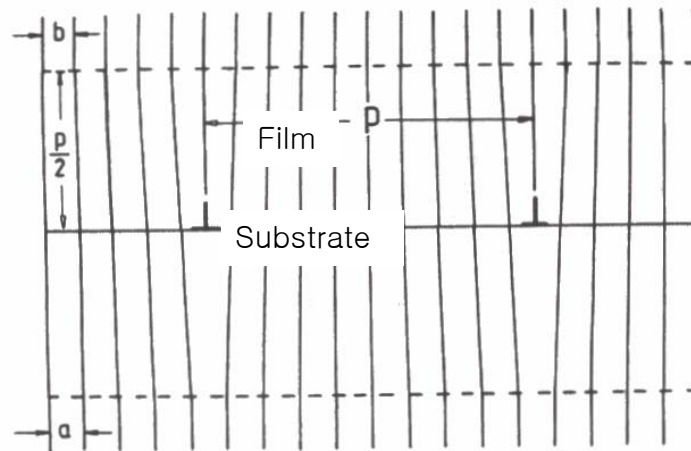


Figure 4-2. Model of epitaxial interface between two semi-infinite crystals resolved in a sequence of misfit dislocations spaced at an average distance  $p$ .

Table 4-3. Physical properties required for the calculation of critical thickness of InN on GaN, AlN, Al<sub>2</sub>O<sub>3</sub>, and Si substrates.

	InN	GaN (0001) substrate	AlN (0001) substrate	Al <sub>2</sub> O <sub>3</sub> (0001) substrate	Si (111) substrate
Poisson's ratio ( $\nu$ )	<sup>d</sup> 0.3	<sup>d</sup> 0.23	<sup>d</sup> 0.2	<sup>a</sup> 0.275	<sup>b</sup> 0.218
Bulk Modulus (GPa)	<sup>c</sup> 165	<sup>c</sup> 236	<sup>c</sup> 248	<sup>a</sup> 338	<sup>b</sup> 98

[<sup>a</sup>Bel80, <sup>b</sup>Geo99, <sup>c</sup>Chi99, <sup>d</sup>Bel04]

In the isotropic materials, the shear modulus ( $G$ ) can be calculated from a bulk modulus ( $B$ ) or tensile (Young's) modulus ( $E$ ) by

$$G = \frac{3(1-2\nu)}{2(1+\nu)} B = \frac{1}{2(1+\nu)} E \quad (4-13)$$

The modulus ( $G$ ) calculated from the given bulk modulus ( $B$ ) for each material using equation (4-13) is shown in Table 4-4.

Table 4-4. Calculated shear moduli for InN, GaN, AlN, Al<sub>2</sub>O<sub>3</sub>, and Si materials.

	InN	GaN (0001) substrate	AlN (0001) substrate	Al <sub>2</sub> O <sub>3</sub> (0001) substrate	Si (111) substrate
Shear modulus (GPa)	76	155	186	179	68

Equating the  $2 E_d$  of a square grid of two perpendicular and noninteracting arrays of misfit dislocations and the energy  $E_{hs}$  of the homogeneous strain gives ( $\nu_a = \nu_b = \nu$ )

$$\frac{h_c}{b} = \frac{G_i}{4\pi^2 G_f} \frac{(1-\nu)}{(1+\nu)} \frac{f(\lambda)}{f^2} \quad (4-14)$$

$$f = \frac{a_f - a_s}{a_f}$$

$$f(\lambda) = 1 + \lambda - \sqrt{1 + \lambda^2} - \lambda \ln(2\lambda\sqrt{1 + \lambda^2} - 2\lambda^2) \quad (4-15)$$

To illustrate the minimum energy considerations, the homogeneous strain energy  $E_{hs}$  is plotted for the number of InN epilayers and the dislocation energy  $E_d$  against the misfit for InN on a GaN substrate (see Fig. 4.3).

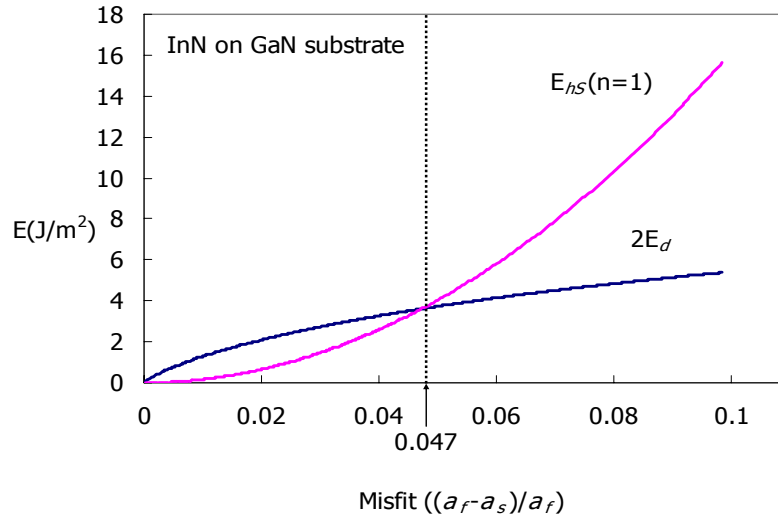


Figure 4-3. Homogeneous strain energy,  $E_{hs}$  for the 1<sup>st</sup> InN epilayer and dislocation energy,  $E_d$  vs. the misfit,  $f$  on GaN substrate.

Based on results presented in Fig.4.3, if the misfit  $f > 0.047$  (the critical value),  $E_{hs}$  is greater than  $E_d$  even for a monolayer, which means that the misfit dislocation occurs during the growth of the 1<sup>st</sup> InN epilayer since the misfit  $f$  between the InN film and the GaN substrate is 0.098. The calculated critical thickness (using Eq. 4-14) of InN on GaN substrate is 3.927 Å.

Identical calculation procedure was performed for the growth of InN on an AlN substrate with the matching result that the misfit dislocation also occurs during the growth of the 1<sup>st</sup> InN epilayer since the misfit ( $f$ ) between InN film and AlN substrate is 0.120, which is larger than 0.048 of the critical value of (Fig.4.4). The critical thickness of InN on AlN substrate is 3.044 Å (using Eq. 4-14).

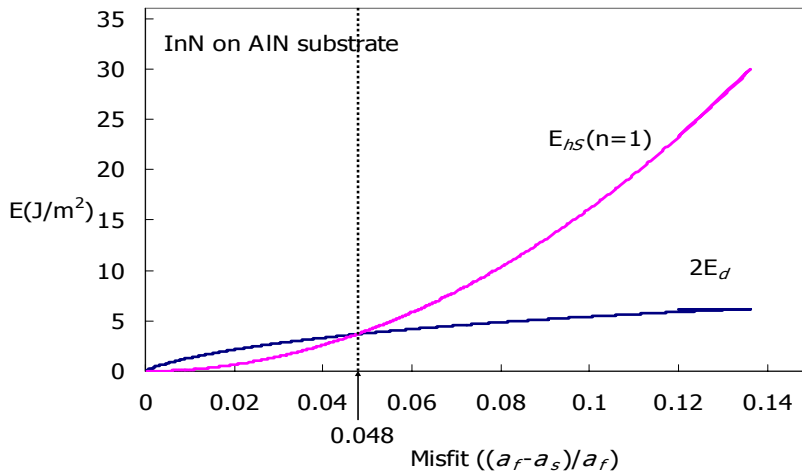


Figure 4-4. Homogeneous strain energy,  $E_{hs}$  for the 1<sup>st</sup> InN epilayer and dislocation energy,  $E_d$  vs. the misfit,  $f$  on AlN substrate.

Similar calculation procedure was performed for the growth of InN on an  $\text{Al}_2\text{O}_3$  substrate with the result pointed to the conclusion that the misfit dislocation also occurs during the growth of the 1<sup>st</sup> InN epilayer since the misfit ( $f$ ) between InN film and  $\text{Al}_2\text{O}_3$  substrate is 0.345, which is larger than 0.061 of the critical value of (Fig.4.5). The critical thickness of InN on  $\text{Al}_2\text{O}_3$  substrate is 0.574 Å from Eq. 4-14.

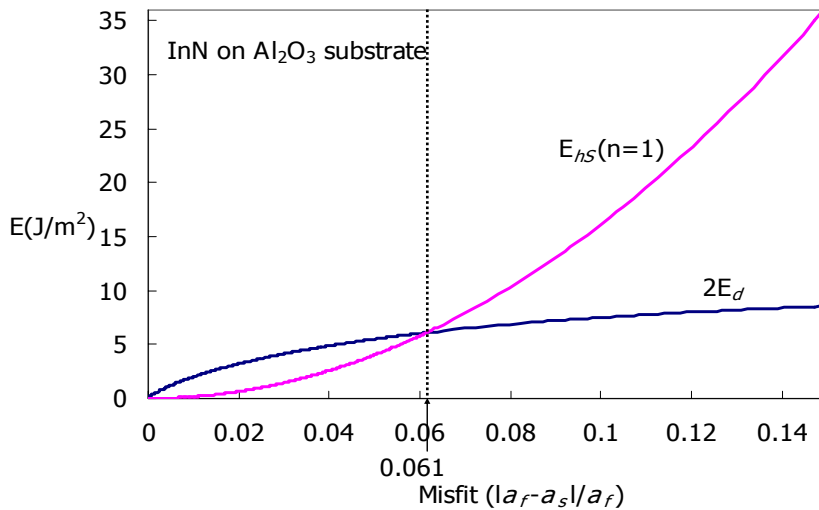


Figure 4-5. Homogeneous strain energy,  $E_{hs}$  for the 1<sup>st</sup> InN epilayer and dislocation energy,  $E_d$  vs. the misfit,  $f$  on  $\text{Al}_2\text{O}_3$  substrate.

Analogous calculation procedure was performed for the growth of InN on Si substrate which led us to the conclusion that the misfit dislocation also occurs during the growth of the 1<sup>st</sup> InN epilayer since the misfit ( $f$ ) between InN film and Si substrate is 0.086, which is larger than 0.039 of the critical value of (Fig.4.6). The critical thickness of InN on Si substrate is 3.450 Å from Eq. 4-14. All of the calculated critical thickness of InN on GaN, AlN, Al<sub>2</sub>O<sub>3</sub>, and Si substrate are given in Table 4-5.

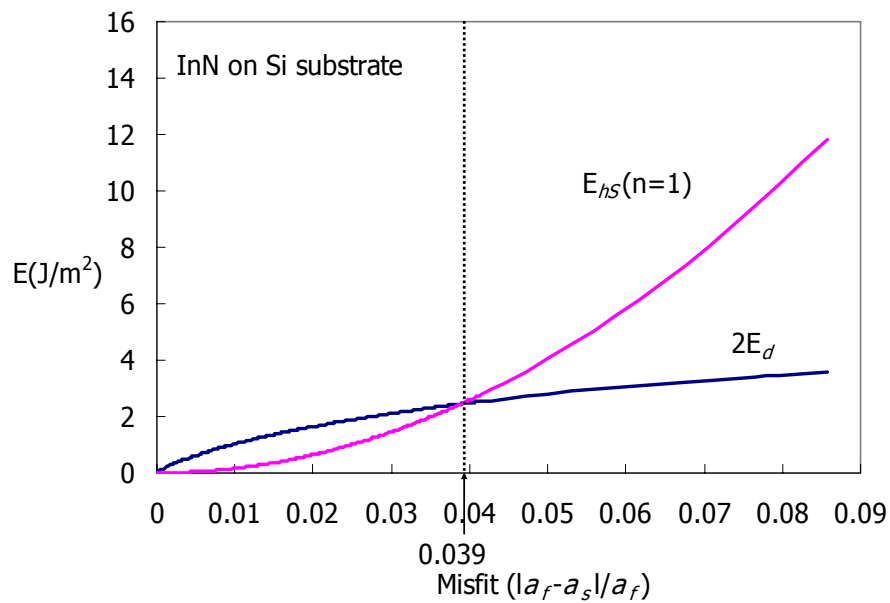


Figure 4-6. Homogeneous strain energy,  $E_{hs}$  for the 1<sup>st</sup> InN epilayer and dislocation energy,  $E_d$  vs. the misfit,  $f$  on Si substrate.

Table 4-5. Calculated critical thickness of InN using van der Merwe's method.

	GaN (0001) substrate	AlN (0001) substrate	Al <sub>2</sub> O <sub>3</sub> (0001) substrate	Si (111) substrate
Critical thickness of InN (Å)	3.927	3.044	0.574	3.450

From these results, the smallest value of the critical thickness is assigned for the InN/Al<sub>2</sub>O<sub>3</sub> system, although it has the biggest lattice mismatch. Substrates with the

lowest lattice mismatch, like Si or GaN, showed significantly higher values of the critical thickness which may be a good indicator that the critical thickness depends not only on the lattice mismatch of InN film and substrate material, but also the shear modulus and Poisson's ratio should be taken into account.

### 4.3 Calculation of Critical Thickness of InN by the Methods of Shen, Jesser, and Wilsdorf.

For the calculations of the critical thickness by Matthews' and van der Merwe's methods, it was assumed in the calculation of strain energy that the crystal structure is the cubic. Although the energy difference between the cubic and the hexagonal wurzite of the group III-nitride is small, the hexagonal structure is more stable one. Shen *et al.* proposed the equation for the calculations of the strain energy for the hexagonal structure [She02]. The compliances,  $s_{11}$  and  $s_{12}$  could be calculated from the elastic constants (a kind of modulus, stress per unit elastic strain)  $c_{11}$ ,  $c_{12}$ ,  $c_{13}$ ,  $c_{33}$ ,  $c_{44}$  (Eq. 4-16). These elastic constants are obtained using theoretical quantum calculation or the scattering and x-ray diffraction experimental method. The  $n$  is the number of layer and  $c$  is the lattice constant (5.704 Å) in the vertical direction. Therefore  $n \times c$  is the thickness of overgrown InN film.

$$E_{strain} = \frac{1}{s_{11} + s_{12}} \left( \frac{b_{II} - b_f}{b_f} \right)^2 \times n \times c \quad (4-16)$$

$$s_{11} = \frac{c_{11}c_{33} - c_{13}^2}{(c_{11} - c_{12})(c_{11}c_{33} + c_{12}c_{33} - 2c_{13}^2)}$$

$$s_{12} = \frac{c_{13}^2 - c_{12}c_{33}}{(c_{11} - c_{12})(c_{11}c_{33} + c_{12}c_{33} - 2c_{13}^2)} \quad (4-17)$$

In addition to the strain energy, the other energy such as dislocation energy should be considered in order to calculate the total energy. Jesser and Wilsdorf suggested the interfacial energy to include the dislocation energy. According to Jesser and Wilsdorf

[Jes67], the energy per unit area of each of the two dislocation arrays in the absence of the other is given by  ${}_x E_d$  and  ${}_y E_d$ , respectively, while the interfacial energy per unit area is given by the energy of the interfacial dislocations added to  $C N$ , the energy which the  $N$  overgrowth atoms per unit area possess when all of them are resting in the potential trough where  $C$  is the minimum interfacial potential energy per atom. Thus, the interfacial energy,  $E_I$  is given by

$$E_I = {}_x E_d + {}_y E_d + C N \quad (4-18)$$

where it has been assumed that there is no interaction energy between the two dislocation arrays. At the same time, the interfacial energy may be written as the sum of the overgrown film and substrate surface energies per unit area,  $E_1$  and  $E_2$ , when the two crystals are separated, less  $E_B$  (the binding energy between the two crystals when joined), i.e.

$$E_I = E_1 + E_2 - E_B \quad (4-19)$$

$E_B$  may be presented in terms of the dislocation energy and binding energy ( $E_b$ ), which would exist when there is no misfit, as

$$E_B = E_b - ({}_x E_d + {}_y E_d) \quad (4-20)$$

so that

$$E_I = {}_x E_d + {}_y E_d + E_1 + E_2 - E_b \quad (4-21)$$

where the binding energy ( $E_b$ ) is independent of misfit by virtue of definition.

By summing the strain equation and the interfacial energy, the total energy is given by

$$\begin{aligned}
E_{\text{interfacial}} &= 2E_d + E_{\text{surface}_b} + E_{\text{surface}_a} - E_{\text{binding}} \\
&= 2 \frac{G_i c}{4\pi^2} f(\lambda) + \frac{K}{4\pi^2 c} (G_b b^2 + G_a a^2 - 2G_i c^2)
\end{aligned} \tag{4-22}$$

$$f(\lambda) = 1 + \lambda - \sqrt{1 + \lambda^2} - \lambda \ln(2\lambda\sqrt{1 + \lambda^2} - 2\lambda^2)$$

$$\lambda = 2\pi \frac{G' c}{G_i p}$$

$$\frac{1}{G'} = \frac{1 - \nu_a}{G_a} + \frac{1 - \nu_b}{G_b}$$

$$G_i = \sqrt{G_a G_b}$$

$$c = \frac{2ab}{(a+b)}$$

$$p = \frac{ab}{(b-a)}$$

$$K = \frac{N_c}{4}$$

$$E_{\text{total}} = E_{\text{interfacial}} + E_{\text{strain}} \times n \times 5.704 \text{ \AA} \quad n=1, 2, 3, \dots \tag{4-23}$$

where 5.704 Å is the lattice constant of *c* of InN (Table 4-6), *n* is the number of the layer of the overgrown film and *N<sub>c</sub>* is the coordination number. As *n* increases, the total energy shows a minimum at the critical thickness. In other words, when  $\frac{dE_{\text{total}}}{d\varepsilon} = 0$ , misfit dislocations occur. The values of the elastic constants and compliances are summarized in Table 4-7.

Table 4-6. Lattice constant (Å) of InN, GaN, AlN.

Material	a (Å)	c (Å)
InN (wurtzite)	<sup>b</sup> 3.537	<sup>b</sup> 5.704
GaN (wurtzite)	<sup>a</sup> 3.189	<sup>a</sup> 5.185
AlN (wurtzite)	<sup>a</sup> 3.112	<sup>a</sup> 4.98

[<sup>a</sup>Mor94, <sup>b</sup>Dav02a]

Table 4-7. Elastic constants  $c_{ij}$  and compliances  $s_{ij}$  of InN.

$c_{ij}$ (GPa)	$c_{11}$	$c_{12}$	$c_{13}$	$c_{33}$	$c_{44}$
	297.5	107.4	108.7	250.5	89.4
$s_{ij}$ (1/GPa)	$s_{11}$	$s_{12}$			
	0.00424	-0.00102			

[Chi99]

Results presented in Figure 4-7 indicate that for the growth of InN on GaN, the total energy shows a minimum at the 1<sup>st</sup> InN epilayer and as the result the misfit dislocation happen from the 1<sup>st</sup> monolayer of InN. The same outcomes were obtained for the growth of InN on AlN, Al<sub>2</sub>O<sub>3</sub>, and Si substrates (Fig. 4.8, Fig 4.9, and Fig.4.10). For the growth of InN on all named substrates, the critical thickness  $h_c$  is less than 5.704 Å which points towards conclusion that the misfit dislocation occurs during the growth of the 1<sup>st</sup> monolayer of InN.

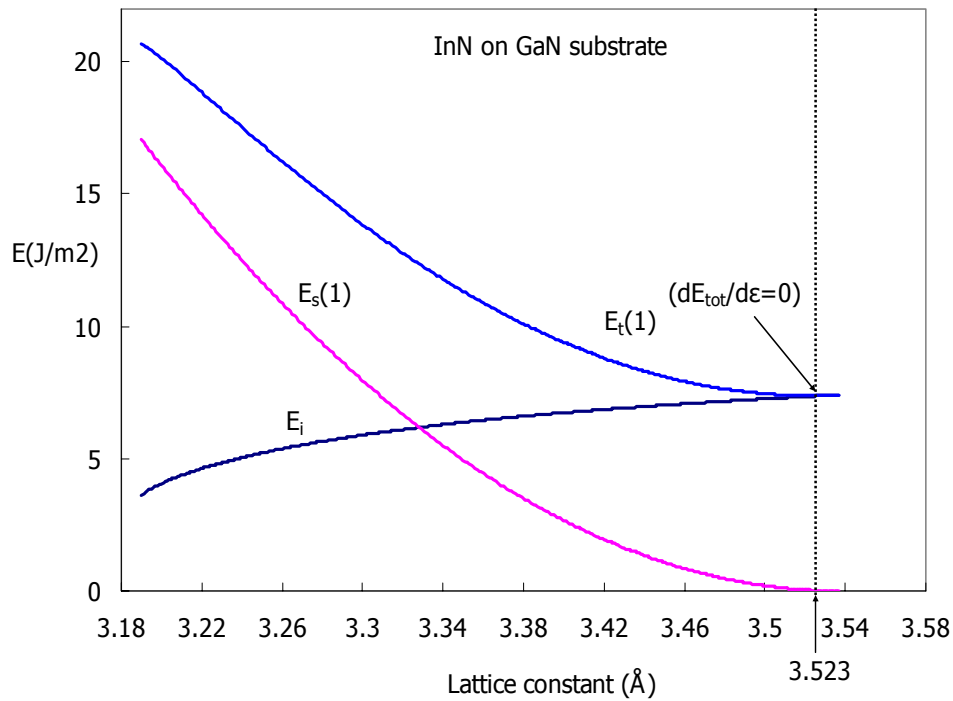


Figure 4-7. Total energy  $E_t$ , strain energy  $E_s$ , interfacial energy  $E_i$  vs. lattice constant of InN for 1<sup>st</sup> epilayer InN on GaN substrate.

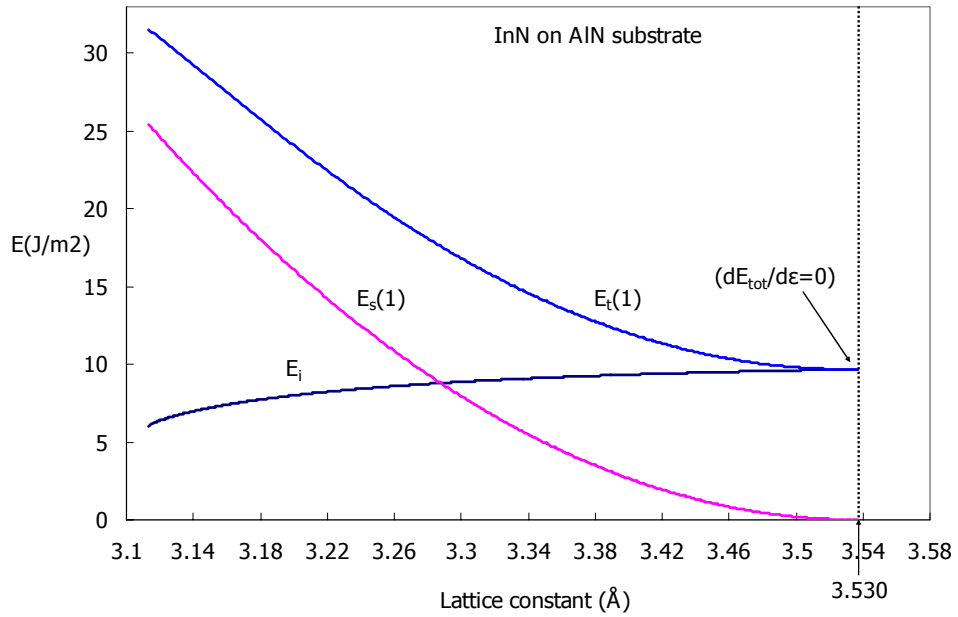


Figure 4-8. Total energy  $E_t$ , strain energy  $E_s$ , interfacial energy  $E_i$  vs. lattice constant of InN for 1<sup>st</sup> epilayer InN on AlN substrate.

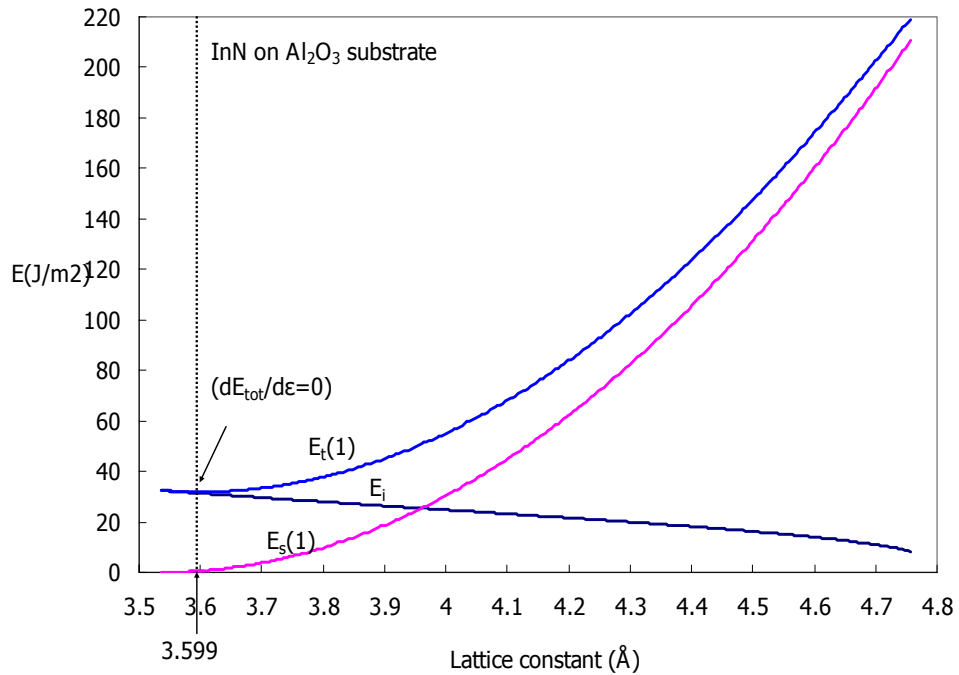


Figure 4-9. Total energy  $E_t$ , strain energy  $E_s$ , interfacial energy  $E_i$  vs. lattice constant of InN for 1<sup>st</sup> epilayer InN on Al<sub>2</sub>O<sub>3</sub> substrate.

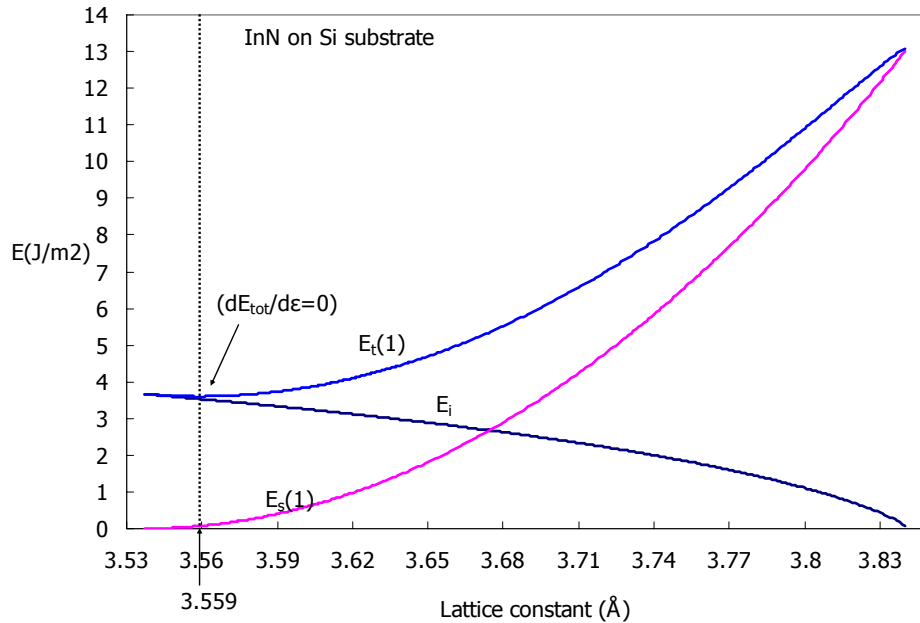


Figure 4-10. Total energy  $E_t$ , strain energy  $E_s$ , interfacial energy  $E_i$  vs. lattice constant of InN for 1<sup>st</sup> epilayer InN on Si substrate.

The critical thickness  $h_c$  of InN on GaN, AlN, Al<sub>2</sub>O<sub>3</sub>, and Si substrates was calculated using three different models and the results are summarized in Table 4-8. Compared with the Matthew's model, the van der Merwe's model shows the different value of critical thickness for all substrate but sapphire since two models come from the different concept. The van der Merwe introduces the new parameters such as the vernier of misfit and shear modulus at the interface, and new concept of  $2E_d=E_{hs}$ . It is considered that this may cause the different result. For sapphire, the similar result happens to be obtained. Each independent calculation showed that the critical thickness of InN film grown on all considered substrates is less than a monolayer width. These results are in good agreement with the experimental data based on HRTEM of InN on GaN [Bel04], which shows that the misfit dislocations were introduced during the growth of the 1<sup>st</sup> epilayer of InN (thickness of the monolayer of InN = 5.704 Å) for InN grown on GaN substrate.

Table 4-8. Critical thickness ( $h_c$ ) calculated of InN using three different models.

	$h_c$ (Å) InN on GaN	$h_c$ (Å) InN on AlN	$h_c$ (Å) InN on Al <sub>2</sub> O <sub>3</sub>	$h_c$ (Å) InN on Si
Matthews	0.658	0.599	0.440	0.760
van der Merwe	3.927	3.044	0.574	3.450
Shen-Jesser- Wilsdorf	< 5.704	< 5.704	< 5.704	< 5.704

In summary, the critical thickness is less than the monolayer width when three theoretical models are used. This result may suggest that the study of suitable substrate be necessary in order to improve the crystallinity of InN. In this chapter, the critical thickness of InN was calculated by taking into account the several energies that can exist in the InN epitaxial film and the physical properties of the epitaxial film and substrate using three different methods. As a result, it is concluded that our calculated values are in good agreement with the experimental results available for the growth of InN on GaN substrate [Bel04]. Considering the theoretical point of view, the model of Shen, Jesser, and Kuhlmann-Wilsdorf is thought to be the most accurate one.

CHAPTER 5  
Indium Nitride (InN) GROWTH BY METAL-ORGANIC VAPOR PHASE EPITAXY  
(MOVPE)

Unlike MOVPE growth of Ga and Al nitride, it is difficult to obtain high quality InN by MOVPE because the temperature range for successful growth is very narrow (500 to 650 °C) and for alloys not well matched to that for the other III-nitrides. Part of the problem is related to the low growth temperature and the low amount of atomic nitrogen given the low decomposition efficiency of ammonia in this temperature range. Furthermore there is no obvious substrate for growth of InN.

In this chapter, results on the optimization of the growth conditions for InN are presented for several substrate and buffer layer combinations. The process variables that were manipulated are growth temperature, N/In ratio, pressure, and the buffer layer growth conditions (temperature, GaN or InN buffer layer, and nitridation). The post-growth annealing of InN film was also studied. The reactor design was modified from a horizontal type to an extended horizontal and vertical geometry by changing the inlet tube.

### **5.1. Indium Nitride (InN) Growth Optimization**

Optimization of MOVPE growth condition is typically accomplished by empirical studies of the key process parameters. This study concentrates on substrate selection, growth temperature, N/In ratio, buffer layer material (GaN or InN), and post-growth annealing. Several film properties are often important for a particular application (e.g., background impurity concentration, defect density, surface roughness). In general, the

optimum conditions for achieving a particular measure of film quality are different from another film property. The quality factors included in this study are crystalline quality (XRD), surface roughness (AFM, SEM), background impurity level (PL, AES), and carrier type and mobility (Hall measurement). These factors are studied for each substrate and buffer layer.

### 5.1.1. Substrate Selection

The selection of substrate is one of the most important considerations for epitaxial growth. In this study, three substrates, Si (111), Al<sub>2</sub>O<sub>3</sub> (0001), and GaN (5μm)/Al<sub>2</sub>O<sub>3</sub> (0001), are explored for the epitaxial growth of InN. Since Al<sub>2</sub>O<sub>3</sub> and Si have different crystal structures than InN, as well as different lattice constants values and thermal expansion coefficients, heteroepitaxy of InN on these substrates is expected to be a challenge. The mismatch in lattice constant important in heteroepitaxy is that which occurs at growth temperature, since growth mechanisms are influenced by the lattice spacing at growth temperature. Subsequent adhesion and cracking issues upon cooling are determined in part by the mismatch in thermal expansion coefficients.

Upon cooling, the mismatch in thermal expansion coefficients can lead to increasing strain, and possibly producing cracking. The lattice constants and thermal expansion coefficients of the substrates and InN are summarized in Table 5-1<sup>[aMor94, bDav02]</sup>. The lattice mismatch ( $f$ ) between InN and substrate is defined by

$$f = \frac{a_f - a_s}{a_f} \times 100(\%) \quad (5-1)$$

where  $a_f$  is the lattice constant of film material (InN) in the bulk or unstrained state,  $a_s$  is the lattice constant of substrate.

The linear thermal expansion coefficient (TEC) mismatch between InN and substrate is calculated in the same way by

$$TEC \text{ mismatch} = \frac{a_f - a_s}{a_f} \times 100 (\%), \quad (5-2)$$

where  $a_f$  is the thermal expansion coefficient of film material in the bulk or unstrained state and  $a_s$  is the thermal expansion coefficient of substrate.

Table 5-1. Structural properties of InN, GaN, Al<sub>2</sub>O<sub>3</sub>, Si, and AlN substrates.

Substrates	Lattice constant a (Å)	Lattice constant c (Å)	Lattice mismatch (%)	TEC (10 <sup>-6</sup> K <sup>-1</sup> )		TEC mismatch (%)
				a	c	
<b>InN-wurtzite</b>	3.537 <sup>b</sup>					
<b>GaN-wurtzite</b>	3.189 <sup>a</sup> (5.524 when rotated 30 °)	5.704 <sup>b</sup> 5.18 <sup>a</sup>	-10.9	5.70 <sup>b</sup> 5.59 <sup>a</sup>	3.70 <sup>b</sup> 3.17 <sup>a</sup>	0 -30.9
<b>Al<sub>2</sub>O<sub>3</sub> – rhombohedral</b>	4.758 <sup>a</sup>	12.991 <sup>a</sup>	25.7	7.5 <sup>a</sup>	8.5 <sup>a</sup>	-48.5
<b>Si (111) – cubic</b>	5.43 <sup>a</sup> (3.84 as hexagonal)		7.9 (hexagonal)	6.2 <sup>a</sup>		-37.7
<b>AlN-wurtzite</b>	3.112 <sup>a</sup>	4.98 <sup>a</sup>	-13.7	4.2 <sup>a</sup>	5.3 <sup>a</sup>	-8.1

When the GaN film is rotated by 30° with respect to the sapphire substrate, the minimum lattice mismatch in the GaN/Al<sub>2</sub>O<sub>3</sub> system occurs so that the (0001)//(0001), [ $\bar{1}1010$ ]/[ $\bar{1}210$ ] GaN/Al<sub>2</sub>O<sub>3</sub> interface is formed and the lattice constant of  $a = 5.524$  Å at room temperature as shown in Fig. 5.1[She02]. Bulk Si crystal has a diamond structure with lattice constant of  $a = 5.43$  Å at room temperature. The Si (111) surface, however,

presents an equivalent hexagonal surface with lattice parameter  $a = 3.84 \text{ \AA}$  as shown in Fig. 5.2 [Shu00].

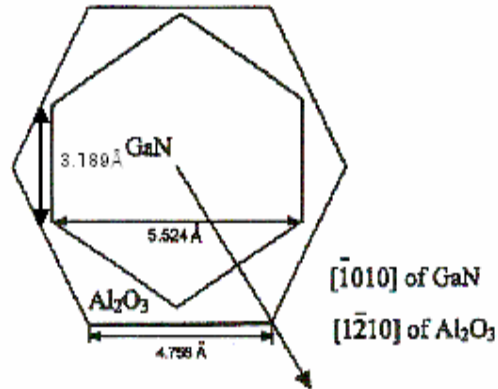


Figure 5-1. Schematic for the deposition of the (0001)//(0001),  $[\bar{1}010]$ // $[\bar{1}210]$  GaN/ $\text{Al}_2\text{O}_3$  system.

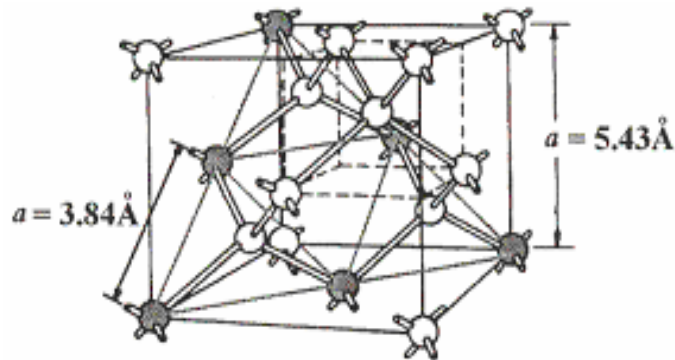


Figure 5-2. Planes of Si (111) substrate.

#### 5.1.1.1. Sapphire (c- $\text{Al}_2\text{O}_3$ (0001))

Sapphire is the most widely used substrate for the epitaxial growth of InN. Relatively large area, good quality crystals of sapphire are commercially available at a reasonable cost. Sapphire is transparent and stable at high temperature. High quality epitaxial InN films can be grown easily on sapphire substrates by popular growth methods such as MOVPE and MBE. Sapphire, however, has a large lattice mismatch of 25.7 % with InN. This large lattice mismatch and thermal expansion coefficient difference can result in an extremely high density of structural defects. Nevertheless, this

disadvantage may be partially overcome with substrate pretreatment and buffer layers [Bhu03b]. For example, nitridation of the sapphire substrate surface significantly improves the crystalline quality of InN as a result of the formation of an AlN interfacial layer, which reduces the lattice mismatch from 25.7 % for InN/c-Al<sub>2</sub>O<sub>3</sub> to 13 % for InN/AlN. Additionally, the InN/AlN has a comparatively small thermal expansion coefficient mismatch of 8.1 %.

This study aims to improve the crystallinity of InN on sapphire substrates through use of different buffer layers, different buffer layer temperature, different growth temperature, post-growth annealing, and modification of the inlet tube.

#### **5.1.1.2. Gallium Nitride (GaN/c-Al<sub>2</sub>O<sub>3</sub> (0001))**

Gallium nitride has a small lattice mismatch of 10.9 % with InN compared with sapphire (25.7 %) and AlN (13 %) substrates, although it is greater than that of silicon (7.9 %). In addition, gallium nitride substrates generally lead to good coverage of InN, which is very difficult to achieve with silicon substrates. It was reported that the highest mobility of InN ( $\sim 700 \text{ cm}^2/\text{V s}$ ) was obtained from MOVPE on GaN substrates [Yam99a]. Therefore, this study explores the feasibility of the gallium nitride on sapphire substrate for the epitaxial growth. The thickness of the GaN layer on Al<sub>2</sub>O<sub>3</sub> is 5  $\mu\text{m}$ .

#### **5.1.1.3. Silicon (Si (111))**

Silicon is an excellent candidate as a substrate for the epitaxial growth of InN because it has a smaller lattice mismatch, 7.9 % for InN (0001)/Si (111), compared with the commonly used insulating sapphire substrates (25.7 % for InN (0001)/c-Al<sub>2</sub>O<sub>3</sub> (0001), and 10.9 % for InN (0001)/GaN (0001)).

Si has been used as a substrate for the epitaxial growth of InN, but the film quality has been very poor to date and there has been no report of the FWHM of XRD principal

reflection to judge the crystal quality. Poor surface coverage of InN on Si is observed. It is believed that MOVPE growth of InN directly onto Si was unsuccessful because of formation of a  $\text{SiN}_x$  interfacial layer. The Si substrate surface is nitrated during growth even at a low growth temperature ( $\sim 400$  °C) [Bhu03b]. Introduction of TMI into the reactor before flowing  $\text{NH}_3$  to prevent amorphous  $\text{SiN}_x$  formation has been tried with the result. Although the previous work has not been encouraging, the high quality and low cost of silicon make it a very attractive substrate. The possibility of integrating optoelectronic InN devices with Si electronic devices is also attractive. This study aims to achieve high quality single crystalline InN growth on Si substrates by adjusting the growth conditions.

#### **5.1.2. Substrate Preparation Procedure**

Sapphire and GaN/sapphire substrates were degreased in boiling solvent in the following sequence, tri-chloroethylene, acetone, and then methanol for 5 min each. In the case of silicon, an etching step was added after the degreasing step in which the silicon substrate was etched in ammonium bifluoride (95 %) for 2 min to obtain an oxide-free and H-terminated silicon substrate. After degreasing and etching, all substrates were rinsed in de-ionized water and dried under nitrogen flow [Etc01].

#### **5.1.3. Metal-Organic Vapor Phase Epitaxy (MOVPE) Reactor**

A horizontal, cold-wall MOVPE reactor (Nippon Sanso) with a RF-induced heated susceptor was used in this study. Trimethylindium (TMI) (99.9995 %, Shipley) and ammonia ( $\text{NH}_3$ ) (99.9999 %, Solktronics) were used as precursors and nitrogen was used as a carrier gas. TMI is kept in the bubbler at 20 °C and is transferred into the reactor via carrier gas. Ammonia is carried directly into the reactor without carrier gas. The outer quartz wall is kept at 25 °C by circulating cooling water in the quartz jacket. The pressure

of the reactor is controlled with a Baratron gauge. A schematic of the MOVPE reactor is shown in Fig. 5.3 and a more detailed description is given elsewhere.

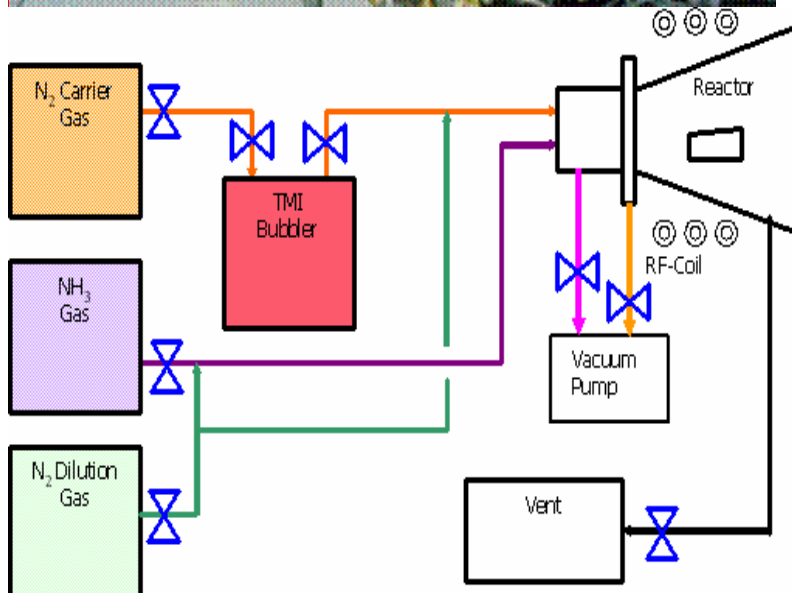
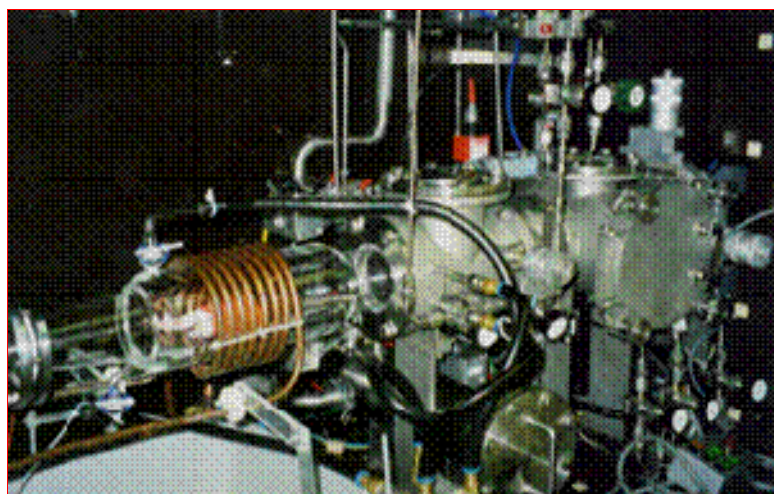
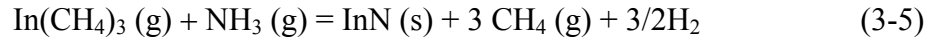


Figure 5-3. Image and schematic of horizontal, cold-wall MOVPE reactor system.

#### 5.1.4. Growth Chemistry and Conditions for InN Growth

The epitaxial growth of InN by MOVPE is a non-equilibrium growth process that relies on vapor transport of precursors to the surface of a heated substrate with subsequent reaction of typically group III alkyls and group V hydrides. The chemicals are transported as a dilute vapor to the surface of the heated substrate where pyrolysis reactions occur [Jac64, Tra78, and Lar85]. The reaction chemistry for deposition of InN

was reviewed in detail in Chapter 3. The overall reaction involves trimethylindium reacting with NH<sub>3</sub> to form InN and the reaction is given by



The N/In ratio (volumetric flow ratio of NH<sub>3</sub> to TMI) is calculated by assuming ideal gas and solution behavior. Therefore, the volumetric flow ratio of NH<sub>3</sub>/TMI at standard temperature and pressure (STP) is equal to the pressure ratio of NH<sub>3</sub>/TMI at constant volume and temperature, according to the equation:

$$P = \frac{RT}{V} \times 22.4 \times n \quad (5-3)$$

Given that the total TMI bubbler pressure is kept at 500 Torr and the vapor pressure of TMI is given by

$$P_{TMI} (\text{Torr}) = 10^{10.98 - (3204/T(K))} \quad (5-4)$$

the volumetric flow of TMI is calculated by

$$V_{TMI} (\text{sccm}) = V_{N_2} \times \frac{P_{TMI} (\text{Torr})}{P_{total} (500 \text{Torr})} \quad (5-5)$$

where  $V_{N_2}$  represents the volumetric flow rate of nitrogen introduced into the TMI bubbler.

The N/In ratio is calculated by

$$\frac{N}{In} = \frac{V_{NH_3}}{V_{TMI}} \quad (5-6)$$

The pressure of MOVPE reactor was 100 Torr during the growth and two different buffer layers of GaN and InN were also studied to check which buffer layer gave better structural quality InN. The range of growth conditions studied for depositing InN is summarized in Table 5-2. When the flow rate of TMI was kept at 0.26 sccm and the N/In ratio was varied from 3000 to 15,000 in the first growth condition set, indium droplets formed at the surface. To prevent indium droplet formation, a low flow rate of TMI (0.03~0.08 sccm) or a high N/In ratio (20,000~50,000) was used in the second growth condition set. In the second growth condition set, the narrower growth temperature range 530 to 570 °C was selected based on the results on the temperature influence on the InN

structural quality obtained from the first growth condition set, which showed that the optimal growth temperature was around 550 °C .

Table 5-2. Range of growth conditions examined for growth of InN.

TMI Flow Rate (sccm)	NH <sub>3</sub> Flow Rate (sccm)	N/In	Growth Temperature (°C)
0.26	800-4000,	3000-15,000	450-750
0.03-0.08	1600	20,000-50,000	530-570

The growth sequence for each substrate is also shown in Fig. 5.4. For Al<sub>2</sub>O<sub>3</sub> (0001), it is generally accepted that nitridation is required to obtain high quality InN by acting as a compliant layer. This effect will be discussed later. For Si (111), nitridation should be avoided because SiN<sub>x</sub> leads to polycrystalline InN. For GaN/Al<sub>2</sub>O<sub>3</sub> (0001), the effect of nitridation will be discussed later.

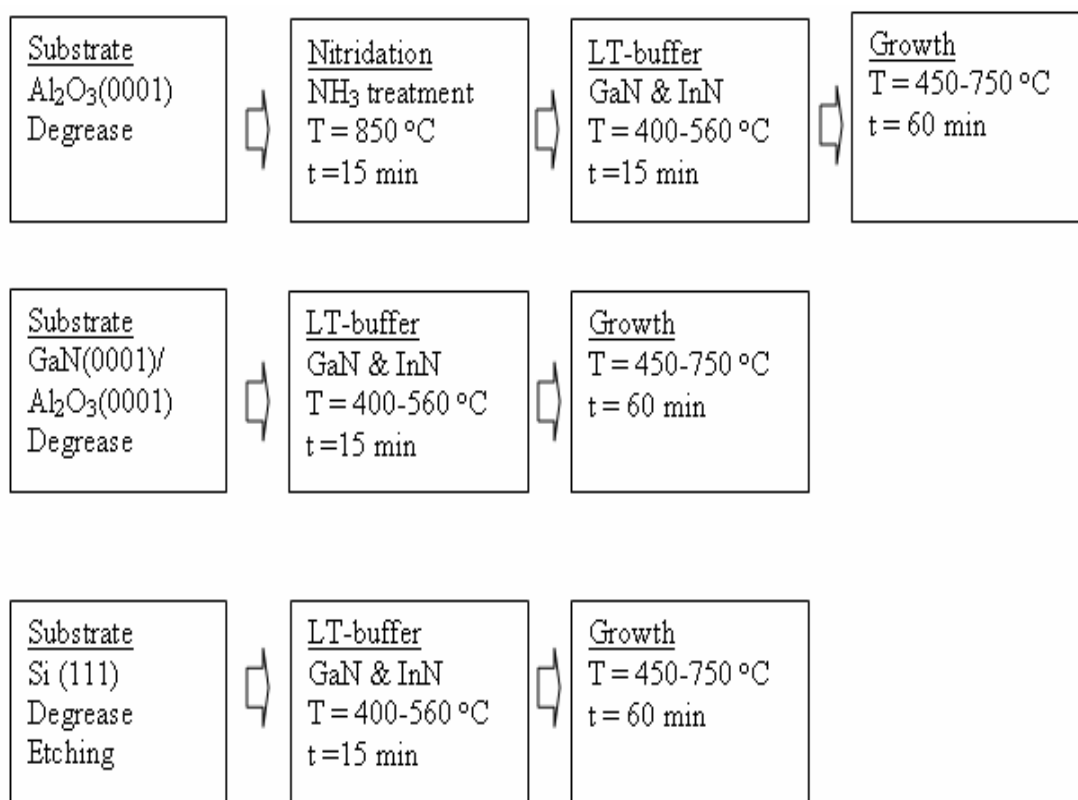


Figure 5-4. Indium Nitride (InN) growth sequence for each of the three substrates.

### 5.1.5. Indium Nitride (InN) Growth and Optimization

#### 5.1.5.1. Influence of Growth Temperature

Among all the factors, the growth temperature has the largest impact on the epitaxial film quality in terms of the growth habit (single crystalline or polycrystalline) and the structural quality. The growth habit was determined by XRD  $\theta$ - $2\theta$  scan (XRD Philips APD 3720) and the structural quality was judged by evaluating the FWHM of X-ray Rocking Curve (XRC) (Philips MRD X'Pert System).

**Substrate Studies** For  $\text{Al}_2\text{O}_3$  (0001), a low temperature GaN buffer layer (LT-GaN) grown at  $T_{\text{LT-GaN}} = 560$  °C, was employed after the nitridation at 850 °C for 15 min. The TMI flow rate was fixed at 0.26 sccm,  $\text{NH}_3$  at 800 sccm, and the N/In ratio was 3000. In this growth condition, indium droplets (metal) formed on the surface in addition to InN (0002) as shown in the XRD spectrum in Fig. 5.5.

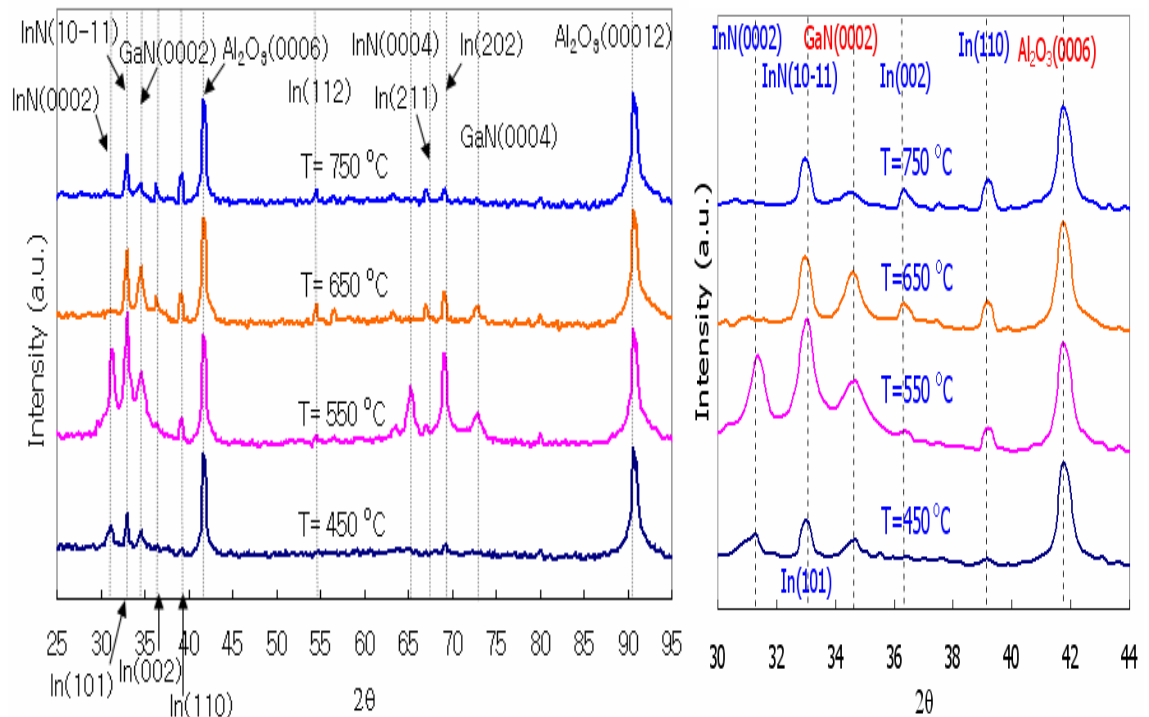


Figure 5-5. X-ray Diffraction (XRD)  $\theta$ - $2\theta$  scans for InN/LT-GaN on (a)  $\text{Al}_2\text{O}_3$  (0001) at N/In = 3000, T = 450, 550, 650, and 750 °C.

With the reference to the peak position of indium droplets that solidified upon cooling, peaks are anticipated at  $36.3^\circ$  corresponding to In (002),  $39.2^\circ$  In (110),  $54.5^\circ$  In (112),  $67.0^\circ$  In (103), and  $69.1^\circ$  In (202). As shown in Figure 5-5, it is clear that In formed.

Indium droplet formation was found to occur when the N/In ratio was low, as will be confirmed by the results of subsequent the study in which the N/In ratio was varied. Wet etching was used to remove the indium with a 15 % HCl solution.

It is noted that the InN (10-11) peak at  $33.1^\circ$  is close to the In (101) reflection at  $32.9^\circ$ , thus the two peaks are likely to overlap. After the indium droplets were removed by etching with HCl, the underlying InN film was characterized again by taking a XRD  $\theta$ - $2\theta$  scan.

For  $\text{Al}_2\text{O}_3$  (0001), single crystal InN (0002) film was obtained and the peak intensity of InN (0002) was the greatest at  $T = 550^\circ\text{C}$ . However, InN (10-11) occurred at  $T = 650^\circ\text{C}$ , which indicates that the growth direction of InN depends on the growth temperature.

A very broad and low intensity peak for InN was observed when growth was at  $T = 450^\circ\text{C}$ , indicative of poor quality InN. No growth of InN was observed at  $T = 750^\circ\text{C}$  (Fig. 5.6). It is generally accepted that InN can not be grown at a growth temperature above  $700^\circ\text{C}$  due to the InN thermal decomposition, nor below a growth temperature of  $400^\circ\text{C}$  due to the low decomposition efficiency of  $\text{NH}_3$ . From these results, it was found that the optimum growth condition is  $550^\circ\text{C}$ .

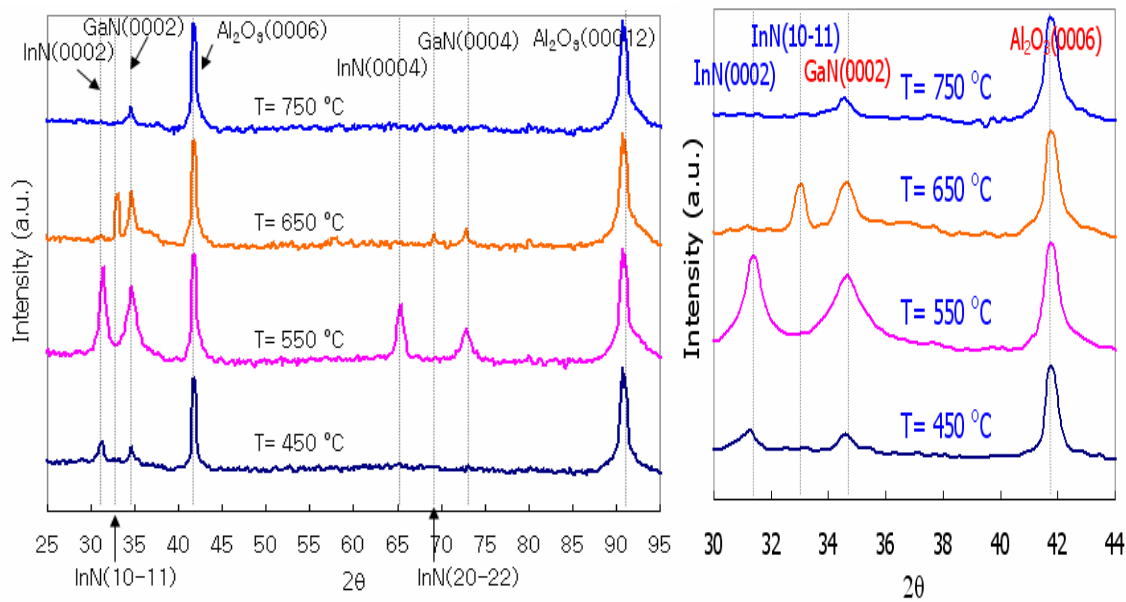


Figure 5-6. X-ray Diffraction (XRD)  $\theta$ - $2\theta$  scan for InN/LT-GaN on (a)  $\text{Al}_2\text{O}_3$  (0001) at  $\text{N}/\text{In} = 3000$ ,  $T = 450, 550, 650,$  and  $750$  °C. Pure In was removed by etching with HCl.

**Growth Temperature** The growth temperature effect was studied over a more limited set of temperatures: 530, 550, and 570 °C to fine tune the optimized growth temperature. A relatively small flow rate of TMI in the range 13 to 44 sccm, and high flow rate of  $\text{NH}_3$  (1600 sccm), gave a high N/In ratio of 50,000 to prevent the indium droplet formation during the growth. As expected, single crystalline InN was grown without indium droplet formation at this growth condition.

For  $\text{Al}_2\text{O}_3$  (0001), the intensity of the peak of the InN (0002) reflection was lower at growth temperatures 530 and 570 °C while the InN (10-11) reflection was evident at  $T = 570$  °C. Therefore, it appears that the optimum growth temperature of InN film is in the vicinity of 550 °C on  $\text{Al}_2\text{O}_3$  (0001) with a LT-GaN buffer layer.

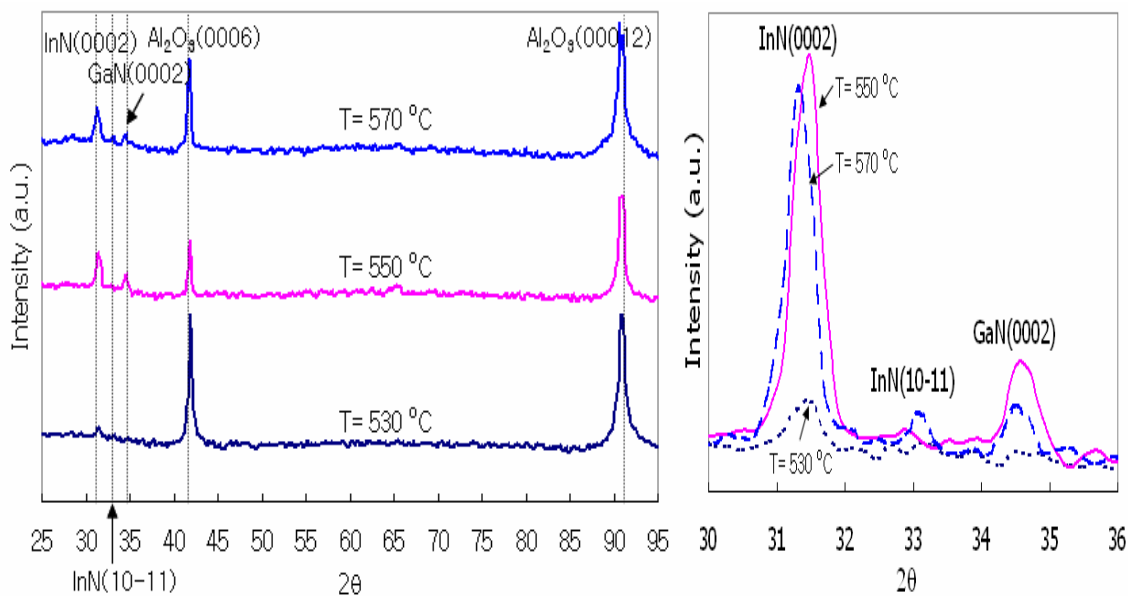


Figure 5-7. X-ray Diffraction (XRD)  $\theta$ - $2\theta$  scan for InN/LT-GaN on  $\text{Al}_2\text{O}_3$  (0001) at  $\text{N}/\text{In} = 50,000$ ,  $T = 530, 550$ , and  $570$  °C.

The growth temperature of LT-InN buffer layer was also examined in the range 500 to 550 °C. The result is an optimum growth temperature for the InN/LT-InN of 530 °C. Polycrystalline InN with the appearance of both InN (10-11) and InN (0002) reflections occurred at 500 and 550 °C, while a single reflection, InN (0002), was the strongest at 530 °C (see Fig. 5.8).

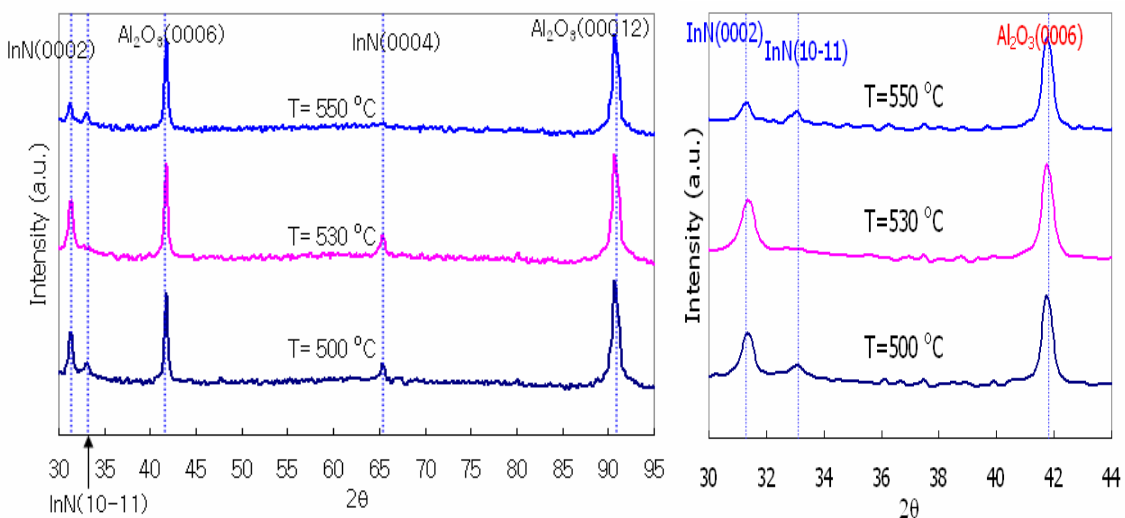


Figure 5-8. X-ray Diffraction (XRD)  $\theta$ - $2\theta$  scan for InN/LT-InN on  $\text{Al}_2\text{O}_3$  (0001) at  $\text{N}/\text{In} = 50,000$  and  $T = 500, 530$ , and  $550$  °C.

The FWHM of the XRC (X-ray rocking curve) for InN on Al<sub>2</sub>O<sub>3</sub> (0001) at N/In = 50,000 and T = 530 °C was 4860 arcsec (see Fig. 5.9).

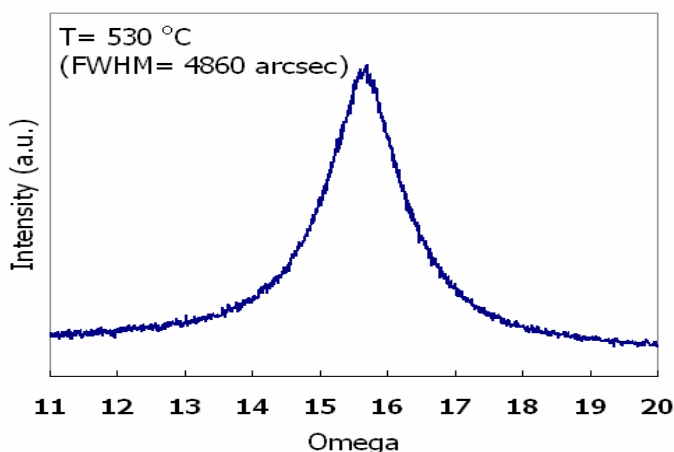


Figure 5-9. Full Width Half Maximum (FWHM) of XRC for InN/LT-InN on Al<sub>2</sub>O<sub>3</sub> (0001) at N/In = 50,000 and T = 500, 530, and 550 °C.

A similar set of runs (T = 500, 530, and 550 °C, and N/In = 50,000 with LT-InN buffer layer) was conducted using GaN/ Al<sub>2</sub>O<sub>3</sub> (0001) substrates. Again polycrystalline InN was observed at the 500 and 550 °C growth temperatures, while single crystalline InN (0002) appeared at 530 °C (see Fig. 5.10).

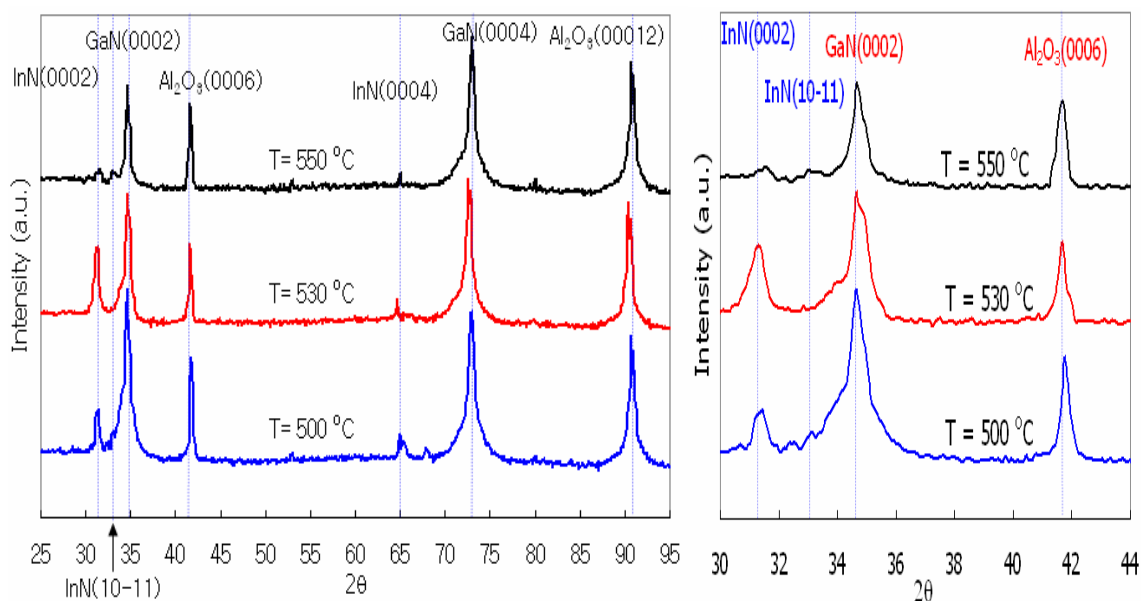


Figure 5-10. X-ray Diffraction (XRD)  $\theta$ - $2\theta$  scan for InN/LT-InN on GaN/Al<sub>2</sub>O<sub>3</sub> (0001) at N/In = 50,000, T = 500, 530, and 550 °C.

The FWHM of the XRCs for the InN film grown at  $T = 530$  and  $550$  °C are shown in Fig. 5.11, with the best crystallinity obtained at  $T = 530$  °C with a FWHM of the XRC of 1039 arcsec. Therefore, the optimum growth temperature of InN/LT-InN is near 530 °C.

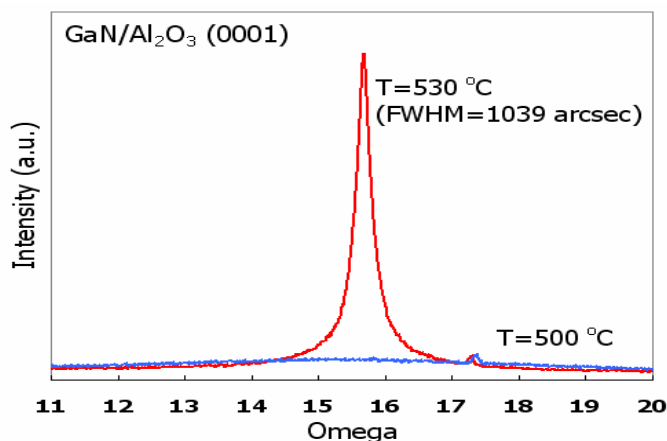


Figure 5-11. Full Width Half Maximum (FWHM) of XRC for InN/LT-InN on GaN/Al<sub>2</sub>O<sub>3</sub> (0001) at N/In = 50,000,  $T = 500, 530,$  and  $550$  °C.

Finally for the third substrate examined, Si (111), InN was grown at  $T = 500, 530, 550,$  and  $570$  °C, and  $N/In = 50,000$  with two buffer layers: LT-GaN and LT-InN. A weak InN (0002) reflection appeared in the films grown at all growth temperatures (see Fig. 5.12 and 5.13). With the LT-GaN buffer layer, the strongest peak of single crystalline InN (0002) occurred at  $T = 530$  °C, while polycrystalline InN (InN (10-11) and InN (0002) reflections) occurred at  $T = 550$  °C (see Fig. 5. 12). For a LT-InN buffer layer on Si, a strong single peak of was recorded, InN (0002), also at  $T = 530$  °C (Fig. 5. 13). The peak intensity of InN grown on Si substrate was smaller compared to those grown on either Al<sub>2</sub>O<sub>3</sub> or GaN/Al<sub>2</sub>O<sub>3</sub>. This is believed to be due to difficulty in wetting InN on Si. From these results, the optimum growth temperature is thought to be 530 °C on Si (111) with both LT-GaN and LT-InN.

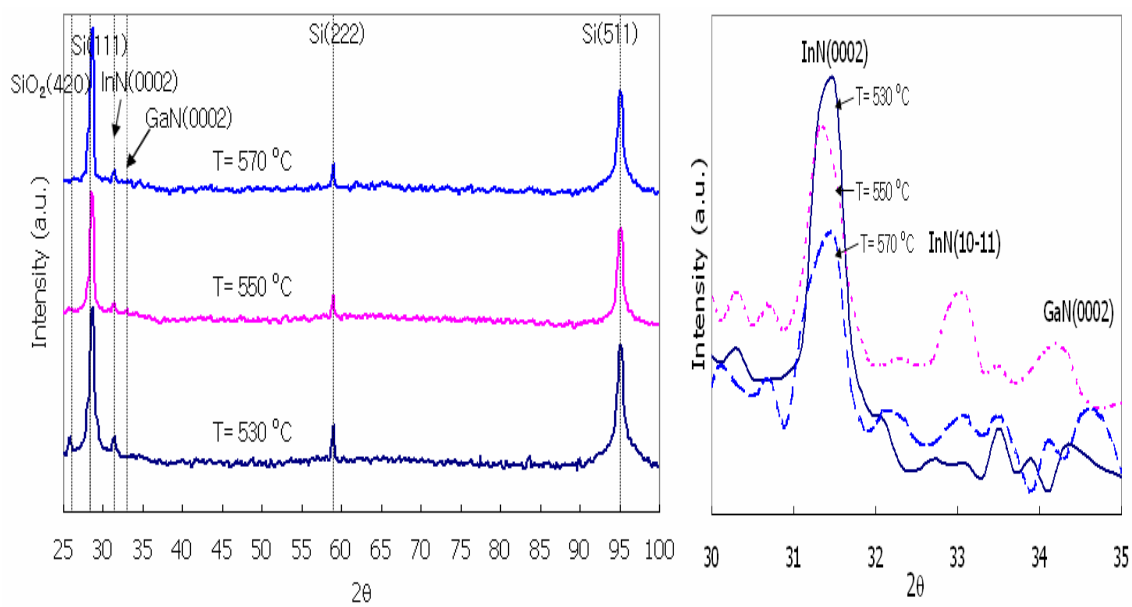


Figure 5-12. X-ray Diffraction (XRD)  $\theta$ - $2\theta$  scan for InN/LT-GaN on Si (111), at N/In = 50,000, T = 500, 530, 550, and 570 °C.

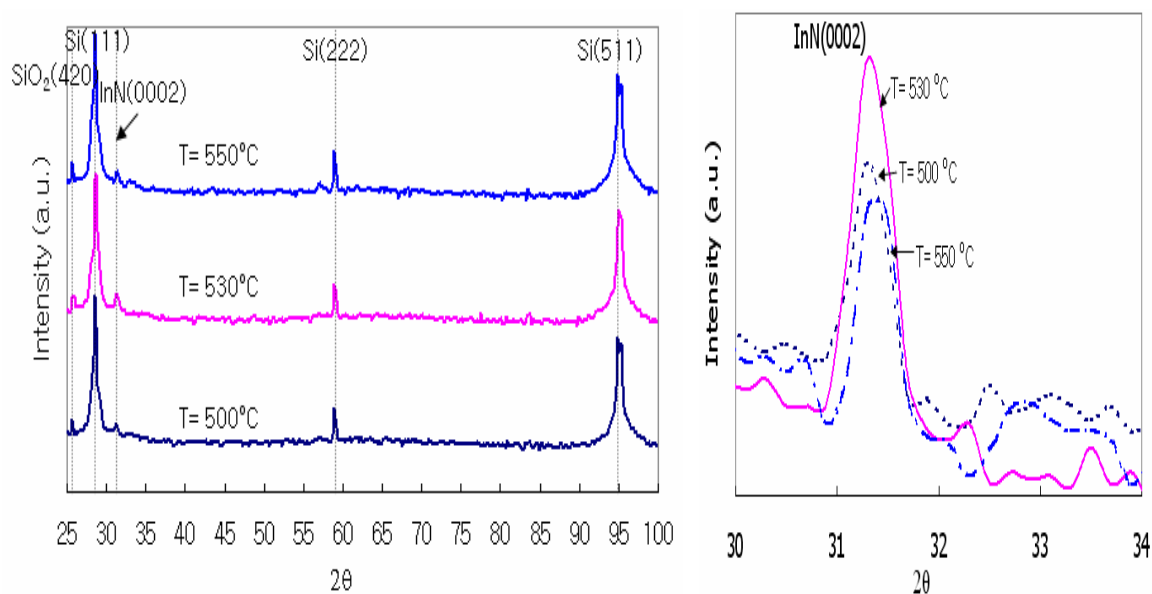


Figure 5-13. X-ray Diffraction (XRD)  $\theta$ - $2\theta$  scan for InN/LT-InN on Si (111), at N/In = 50,000, T = 500, 530, 550, and 570 °C.

***Growth Rate Studies*** The growth rate was determined as a function of the N/In ratio on  $\text{Al}_2\text{O}_3$  (0001). In these studies InN was grown for 1 hr at selected growth temperatures in the range 450 to 650 °C (N/In = 3000) and 500 to 550 °C (N/In = 50,000) to determine if the growth is chemical reaction-limited or transport-limited. The thickness was measured

on cross-sections by SEM (FEG-SEM JEOL JSM 6335F) and the results are displayed in Figures 5.14 and 5.15. As shown in Fig. 5.14, the temperature dependence changed depending on the kind of substrate, presumably because of different texture of the InN. Figure 5- 14 (a) and (b) show that the growth rate remained unchanged in the range 550 to 650 °C at N/In = 3000 and in the range 530 to 570 °C at N/In = 50,000 for Al<sub>2</sub>O<sub>3</sub> (0001), which is expected for a mass transfer limited growth condition. For N/In = 3000 run, the low growth rate (T = 450 °C) was a result of the lower efficiency of NH<sub>3</sub> decomposition at the relatively low temperature (Fig. 5.14 (a)). For the N/In = 50,000 condition on Al<sub>2</sub>O<sub>3</sub> (0001) the growth rate remains unchanged in the range 530 to 570 °C (Fig. 5.14 (b)), and thus mass transport-limited. The same results is seen for GaN/Al<sub>2</sub>O<sub>3</sub> (0001) and Si (111) (Fig. 5. 14 (c) and (d)). Furthermore the growth rate is independent of the substrate for the last 3 conditions. When the growth rate was compared between the N/In ratios of 3000 and 50,000, the rate at N/In = 3000 is higher than that at N/In = 50,000 because of the increased flow rate of TMI, the limiting reagent, from 0.03 to 0.26 sccm.

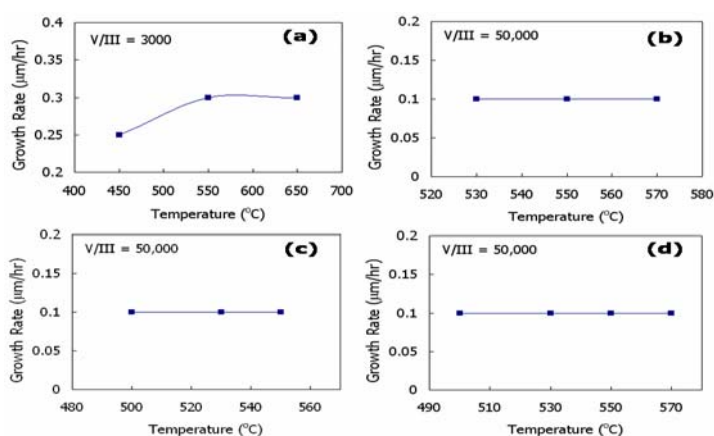


Figure 5-14. Growth rate of InN on various substrates (a) InN/LT-GaN on Al<sub>2</sub>O<sub>3</sub> (0001) at N/In = 3000, (b) for InN/LT-GaN on Al<sub>2</sub>O<sub>3</sub> (0001) at N/In = 50,000, (c) InN/LT-InN on GaN/Al<sub>2</sub>O<sub>3</sub> (0001) at N/In = 50,000, and (d) InN/LT-InN on Si (111) at N/In = 50,000

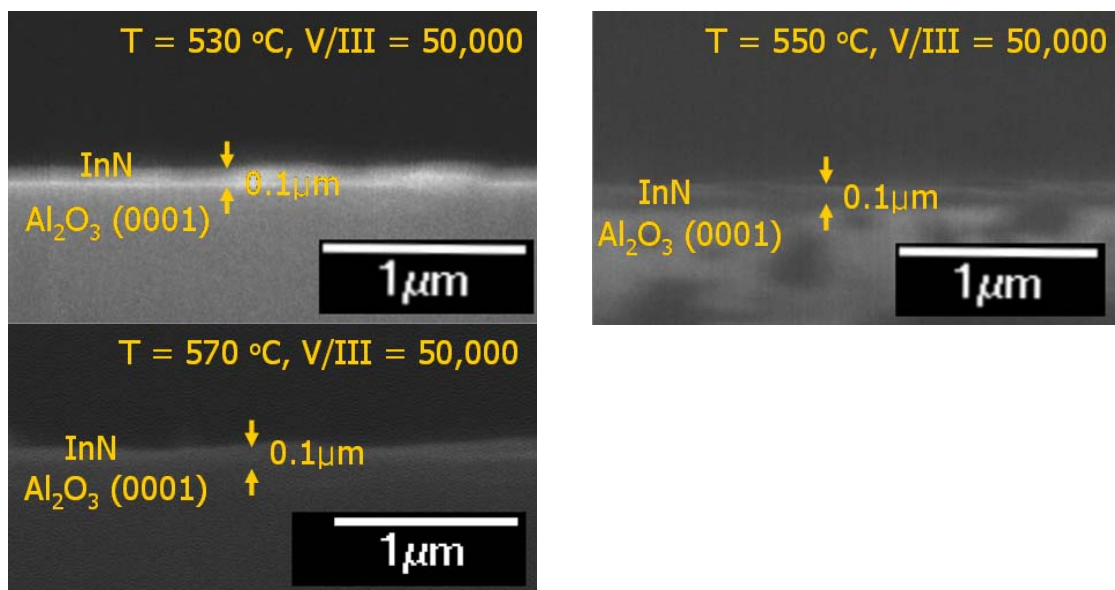


Figure 5-15. Cross-sectional SEM micrographs of InN for 60 min growth at 530, 550, and 570 °C, and N/In = 50,000 with LT-GaN buffer.

Table 5-3. Optimum growth temperature of InN on LT-GaN and LT-InN buffer layers on various substrates.

Buffer layer	Al <sub>2</sub> O <sub>3</sub> (0001)	GaN/ Al <sub>2</sub> O <sub>3</sub> (0001)	Si (111)
LT-GaN	T = 550 °C	-	T = 530 °C
LT-InN	T = 530 °C	T = 530 °C	T = 530 °C

In summary, the optimum growth temperature of InN was near 550 °C for LT-GaN and 530 °C for the LT-InN buffer layer on Al<sub>2</sub>O<sub>3</sub> (0001), and 530 °C for both GaN/Al<sub>2</sub>O<sub>3</sub> (0001) and Si (111). The growth of InN was not chemical reaction-limited but mass transport-limited. The results for the optimized growth temperature are summarized in Table 5-3.

#### 5.1.5.2. Influence of Substrate Nitridation

The nitridation of Al<sub>2</sub>O<sub>3</sub> is an important step to enhance the quality of InN film. For Al<sub>2</sub>O<sub>3</sub> (0001), it has been reported that the nitridation treatment results in the formation of an AlN or amorphous AlO<sub>x</sub>N<sub>1-x</sub> layer on the Al<sub>2</sub>O<sub>3</sub> substrate, which was

confirmed by several scientists with XPS and EDS [Bry92a, Yam94b, Uch96, Pan99, Tsu99]. The results presented below are based on growth of InN on sapphire prepared with the  $\text{AlO}_x\text{N}_{1-x}$  layer by the procedure previously described.

The first run compared the InN quality with and without using nitridation of the sapphire on an InN/LT-InN ( $T_{\text{LT-InN}} = 450\text{ }^\circ\text{C}$ )/ $\text{Al}_2\text{O}_3$  (0001) substrate with the conditions  $\text{N/In} = 50,000$  and  $T_{\text{LT-InN}} = 450\text{ }^\circ\text{C}$ . The result of a XRD  $\theta$ - $2\theta$  scan showed that the InN (0002) is single crystal using nitridation ( $T = 850\text{ }^\circ\text{C}$  in  $\text{NH}_3$  for 15 min), while without the nitridation, both InN (0002) and InN (10-11) were evident (Fig. 5.16). For InN/LT-InN GaN/ $\text{Al}_2\text{O}_3$  (0001) at  $\text{N/In} = 50,000$ ,  $T = 530\text{ }^\circ\text{C}$ , and  $T_{\text{LT-InN}} = 450, 500\text{ }^\circ\text{C}$

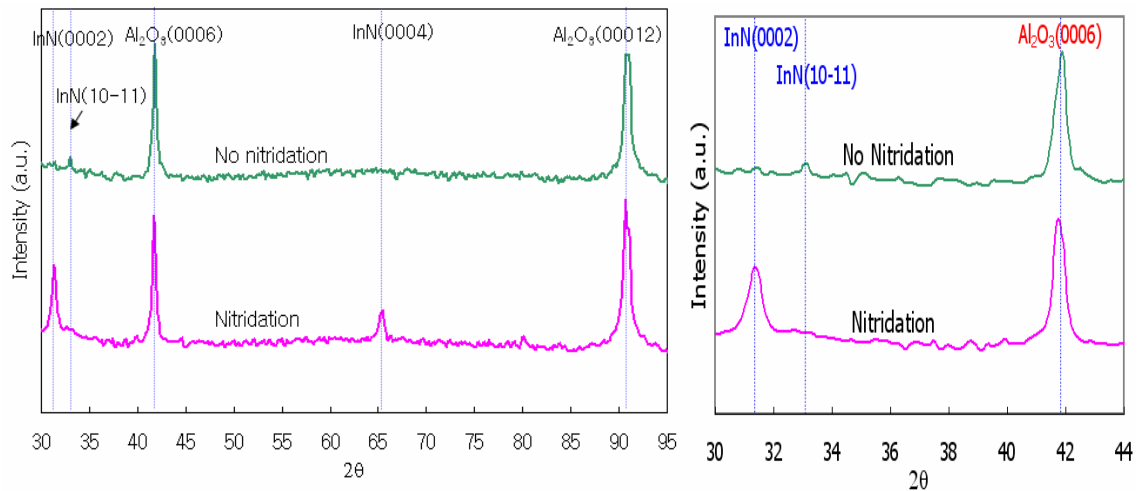


Figure 5-16. X-ray Diffraction (XRD)  $\theta$ - $2\theta$  scan for InN/LT-InN ( $T_{\text{LT-InN}} = 450\text{ }^\circ\text{C}$ ) on  $\text{Al}_2\text{O}_3$  (0001) at  $\text{N/In} = 50,000$ , and  $T_{\text{LT-InN}} = 450\text{ }^\circ\text{C}$  without and with nitridation.

The presence of the nitrated  $\text{Al}_2\text{O}_3$  layer is believed to promote wetting of the successive InN over layer and therefore to improve the film quality. The nitridation of the  $\text{Al}_2\text{O}_3$  surface significantly improves the crystalline quality of InN as a result of the formation of AlN or  $\text{AlO}_x\text{N}_{1-x}$  layer through the reaction of nitrogen at the  $\text{Al}_2\text{O}_3$  surface as discussed above. The marked improvement of InN film quality by the formation of this layer reduces the mismatch between the sapphire and III nitride layer. For example, AlN

has the same lattice structure as InN, and the lattice mismatch is reduced from 25.7 % for InN/Al<sub>2</sub>O<sub>3</sub> to 13.7 % for InN/AlN.

Another set of runs were made using LT-InN GaN/Al<sub>2</sub>O<sub>3</sub> (0001) with and without nitridation of the GaN buffer (nitridation performed at 850 °C for 15 min in NH<sub>3</sub>). The growth of InN was performed at T = 530 °C, while two buffer layer temperatures were compared; T<sub>LT-InN</sub> = 450 and 500 °C at N/In = 50,000. The subsequent XRD patterns shown in Fig. 5.17 reveal that nitridation again had an impact on the crystallinity. In contrast to previous results, the nitridation of sapphire produced polycrystalline InN with the InN (10-11) peak increasing in intensity and the peak of InN (0002) broader.

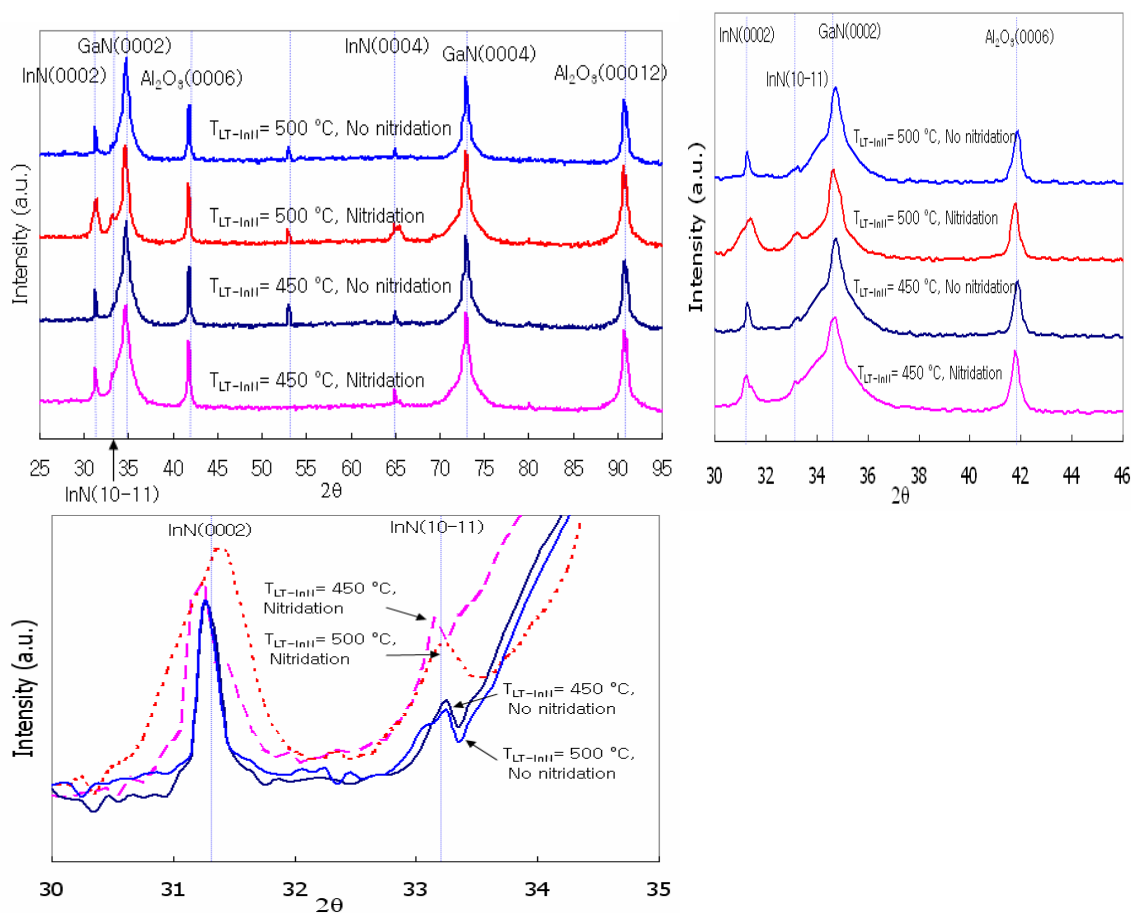


Figure 5-17. X-ray Diffraction (XRD)  $\theta$ - $2\theta$  scan for InN/LT-InN GaN/Al<sub>2</sub>O<sub>3</sub> (0001) at N/In = 50,000, T = 530 °C, and T<sub>LT-InN</sub> = 450, 500 °C with and without nitridation.

A final set of runs was performed with Si (111) with and without nitridation at  $T = 850$  °C for 15 min in  $\text{NH}_3$  ambient. For this study, the growth of InN was performed  $530$  °C using a  $T_{\text{LT-InN}} = 450$  or  $500$  °C, and  $\text{N/In} = 50,000$ . Although good results were noted, for completeness this experiment was performed. The film with the nitridation treatment showed an InN (0002) peak while the one without nitridation did not show this peak (see Fig. 5.18). It is known that the nitridation of Si gives amorphous  $\text{SiN}_x$  formation, which was reported to severely degrade the film quality [Yan02c]. However, the result of this study indicates that the nitridation process improved the structural properties of InN.

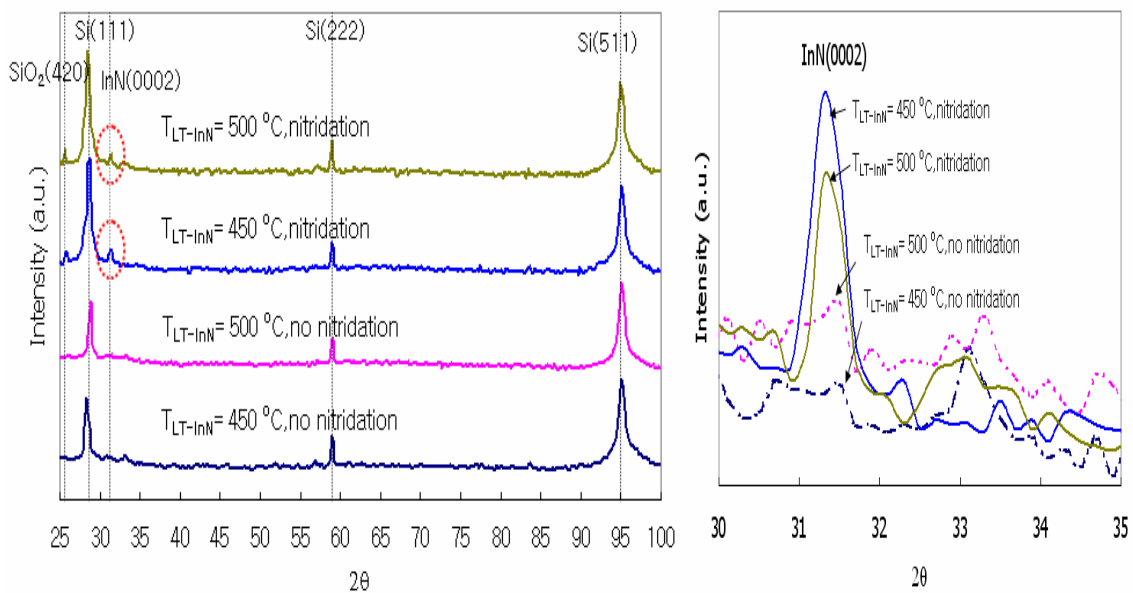


Figure 5-18. X-ray Diffraction (XRD)  $\theta$ - $2\theta$  scan for (a) InN/LT-InN on Si (111), at  $\text{N/In} = 50,000$ ,  $T = 530$  °C, and  $T_{\text{LT-InN}} = 450, 500$  °C with the nitridation and without the nitridation.

During the nitridation treatment in this system, the  $\text{SiO}_x\text{N}$  formation on Si substrate was thought to exist on the surface of Si substrate as shown by the analysis using ESCA by a previous student in the group [Mas01].  $\text{SiO}_x\text{N}$  formation on Si (111), instead of  $\text{SiN}_x$  formation, is believed to lead to the growth of the single crystalline InN (Fig. 5.19)

[Mas01]. To understand the initial stages of InN growth on Si,  $\text{NH}_3$  treatment on bare silicon was studied. Figures 5.19 shows ESCA spectra of the Si  $2p_3$  peak for bare silicon treated with and without  $\text{NH}_3$  at  $T = 850^\circ\text{C}$ . The bulk Si-Si bonds have a binding energy at 100.1 eV. This peak shows a doublet splitting of the 2p subshell into  $2p_{3/2}$  and  $2p_{1/2}$  bands with an intensity ratio of 1:2. Emission of an electron with up or down spin from a p-type orbital creates a photoelectron with two possible energy levels. These two emission levels separated by 0.6 eV create an asymmetry in the overall Si peak. Strained Si-Si bonds near the Si/SiO<sub>x</sub> interface are distorted from their typical tetragonal bonding configuration. This compressive distortion results in a silicon bonding peak shifted to 102.2 eV. A strong peak observed at 104.1 eV was assigned to the Si-O bond. For samples treated in ammonia, a strong peak from the Si-N bond was observed at 103.3 eV. By integrating the area of each peak, an estimation of the bonding configuration of the surface atoms is possible. Table 5-4 showed that nitrogen incorporates into the SiO<sub>x</sub> film for samples annealed in  $\text{NH}_3$  [Mas01].

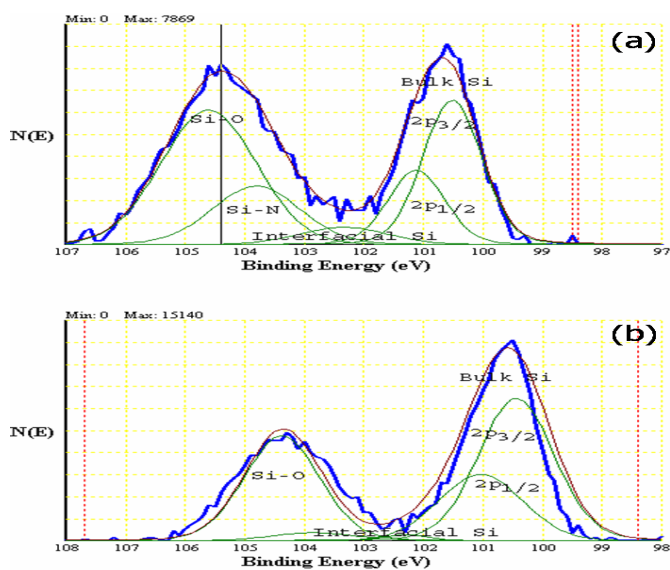


Figure 5-19. Electron Spectroscopy of Chemical Analysis (ESCA) spectra of Si  $2p_3$  peak for Si annealed at  $850^\circ\text{C}$  in 1.0 slm  $\text{N}_2$  (a) with 100%  $\text{NH}_3$  at 1.0 slm (b) without  $\text{NH}_3$ .

Table 5-4. Comparison by ESCA of Si anneals.

Temperature	NH <sub>3</sub>	%Bulk Si Bonds	%Si-O Bonds	%Si-N Bonds
High (850 °C)	Yes	40.2	38.8	16.2
High (850 °C)	No	64.6	31.5	Negligible

In summary, it was confirmed that the nitridation of Al<sub>2</sub>O<sub>3</sub> (0001) can improve the structural quality of single crystalline InN film through the formation of an AlN layer, the nitridation of GaN/Al<sub>2</sub>O<sub>3</sub> (0001) is not favorable for the growth of InN, and during the nitridation of Si (111), the SiO<sub>x</sub>N formation on Si (111), instead of SiN<sub>x</sub> formation, is led to the improved structural quality of InN.

### 5.1.5.3. Influence of N/In Ratio

The N/In ratio is a key factor for InN growth especially to prevent indium droplet formation and is also an important factor to influence the structural quality of InN. For the study of N/In effect on the indium droplet formation, the flow rate of TMI was varied from 0.03 to 0.08 sccm and the flow rate of NH<sub>3</sub> was fixed at 1600 sccm to optimize the ratio of N/In, which leads to the growth of single crystalline InN without indium droplet formation. From the results of XRD  $\theta$ -2 $\theta$  (Fig. 5.20) scans and SEM images of the surface, the optimum ratio of N/In was found to be 50,000 for InN/LT-GaN on Al<sub>2</sub>O<sub>3</sub> (0001).

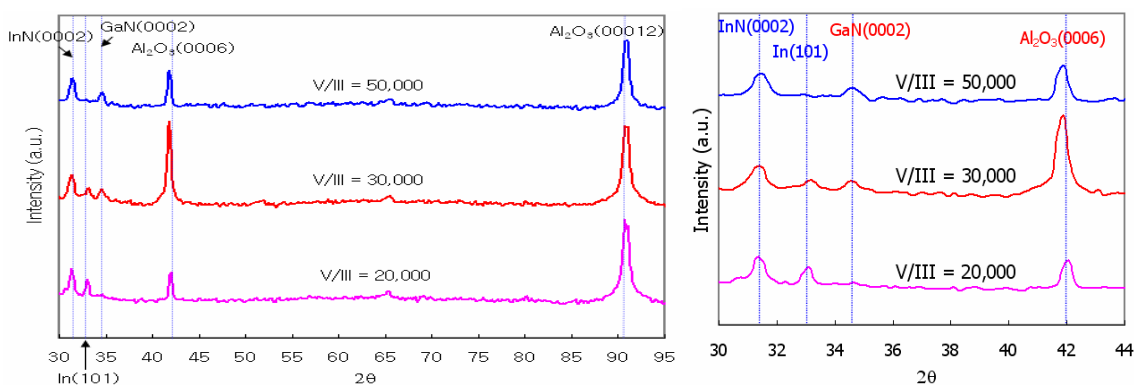


Figure 5-20. X-ray Diffraction (XRD)  $\theta$ -2 $\theta$  scan at N/In=20,000, 30,000, and 50,000, T = 550 °C for InN/LT-GaN on Al<sub>2</sub>O<sub>3</sub> (0001) at N/In of 50,000.

Single crystalline InN (0002) was obtained at N/In = 50,000 and the indium droplet were observed at N/In = 20,000 and 30,000. The FWHM of XRC of InN was 14868 arcsec at N/In = 50,000 with LT-GaN buffer layer (Fig. 5. 21).

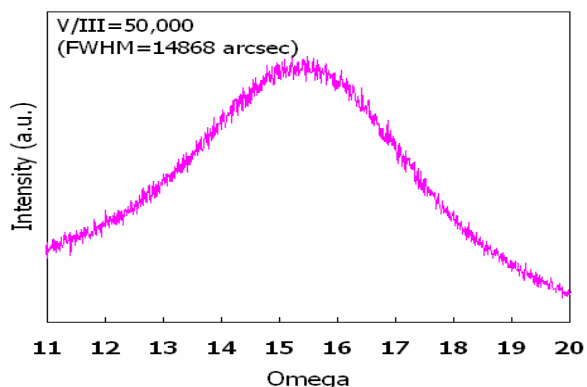


Figure 5-21. Full Width Half Maximum (FWHM) of XRC for InN/LT-GaN on Al<sub>2</sub>O<sub>3</sub> (0001) at N/In of 50,000.

For GaN/ Al<sub>2</sub>O<sub>3</sub> (0001), InN was grown at T = 530 °C, T<sub>LT-InN</sub> = 400 °C, and N/In = 30,000 and 50,000. At N/In = 30,000, indium droplet formation was observed but at N/In = 50,000 the single crystalline InN (0002) was grown without the indium droplet formation. From these results, the optimum N/In ratio is for high values, e.g. 50,000 (Fig. 5.22).

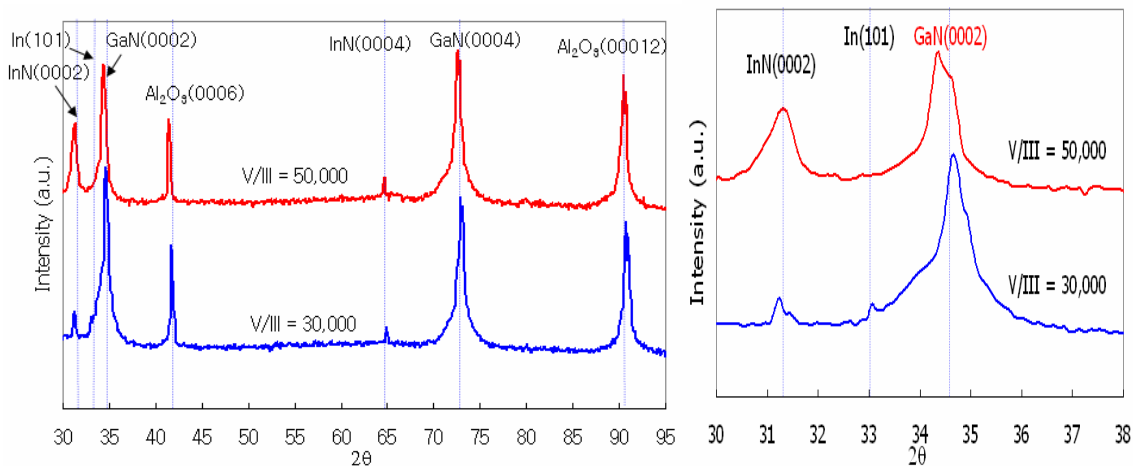


Figure 5-22. X-ray Diffraction (XRD)  $\theta$ - $2\theta$  scan for InN/LT-InN on GaN/Al<sub>2</sub>O<sub>3</sub> (0001) at, T = 530 °C, T<sub>LT-InN</sub> = 400 °C, and N/In = 30,000 and 50,000.

For Si (111), InN was grown at N/In ratios of 20,000, 30,000, and 50,000, and  $T = 530\text{ }^{\circ}\text{C}$  with a LT-GaN buffer layer. Indium droplet formation occurred at N/In = 20,000 and 30,000, while the growth of single crystalline InN (0002) was achieved at N/In = 50,000, consistent with the results on other substrates (Fig. 5.23).

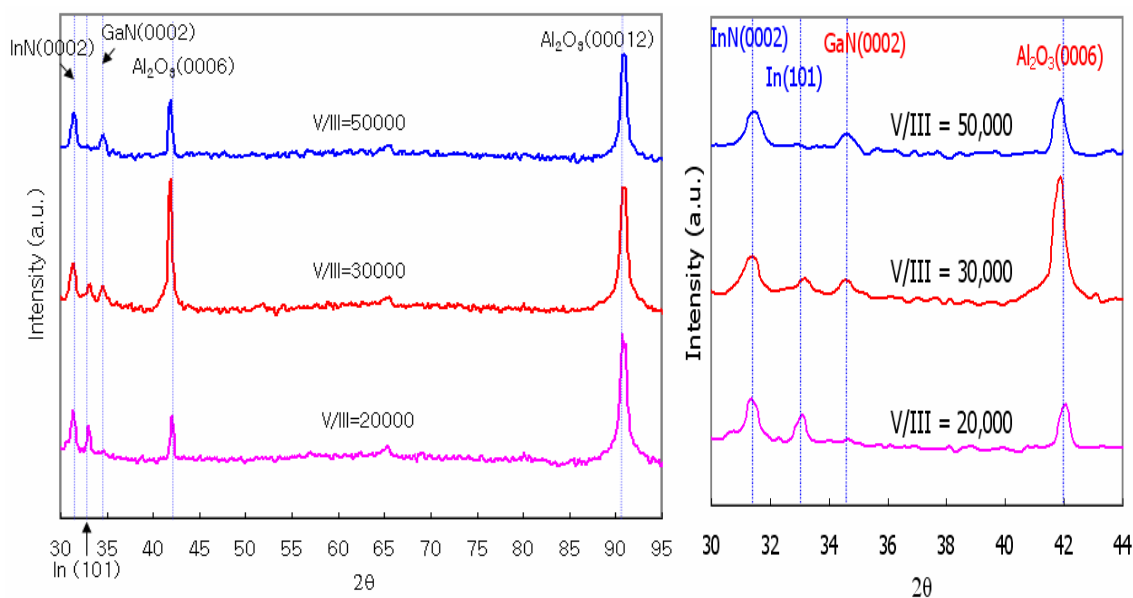


Figure 5-23. X-ray Diffraction (XRD)  $\theta$ - $2\theta$  scan for InN/LT-GaN on Si (111) at N/In = 20,000, 30,000 and 50,000,  $T = 530\text{ }^{\circ}\text{C}$ .

The growth rate vs. N/In ratio was studied and the results are presented in Fig. 5.20. The N/In ratio was increased from 3000 to 15,000 by increasing the flow rate of  $\text{NH}_3$  in the growth of InN/LT-GaN on  $\text{Al}_2\text{O}_3$  (0001). After wet etching to remove the indium droplets, cross-section SEM images showed that the growth rate decreased with increasing amount of  $\text{NH}_3$  (i.e., increase flow rate of  $\text{NH}_3$ ). The growth rate vs. N/In ratio was same for each of the three substrates  $\text{Al}_2\text{O}_3$  (0001), GaN/ $\text{Al}_2\text{O}_3$  (0001), and Si (111) (see Fig. 5.24). The growth rate of InN was  $0.27\text{ }\mu\text{m/hr}$  at N/In = 6000,  $0.21\text{ }\mu\text{m/hr}$  at N/In = 9000,  $0.17\text{ }\mu\text{m/hr}$  at N/In = 12,000, and  $0.13\text{ }\mu\text{m/hr}$  at N/In = 15,000 (Fig. 5.24). This phenomenon can be also explained by thermodynamic reasoning. When the N/In ratio increases, the amount of  $\text{H}_2$  also increases due to the decomposition of  $\text{NH}_3$ . The

increase of  $H_2$  drives the reaction to the left, namely the etching process (Eq. (3-5)). In terms of the growth rate vs. N/In ratio, the results obtained for  $Al_2O_3$  substrate, were the same as the results for GaN/ $Al_2O_3$  and Si substrate because the growth rate is independent of the kind of substrate but is dependent on the mass flow rate of the source materials.

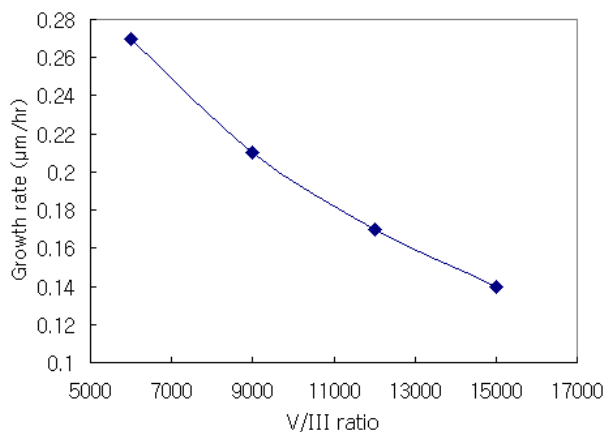


Figure 5-24. Growth rate vs. N/In ratio for InN/LT-GaN on  $Al_2O_3$  (0001), GaN/ $Al_2O_3$  (0001), and Si (111) at N/In = 6000, 9000, 12,000, and 15,000 with  $T = 550$  °C, TMI = 0.26 sccm and  $NH_3 = 1600-4000$  sccm.

In summary, the growth rate decreases with increasing N/In ratio. However, indium droplet formation can be prevented during the growth of InN by growing at high N/In ratio. Therefore, the relatively large ratio of N/In is required to avoid the indium droplets formation, although accompanied by a decrease of growth rate. It is also found that the growth rate is independent of the kind of substrate.

#### 5.1.5.4. Influence of Buffer Layer and Morphological Study

The growth temperature of the buffer layer is also a significant factor because the buffer layer usually fails to act as a nucleation layer and stress-relieving (compliant) layer in some temperature regions. Buffer layer can be used to improve the crystallinity of an InN film by first providing the nucleation site and thus leading to lateral growth and

second reducing the lattice mismatch between the substrate and epitaxial film as a compliant layer. Therefore, it is also essential to find the optimized temperature for the InN buffer layer. A LT-InN buffer layer was used for this study because the optimized growth temperature of LT-GaN was already found to be 560 °C by a previous student in our group [San04]. Without buffer layers, the growth of single crystalline InN (0002) was difficult for Al<sub>2</sub>O<sub>3</sub> (0001), and GaN/Al<sub>2</sub>O<sub>3</sub> (0001), and Si (111). Therefore, the optimization of buffer layer growth temperature is required.

For Al<sub>2</sub>O<sub>3</sub> (0001), polycrystalline InN with peaks of InN (10-11) and/or InN (11-20) appeared at  $T_{\text{LT-InN}} = 400$  and  $T_{\text{LT-InN}} = 500$  °C (Fig. 5.25). The InN buffer layer is thought to fail to relieve the stress in the overgrown InN film because the InN with (10-11) surface structure found is different from the (0001) found on the Al<sub>2</sub>O<sub>3</sub>. The optimized growth temperature of InN buffer layer was found to be 450 °C because the single crystalline InN (0002) was achieved at  $T_{\text{LT-InN}} = 450$  °C, thus pointing to the temperature sensitivity of the buffer layer growth temperature.

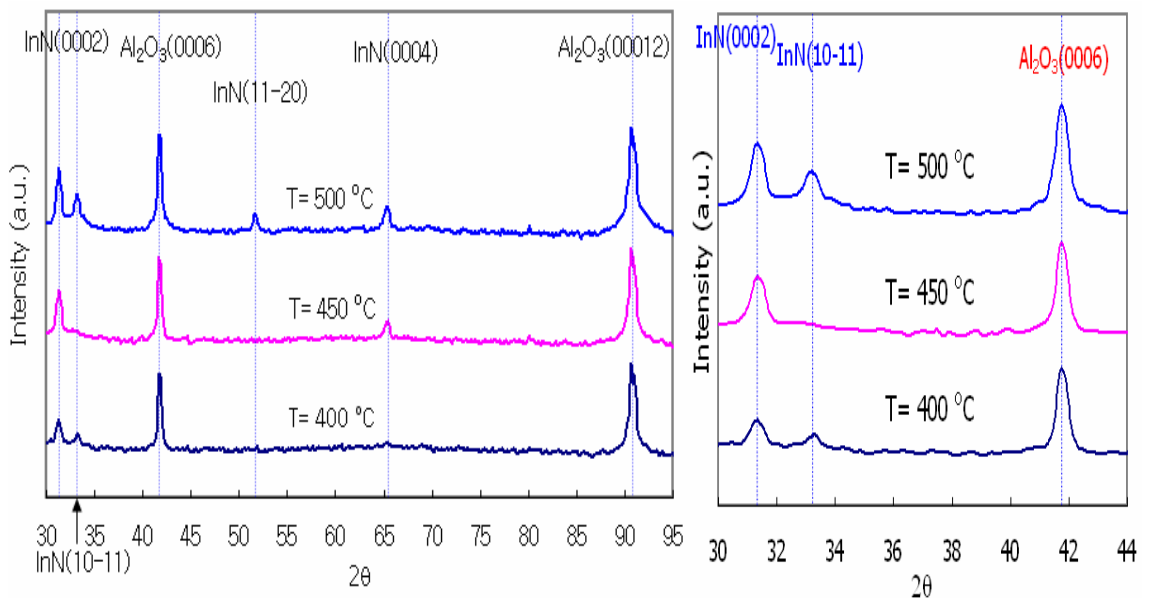


Figure 5-25. X-ray Diffraction (XRD)  $\theta$ - $2\theta$  scan for InN/LT-InN on Al<sub>2</sub>O<sub>3</sub> (0001) at N/In = 50,000,  $T = 530$  °C, and  $T_{\text{LT-InN}} = 400, 450,$  and  $500$  °C.

For GaN/Al<sub>2</sub>O<sub>3</sub> (0001) starting substrates, the growth of InN was performed at T = 530 °C and N/In = 50,000, with several buffer layer growth temperatures: T<sub>LT-InN</sub> = 350, 400, 450, and 500 °C. Single crystalline InN (0002) was obtained at T<sub>LT-InN</sub> = 350 and 400 °C while polycrystalline InN with the presence of InN (10-11) and InN (0002) was found for T<sub>LT-InN</sub> = 450 and 500 °C (Fig. 5.26). When the crystalline quality of InN grown at T<sub>LT-InN</sub> = 350 and 400 °C were compared, the InN grown at T<sub>LT-InN</sub> = 400 °C showed smaller FWHM of XRC (1039 arcsec) than that (6386 arcsec) of InN grown at T<sub>LT-InN</sub> = 350 °C (Fig. 5.27).

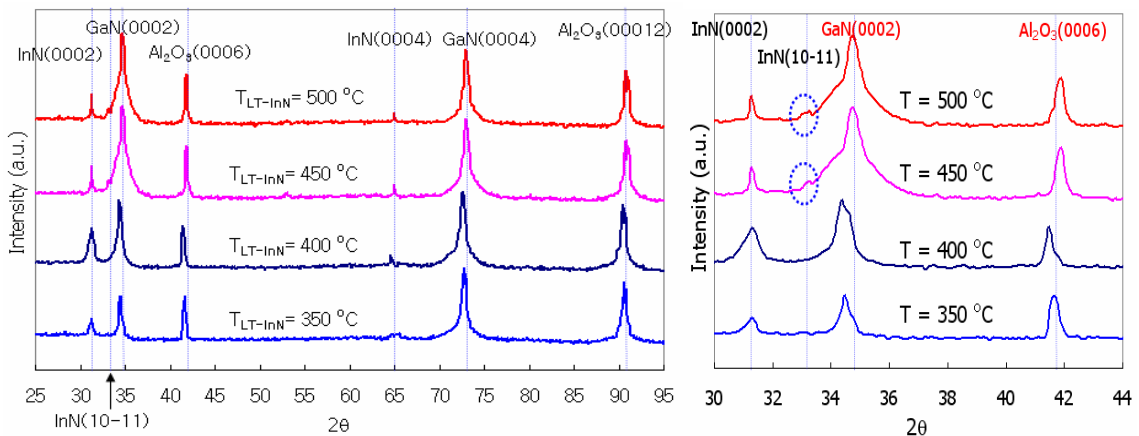


Figure 5-26. X-ray Diffraction (XRD)  $\theta$ - $2\theta$  scan for InN/LT-InN on GaN/Al<sub>2</sub>O<sub>3</sub> (0001) at T = 530 °C, T<sub>LT-InN</sub> = 350, 400, 450, and 500 °C, and N/In = 50,000.

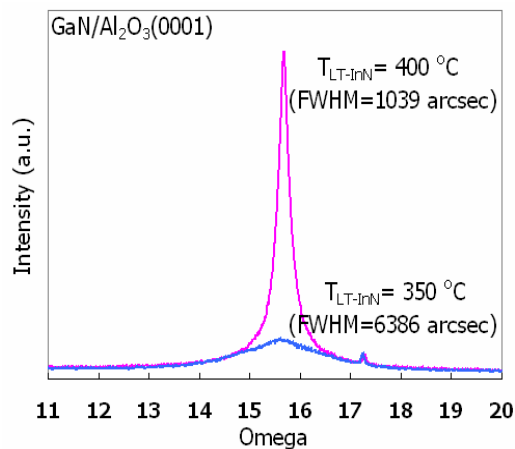


Figure 5-27. Full Width Half Maximum (FWHM) of XRC for InN/LT-InN on GaN/Al<sub>2</sub>O<sub>3</sub> (0001) at T = 530 °C, T<sub>LT-InN</sub> = 350, 400, 450, and 500 °C, and N/In = 50,000.

Finally for Si (111) starting substrates, the growth of InN was performed at  $N/In = 50,000$  and  $530\text{ }^{\circ}\text{C}$ , and three buffer layer temperatures:  $T_{LT-InN} = 400, 450,$  and  $500\text{ }^{\circ}\text{C}$ . Single crystalline InN (0002) was obtained at  $T_{LT-InN} = 400, 450,$  and  $500\text{ }^{\circ}\text{C}$ , but the intensity of InN (0002) was the strongest at  $T_{LT-InN} = 450\text{ }^{\circ}\text{C}$  (Fig. 5.28). The scan in Figure 5- 29 shows that the peak intensity of InN (0002) does not increase when the growth time for LT-InN buffer layer is longer than  $t = 15\text{ min}$ .

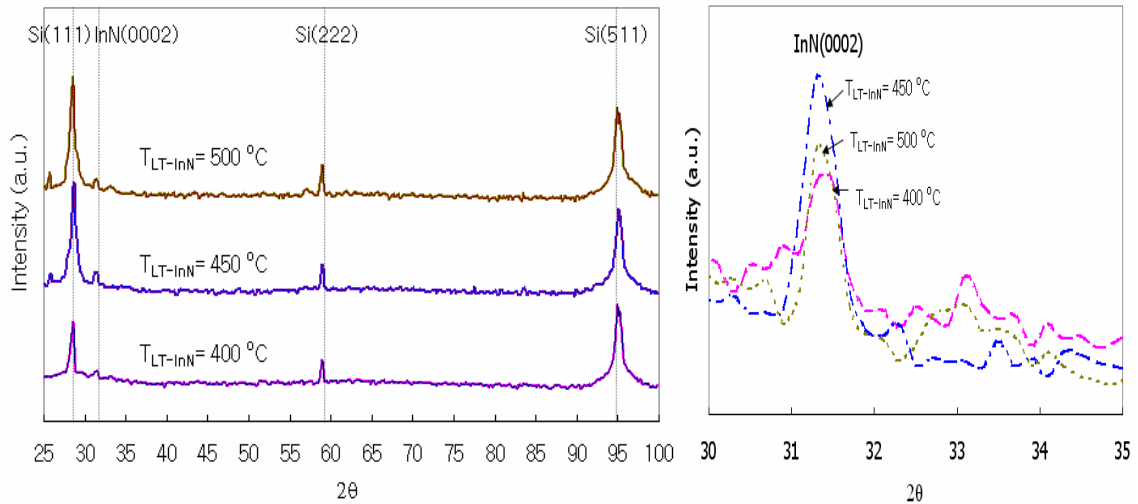


Figure 5-28. X-ray Diffraction (XRD)  $\theta$ - $2\theta$  scan for InN/LT-InN on Si (111) at  $N/In = 50,000$ ,  $T = 530\text{ }^{\circ}\text{C}$ , and  $T_{LT-InN} = 400, 450,$  and  $500\text{ }^{\circ}\text{C}$ .

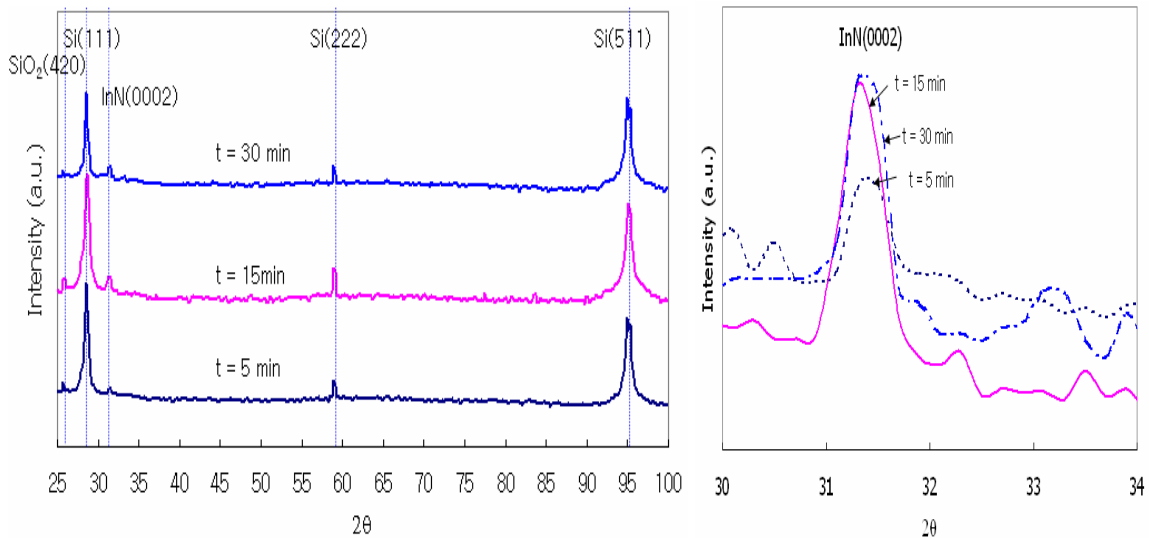


Figure 5-29. X-ray Diffraction (XRD)  $\theta$ - $2\theta$  scan for InN/LT-InN on Si (111) at  $N/In = 50,000$ ,  $T = 530\text{ }^{\circ}\text{C}$ ,  $T_{LT-InN} = 450\text{ }^{\circ}\text{C}$ , and  $t = 5, 15,$  and  $30\text{ min}$ .

In summary, the optimum growth temperature of LT-InN buffer layer was found to be 450 °C for Al<sub>2</sub>O<sub>3</sub> (0001), 400 °C for GaN/Al<sub>2</sub>O<sub>3</sub> (0001), and 450 °C for Si (111) to obtain single crystalline InN without indium droplet formation. These results were summarized in Table 5-5.

Table 5-5. Optimum growth temperature of LT-InN buffer layer depending on Al<sub>2</sub>O<sub>3</sub> (0001).

Buffer layer	Al <sub>2</sub> O <sub>3</sub> (0001)	GaN/Al <sub>2</sub> O <sub>3</sub> (0001)	Si (111)
LT-InN	T <sub>LT-InN</sub> = 450 °C	T <sub>LT-InN</sub> = 400 °C	T <sub>LT-InN</sub> = 450 °C

The choice of low temperature buffer layer is also an important factor that influences the crystallinity of InN. LT-GaN (560 °C) and LT-InN (450 °C) buffer layer were used to compare the effect of both buffer layers on the structural quality of InN grown on Al<sub>2</sub>O<sub>3</sub> (0001). The LT-InN buffer layer enhanced the crystallinity of InN film more significantly than LT-GaN buffer layer as shown in Fig. 5.30, where the peak intensity was much stronger when using the LT-InN rather than the LT-GaN. The FWHM (4860 arcsec) for LT-InN was much narrower than that (FWHM=14868 arcsec) of LT-GaN (Fig. 5.31).

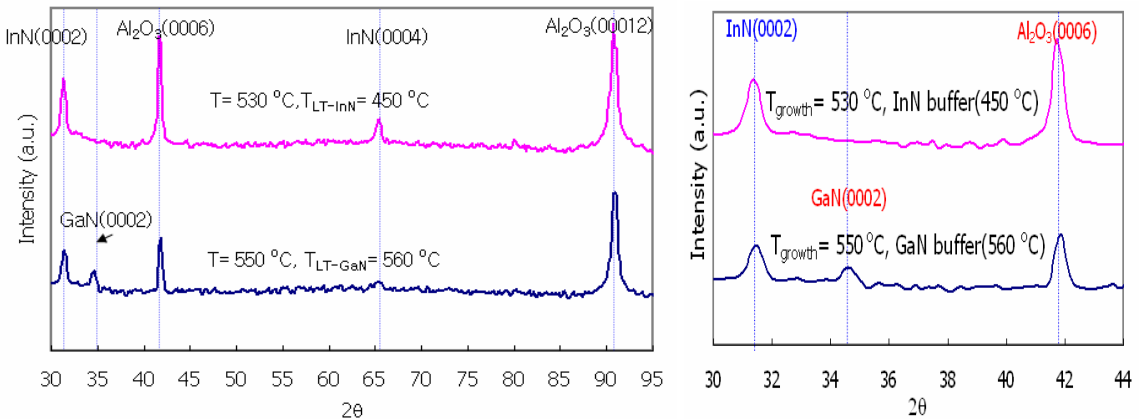


Figure 5-30. X-ray Diffraction (XRD)  $\theta$ - $2\theta$  scan for InN/LT-InN (TLT-InN = 450 °C) and LT-GaN (TLT-GaN = 560 °C) on Al<sub>2</sub>O<sub>3</sub> (0001) at N/In = 50,000, T = 530 °C (LT-InN buffer) and T = 550 °C (LT-GaN buffer).

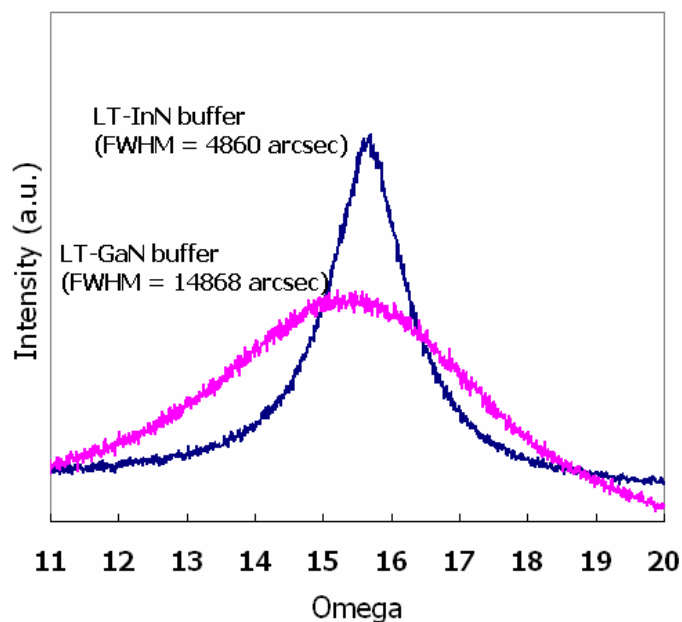


Figure 5-31. Full Width Half Maximum (FWHM) of XRC for InN/LT-InN ( $T_{\text{LT-InN}} = 450\text{ }^{\circ}\text{C}$ ) and LT-GaN ( $T_{\text{LT-GaN}} = 560\text{ }^{\circ}\text{C}$ ) on  $\text{Al}_2\text{O}_3$  (0001) at  $\text{N/In} = 50,000$ ,  $T = 530\text{ }^{\circ}\text{C}$  (LT-InN buffer) and  $T = 550\text{ }^{\circ}\text{C}$  (LT-GaN buffer).

**Surface Morphology** The surface morphology was also considered using Atomic Force Microscopy (AFM). In this study, InN was grown on  $\text{Al}_2\text{O}_3$  (0001) at  $T = 530\text{ }^{\circ}\text{C}$  using a LT-InN buffer layer ( $T_{\text{LT-InN}} = 450\text{ }^{\circ}\text{C}$ ) and at  $T = 550\text{ }^{\circ}\text{C}$  for LT-GaN buffer layer ( $T_{\text{LT-GaN}} = 560\text{ }^{\circ}\text{C}$ ), respectively, where the temperatures were selected according to Table 5-5.

When the roughness of InN films obtained using the LT-InN and LT-GaN buffer layers was compared, the RMS roughness of InN film (4.2 nm) with LT-InN buffer layer was smaller than that (18.1 nm) with LT-GaN buffer layer (Fig. 5.32).

The roughness of as-grown LT-InN buffer layer and LT-GaN buffer layer was compared to study the relation between the roughness of InN film and that of as-grown buffer layer. The RMS roughness of as-grown LT-InN buffer layer (1.9 nm) was smaller than that (10.2 nm) of as-grown LT-GaN (Fig. 5.32).

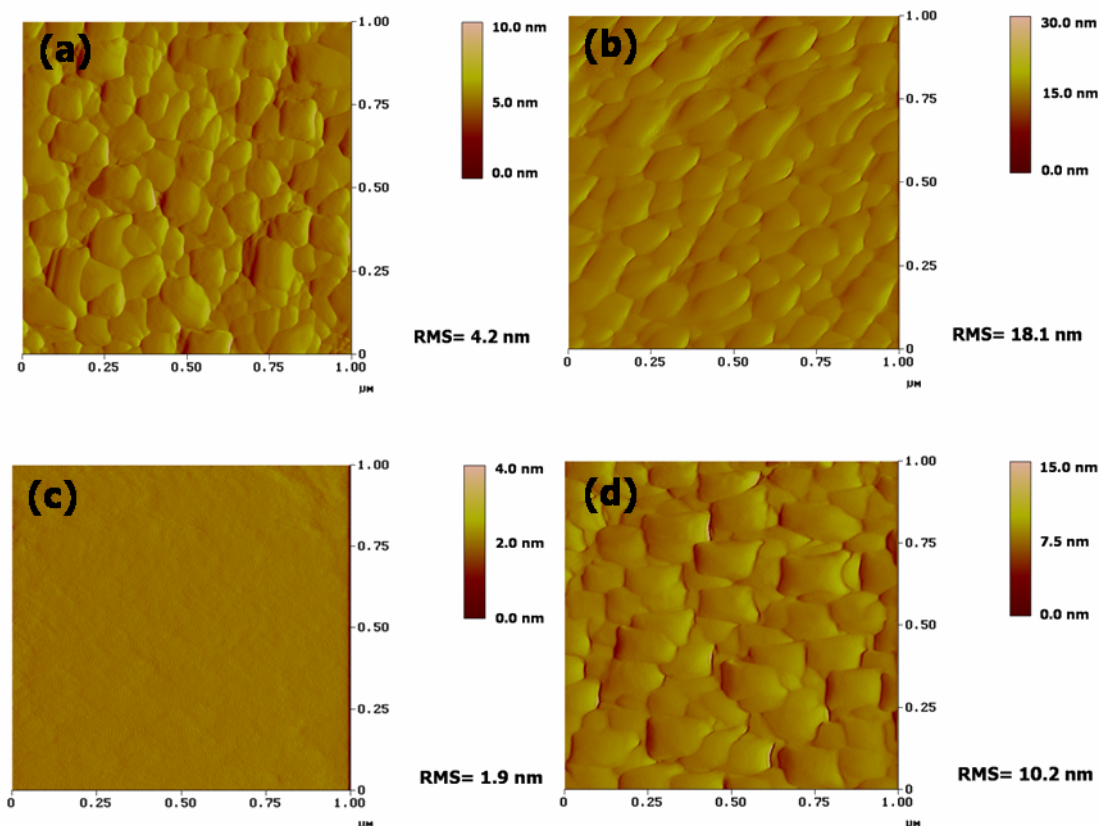


Figure 5-32. Root Mean Square (RMS) roughness by AFM for (a) InN/LT-InN ( $T = 530$  °C,  $T_{\text{LT-InN}} = 450$  °C), (b) InN/LT-GaN ( $T = 550$  °C,  $T_{\text{LT-GaN}} = 560$  °C), (c) as-grown LT-InN ( $450$  °C), and (d) as-grown LT-GaN ( $560$  °C) on  $\text{Al}_2\text{O}_3$  (0001) at  $\text{N/In}=50,000$ .

Material	RMS (nm)	Material	RMS (nm)
As-grown LT-InN	1.9	As-grown LT-GaN	10.2
InN/LT-InN	4.2	InN/LT-GaN	18.1

When the quality of the grown InN using either a LT-GaN or a LT-InN buffer layer on Si (111) was compared, the LT-InN buffer layer gave a higher intensity InN (0002) peak than that of LT-GaN (Fig. 5.33). This indicated that the LT-InN buffer layer is more favorable than LT-GaN buffer layer for the growth of InN.

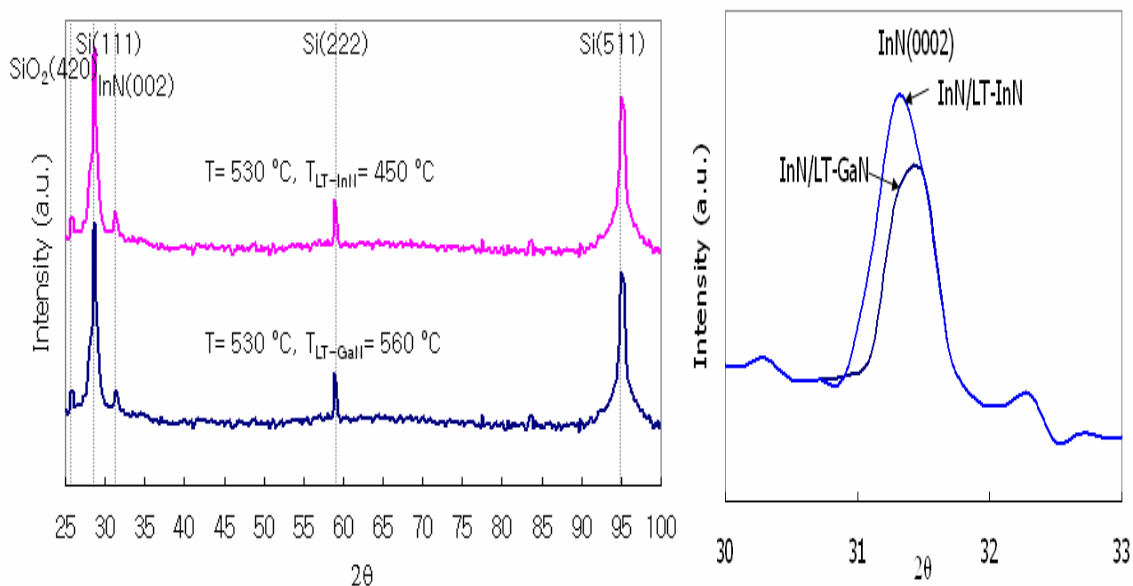


Figure 5-33. X-ray Diffraction (XRD)  $\theta$ - $2\theta$  scan for InN/LT-InN and InN/LT-GaN on Si (111) at N/In = 50,000,  $T = 530$  °C,  $T_{\text{LT-InN}} = 450$  °C, and  $T_{\text{LT-InN}} = 560$  °C.

In summary, it is concluded that the roughness of the as-grown buffer layer affects the roughness of the InN film and the LT-InN buffer layer gives better surface morphology of InN film than the LT-GaN buffer layer (Table 5-6). Therefore, the LT-InN buffer layer appears to be a more suitable substrate than LT-GaN to improve the crystalline quality and surface morphology of InN.

#### 5.1.5.5. Influence of Pressure

The growth pressure effect on the crystallinity of InN was studied. To understand the growth pressure effect on InN growth, two different pressures of 60 and 100 Torr were used during the growth of the LT-InN buffer layer. The growth pressure for the growth of InN film was 100 Torr after the growth of LT-InN buffer layer. The growth temperature was 530 °C and the InN buffer layer temperatures were 450 and 500 °C, at N/In ratio = 50,000 on GaN/Al<sub>2</sub>O<sub>3</sub> (0001). The application of  $P_{\text{LT-InN}} = 60$  Torr in the growth of LT-InN buffer layer at  $T_{\text{LT-InN}} = 450$  and 500 °C made the peak intensity of InN (10-11) stronger (Fig. 5.34).

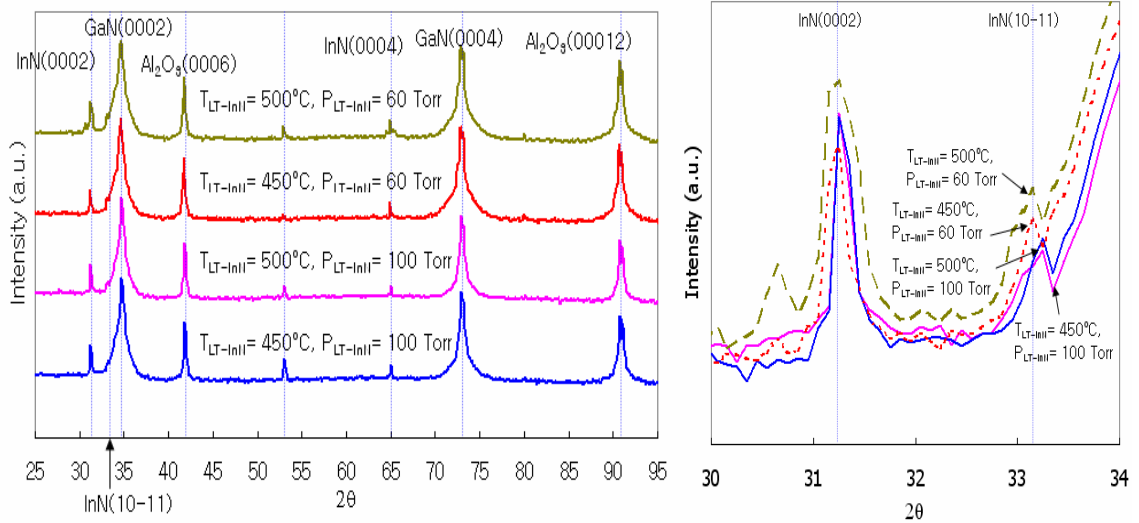


Figure 5-34. X-ray Diffraction (XRD)  $\theta$ - $2\theta$  scan for InN/LT-InN on GaN/ $\text{Al}_2\text{O}_3$  (0001) at N/In = 50,000,  $T_{\text{LT-InN}} = 450$  and  $500$  °C and  $T = 530$  °C with the different growth pressure of LT-InN.

For Si (111), the growth temperature was  $530$  °C, InN buffer layer temperatures were  $450$  and  $500$  °C, at N/In ratio = 50,000. The application of  $P_{\text{LT-InN}} = 60$  Torr in the growth of LT-InN buffer layer at  $T_{\text{LT-InN}} = 450$  and  $500$  °C made the peak intensity of InN (10-11) stronger (Fig. 5.35).

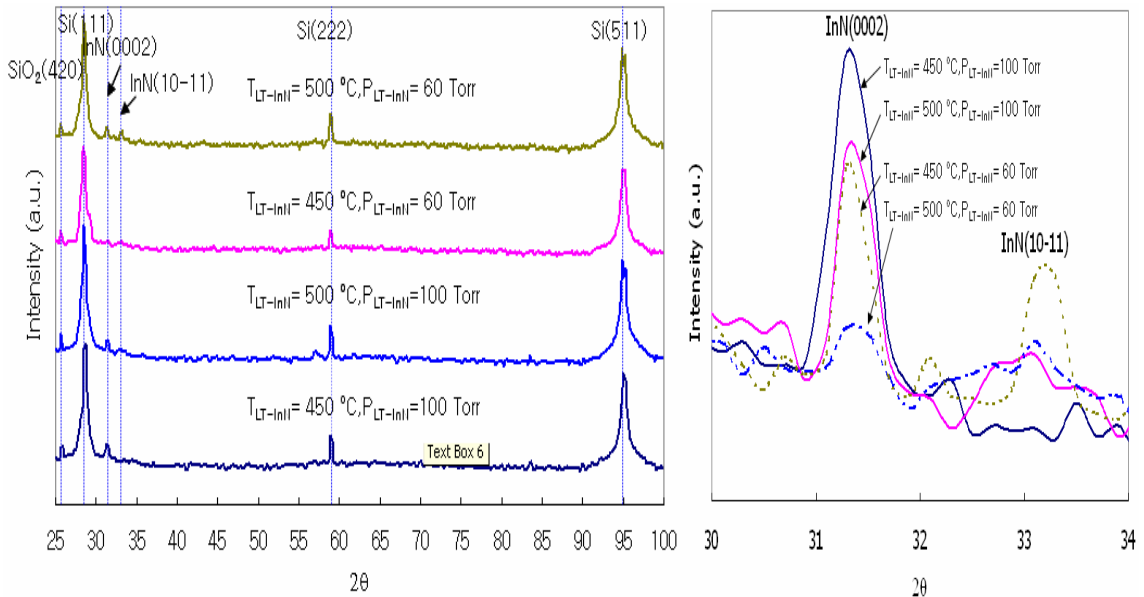


Figure 5-35. X-ray Diffraction (XRD)  $\theta$ - $2\theta$  scan for InN/LT-InN on Si (111) at N/In = 50,000,  $T_{\text{LT-InN}} = 450$  and  $500$  °C and  $T = 530$  °C with two different growth pressures for LT-InN.

From these results, it was found that the low pressure (60 Torr) was not preferable for the growth of single crystalline InN, compared to the relatively high pressure (100 Torr). High pressure at constant mass flow is usually thought to be favorable for the growth of InN since the high pressure can enhance the  $\text{NH}_3$  decomposition as a result of reduced flow velocity of the reactant gases and thus, can suppress nitrogen evaporation during the growth.

#### **5.1.5.6. Optical and Electrical Properties**

The band gap energy of InN has been known to be 1.89 eV for a long time [Tan86a]. However, the band gap energy of InN has been recently reported to be around 0.7 eV. Most recently the reported band gap energy of InN is in the range 0.7 to 1.0 eV [Dav02a, Dav02b, Dav02c, Wu02, Tat02, Hor02, Sai02, and Miy02].

The PL data of our InN films showed that the band gap energy is 0.84 eV for  $\text{Al}_2\text{O}_3$  (0001), 0.94 eV for  $\text{GaN}/\text{Al}_2\text{O}_3$  (0001), and 1.07 eV for Si (111), which are in good agreement with the recently reported data (Fig. 5.36).

The band gap energy of InN grown on  $\text{GaN}/\text{Al}_2\text{O}_3$  (0001) is 0.94 eV, which is higher than 0.84 eV for  $\text{InN}/\text{Al}_2\text{O}_3$  (0001). This is related to the interfacial layer that exists between InN film and GaN substrate.

The recently reported best electron density of InN is  $\sim 5.8 \times 10^{18} \text{ cm}^{-3}$  and best mobility is  $\sim 900 \text{ cm}^2/\text{Vs}$  [Yam04b]. The carrier concentrations and mobilities of the several InN films grown with different conditions are shown in Fig. 5.37 and the growth conditions are summarized in Table 5-7.

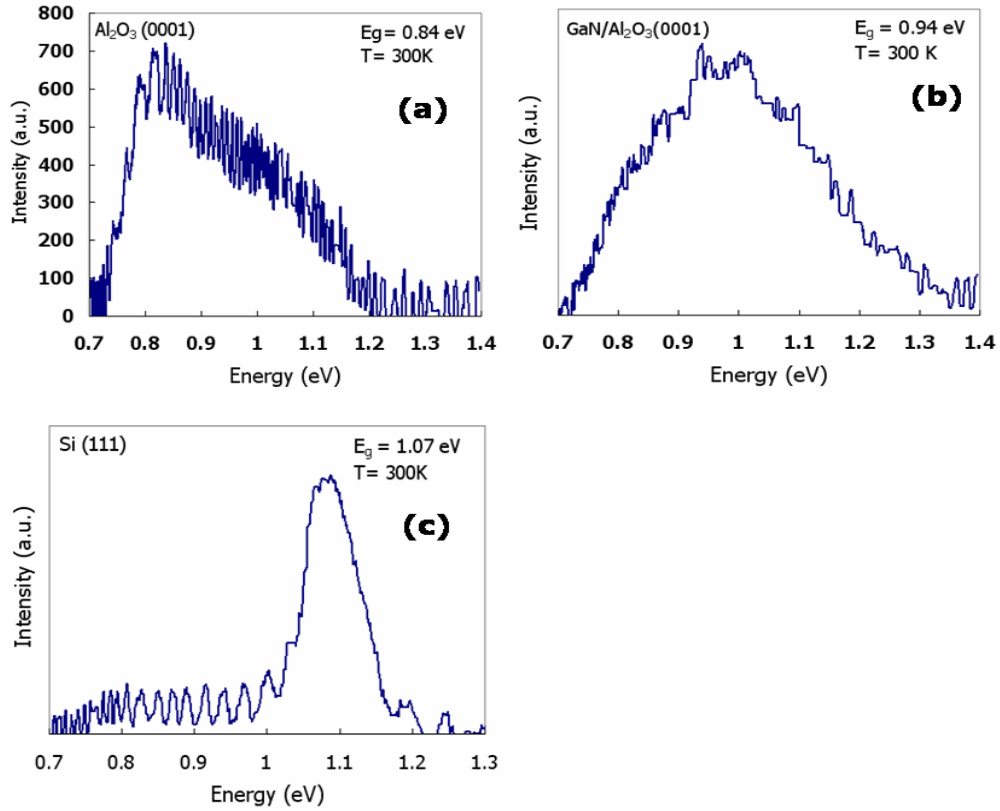


Figure 5-36. Photoluminescence for (a) InN grown on  $\text{Al}_2\text{O}_3$  (0001) at  $T = 530\text{ }^\circ\text{C}$ ,  $T_{\text{LT-InN}} = 500\text{ }^\circ\text{C}$ , (b) InN grown on  $\text{GaN}/\text{Al}_2\text{O}_3$  (0001) at  $T = 530\text{ }^\circ\text{C}$ ,  $T_{\text{LT-InN}} = 400\text{ }^\circ\text{C}$ , (c) InN grown on Si (111) substrate at  $T_{\text{LT-GaN}} = 560\text{ }^\circ\text{C}$ ,  $T = 550\text{ }^\circ\text{C}$  and  $\text{N}/\text{In} = 50,000$ .

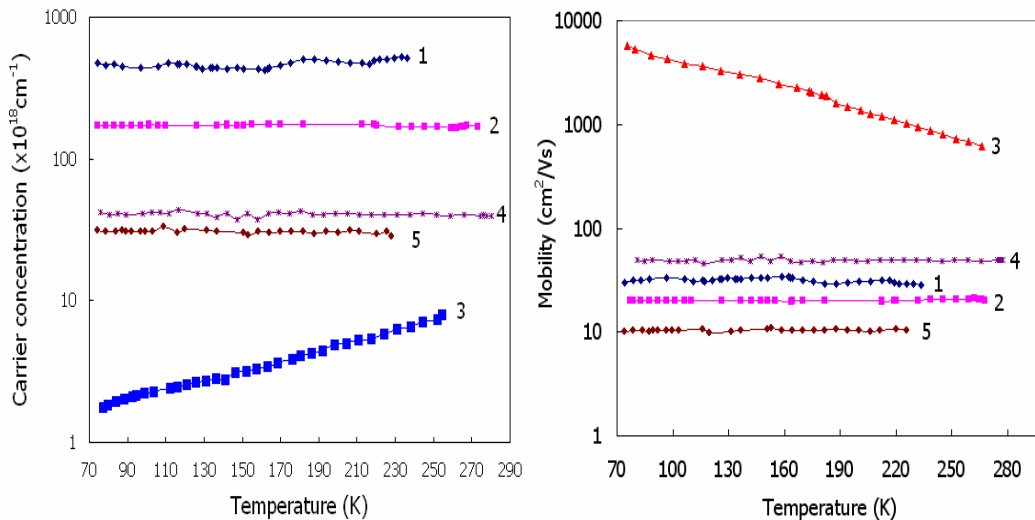


Figure 5-37. Carrier concentrations and mobilities of InN films grown with different growth conditions at different characterization temperature using Hall measurement.

Table 5-7. Growth conditions for InN.

Sample	Growth condition
1	Al <sub>2</sub> O <sub>3</sub> -LTGaN-InN, N/In = 50K
2	Al <sub>2</sub> O <sub>3</sub> -LTInN-InN, N/In = 50K
3	Si(111)-LTGaN-InN, N/In = 6K, after etching
4	GaN/Al <sub>2</sub> O <sub>3</sub> -LTInN-InN, N/In = 50K, vertical inlet tube
5	Al <sub>2</sub> O <sub>3</sub> -LTInN-InN, N/In = 50K, vertical inlet tube

The best electrical properties of our InN film were obtained from InN on Si (111) and the net electron carrier concentration is  $7.0 \times 10^{18} \text{ cm}^{-3}$  at  $T = 266 \text{ K}$  and  $4.5 \times 10^{17} \text{ cm}^{-3}$  at  $T = 41 \text{ K}$ , and the mobility is  $623 \text{ cm}^2/\text{Vs}$  at  $T = 266 \text{ K}$  and  $9288 \text{ cm}^2/\text{Vs}$  at  $T = 45 \text{ K}$  (Fig. 5.37 and Fig. 5.38).

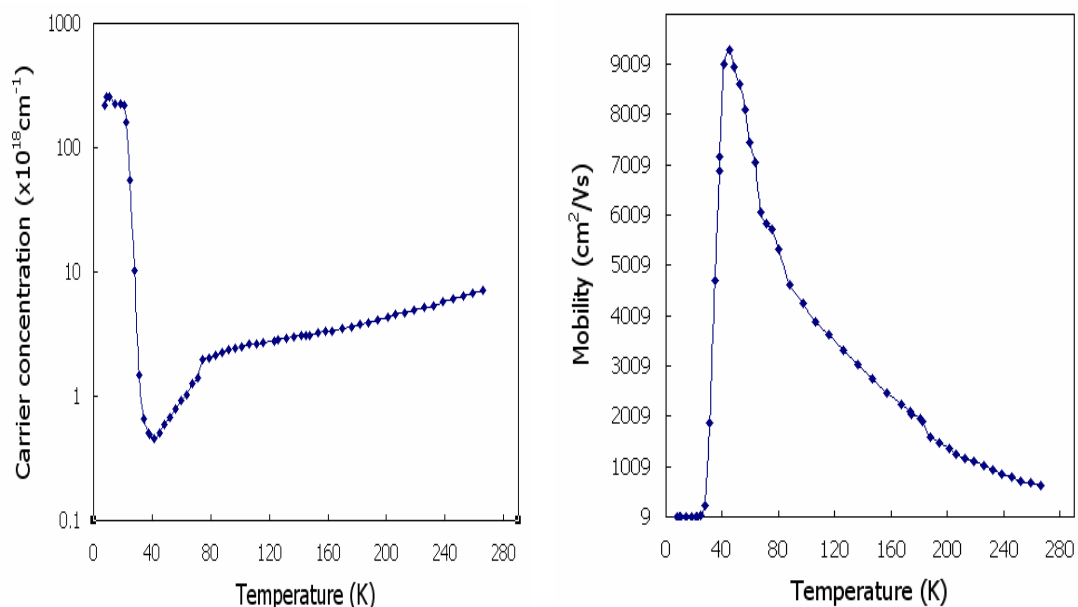


Figure 5-38. Carrier concentration and mobility of InN on Si (111) at different characterization temperature using Hall measurement.

### 5.1.5.7. Summary

For Al<sub>2</sub>O<sub>3</sub> (0001), the optimized growth condition of InN was found in terms of the growth temperature, N/In ratio, buffer layer growth temperature, substrate nitridation.

The results are summarized in Table 5-8.

Table 5-8. Optimum growth condition of InN for Al<sub>2</sub>O<sub>3</sub> (0001), GaN/Al<sub>2</sub>O<sub>3</sub> (0001), Si (111).

Substrate	Buffer layer	Growth temperature	Buffer layer temperature	N/In ratio
Al <sub>2</sub> O <sub>3</sub> (0001)	LT-InN	T = 530 °C	T <sub>LT-InN</sub> = 450 °C	50,000
	LT-GaN	T = 550 °C	T <sub>LT-GaN</sub> = 560 °C	50,000
GaN/Al <sub>2</sub> O <sub>3</sub> (0001)	LT-InN	T = 530 °C	T <sub>LT-InN</sub> = 400 °C	50,000
Si (111)	LT-InN	T = 530 °C	T <sub>LT-InN</sub> = 450 °C	50,000

The mirror-like surface of InN was obtained using a LT-InN buffer (RMS roughness = 4.2 nm). The best quality single crystalline InN grown on GaN/Al<sub>2</sub>O<sub>3</sub> (0001) showed that the FWHM of XRC is 1039 arcsec with LT-InN buffer layer. The growth of InN was found to be the transport-limited under most conditions. The growth rate decreased with N/In ratio due to the increased amount of H<sub>2</sub> produced by thermal decomposition of NH<sub>3</sub>. The band gap energy of InN films on Al<sub>2</sub>O<sub>3</sub> (0001) is 0.84 eV. The carrier concentration of  $7.0 \times 10^{18} \text{ cm}^{-3}$  at T = 266 K and  $4.5 \times 10^{17} \text{ cm}^{-3}$  at T = 41 K and the mobility of 623 cm<sup>2</sup>/Vs at T = 266 K and 9288 cm<sup>2</sup>/Vs at T = 45 K were obtained on InN grown on Si (111).

#### 5.1.6. Indium Nitride (InN) Droplet Formation

Indium droplets normally occurred during the growth of InN at low N/In ratio. In this part, indium droplet formation was studied in more detail through XRD, Scanning Electron Microscopy (SEM), Energy Dispersive Microscopy (EDS), and Auger Electron Spectroscopy (AES) (AES Perkin-Elmer PHI 660 Scanning Auger Multiprobe). For this study, InN was grown on Al<sub>2</sub>O<sub>3</sub> (0001) and Si (111) at T = 550 °C, T<sub>LT-GaN</sub> = 560 °C, and N/In = 3000 to 50,000 with LT-GaN buffer layer.

At  $N/In = 3000$ , a high density of indium droplets formed at the surface. As the  $N/In$  ratio increases from 3000 to 50,000, the indium droplet density decreases and finally disappears. From  $N/In = 20,000$ , the size of the indium droplet is reduced significantly. Finally, at  $N/In = 50,000$ , indium droplets completely disappeared (Fig. 5.39). These results show that an increase of the  $N/In$  ratio effectively reduces and then eliminates indium droplet formation.

At  $N/In = 6000$ , the indium and InN phases were characterized by EDS (Fig. 5.39). For the indium phase, the strong intensity of indium peak was obtained from thick indium precipitates. The weak Al peak was also obtained from  $Al_2O_3$  substrate due to the depth penetration of EDS to  $\sim 1 \mu m$ . For the InN phase, a weaker peak intensity was obtained compared to that of indium phase and a stronger Al peak was obtained from the  $Al_2O_3$  substrate and thin InN film (Fig. 5.40).

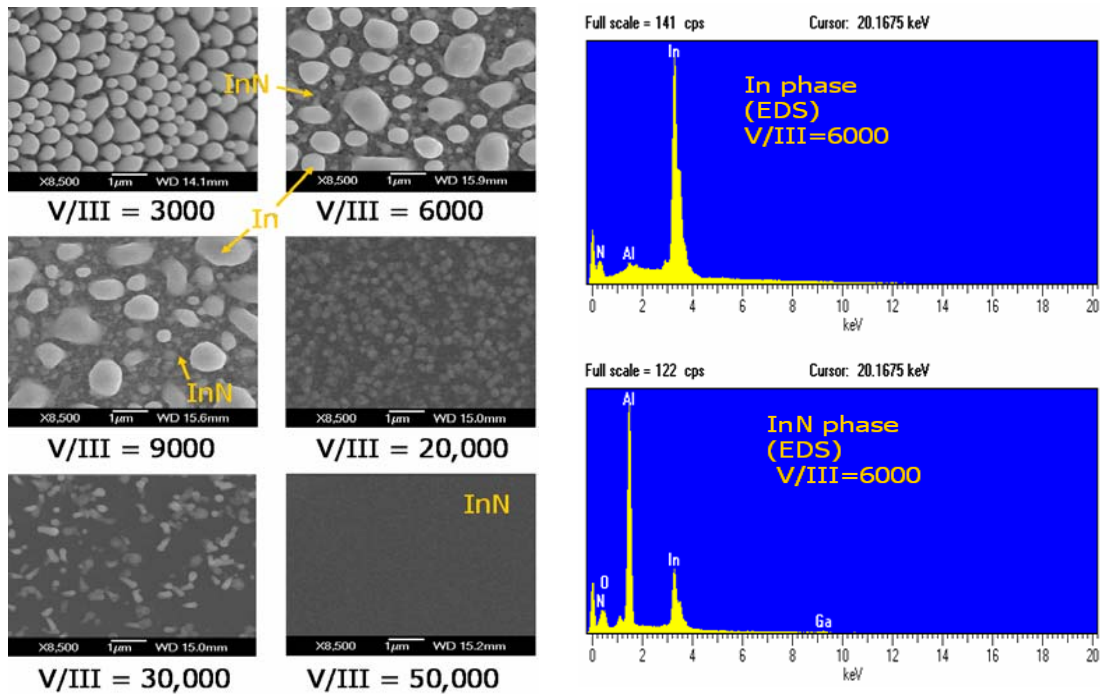


Figure 5-39. Scanning Electron Microscopy (SEM) and EDS for the surface of InN/LT-GaN on  $Al_2O_3$  (0001) at  $N/In = 3000, 6000, 9000, 20,000, 30,000,$  and  $50,000$ .

The relation between the number of indium droplets per unit area and N/In ratio was studied in the range of N/In = 3000 to 30,000. The percent of the indium droplets with small size was increased with the N/In ratio (Fig. 5.40 and Fig. 5.41). The number density of indium droplets increases again from N/In = 9000 to 20,000 because the big indium droplets break into many small indium droplets (Fig. 5.39). The density of indium droplets continued to be decreased as the N/In ratio changed from 20,000 to 30,000. These results indicated that the indium droplets formation can be reduced by increasing the N/In ratio.

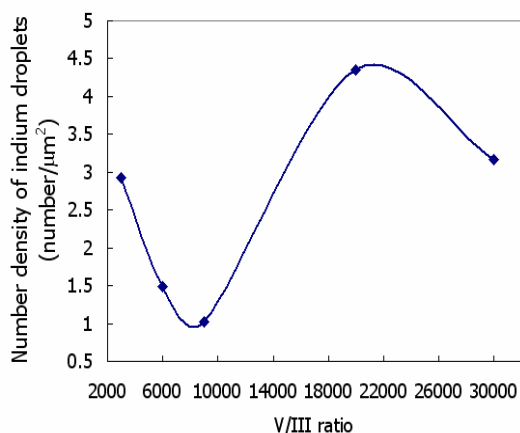


Figure 5-40. Number density of indium droplets vs. N/In ratio depending on different N/In, when InN was grown on Al<sub>2</sub>O<sub>3</sub> (0001) at T = 550 °C and N/In = 3000, 6000, 9000.

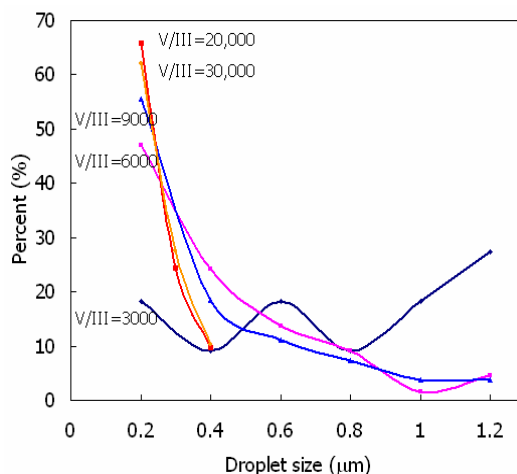


Figure 5-41. Percent (%) vs. indium droplet size depending on different N/In, when InN was grown on Al<sub>2</sub>O<sub>3</sub> (0001) at T = 550 °C and N/In = 3000, 6000, 9000.

The possibility that the residual indium can be etched in the diluted HCl solution (15 %), was studied using XRD and AES. For this study, the growth of InN was performed on Si and Al<sub>2</sub>O<sub>3</sub> substrates at N/In = 3000, and T = 450, 550, 650, and 750 °C. The results of XRD  $\theta$ -2 $\theta$  scans of InN grown on Al<sub>2</sub>O<sub>3</sub> (0001) and Si (111) showed that after HCl etching all peaks of indium droplets disappeared on both substrates (Fig. 5.42 to Fig. 5.45). Because the InN (10-11) peak is at 33.1° and In (101) peak at 32.9°, these two peaks overlapped before the HCl wet etching.

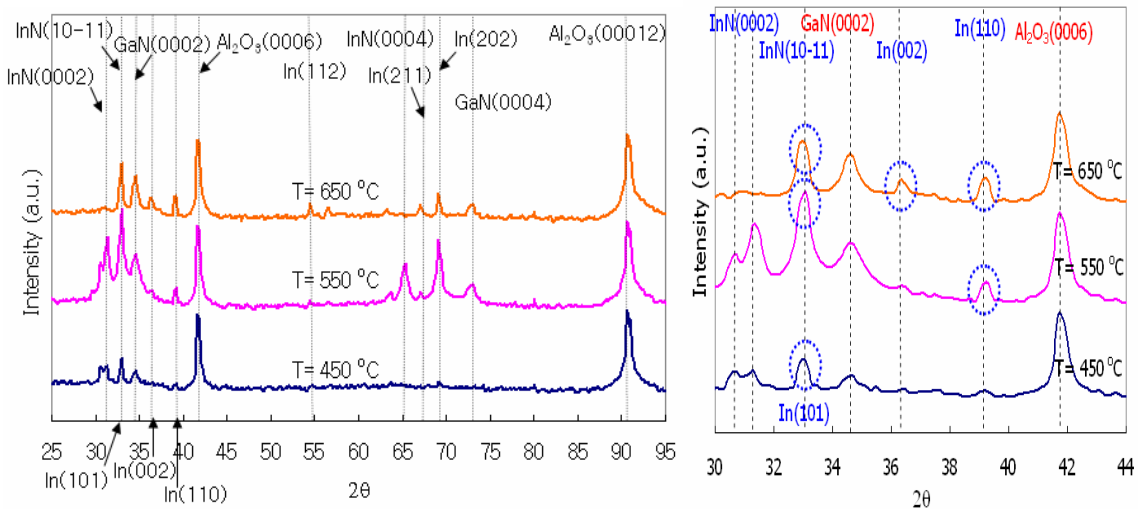


Figure 5-42. X-ray Diffraction (XRD)  $\theta$ -2 $\theta$  scans for InN/LT-GaN on Al<sub>2</sub>O<sub>3</sub> (0001) at N/In = 3000, T = 450, 550, 650, and 750 °C before HCl wet etching.

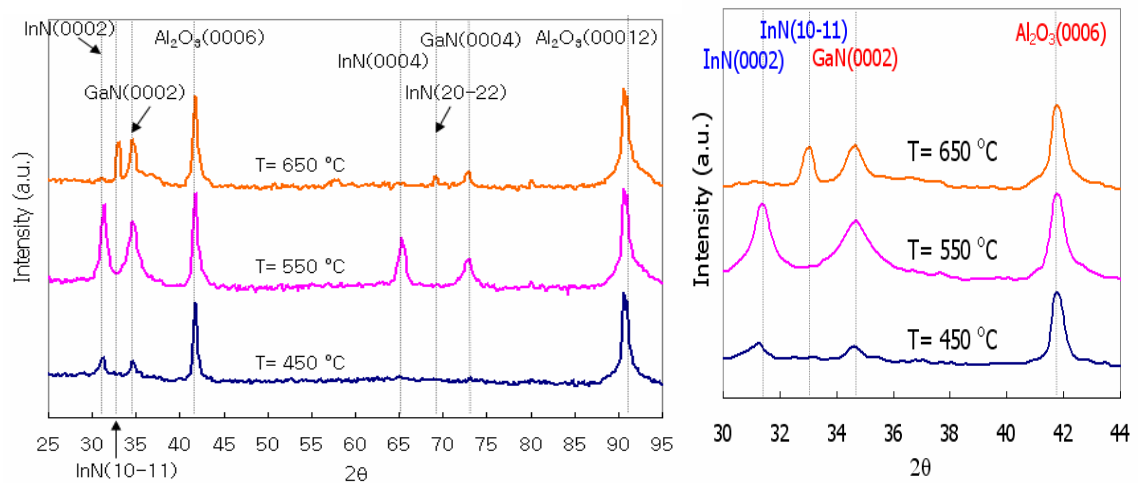


Figure 5-43. X-ray Diffraction (XRD)  $\theta$ -2 $\theta$  scans for InN/LT-GaN on Al<sub>2</sub>O<sub>3</sub> (0001) at N/In = 3000, T = 450, 550, 650, and 750 °C after HCl wet etching.

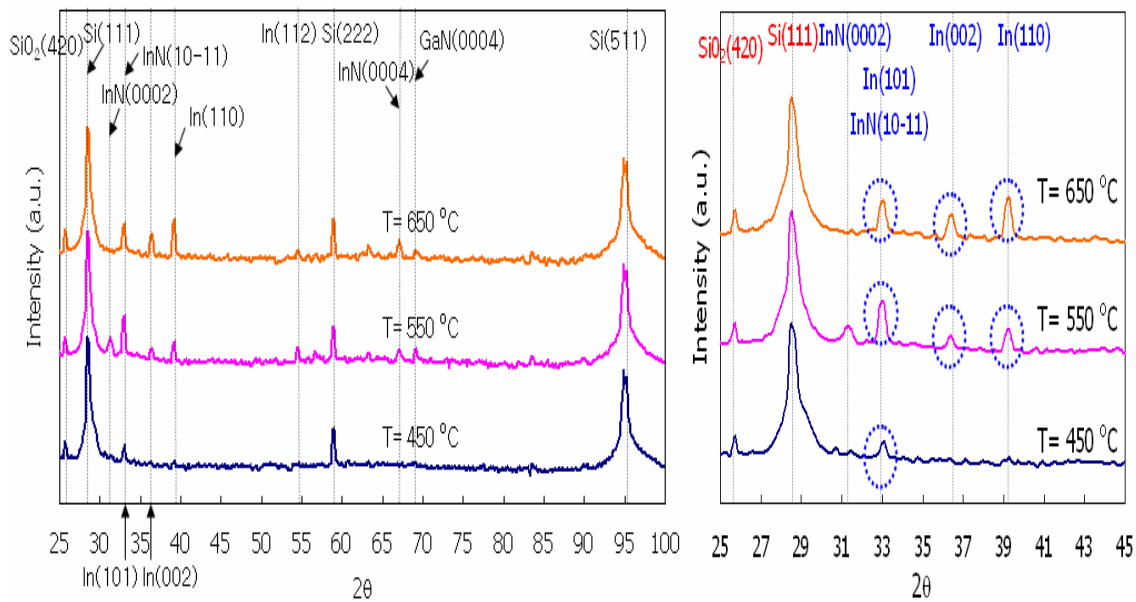


Figure 5-44. X-ray Diffraction (XRD)  $\theta$ - $2\theta$  scan for InN/LT-GaN on Si (111) at N/In = 3000, T = 450, 550, 650, and 750 °C before HCl wet.

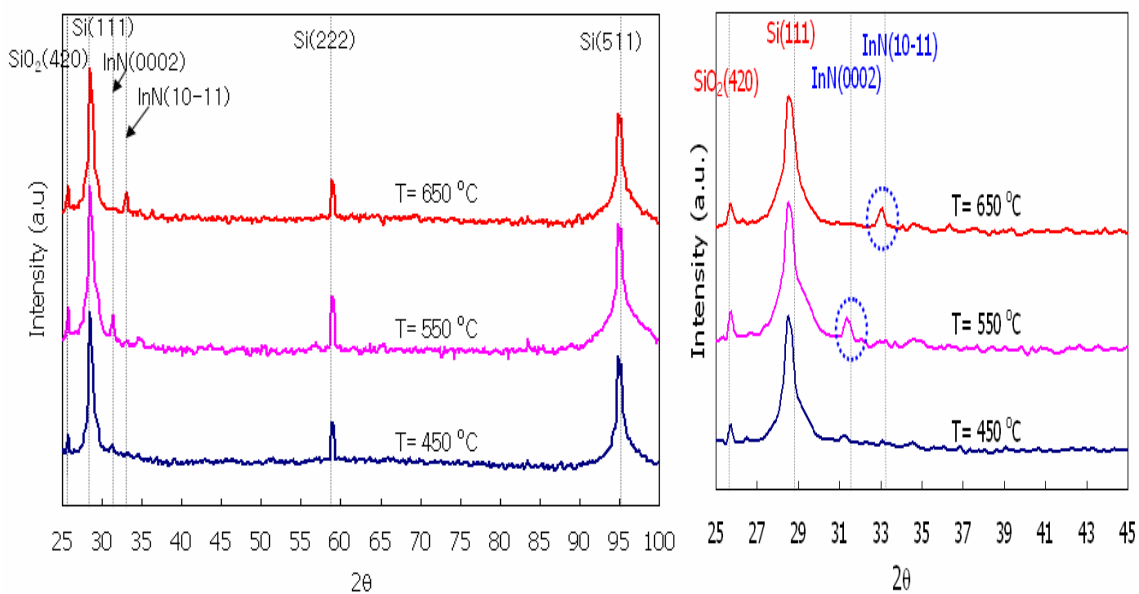


Figure 5-45. X-ray Diffraction (XRD)  $\theta$ - $2\theta$  scan for InN/LT-GaN on Si (111) at N/In = 3000, T = 450, 550, 650, and 750 °C after HCl wet etching.

AES characterization also showed that the indium droplets could be removed in HCl solution (Fig. 5.46). Before the HCl wet etching, only the peak due to indium droplets was detected with the indium atomic concentration 37.2 % and the peak of

nitrogen was not detected. After the HCl wet etching, the indium atomic concentration was decreased from 37.2 to 18 % and the peaks of In and N were detected together, which came from the InN film obtained after the HCl wet etching.

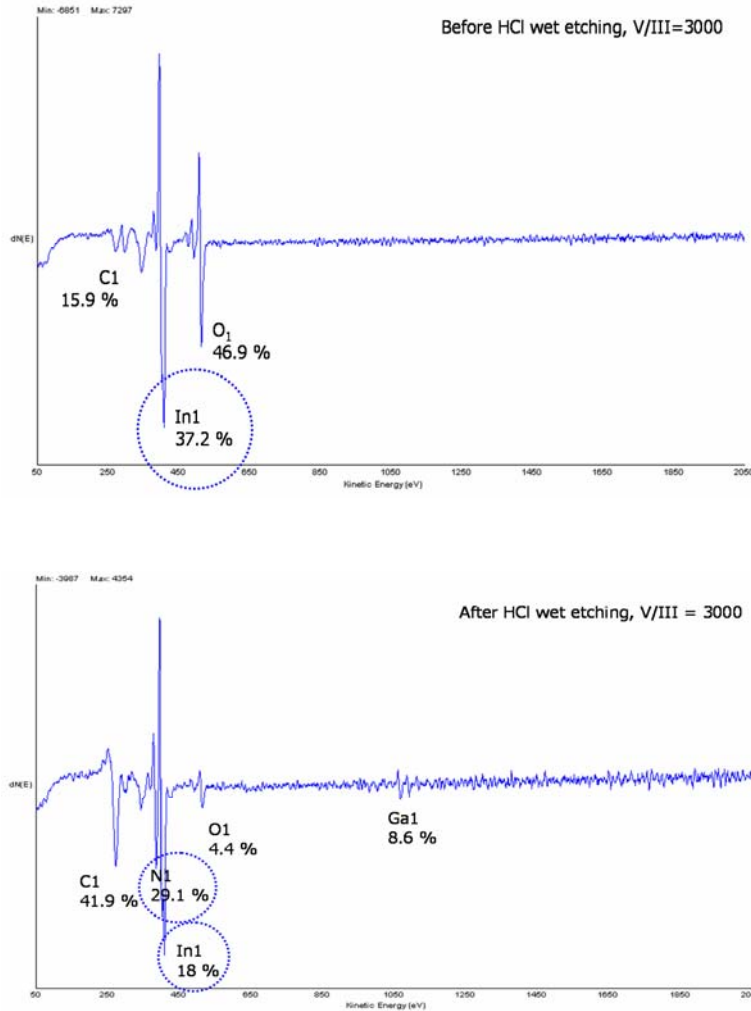


Figure 5-46. Characterization result by AES for In droplets formed during the growth of InN on Al<sub>2</sub>O<sub>3</sub> (0001) with LT-GaN buffer layer before the HCl wet etching after the HCl wet etching at N/In = 3000.

The indium atomic concentration obtained from InN is 18 % and the nitrogen atomic concentration obtained from InN film and LT-GaN buffer layer was 29.1 %.

Through the characterization results of XRD, SEM, EDS and AES, it is concluded that the increase of N/In ratio can reduce indium droplet formation effectively during the growth of InN.

### 5.1.7. Annealing Effect

The crystalline quality of an epitaxial film can often be improved further by post-growth annealing. The post-growth annealing is thought to cause the rearrangement of crystallites. The as-grown single crystal InN films consist of mosaic crystallites with slightly different orientations nearly along the (0002) direction. Many dislocations with an edge component must be arranged at the boundary between the crystallites. This climbing motion (nonconservative motion) of the boundary dislocations is strongly temperature dependent and is accommodated only through a transfer of matter by atomic diffusion. Therefore, thermal annealing may cause climbing motion of dislocations [Guo94c]. The movement of boundaries and some of the small crystallites begin to rotate, so that the free energy of the system may be reduced. This behavior will result in an improvement in crystalline quality of a mosaic crystal and the crystalline quality of InN film. Therefore, the annealing effect was studied for improving the crystalline quality of InN on Al<sub>2</sub>O<sub>3</sub> (0001) and GaN/Al<sub>2</sub>O<sub>3</sub> (0001). The annealing test was performed at T = 450 °C in N<sub>2</sub> flow with different annealing time (0, 10, 30, 60, and 90 min).

For InN on Al<sub>2</sub>O<sub>3</sub> (0001), the average FWHM of XRC of InN film is 7488 arcsec before the annealing test and FWHM of XRC was reduced with annealing (Fig. 5.47). The instrument error for FWHM of XRC is  $\pm 1.8$  arcsec ( $\pm 0.0005$ ). Above 60 min of annealing time, the FWHM of XRC remained unchanged. For GaN/Al<sub>2</sub>O<sub>3</sub> (0001), the average FWHM of XRC of the InN film was 1779 arcsec before the annealing test and FWHM of XRC was reduced after annealing (Fig. 5.48). Above 30 min of annealing time, the FWHM of XRC remained same.

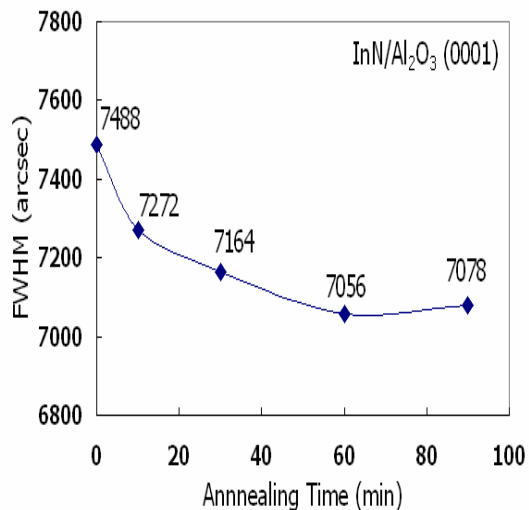


Figure 5-47. Full Width Half Maximum (FWHM) of XRC of InN/LT-InN (450 °C) on Al<sub>2</sub>O<sub>3</sub> (0001) at T = 450 °C in N<sub>2</sub> flow with different annealing time (0, 10, 30, 60 and 90 min).

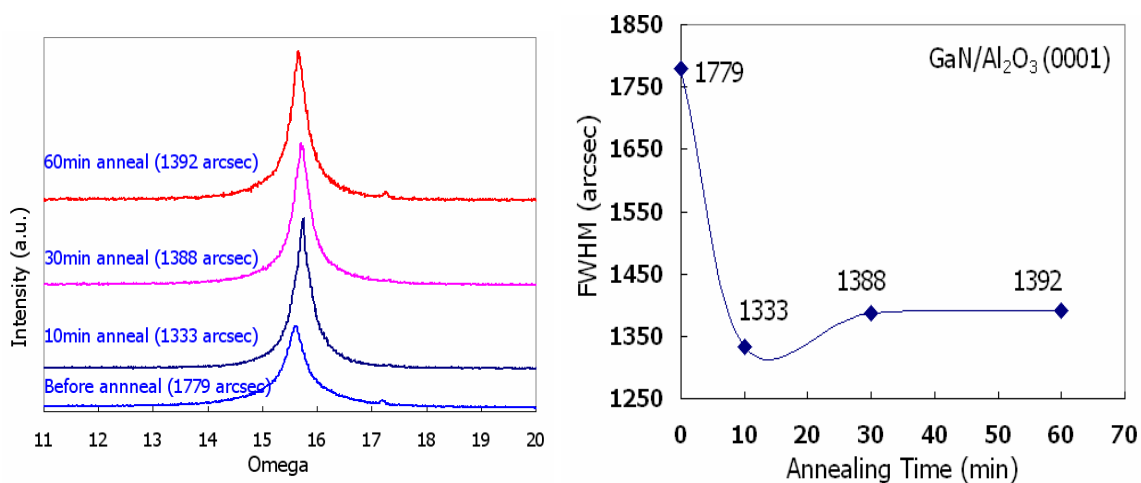


Figure 5-48. Full Width Half Maximum (FWHM) of XRC of InN/LT-InN (400 °C) on GaN/Al<sub>2</sub>O<sub>3</sub> (0001) at T = 450 °C in N<sub>2</sub> flow with different annealing time (0, 10, 30, and 60 min).

Based on 30 min of the annealing time, the FWHM of XRC was reduced from 7488 arcsec to 7264 arcsec by 4 % for InN on Al<sub>2</sub>O<sub>3</sub> (0001) and the FWHM of XRC was reduced from 1779 arcsec to 1388 arcsec by 22 % for InN on GaN/Al<sub>2</sub>O<sub>3</sub> (0001). Therefore, it was concluded that the annealing effect was larger for InN on GaN/Al<sub>2</sub>O<sub>3</sub> (0001) rather than for InN on Al<sub>2</sub>O<sub>3</sub> (0001). This difference in the annealing efficiency for the two substrates was thought to come from the different degree of rearrangement of

mosaic crystallite with different orientation along the (0002) direction and the different degree of the misorientation along the (0002) direction.

It is concluded that the annealing method can improve the crystalline quality of InN film and the most effective annealing was achieved within approximately 30 min.

## 5.2. Computational Fluid Dynamic Analysis of the Flow of NH<sub>3</sub> and Proposed Inlet Tube Modification to Improve Flow Pattern of NH<sub>3</sub>

Ammonia (NH<sub>3</sub>) is a widely used nitrogen precursor for InN growth. It is very difficult to produce active nitrogen due to the low decomposition efficiency at the relatively low growth temperature of 530 °C. This causes poor crystallinity of InN and low growth rate. Therefore, the modification of inlet tube was proposed to figure out the flow pattern of NH<sub>3</sub> in the MOVPE reactor with the current horizontal inlet tube and two modified inlet tubes. Thus, the approach to optimize the flow pattern through the inlet tube to induce the uniform flow and enhance the amount of NH<sub>3</sub> on the substrate was studied.

The inlet velocity  $\langle v \rangle_{inlet}$  of NH<sub>3</sub> is 0.94 m/s obtained when the flow rate (1.6 slm) of NH<sub>3</sub> and the radius of inlet tube is 0.3 cm (Eq. (5-7)).

$$\langle v \rangle_{inlet} = \frac{1600 \text{ cm}^3}{60 \text{ s}} \times \frac{1}{\pi \times (0.3 \text{ cm})^2} = 94 \text{ cm/s} \quad (5-7)$$

It was assumed that the temperature in the inlet tube is 25 °C and the temperature in the reactor changes from 25 °C (at the wall of the reactor) to 530 °C (at the substrate). The density and viscosity of NH<sub>3</sub> change depending on the temperature (Eq. (5-8) and (5-9)), and the velocity  $\langle v \rangle$  also changes due to the change of the diameter in inlet tube and the reactor (Eq. (1)). The operating pressure is 100 Torr.

For calculation of the density of NH<sub>3</sub>, it was assumed that NH<sub>3</sub> follows the ideal gas law. The density of NH<sub>3</sub> can be calculated as

$$\rho = \frac{PM}{RT} \quad (5-8)$$

where the unit of viscosity  $\mu$  is micropoise ( $10^{-7}$  kg/ms) and the unit of temperature, Kelvin (Table 5-9).

Table 5-9. Density and velocity of NH<sub>3</sub> at reactor wall and substrate.

Property	Inlet tube (25°C)	Reactor wall (25 °C, P = 100 Torr)	Substrate (530 °C, P = 100 Torr)
$D$	0.006 m	0.081 m	0.081 m
$\langle v \rangle$	0.940 m/s	0.005 m/s	0.005 m/s
$\rho$	0.092 kg/m <sup>3</sup>	0.092 kg/m <sup>3</sup>	0.033 kg/m <sup>3</sup>

Reynolds number can be calculated as

$$Re = \frac{D\langle v \rangle \rho}{\mu} \quad (5-9)$$

where  $D$  is the diameter of the reactor,  $\langle v \rangle$  the average velocity in the reactor of NH<sub>3</sub>,  $\rho$  is the density of NH<sub>3</sub>, and  $\mu$  is the viscosity of NH<sub>3</sub>.

The  $Re$  in the inlet tube is 49.8 at  $T = 25$  °C and  $Re$  in the reactor is 3.72 in the position at  $T = 25$  °C (wall of reactor) and 0.47 in the position at  $T = 550$  °C (substrate), respectively (Eq. 5.9, Table 5-10).

Table 5-10. Reynolds number ( $Re$ ) calculated in the inlet tube and in the reactor depending on temperature.

	Inlet tube ( $T = 25$ °C)	Reactor Wall ( $T = 25$ °C)	Substrate in reactor ( $T = 550$ °C)
$Re$	49.83	3.72	0.47

Considering the Fanning friction factor  $\left(\frac{16}{Re}\right)$ , the values  $Re$  indicate laminar flow

because the critical number is 2000, at which the flow changes from laminar flow to turbulent flow. The thermal expansion coefficient ( $\beta$ ) of  $\text{NH}_3$  was calculated by

$$\beta = \frac{\left(\frac{\Delta\rho}{\rho}\right)}{\Delta T} \quad (5-10)$$

$$\begin{aligned} \Delta\rho &= \rho_{\text{wall}} - \rho_{\text{substrate}} \\ \rho &= \rho\left(T = \frac{(T_{\text{wall}} + T_{\text{substrate}})}{2}\right) \\ \beta &= \beta\left(T = \frac{(T_{\text{wall}} + T_{\text{substrate}})}{2}\right) \end{aligned}$$

The thermal expansion coefficient of  $\text{NH}_3$  was calculated to be  $0.0025 \text{ K}^{-1}$  at the average temperature. The importance of buoyancy forces in a mixed convection flow can be measured by the ratio of the Grashof and Reynolds numbers;

$$\begin{aligned} \frac{Gr}{\text{Re}^2} &= \frac{\text{buoyancy force}}{\text{inertia force}} = \frac{g\beta(T_2 - T_1)L}{\langle v \rangle^2} \quad (5-11) \\ \rho &= \rho\left(T = \frac{(T_{\text{wall}} + T_{\text{substrate}})}{2}\right) \end{aligned}$$

where  $g$  is the gravity acceleration and  $(T_2 - T_1)$  is the temperature difference between the substrate and the wall of the reactor and  $L$  is the length between two temperature zones (0.0393 m).

When this number approaches or exceeds unity, strong buoyancy is expected. Conversely, if it is very small, buoyancy forces may be ignored in our simulation. For the operating condition of the reactor at  $P = 100 \text{ Torr}$ , the ratio of  $\frac{Gr}{\text{Re}^2}$  is 19450 near the substrate ( $T = 530 \text{ }^\circ\text{C}$ ).

From this result, it was found that the effect of convective flow should be taken into account because the ratio of  $\frac{Gr}{\text{Re}^2}$  is much greater than unity. Therefore, our calculation includes the gravity term to take into account the effect of the buoyancy

forces. The schematic for three types of inlet tubes used in the Fluent simulation is shown in Fig. 5.49. The first one is the currently used conventional horizontal inlet tube and the second and third ones are proposed inlet tube based on the results of the computational fluid dynamic analysis.

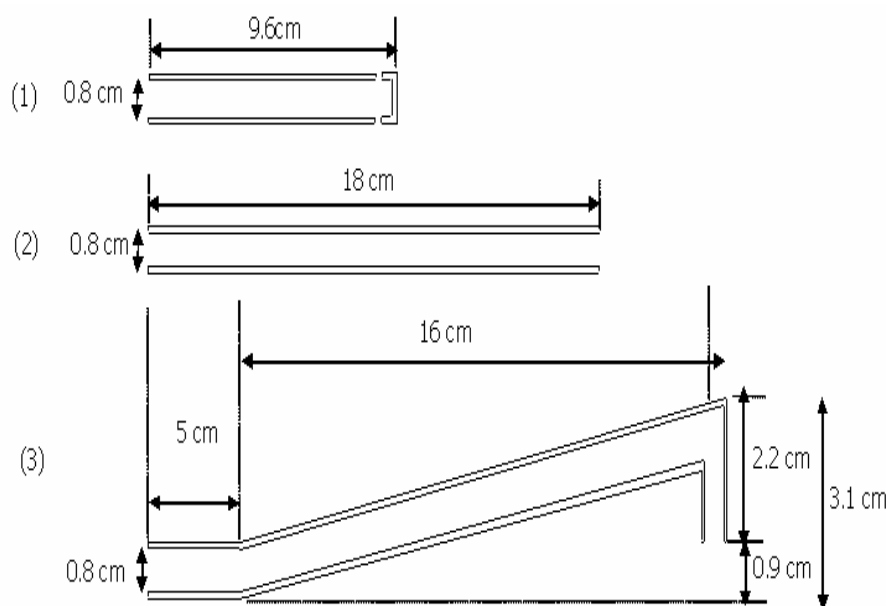


Figure 5-49. Schematic for three types of inlet tubes used for the Fluent simulation.

The physical properties of  $\text{NH}_3$  such as the density, thermal conductivity, viscosity and heat capacity of  $\text{NH}_3$  were obtained from the data set of Fluent. The flow of  $\text{NH}_3$  in the reactor using the current inlet tube is shown in Fig. 5.50. Figure 5-51 shows the flow of  $\text{NH}_3$  1 mm above the substrate. These results demonstrated that most of the  $\text{NH}_3$  passed along the wall of the reactor due to the structure of the inlet tube and the low density of  $\text{NH}_3$  and therefore the flow of  $\text{NH}_3$  was very small near the substrate and not uniform. This was thought to deteriorate the structural quality of InN and lead to low growth rate.

The first modified inlet tube is the horizontally extended one with the outlet located at the front side of the end of the inlet tube (Fig. 5.52). The simulation results also

indicated that most of the  $\text{NH}_3$  moved up to the top of the reactor due to the low density and therefore most of the  $\text{NH}_3$  still did not reach the surface of the substrate.

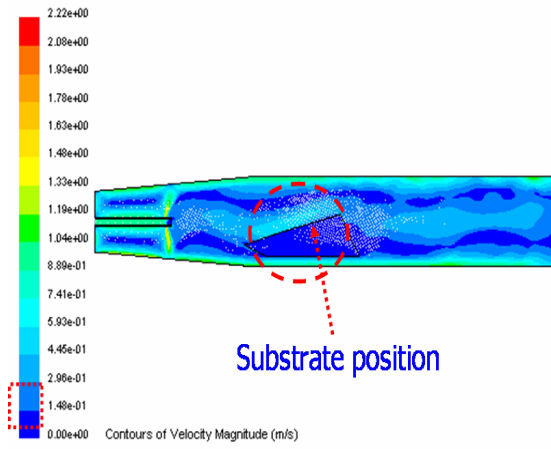


Figure 5-50. Flow of  $\text{NH}_3$  in the reactor with the current inlet tube.

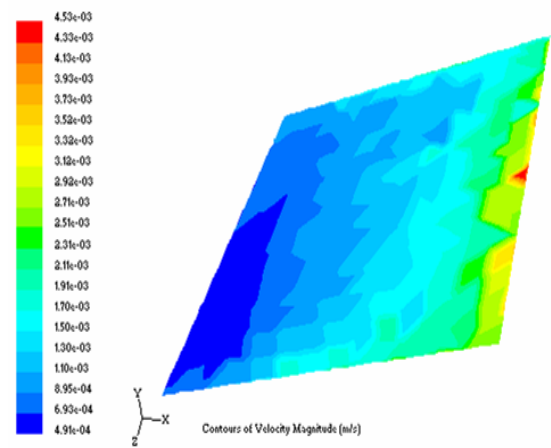


Figure 5-51. Flow of  $\text{NH}_3$  1 mm above the surface of substrate with the current inlet tube.

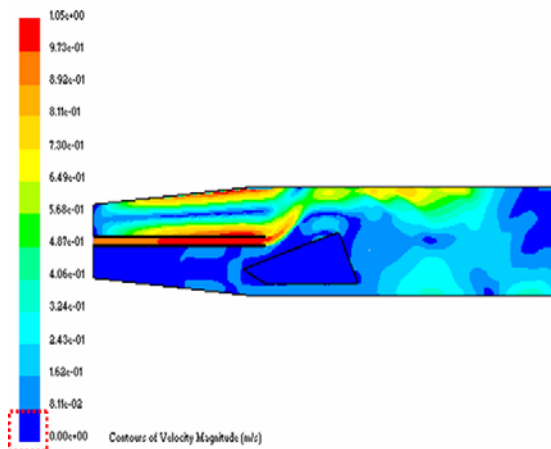


Figure 5-52. Flow of  $\text{NH}_3$  in the reactor with the horizontally extended inlet tube.

The second proposed inlet modification is the vertical inlet tube as shown in Fig. 5.53. These results showed that more of the  $\text{NH}_3$  reached the surface of the substrate and a uniform flow could be obtained on the surface of substrate with this vertical inlet tube design (Fig. 5.54).

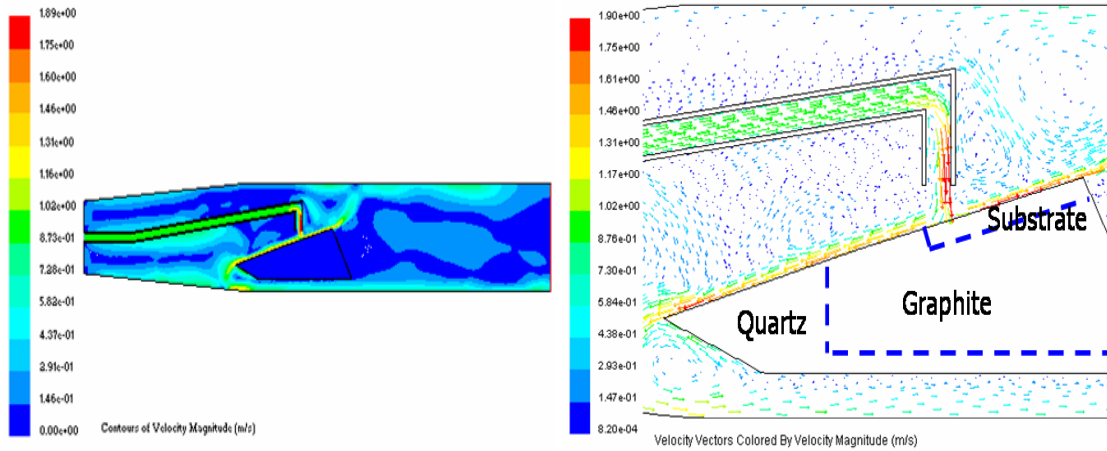
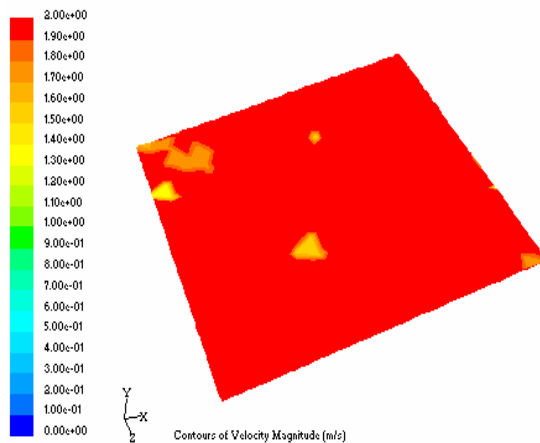


Figure 5-53. Flow in the reactor with the vertical inlet tube.



(c)

Figure 5-54. Flow of  $\text{NH}_3$  1 mm above the surface of substrate with the vertical inlet tube.

It was thought that fast flow rate of  $\text{NH}_3$  on the substrate can reduce the boundary layer and improve the diffusion of the  $\text{NH}_3$  into the substrate due to the decrease of the mass-transport boundary layer thickness, and finally leads to high growth rate according to Eq. (5-13). The MOVPE reactor is usually modeled by a boundary-layer flow over a

flat plate using the empirical expression [Yan99]. The following explanation showed the application of the scaling concept to the Navier-Stokes equation.

$$\frac{\partial \vec{V}}{\partial t} + \vec{V} \cdot \nabla \vec{V} = -\nabla P / \rho + \nu \nabla^2 \vec{V} + \vec{g} : \text{Navier - Stokes Equation} \quad (5-12)$$

Where the second term on the left side corresponds to momentum by convection and the second term on the right side corresponds to the momentum by diffusion.

When the scaling concept was used in Navier-Stokes equation, the velocity was scaled by  $V$  and the length is scaled by  $L$ . Then the velocity, the longitudinal length ( $x$ ), and transverse length ( $y$ ) is expressed as Eq. (5-13).

$$\begin{aligned} \vec{V} &= V \vec{V}^* \\ x &= L x^* \\ y &= \delta y^* \\ P &= \rho V^2 P^* \\ \vec{g} &= \frac{V^2}{L} \vec{g}^* \end{aligned} \quad (5-13)$$

where  $\vec{V}^*$ ,  $x^*$ ,  $y^*$ ,  $P^*$ ,  $\vec{g}^*$  is the dimensionless velocity, dimensionless longitudinal length, dimensionless transverse length, and dimensionless gravity acceleration, respectively. All terms in Eqn. (5-12) correspond to  $V^2/L$ . Therefore, in the boundary layer,

$$\frac{V^2}{L} = \frac{\nu V}{\delta^2} \quad (5-14)$$

Therefore, the boundary layer thickness is given by

$$\delta = \left( \frac{\mu L}{\rho V_\infty} \right)^{1/2} \quad (5-15)$$

where  $\delta$  is the boundary layer thickness for mass transport,  $\mu$  is the dynamic viscosity,  $x$  is the axial distance,  $\nu (\mu / \rho)$  is the kinematic viscosity,  $\rho$  is density, and  $V_\infty$  is the free stream velocity. The uniform flow of  $\text{NH}_3$  is supposed to enhance the structural quality of

InN. Equation (5-15) indicates that the increased velocity leads to the reduced thickness of boundary layer and therefore increased diffusion into the film. The growth rate can be increased.

In summary, based on the simulation results using the Fluent software, it was proposed that the vertical inlet tube would deliver more  $\text{NH}_3$  flow and TMI to the substrate and thus improve the growth rate and perhaps structural quality of InN.

### **5.3. Inlet Tube Modification and Growth Results**

From the result of the simulation obtained with Fluent software, the possibility to improve the structural quality of InN film by using the vertical inlet tube was studied. Two types of inlet tubes, an extended horizontal and a vertical design, were used for this experiment. The vertical inlet tube is expected to improve the crystallinity of InN film through the more uniform flow of  $\text{NH}_3$  and is also expected to increase the growth rate through the enhanced amount of the precursors such as TMI and  $\text{NH}_3$  on the substrate.

Using  $\text{Al}_2\text{O}_3$  (0001) as the substrate, Figure 5.55 and 5.56 shows that the single crystalline InN was obtained and a significantly reduced FWHM of the XRC was also found, from 4860 arcsec (the previous horizontal inlet tube) to 1339 arcsec by using the vertical inlet tube. However the extended horizontal inlet tube caused In droplet formation since most of the  $\text{NH}_3$  circulated away from the substrate due to the low density, and because a relatively large amount of TMI was delivered to the  $\text{Al}_2\text{O}_3$  (0001) due to the high density of TMI, which leads to a small N/In ratio at the surface. These results show that the structural quality of InN was significantly improved by using the vertical inlet tube for  $\text{Al}_2\text{O}_3$  (0001).

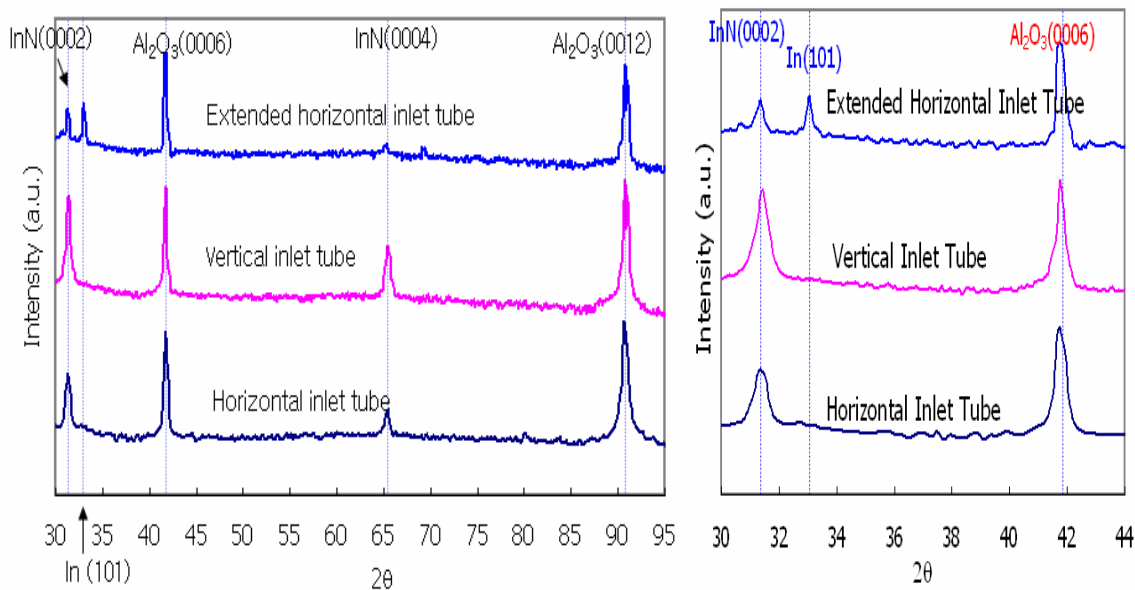
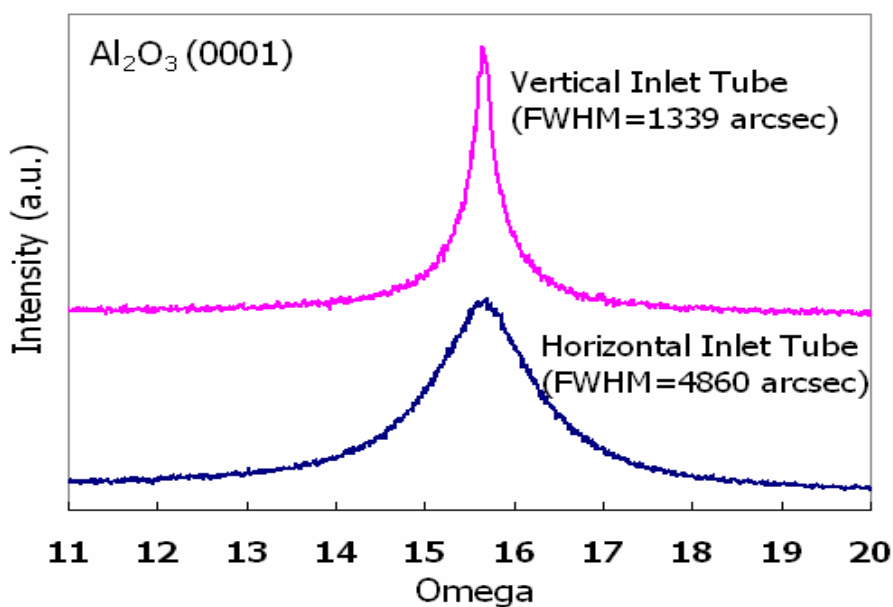


Figure 5-55. X-ray Diffraction (XRD)  $\theta$ - $2\theta$  scan for InN/LT-InN on  $\text{Al}_2\text{O}_3$  (0001) at  $\text{N/In} = 50,000$ ,  $T = 530\text{ }^\circ\text{C}$  and  $T_{\text{LT-InN}} = 450\text{ }^\circ\text{C}$  with different inlet tubes.



(b) FWHM of XRC

Figure 5-56. Full Width Half Maximum (FWHM) of XRC for InN/LT-InN on  $\text{Al}_2\text{O}_3$  (0001) at  $\text{N/In} = 50,000$ ,  $T = 530\text{ }^\circ\text{C}$  and  $T_{\text{LT-InN}} = 450\text{ }^\circ\text{C}$  with different inlet tubes.

The growth rate of InN with the vertical inlet tube increased from  $0.1\text{ }\mu\text{m/hr}$  (the previous horizontal inlet tube) to  $0.3\text{ }\mu\text{m/hr}$  due to the increased flow rate of TMI and  $\text{NH}_3$  on  $\text{Al}_2\text{O}_3$  (0001), where InN was grown for 3 hrs (Fig. 5.57).

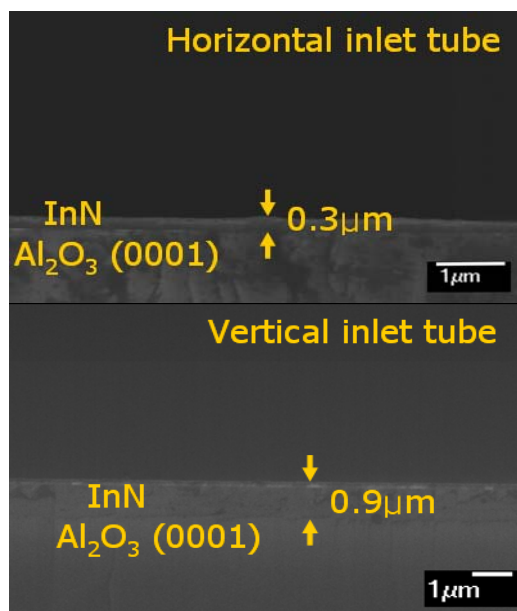


Figure 5-57. Cross-sectional SEM for InN/LT-InN on Al<sub>2</sub>O<sub>3</sub> (0001) at N/In = 50,000, T = 530 °C, and T<sub>LT-InN</sub> = 450 °C with the horizontal and vertical inlet tubes.

For GaN/ Al<sub>2</sub>O<sub>3</sub> (0001), the results shown in Figure 5.58 and 5.59 indicate that single crystalline InN was obtained and the FWHM of XRD of InN film was also significantly reduced from 1039 arcsec (the previous horizontal inlet tube) to 611 arcsec by using the vertical inlet tube. These results suggest that the structural quality of InN was also significantly improved by using the vertical inlet tube for GaN/Al<sub>2</sub>O<sub>3</sub> (0001).

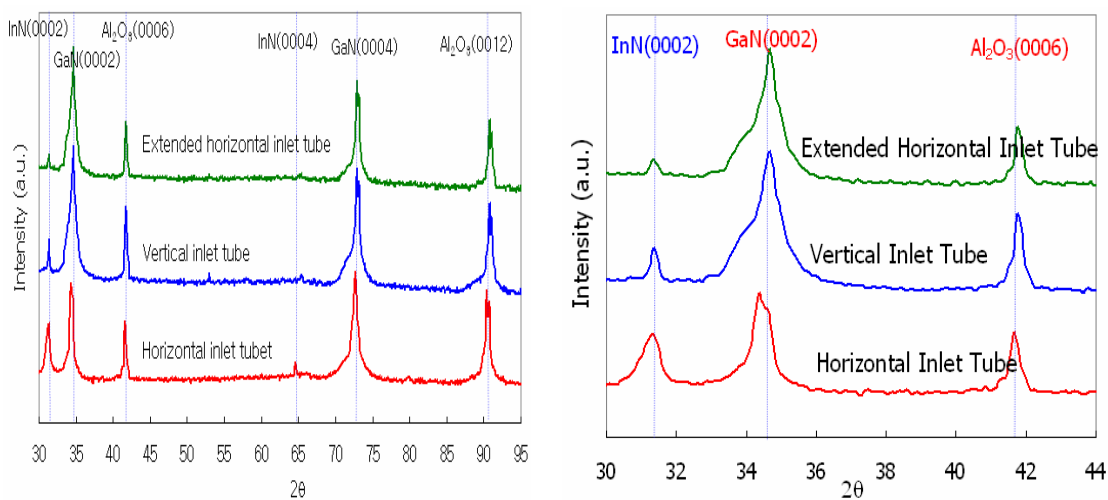


Figure 5-58. X-ray Diffraction (XRD)  $\theta$ -2 $\theta$  scan for InN/LT-InN on GaN/Al<sub>2</sub>O<sub>3</sub> (0001) at N/In = 50,000, T = 530 °C and T<sub>LT-InN</sub> = 450 °C with different inlet tubes.

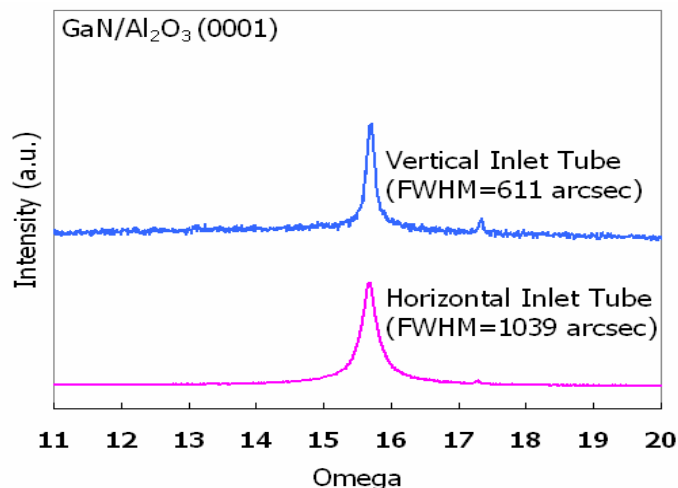


Figure 5-59. Full Width Half Maximum (FWHM) of XRC for InN/LT-InN on GaN/Al<sub>2</sub>O<sub>3</sub> (0001) at N/In = 50,000, T = 530 °C and T<sub>LT-InN</sub> = 450 °C with different inlet tubes.

The growth rate of InN with the vertical inlet tube increased from 0.1 μm/hr (the previous horizontal inlet tube) to 0.3 μm/hr due to the increased flow rate of TMI and NH<sub>3</sub> on GaN/Al<sub>2</sub>O<sub>3</sub> (0001), where InN was grown for 3 hrs (Fig. 5.60).

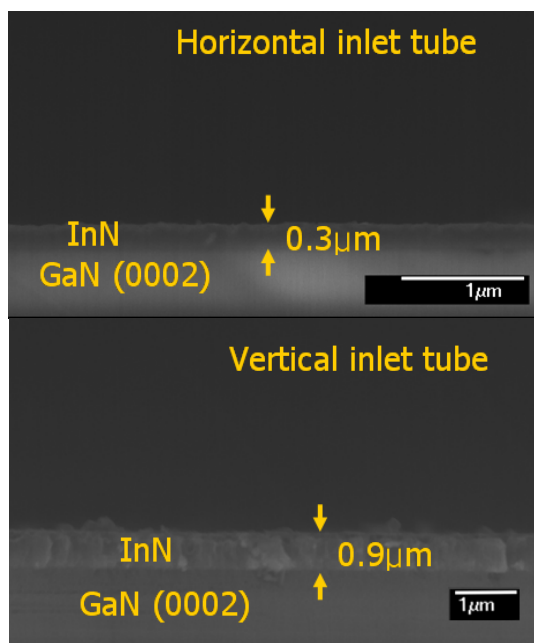


Figure 5-60. Cross-sectional SEM for InN/LT-InN on GaN/Al<sub>2</sub>O<sub>3</sub> (0001) at N/In = 50,000, T = 530 °C and T<sub>LT-InN</sub> = 400 °C with the horizontal and the vertical inlet tubes.

The crystallinity of InN on the surface was characterized for InN grown on  $\text{Al}_2\text{O}_3$  (0001) and  $\text{GaN}/\text{Al}_2\text{O}_3$  (0001) with GIXD (Grazing Angle Incident X-ray Diffraction). GIXD is used for the characterization of the crystallinity of the film on the surface because the incident angle of X-ray is very small. For GIXD characterization, the film with the better crystallinity does not show any peak because the incident angle is fixed at the angle less than 3 degrees. When any peak exists, this represents that the film with the growth direction corresponding to the  $2\theta$ , was grown with the tilt.

For this GIXD characterization, the incident angle was fixed at 1 degree. For InN grown with the horizontal inlet tube, InN on  $\text{GaN}/\text{Al}_2\text{O}_3$  (0001) showed the better crystallinity compared with that of InN on  $\text{Al}_2\text{O}_3$  (0001) as shown in Fig. 5.61 and 5.62.

When InN was grown on  $\text{GaN}/\text{Al}_2\text{O}_3$  (0001), most of InN (0002) was grown perpendicular to the surface of  $\text{GaN}/\text{Al}_2\text{O}_3$  (0001) without the tilting. When InN was grown on  $\text{Al}_2\text{O}_3$  (0001), some of InN (0002) was grown in the different direction from the perpendicular direction to the surface of  $\text{Al}_2\text{O}_3$  (0001) with the tilting. The same explanation was applied to the InN (10-13) and InN (20-21).

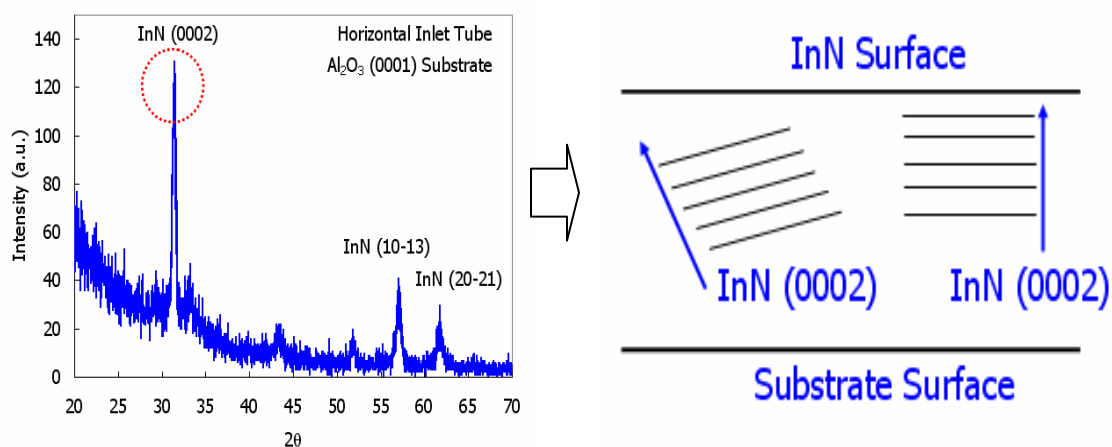


Figure 5-61. Grazing Angle Incident X-ray Diffraction (GIXD) for InN grown on  $\text{Al}_2\text{O}_3$  (0002) with the incident angle of 1 degree when the horizontal inlet tube was used.

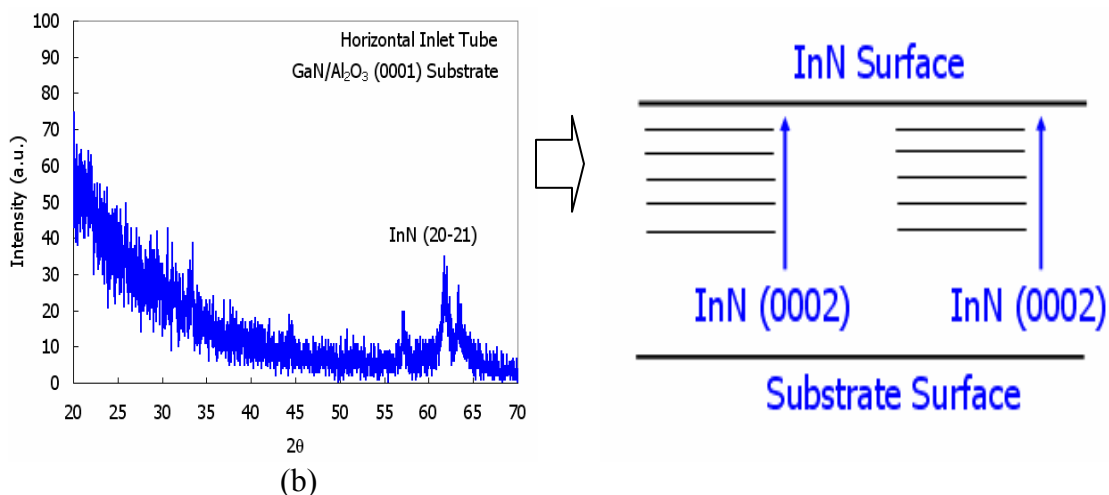


Figure 5-62. Grazing Angle Incident X-ray Diffraction (GIXD) for InN grown on GaN/Al<sub>2</sub>O<sub>3</sub> (0002) with the incident angle of 1 degree when the horizontal inlet tube was used.

When the vertical inlet tube was used for the growth of InN on Al<sub>2</sub>O<sub>3</sub> (0001) and GaN/Al<sub>2</sub>O<sub>3</sub> (0001), the crystallinity of InN on the surface was also characterized with GIXD and compared with that of the horizontal inlet tube (Fig. 5.63). The intensity of InN (0002) peak was reduced significantly on InN grown on both Al<sub>2</sub>O<sub>3</sub> (0001) and GaN/Al<sub>2</sub>O<sub>3</sub> (0001) using the vertical inlet tube. Therefore, the vertical inlet tube was found to improve the crystallinity on InN on the surface compared to that of the horizontal inlet tube. The best crystallinity of InN on the surface was obtained for InN on GaN/Al<sub>2</sub>O<sub>3</sub> (0001) with the vertical inlet tube. For growth of InN on Si (111), the films grown with both the vertical and the extended horizontal inlet tube designs showed single crystalline InN (002) growth, but the intensity of InN (002) peak was not significantly increased (Fig. 5.64). No XRC was taken for InN grown on Si (111). From this result, it is concluded that for Si (111), the quality InN film is believed not to be improved through the induced increased mass flow of TMI and NH<sub>3</sub>. There needs to be studied further in terms of the reaction at the surface of silicon substrate.

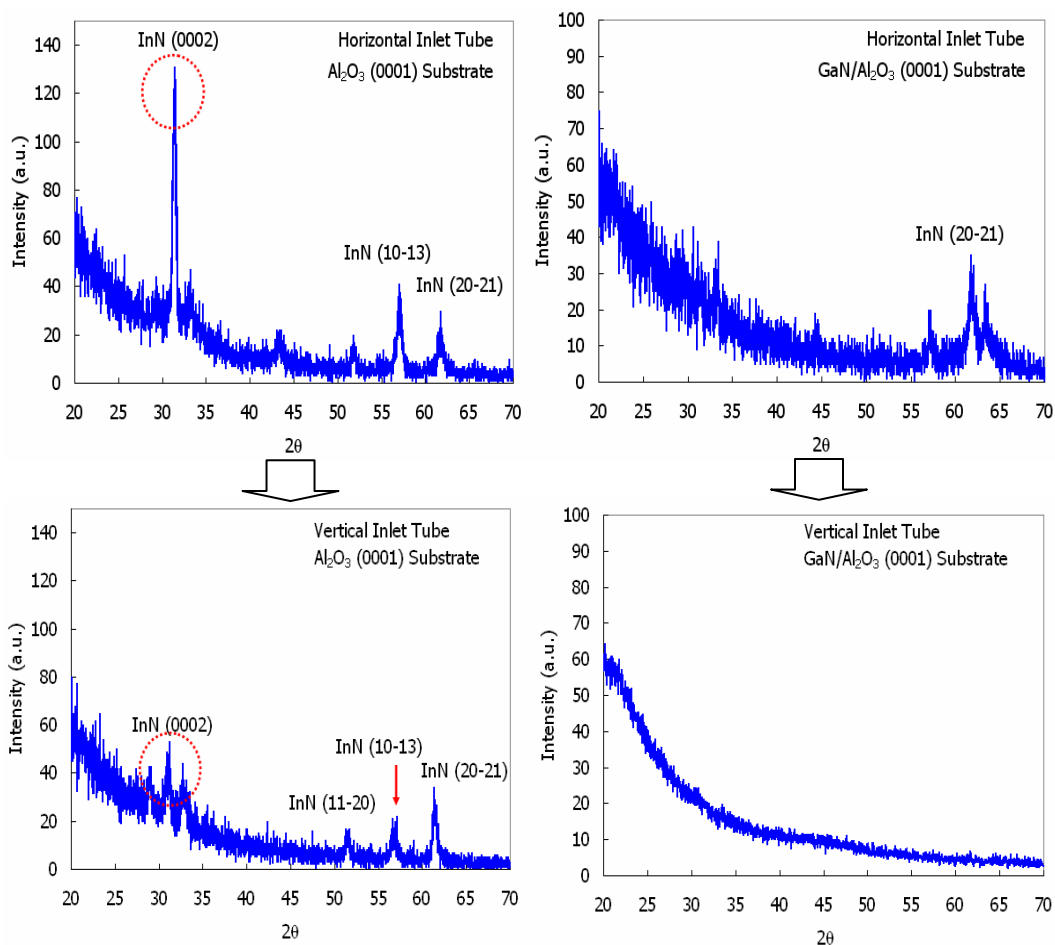


Figure 5-63. Grazing Angle Incident X-ray Diffraction (GIXD) for InN grown on (a)  $\text{Al}_2\text{O}_3$  (0002) and (b)  $\text{GaN}/\text{Al}_2\text{O}_3$  (0002) with the incident angle of 1 degree when the vertical inlet tube was used.

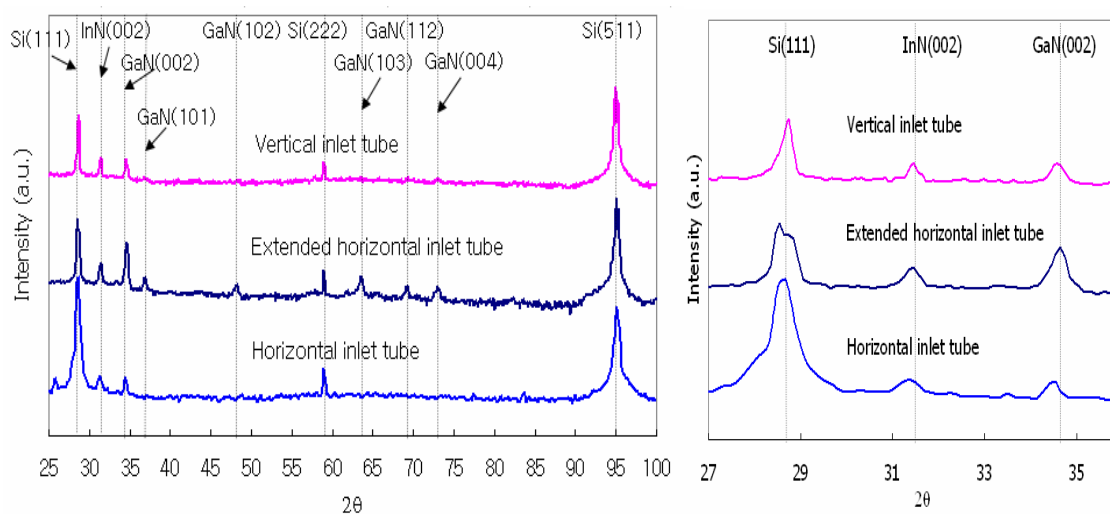


Figure 5-64. X-ray Diffraction (XRD)  $\theta$ - $2\theta$  scan of InN/LT-InN/GaN/LT-GaN on Si (111) at  $\text{N}/\text{In} = 50,000$ ,  $T = 530^\circ\text{C}$  and  $T_{\text{LT-InN}} = 400^\circ\text{C}$  for both horizontal and vertical inlet tubes.

The crystalline quality of InN can be improved further by post-growth annealing presumably through rearrangement of the crystallites. Therefore, the post-growth annealing for 30 min was applied for the further improvement of the structural quality of InN on Al<sub>2</sub>O<sub>3</sub> (0001) and GaN/Al<sub>2</sub>O<sub>3</sub> (0001). This annealing test was performed at T = 450 °C in N<sub>2</sub> flow. The annealing found not to be effective for InN grown on Al<sub>2</sub>O<sub>3</sub> (0001), but effective for InN grown on GaN/Al<sub>2</sub>O<sub>3</sub> (0001) (Fig. 5.65 and 5.66). The FWHM of 574 arcsec was obtained for GaN/Al<sub>2</sub>O<sub>3</sub> (0001) after the annealing for 30 min. This FWHM of 574 arcsec is the smallest one known so far among the single crystalline InN film. This result showed a similar trend to the result of the annealing test previously done for Al<sub>2</sub>O<sub>3</sub> (0001) and GaN/Al<sub>2</sub>O<sub>3</sub> (0001), where the annealing effect was much larger for GaN/Al<sub>2</sub>O<sub>3</sub> (0001) than for Al<sub>2</sub>O<sub>3</sub> (0001) (Fig. 5.65 and Fig. 5.66).

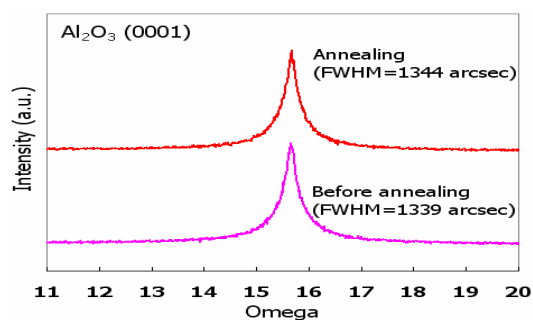


Figure 5-65. Full Width Half Maximum (FWHM) of XRC of InN/LT-InN on Al<sub>2</sub>O<sub>3</sub> (0001) at N/In = 50,000, T = 530 °C for both horizontal and vertical inlet tubes. The annealing test is performed at T = 450 °C for 30 min.

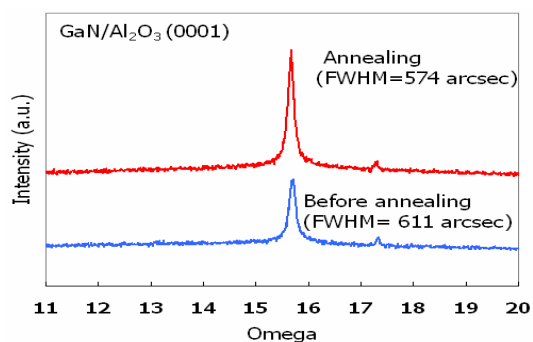


Figure 5-66. Full Width Half Maximum (FWHM) of XRC of InN/LT-InN on GaN/Al<sub>2</sub>O<sub>3</sub> (0001) at N/In = 50,000, T = 530 °C for both horizontal and vertical inlet tubes. The annealing test is performed at T = 450 °C for 30 min.

Table 5-11. Typical values of FWHM depending on different reactor systems.

Reactor	FWHM (arcsec)
MOVPE	~ 4000-5500
ME-MOVPE	~ 420-2000
MEE (Lu,2000)	~ 3120

[Che97, Lu00, Oian02b]

Table 5-12. Reference data available for FWHM for MOVPE reactor.

Researcher	FWHM (arcsec)	Single/ Polycrystal	Growth method	Reactor
Y.C. Pan(1999)	~ 700	Polycrystal	InN/sapphire	MOVPE
S. Yamaguchi(1999)	~ 1700	Polycrystal	InN/LT-AIN/GaN	MOVPE
A. Yamamoto(2001)	~ 1500	Polycrystal	InN/GaN Sap	MOVPE
F.H. Yang(2002)	476	Polycrystal	InN/GaN Sap	MOVPE
A. Yamamoto(2004)	~ 2000	Single	InN/LT-AIN/Sap	MOVPE

[Pan99, Yam99a, Yam01b, Yan02a, Yam04a]

In summary, it is found that the vertical inlet tube design enhances the crystalline quality of InN through the increased mass flow rates of TMI and NH<sub>3</sub>. These results show that the smallest FWHM of InN/LT-InN grown on Al<sub>2</sub>O<sub>3</sub> (0001) and GaN/Al<sub>2</sub>O<sub>3</sub> (0001) is 1339 and 574 arcsec, respectively. For Al<sub>2</sub>O<sub>3</sub> (0001), the optimized growth temperature is 530 °C with N/In = 50,000 and T<sub>LT-InN</sub> = 450 °C and for GaN/Al<sub>2</sub>O<sub>3</sub> (0001), the optimized growth temperature is 530 °C with N/In = 50,000 and T<sub>LT-InN</sub> = 400 °C. When these values of FWHM are compared to other ones (Table 5-11 and 5.12), they show that the FWHM of XRC for InN film grown on GaN/Al<sub>2</sub>O<sub>3</sub> (0001) (FWHM of 574 arcsec) corresponds to the very high quality single crystalline InN.

## CHAPTER 6 CONCLUSIONS

The suitable growth region of InN and  $\text{In}_x\text{Ga}_{1-x}\text{N}$  was calculated thermodynamically in terms of temperature and pressure using ThermoCalc software. Based on the result of the calculation, the growth of InN occurs at temperatures below  $T = 800\text{ }^\circ\text{C}$  at V/III ratio = 50,000 and  $P = 100\text{ Torr}$ . These theoretical results are in a good agreement with the experimental data ( $T_{\text{growth}}, 450\text{-}700\text{ }^\circ\text{C}$ ). For  $\text{In}_{0.3}\text{Ga}_{0.7}\text{N}$ , a maximum growth temperature of  $780\text{ }^\circ\text{C}$  was estimated, which is in a good agreement with the experimental data ( $730 \sim 780\text{ }^\circ\text{C}$ ). Some disagreement between the calculated values and experimental data may be attributed to the fact that the epitaxial growth of InN and  $\text{In}_x\text{Ga}_{1-x}\text{N}$  by MOVPE is a non-equilibrium reaction and the calculation assumes equilibrium conditions. The growth temperature was almost independent of the operation pressure for both InN and  $\text{In}_x\text{Ga}_{1-x}\text{N}$ .

For  $\text{In}_x\text{Ga}_{1-x}\text{N}$ , the phase separation diagram was estimated using a 2-sublattice regular solution model and a quantum calculation method. The 2-sublattice model showed that the phase separation occurred at  $x_{\text{In}} \geq 0.1$  when  $T = 730\text{ }^\circ\text{C}$  and  $P = 100\text{ Torr}$ . The quantum calculation predicted that the onset of phase separation occurs at  $0.25 \leq x_{\text{In}} \leq 0.38$ . The phase separation experimentally occurs from the indium mole fraction of 0.25-0.3 depending on the growth condition. Since the quantum calculation is the theoretical method with the least assumptions, it shows better agreement with experimental data.

The critical thickness of InN on GaN (0001), AlN (0001), Al<sub>2</sub>O<sub>3</sub> (0001), and Si (111) was calculated using three type of models, and all showed that the dislocation occurs at 1<sup>st</sup> monolayer of InN. Calculated values were consistent with the experimental result obtained by TEM. Based on the calculated and available experimental data, we could conclude that there is no suitable substrate for the growth of InN and that a LT-buffer layer is necessary for the growth of high quality InN.

The growth conditions of InN on substrates such as Al<sub>2</sub>O<sub>3</sub> (0001), GaN/Al<sub>2</sub>O<sub>3</sub> (0001), and Si (111) substrate were also optimized with growth temperature, growth pressure, buffer layer materials (InN and GaN), growth condition of buffer, V/III ratio and annealing. The InN buffer was first introduced in InN growth by MOVPE. It was clearly shown that the structural quality of InN film was improved dramatically. The effect of SiO<sub>x</sub>N compliant layer was also studied for the growth of InN film.

From this study, the optimum V/III ratio was 50,000 and the optimized growth temperature of InN was 550 °C for LT-GaN buffer layer and 530 °C for LT-InN buffer layer. High V/III ratio could prevent the indium droplets formation during the InN growth by MOVPE. The mirror-like surface and the improved structural quality of InN film was obtained with LT-InN buffer layer (FWHM of XRC ~ 4860 arcsec for InN on Al<sub>2</sub>O<sub>3</sub>) rather than with LT-GaN buffer layer (FWHM of XRC ~ 14868 arcsec for InN on Al<sub>2</sub>O<sub>3</sub>). The SiO<sub>x</sub>N compliant layer improved the structural quality of InN film.

Using the Fluent software, the flow pattern of NH<sub>3</sub> in the MOVPE reactor was studied, for the three types of inlet tube such as the conventional horizontal, extended horizontal and vertical inlet tube. From the results of this simulation, it was suggested that the vertical inlet tube could increase amount of NH<sub>3</sub> and TMI on the substrate and

therefore, introduce more amount of active nitrogen over the substrate. The results of simulation also indicated that the uniform flow of  $\text{NH}_3$  could be obtained on the substrate with the vertical inlet tube.

Experimentally, using vertical inlet tube the crystalline quality of InN was improved significantly and the growth rate of InN was increased from 0.1 to 0.3  $\mu\text{m/hr}$ . For  $\text{Al}_2\text{O}_3$  (0001), FWHM of XRC of InN was decreased from 4860 to 1339 arcsec. For  $\text{GaN}/\text{Al}_2\text{O}_3$  (0001), FWHM of XRC of InN was decreased from 1039 to 611 arcsec. The characterization of GIXD also showed that the InN film was grown with much smaller tilt along the (0002) direction with the vertical inlet. These studies of the inlet tube modification suggested that the change of the flow pattern can be one of key factor to influence the structural quality of InN.

The effect of post-growth annealing was studied and further improvement in InN film quality was achieved. FWHM of InN was decreased further from 611 to 574 arcsec on  $\text{GaN}/\text{Al}_2\text{O}_3$  (0001) after annealing at  $T=450^\circ\text{C}$  for 30 min in  $\text{N}_2$  environment.

Optical and electrical properties of the InN film on different substrate were studied using Hall measurement and PL. The band-gap energy of InN on Si (111),  $\text{Al}_2\text{O}_3$  (0001), and  $\text{GaN}/\text{Al}_2\text{O}_3$  (0001) was 0.82, 0.84, and 0.94 eV respectively. The mobility of InN on Si (111),  $\text{Al}_2\text{O}_3$  (0001), and  $\text{GaN}/\text{Al}_2\text{O}_3$  (0001) was 623, 35, and 115  $\text{cm}^2/\text{Vs}$  respectively.

The carrier concentration of InN on Si (111),  $\text{Al}_2\text{O}_3$  (0001), and  $\text{GaN}/\text{Al}_2\text{O}_3$  (0001) was  $7.05 \times 10^{18}$ ,  $8.67 \times 10^{19}$ , and  $4 \times 10^{19} \text{ cm}^{-3}$  respectively.

In future work, understanding why the electrical and optical properties of InN films differ with substrate will be studied in detail. These future studies are important to produce the high mobility and low carrier concentrations that are necessary for InN

devices. It is suggested that the use of other substrates be explored and the effect of different growth conditions such as using double buffer layer and pressure are also investigated. The structural quality of InN film has been found to be dependent of the flow pattern and rate. When the vertical inlet tube is studied further, the effect of the position of the outlet and the flow rate are also suggested for the future work.

## LIST OF REFERENCES

- Abe93 C. R. Abernathy, S. J. Pearton, F. Ren, and P. W. Wisk, *J. Vac. Sci. Technol. B* **11**, 179 (1993).
- Abe97 C. R. Abernathy, J. D. MacKenzie, and S. M. Donovan, *J. Cryst. Growth* **178**,74 (1997).
- Ada00 M. Adachi, Y. Murakami, A. Hashimoto, and A. Yamamoto, Proceedings of the International Workshop on Nitride Semiconductors (IWN' 2000), Nagoya, Japan, September 24-27, 2000, IPAP conference series 1, p. 339.
- Ade01 J. Aderhold, V. Yu. Davydov, F. Fedler, H. Klausning, D. Mistele, T. Rotter, O. Semchinova, J. Stemmer, and J. Graul, *J. Cryst. Growth* **222**, 701 (2001).
- Aka93 I. Akasaki, H. Amano, N. Koide, M. Kotaki, and K. Manabe, *Physica B* **185**,428 (1993).
- Aka94 I. Akasaki, and H. Amano, *J. Electrochem. Soc.* **141**, 2266 (1994).
- Amb96 O. Ambacher, M. S. Brandt, R. Dimitrov, T. Metzger, M. Stutzmann, R. A.Fischer, A. Miehr, A. Bergmayer, and G. Dollinger, *J. Vac. Sci. Technol. B* **14**, 3532 (1996).
- Amb98 O. Ambacher, *J. Phys. D* **31**, 2653 (1998).
- And74 A. F. Andreevya and O. J. Eliseevja, *Z. Neorg. Chim.* **13**, 185 (1974).
- Art67 J. R. Arthur, *J. Phys. Chem. Solids* **28**, 2557 (1967).
- Bac97 K. J. Bachmann, C. Hoepfner, N. Sukidi, A. E. Miller, C. Harris, D. E. Aspnes *et al. Appl. Surf. Sci.* **112**, 38 (1997).
- Bea97 B. Beaumont, M. Vaille, T. Boufaden, B. E. Jani, and P. Gibart, *J. Cryst. Growth* **170** 316 (1997).
- Bed97 S. M. Bedair, F. G. McIntosh, J. C. Roberts, E. L. Piner, K. S. Boutros, and N. A.El-Masry, *J. Cryst. Growth* **178**, 32 (1997).
- Bel80 L. M. Belyaev, Rubby and Sapphire, Amerind Publishing Co., New Delhi 1980, p.1.

- Bel99 E. Bellotti, B.K. Doshi, K.F. Brennan, J.D. Albrecht, and P.P. Ruden, *J. Appl.Phys.* **85**, 916 (1999).
- Bel04 E. Bellet-Amalric, C. Adelman, E. Sarigiannidou, J. L. Rouvière, G. Feuillet, E. Monroy, and B. Daudin, *J. Appl. Phys.* **95**, 1127 (2004).
- Bha02 P. Bhattacharya, T. K. Sharna, S. Singh, A. Ingale, and L. M. Kukreja, *J. Cryst. Growth* **236**, 5 (2002).
- Bhu00a A. G. Bhuiyan, A. Hashimoto, A. Yamamoto, and R. Ishigmi, *J. Cryst. Growth* **212**, 379 (2000).
- Bhu00b A. G. Bhuiyan, A. Yamamoto, A. Hashimoto and R. Ishigmi, *Proceedings of the International Workshop on Nitride Semiconductors (IWN' 2000)*. Nagoya, Japan. September 24-27, 2000. IPAP conference series 1, p. 343.
- Bhu01 A. G. Bhuiyan, A. Yamamoto. and A. Hashimoto, *Phys. Status Solidi B* **228**. 27(2001).
- Bhu02a A. G. Bhuiyan, T. Tanaka, A. Yamamoto, and A. Hashimoto, *Phys. StatusSolidi A* **194**, 502 (2002).
- Bhu02b A. G. Bhuiyan, A. Yamamoto, A. Hashimoto, and Y. Ito, *J. Cryst. Growth* **236**.59 (2002).
- Bhu03a A. G. Bhuiyan, T. Tanaka, K. Kasashima, A. Hadhimoto, and A. Yamamoto, *5th International Conference on Nitride Semiconductors (ICNS-5)*, Nara, Japan, May 25-30, 2003.
- Bhu03b A. G. Bhuiyan, A. Hadhimoto, and A. Yamamoto, *J. Appl. Phys.* **94**, 2779 (2003).
- Bot95 A. Botchkarev, A. Salvador, B. Sverdlov, J. Myoung, and H. Morkoc, *J. Appl. Phys.* **77**,4455 (1995).
- Bou94 D. P. Bour, R. S. Geels, D. W. Treat, T. L. Paoli, F. Ponce, R. L. Thornton, B. S. Kunsor, R. D. Bringans, D. F. Welch. *IEEE J Quantum Electron.* QE-**30**, 593(1994).
- Bro98 A. Brown et al., *J. Vac. Sci. Technol. B* **16**, 1300 (1998).
- Bry90 W. A. Bryden, J. S. Morgan, T. J. Kistenmacher, D. Dayan, R. Fainchtein, and T. O. Poehler, *Mater. Res. Soc. Symp. Proc.* **162**, 567 (1990).
- Bry92 T. L. Tansley and R. J. Egan, *Phys. Rev. B* **45**, 10942 (1992).
- Bry92a W. A. Bryden, Y. H. Lee, O. Miki, R. Fainchtein and T. J. Kistenmacher, *Thin Solid Films* **213** (1992) 86.

- Bry94 W. A. Bryden, S. A. Eeelberger, and T. J. Kistenmacher, *Appl. Phys. Lett.* **64**, 2864 (1994).
- Buc88 Buchan, N.I., C.A. Larsen and G.B. Stringfellow, *J. Cryst. Growth*, **92**, 591-604 (1988).
- But02a K. S. A. Butcher, M. Wintrebert-Fouquet, P. P.T. Chen, T. L. Tansley, and S. Srikeaw, *Mater. Res. Soc. Symp. Proc.* **693**, 341 (2002).
- But02b K. S. A. Butcher, H. Dou, E. M. Goldys, T. L. Tansley, and S. Srikeaw, *Phys. Status Solidi C* **0**, 373 (2002).
- Cam90 P.E. van Camp, V. E. van Doren, and J. T. Devreese, *Phys. Rev. B (USA)*. **41**.1598 (1990).
- Che91 C. H. Chen, Z. M. Fang, G. B. Stringfellow, and R. W. Gedridge, *J. Appl. Phys.* **69**, 7605 (1991).
- Che97 W. K. Chen, Y. C. Pan, H. C. Lin, J. Ou, W. H. Chen, and M. C. Lee, *Jpn. J. Appl Phys.*, Part 2 **36**, L1625 (1997).
- Che98 W. K. Chen, H. C. Lin, Y. C. Pan, J. Ou, C. K. Shu, W. H. Chen, and M. C. Lee, *Jpn. J. Appl. Phys.*, Part 1 **37**,4870 (1998).
- Che00 H. Chen, R. M. Feenstra, J. E. Northrup, T. Zywiets, J. Neugebauer, and D. W. Greve, *J. Vac. Sci. Technol. B* **18(4)**, 2284 (2000).
- Chen06 Jeng-Hung Chen, Zhe-Chuan Feng, Hung-Ling Tsai, Jer-Ren Yang, P. Li, C. Wetzel, T. Detchprohm and J. Nelson, *Thin Solid Films, Volume 498, Issues 1-2, 1 March 2006, Pages 123-127*
- Chi94 V. W. Chin, T.L. Tansley, and T. Osotchan, *J. Appl. Phys.* **75**, 7365 (1994).
- Chi96 S. Chichibu, T. Azuhata, T. Sota, and S. Nakamura: *Appl. Phys. Lett.* **69**, 4188 (1996).
- Chi99 J. A. Chisholm, D. W. Lewis, and P. D. Bristowe, *J. Phys. Condens. Matter.* **11**. L235 (1999).
- Cho00a H. K. Cho, J. Y. Lee, K. S. Kim, and G. M. Yang: *Appl. Phys. Lett.* **77**, 247 (2000).
- Cho00b K. L. Choy, *Handbook of nanostructured materials and nanotechnology*, vol.1, synthesis and processing, Academic Press, San Diego, CA, P533 (2000).
- Cho03 K. L. Choy, *Progress in Materials Science* **48**, 57 (2003).
- Cho04 H. K. Cho, J. Y. Lee and J. Y. Leem, *Applied Surface Science, Volume 221, Issues 1-4, 15 January 2004, Pages 288-292*

- Cht97 D. G. Chtchekine, L. P. Fu, G. D. Gilliland, Y. Chen, S. E. Ralph, K. K. Bajaj, Y. Bu, M. C. Lin, F. T. Bacalzo, and S. R. Stock, *J. Appl. Phys.* **81** 2197 (1997).
- CVD93 *CVD metalorganics for vapor phase epitaxy, product guide and literature review*, Morton International, Advanced Materials, Danvers, MA, (1993).
- Dad00 A. Dadgar, J. Blasing, A. Diez, A. Alam, M. Heuken, and A. Krost, *Jpn. J. Appl. Phys. Lett.* **39**, L1183 (2000).
- Dad01a A. Dadgar, J. Christen, T. Riemann, S. Richter, J. Blading, A. Diez, and A. Krost, *Appl. Phys. Lett.* **78**, 2211 (2001).
- Dad01b A. Dadgar A. Alam, T. Riemann, J. Blasing, A. Diez, M. Poschenrieder, M. Stressburg, M. Heuken, J. Christen, and A. Krost, *Phys. Stat. Sol. (a)* **188**, 155 (2001).
- Dad02 A. Dadgar A. M. Poschenrieder, O. Contreras, J. Christen, K. Fense, J. Blasing, A. Diez, F. Schulze, T. Riemann, F. A. Ponce, and A. Krost, *Phys. Stat. Sol. (a)* **192**, 308 (2002).
- Dav97 R. F. Davis, M. J. Paisley, Z. Sitar, D. J. Kester, K. S. Ailey, K. Linthicum, L. B. Rowland, S. Tanaka, and R. S. Kern, *J. Cryst. Growth* **178**, 87 (1997).
- Dav99a V. Y. Davydov, *Appl. Phys. Lett.* **75**, 3297 (1999).
- Dav99b V. Y. Davydov, *Phys. Status Solidi B* **216**, 779 (1999).
- Dav02a V.Y. Davydov, *Phys. Status Solidi B* **229**, R1 (2002).
- Dav02b V.Y. Davydov, *Phys. Status Solidi B* **230**, R4 (2002).
- Dav02c V.Y. Davydov., *Phys. Status Solidi B* **234**, 787 (2002).
- Duc78 Duchemin JP, Bonnet M, Koelsch F, Huyghe D. *J Cryst Growth* **45**. 181 (1978).
- Dup95 Dupuis RD. In: Glocker DA, Shah SI, editors. *Handbook of thin film process technology*, B1.1:1. Institute of Physics, Bristol,UK, (1995).
- Dyc98 J. S. Dyck, K. Kash, K. Kim, W. R. L. Lambrecht, C. C. Hayman, A. Argoitia, M. T. Grossner, W. L. Zhou, and J. C. Angus, *Mater. Res. Soc. Symp. Proc.* **482**, 549 (1998).
- Edg94 J. H. Edgar, *Properties of Group III Nitrides*, INSPC, the Institution of Electrical Engineers, London, UK (1994).
- Ega00 T. Egawa, H. Ishikawa, T. Jimbo, M. Unemo. *Bull Mater Sci.* **22**, 363 (2000).

- Ega02 T. Egawa, B. Zhang, N. Nishikawa, H. Ishikawa, T. Jimbo, and M. Umeno, *J. Appl. Phys.* **91** 528 (2002).
- Elm98 N. A. El-Mastry, E. L. Piner, S. X. Liu, and S. M. Bedair, *Appl. Phys. Lett.* **72**, 40 (1998).
- Erb92 A. Erbil, W. Braun, B. S. Zwak, B. J. Wilkens, L. A. Boatner, J. D. Budai. *J. Cryst Growth.* **24**, 84 (1992).
- Etc01 Etching Bulk GaAs wafer for use as cathodes,  
[www.jlab.org/accel/inj\\_group/docs/etch.htm](http://www.jlab.org/accel/inj_group/docs/etch.htm), June 2, 2005.
- Far00 Q. Fareed, J. Yang, J. Zhang, V. Adivarahan, and M. A. Khan, *Proceedings of the International Workshop on Nitride Semiconductors (IWN' 2000)*, Nagoya, Japan, September 24-27, 2000, IPAP conference series 1, p. 237.
- Fei97 D. Feiler, R. S. Williams, A. A. Talin, H. Yoon, and M. S. Goorsky, *J. Cryst. Growth* **171**, 12 (1997).
- Fol85 C.P. Foley and T. L. Tansley, *Appl. Surf. Sci.* **22/23**, 663 (1985).
- Fol86 C.P. Foley and T. L. Tansley, *Phys. Rev. B* **33**, 1430 (1986).
- Fol87 C.P. Foley and J. Lyngdal, *J. Vac. Sci. Technol. A* **5**, 1708 (1987).
- Fou99 B.E. Foutz, S.K. O'Leary, M.S. Shur, and L.F. Eastman, *J. Appl. Phys.* **85**, 7727 (1999).
- Gas86 D. K. Gaskill, N. Bottka, and M. C. Lin, *J. Cryst. Growth* **77**, 418 (1986).
- Geo99 A. George, in : Robert Hull (Ed.), *Properties of Crystalline Silicon*, IEEE, London, 1999, p98.
- Gha88 S. K. Ghandhi, I. B. Bhat. *MRS Bulletin*, 11, 37 (1988).
- Gra96 N. Grandjean, J. Massies, and M. Leroux, *Appl. Phys. Lett.* **69**, 2071 (1996).
- Gru91 M. Grundmann, A. Krost, and D. Bimberg, *Appl. Phys. Lett.* **58**, 284 (1991).
- Guo92 Q. Guo, O. Kato, and A. Yoshida, *J. Electrochem. Soc.* **139**, 2008 (1992).
- Guo93 Q. Guo, O. Kato, and A. Yoshida, *J. Appl. Phys.* **73**, 7969 (1993).
- Guo94a Q. Guo and A. Yoshida, *Jpn. J. Appl Phys.*, Part 1 **33**, 90 (1994).
- Guo94b Q. Guo and A. Yoshida, *Jpn. J. Appl Phys.*, Part 1 **33**, 2453 (1994).
- Guo94c Q., Guo, T. Yamamura, A. Yoshida, and N. Itoh, *J. Appl. Phys.* **75**, 4927 (1994).

- Guo95a Q. Guo, H. Ogawa, and A. Yoshida, *J. Cryst. Growth* **146**, 462 (1995).
- Guo95b Q. Guo, H. Ogawa, H. Yamano, and A. Yoshida, *Appl. Phys. Lett.* **66**, 715 (1995).
- Guo98a Q. X. Guo, M. Nishio, H. Ogawa, A. Wakahara, and A. Yoshida, *Phys. Rev. B* **58**, 15304 (1998).
- Guo98b Q. X. Guo, N. Shingai, M. Nishio, and H. Ogawa, *J. Cryst. Growth* **189/190**, 466 (1998).
- Guo99 Q. X. Guo, M. Nishio, H. Ogawa, and A. Yoshida, *Jpn. J. Appl. Phys.*, Part 238, L490 (1999).
- Guo00 Q. Guo, M. Matsuse, M. Nishio, and H. Ogawa, *Jpn. J. Appl. Phys.*, Part 1 **39**, 5048 (2000).
- Guo02 Q. X. Guo, A. Okade, H. Kidera, T. Tanaka, M. Nishio, and H. Ogawa, *J. Cryst. Growth* **237-239**, 1032 (2002).
- Gup98 J. A. Gupta, J. C. Woicik, S. P. Watkins, K. E. Miyano, J. G. Pellegrino, E. D. Crozier, *J. Cryst. Growth* **34**, 195 (1998).
- Hah40 H. Hahn, R. Juza, *Z. Anorg. Allg. Chem. (Germany)*. **244**. 111 (1940).
- Har98 P. Hartmann, R. Haubner, B. Lux. *Int. J. Refract. Met. Hard. Mater.* **16**, 207 (1998).
- Hel98 E. S. Hellman, *MRS Intemet J. Nitride Semicond. Res.* **3**, 11 (1998).
- Her99 M. A. Herman, J. T. Sadowski. *Crystal Res. Technol.* **34**, 153 (1999).
- Hig02 M. Higashiwaki and T. Matsui, *Jpn. J. Appl. Phys.*, Part 2 **41**, L540 (2002).
- Hir90 B. Hirsch, *Proceedings of the 2<sup>nd</sup> International Conference on Polycrystalline Semiconductors*, 470 (1990).
- Hir94 Y. S. Hiraoka and M. Mashita, *J. Cryst. Growth* **136**, 94 (1994).
- Hit93 M. L. Hitchman, Jensen KF, editors. *CVD principles and applications*, Academic Press San Diego (1993).
- Ho96 I. Ho and G. B. Stringfellow, *Appl. Phys. Lett.* **69**, 2701 (1996).
- Hoc89 M. G. Hocking , V. Vasantasree, P. S. Sidky. *Metallic and ceramic coatings: production, high temperature properties and applications*, John Wiley & Sons, New York (1989).
- Hok91 W. E. Hoke, P. J. Lemonias and D. G. Weir, *J. Cryst. Growth* **111**, 1024 (1991).

- Hol80 N. Holonyak, R. M. Kolbas, R. D. Dupuis, P. D. Dapkus. *IEEE J Quant Electron.* **QE-16**, 170 (1980).
- Hor02 M. Hori, K. Kano, T. Yamaguchi, Y. Saito, T. Araki, Y. Nanishi, N. Teraguchi, and A. Suzuki, *Phys. Status. Solidi B* **234**, 750 (2002).
- Hov72 H. J. Hovel and J. J. Cuomo, *Appl. Phys. Lett.* **20**, 71 1972. 31 J. W. Trainor and K. Rose, *J. Electron. Mater.* 3,821 (1974).
- Hsu98 C. T. Hsu., *Thin Solid Films* 335, 284 (1998).
- Hug95 W. C. Hughes, W. H. Rowland, Jr., M. A. L. Johnson, S. Fujita, J. w. Cook, Jr., J. F. Schetzina, J. Ren, and J. A. Edmond, *J. Vac. Sci. Technol. B* **13**, 1571 (1995).
- Hwa01 J. S. Hwang, C. H. Lee, F. H. Yang, K. H. Chen, L. G. Hwa, Y. J. Yang, and L. C. Chen, *Mat. Chem. and Phys.* **72**, 290 (2001).
- Hwa04 J.Y. Hwang Dissertation (2004).
- Ich86 M. Ichimura and A. Sasaki, *J. Appl. Phys.* **60**, 3850 (1986).
- Iga92 O. Igarashi, *Jpn. J. Appl. Phys.*, Part 1 **31**, 2665 (1992).
- Ina01 Y. Inaba, T. Onozu, S. Takami, M. Kubo, A. Miyamoto, and A. Imamura, *Jpn. J. Appl. Phys.* **140**, 2991 (2001).
- Inu99 T. Inushima, T. Shiraishi, V. Y. Davydov, *Solid State Commun.* **110**, 491 (1999).
- Inu01 T. Inushima, V. V. Mamutin, V. A. Vekshin, S. V. Ivanov, T. Sakon, M. Motokawa, and S. Ohoya, *J. Cryst. Growth* **227-228**, 481 (2001).
- Ish97a T. Ishi, Y. Tazoh, and S. Miyazawa, *Mater. Res. Soc. Symp. Proc.* **468**, 155 (1997).
- Ish97b M. Ishii, S. Iwai, H. Kawata, T. Ueki, Y. Aoyagi, *J. Cryst. Growth* **180**, 15 (1997).
- Ish98 H. Ishikawa, K. Yamamoto, T. Egawa, T. Soga, T. Jimbo, and M. Umeno: *J. Crystal Growth* **189/190**, 178 (1998).
- Isl95 M. R. Islam, R. V. Chelakara, J. G. Neff, K. G. Fertitta, P. A. Grudowski, A. L. Holmes, *J Electron Mater* **24**, 181 (1995).
- Ito97 T. Ito, *Jpn. J. Appl. Phys.* **36**, L1065 (1997).
- Iwa95 K. Iwata, H. Asahi, S. J. Yu, K. Asami, H. Fujita, M. Fushida, and S. Gonda, *Jpn. J. Appl. Phys.*, Part 2 **35**, L289 (1996).

- Jac64 M. G. Jacko and S. J. W. Price, *Can. J. Chem.* **42**, 1198 (1964).
- Jan00 S.C. Jain, M. Willander, J. Narayanan and R.V. Overstrachten, *J. Appl. Phys.* **87**, 965 (2000).
- Jen89 D. W. Jenkins and J. D. Dow, *Phys. Rev. B* **39**, 3317 (1989).
- Jes67 W. A. Jesser and D. Kuhlmann-Wilsdorf, *Phys. Stat. Sol.* **19**, 95 (1967).
- Jin06 J.R. Jinschek and C. Kisielowski, *Physica B: Condensed Matter, Volumes 376-377, 1 April 2006, Pages 536-539*
- Joh94 A. C. Jones, J. Alud, S. A. Rushworth, G. W. Critchow. *J Cryst Growth* **135**, 285(1994).
- Juz38 R. Juza and H. Jahn, *Z. Anorg. Allg. Chem.* **239**, 282 (1938).
- Juz56 R. Juza and A. Rabenau, *Z. Anorg. Allg. Chem.* **285**, 212 (1938).
- Kac00 G. Kaczmarczyk, A. Kaschner, S. Reich, A. Hoffman, C. Thomsen., *Appl. Phys. Lett.* **76**, 2122 (2000).
- Kan04. Sangwon Kang Dissertation 2004, University of Florida.
- Kap97 S. Kapov: *MRS Internet J. Nitride Semicond. Res.* **3**, 16 (1997).
- Kea66 P. N. Keating: *Phys. Rev.* **145** (1966) 637; R. M. Martin: *Phys Rev.* **1B**, 4005 (1970).
- Kel98 S. Keller, U. K. Misura, S. P. Denbaars, and W. Seifert: *Jpn. J. Appl. Phys.* **37**, L431 (1998).
- Kel00 S. Keller, I. Ben-yaacov, S. P. Denvers, and U. K. Mishra, *Proceedings of the International Workshop on Nitride Semiconductors (IWN' 2000)*, Nagoya, Japan, September 24-27, 2000, IPAP conference series 1, p. 233.
- Kam97 M. Kamp, M. Mayer, A. Pelzmann, and K. J. Ebeling, *Mater. Res. Soc. Symp. Proc.* **449**, 161 (1997).
- Kan05 S. W. Kang, H. J. Park, T. W. Kim, T. Dann, O. Kryliouk, T. Anderson, *Phys. stat. sol. (c)* **2**, 2420 (2005).
- Kim96a K. Kim, W. R. L. Lambrecht and B. Segall, *Phys. Rev. B* **53**, 16310 (1996).
- Kim96b W. Kim, A. Salvador, A. E. Botchkarev, O. Aktas, S. N. Mohammad, and H. Morkoc, *Appl. Phys. Lett.* **69**, 559 (1996).

- Kis90a T. J. Kistenmacher, D. Dayan, R. Fainchtein, W. A. Bryden, J. S. Morgan, and T. O. Poehler, *Mater. Res. Soc. Symp. Proc.* **162**, 573 (1990).
- Kis90b T. J. Kistenmacher, W. A. Bryden, J. S. Morgan, and T. O. Poehler, *J. Appl. Phys.* **68**, 1541 (1990).
- Kis91 T. J. Kistenmacher and W. A. Bryden, *Appl. Phys. Lett.* **59**, 1844 (1991).
- Kis92 T. J. Kistenmacher, S. A. Ecelberger, and W. A. Bryden, *Mater. Res. Soc. Symp. Proc.* **242**, 441 (1992).
- Kis93a T. J. Kistenmacher and W. A. Bryden, *Appl. Phys. Lett.* **62**, 1221 (1993).
- Kis93b T. J. Kistenmacher, S. A. Ecelberger, and W. A. Bryden, *J. Appl. Phys.* **74**, 1684 (1993).
- Kou96 A. Koukitu, N. Takahashi, T. Taki, and H. Seki, *Jpn. J. Appl. Phys., Part 2* **35**, L673 (1996).
- Kou97a A. Koukitu and H. Seki, *Jpn. J. Appl. Phys., Part 2* **36**, L750 (1997).
- Kou97b A. Koukitu, N. Takahashi, and H. Scki, *Jpn. J. Appl. Phys., Part 2* **36**, L1136 (1997).
- Kou97c A. Koukitu, T. Taki, *Appl. Surf. Sci.* **112**, 63 (1997).
- Kou99a A. Koukitu, T. Taki, N. Takahashi, and H. Seki, *J. Cryst. Growth* **197**, 99 (1999).
- Kou99b A. Koukitu, y: Kumagai, N. Kubota, and H. Scki, *Phys. Status Solidi B* **216**, 707 (1999).
- Kwo96 H. J. Kwon, Y.H. Lee, O. Miki, H. Yamano, and A. Yoshida, *Appl. Phys. Lett.* **69**, 937 (1996).
- Kub89 K. Kubota, Y. Kobayashi, and K. Fujimoto, *J. Appl. Phys.* **66**, 2984 (1989).
- Kum94 N. D. Kumar, M. N. Kamalasanan, S. Chandra, *Appl. Phys. Lett.* **65**, 1373 (1994).
- Kun96 P. Kung, A. Saxler, X. Zhang, D. Walker, R. Lavado, and M. Razcghi, *Appl. Phys. Lett.* **69**, 2116 (1996).
- Kur94 K. Kurishima, H. Nakajima, S. Yamahata, T. Kobayashi, Y. Matsuoka, *Appl. Phys. Lett.* **64**, 1111 (1994).
- Kur01 E. Kurimoto, H. Harima, A. Hashimoto, and A. Yamamoto, *Phys. Status Solidi B* **228**, 1 (2001).

- Lah00 H. Lahreche, V. Bousquet, M. Lahgt, P. Venegues, B. Beaumont, and P. Gibert, *Proc. Int. Conf. Sic & Relat. Mater.* **99**, North Carolina, 273 (2000).
- Lar86 C. A. Larsen, G. B. Stringfellow, *J. Cryst. Growth* **75**, 247 (1986).
- Lau98 J. E. Lau, K. W. Barth, G. G. Peterson, D. Endisch, A. Topol, A. E. Kaloyeros, *J. Electrochem. Soc.* **145**, 4271 (1998).
- Lee85 W. E. Lee, K. P. D. Lagerlof, *J. Electron. Microsc. Technol.* **2**, 247 (1985).
- Lee91 R. R. Lee, *J. Am. Cerem. Soc.* **74 (9)**, 2242 (1991).
- Lee95 N. E. Lee, R. C. Powell, Y. W. Kim, and J. E. Greene, *J. Vac. Sci. Technol. A* **13**, 2293 (1995).
- Lee02a I. J. Lee, J. W. Kim, T.B. Hur, Y.H. Hwang, and H.K. Kim, *Appl. Phys. Lett.* **81**, 475 (2002).
- Lee02b I. J. Lee, J. W. Kim, Y.H. Hwang, and H.K. Kim, *J. Appl. Phys.* **92**, 5814 (2002).
- Les95 S.D. Lester, F. A. Ponce, M. G. Craford, and D.A. Steigerwald, *Appl. Phys. Lett.* **67**, 1249 (1995).
- Li94 X. Li, B. Zhou, K. S. A. Butcher, E. Florido, N. Syakir, and T. L. Tansley, *Proceedings of the Australian Compound Optoelectronic Materials Devices Conference*, Sydney, Australia, December 12-14, 1994, p. 43.
- Lil06 Z. Liliental-Weber, D.N. Zakharov, K.M. Yu, J.W. Ager III, W. Walukiewicz, E.E. Haller, H. Lu and W.J. Schaff, *Physica B: Condensed Matter, Volumes 376-377, 1 April 2006, Pages 468-472*
- Lim99 A. P. Lirna, A. Tabata, J. R. Lcitic, S. Kaiser, D. Schikora, B. Schottker, T. Frey, D. J. As, and K. Lischka, *J. Cryst. Growth* **201/202**, 396 (1999).
- Liu02 L. Liu and J. H. Edgar, *Mat. Sci. and Eng.*, **R37**, 61 (2002).
- Liu02a C. H. Liu, R. W. Chuang, S. J. Chang, Y. K. Su, C. H. Kuo, J. M. Tsai and C. C. Lin, *Materials Science and Engineering B, Volume 111, Issues 2-3, 25 August 2004, Pages 214-217*
- Loo02 D. C. Look, H. Lu, W. J. Schaff, J. Jasinski, and Z. Liliental-Weber, *Appl. Phys. Lett.* **80**, 258 (2002).
- Lu97 H. Lu, M. Thothathiri, Z. Wu, and I. Bhat: *J. Electron. Mater.* **26**, 281 (1997).
- Lu00 H. Lu, W. J. Schaff, J. Hwang, H. Wu, W. Yeo, A. Pharkya, and L. Eastman, *Appl. Phys. Lett.* **77**, 2548 (2000).

- Lu01a H. Lu, W. J. Schaff, J. Hwang, H. Wu, G. Koley, and L. Eastman, *Appl. Phys. Lett.* **79**,1489 (2001).
- Lu01b H. Lu, W. J. Schaff, J. Hwang, and L. F. Eastman, *Mater. Res. Soc. Symp. Proc.* **680E**, E3.2 (200).
- Lu02a H. Lu, W. J. Schaff, L. F. Eastman, J. Wu, W. Walukiewicz, K. M. Yu, J. W. Auger III, E. E. Haller, and O. Ambacher, *Abstract of the 44th Electronic Material Conference*, Santa Barbara, CA, June 26-28, 2002.
- Lu02b H. Lu, W. J. Schaff, L. F. Eastman, and C. Wood, *Mater. Res. Soc. Symp. Proc.* **693**, 9 (2002).
- Mam99a V. V. Mamutin, T. Renner, R. R. Parrsons. *Phys. Status Solidi A* **176**,247 (1999).
- Mam99b V. V. Mamutin, V. A. Vekshin, V. Y. Davydov, V. V. Ratnikov, Y. A. Kudriavtsev, B. Y. Ber, V. v: Emtsev, and S. V. Ivanov, *Phys. Status Solidi A***176**, 373 (1999).
- Man75 H. M. Manasevit, W. I. Simpson, *J. Electrochem. Soc.* **122**, 144 (1975).
- Mar77 L. A. Marasina, I. G. Pichugin, and M. Tlaczala, *Krist. Tech.* **12**, 541 (1977).
- Mar98 A. A. Marmalyuk, R. K. Akchurin, and V. A. Gorbylev, *Inorg. Mater. (Transl. of Neorg. Mater.)*. **34**. 691 (1998).
- Mar99 P. Martensson, M. Juppo, M. Ritala, M. Leskela, J. O. Carlsson, *J. Vac. Sci. Technol. B*, **17**, 2122 (1999).
- Mar03 I. V. Markov, *Crystal Growth for Beginners*, World Scientific, 360 (2003).
- Mas01 Mike Mastro “GROWTH AND CHARACTERIZATION OF THIN AND THICK GALLIUM NITRIDE” University of Florida, Gainesville, Florida, 2001.
- Mat75 J. W. Matthews, *J. Vac. Sci. Technol.* **12**, 126(1975).
- Mat89 T. Matsuoka, H. Tanaka, T. Sasaki, and A. Katsui, *Inst. Phys. Conf. Ser.* **106**, 141(1989).
- Mat90 T. Matsuoka, H. Tanaka, T. Sasaki, and A. Katsui, *Proceedings of the Sixteenth International Symposium on GaAs and Related Compounds*, Karuizawa, Japan, September 25-29,1989 (Institute of Physics, Bristol, 1990), p. 141.
- Mat92 T. Matsuoka, N Yoshimoto, T. Sasaki, and A. Katsui, *J. Electron. Mater.* **21**, 157 (1992).

- Mat97 T. Matsuoka, in *GaN and Related Materials*, edited by S. J. Pearton (Gordon and Breach, New York, 1997), pp. 53-59.
- Mat02 T. Matsuoka, H. Okamoto, M. Nakao, H. Harima, and E. Kurimoto, *Appl. Phys. Lett.* **81**, 1246 (2002).
- May90 James W. Mayer, *Electronic Materials Science for Intergrated Circuits in Si and GaAs*, Macmillan Publishing Company, New York (1990).
- McC70 J. B. McChesney, P. M. Bridenbaugh, and P. B. O'Connor, *Mater. Res. Bull.* **5**, 783 (1970).
- Mil96 J. R. Mileham, S. J. Pearton, C. R. Abernathy, J. D. Mackenzie, R. J. Shul, and S. P. Kilcoyne, *J. Vac. Sci. Technol. A* **14**, 836 (1996).
- Miy02 T. Miyajima, Y. Kudo, K. L. Liu, T. Honma, Y. Sato., *Phys. Status Solidi B* **234**, 801 (2002).
- Moh96 S. N. Mohammad and H. Morkoc, *Prog. Quantum Electron.* **20**, 361 (1996).
- Mol02 Motlan, E. M. Goldys, and T. L. Tansley, *J. Cryst. Growth* **241**, 165 (2002).
- Mol94 R. J. Molnar and T. D. Moustakas, *J. Appl. Phys.* **76**, 4587 (1994).
- Mor90 J. S. Morgan, T. J. Kistenmaeher, W. A. Bryden, and T. O. Pochler, *Mater. Res. Soc. Symp. Proc.* **162**, 579 (1990).
- Mor91 J. S. Morgan, T. J. Kistenmacher, W. A. Bryden, and S. A. Ecelberger, *Mater. Res. Soc. Symp. Proc.* **202**, 383 (1991).
- Mor94 H. Morkoc, S. Strite, G. B. Gao, M.E. Lin, B. Sverlov, and M. Burns, *J. Appl. Phys.* **76**, 1363 (1994).
- Mot94 T. Motoda, M. Kato, K. Kadoiwa, A. Shima, M. Tsugami, T. Sonoda, *et al. J. Cryst Growth* **145**, 650 (1994).
- Nag89 T. Nagatomo, T. Kuboyama, H. Minamino, and O. Omoto: *Jpn. J. Appl. Phys. Lett.* **28**, L1334 (1989).
- Nag02 B.R. Nag, *Phys. Status Solidi B* **233**, R8-R9 (2002).
- Nak91 S. Nakamura, Y. Harada, and M. Seno, *Appl. Phys. Lett.* **58**, 2021 (1991).
- Nak92 Shuji Nakamura and Takashi Mukai, *Jpn. J. Appl. Phys.* **31**, L1457 (1992).
- Nak93 S. Nakamura, M. Senoh, and T. Mukai, S. Nagahama, and N. Iwasa, *J. Appl. Phys.*, **74**. 3911 (1993).
- Nak94 S. Nakamura, *Microelectron. J.* **25**. 651 (1994).

- Nak96 S. Nakamura, M. Senoh, S. Nagahama, N. Iwasa, T. Yamada, T. Matsushita, H. Kiyoku, and Y. Sugimoto, *Jpn. J. Appl. Phys., Part 2* **35**, L74 (1996).
- Nak00 Shuji Nakamura: *IEICE Trans. Electronics*. **E83-C** 529 (2000).
- Nat80 B.R.Natarajan, A.H. Eltoukhy, J.E. Greene, T.L. Barr, *Thin Solid Films* **69**, 201 (1980).
- Nat86 B.R. Natarajan, A. H. Eltoukhy, J. E. Greenc, and T. L. Barr, *Thin Solid Films* **69**, 201 (1980).
- Ng02 Y. F. Ng, Y. G. Cao, M. H. Xie, X. L. Wang, and S. Y. Tong, *Appl. Phys. Lett.* **81**, 3960 (2002).
- Nic96 J. H. M. Nicholls, H. Gallagher, B. Henderson, C. Trager, Cowan. P. G. Middleton, K. P. O'Donnel. T. S. Cheng, C. T. Foxon, and B. H. T. Chai, *Mater. Res. Soc. Symp. Proc.* **395**, 535 (1996).
- Nii96 L. Niinisto, M. Ritala, M. Leskela, *Mat. Sci. Enging. B. Solid-State Mat. Adv. Technol.* **41**, 23 (1996).
- Nil99. S. A. Nilishin, N. N. Faleev, V. G. Antopov, S. Francoeur and L. Grave de Peralta, *Appl. Phys. Lett.* **75**, 736 (1999).
- Nis97 K. Nishida, S. Haneda, K. Hara, H. Munekata, and H. Kukimoto, *J. Cryst. Growth* **170**, 312 (1997).
- Nör02a C. Nörenberg, M.G. Martin, R. A. oliver, M. R. Castell, and G. A. D. Briggs, *J. Phys. D* **35**, 615 (2002).
- Nör02b C. Norenberg, R. A. Oliver, M. G. Martin, L. Allers, M. R. Castell, and G.A.D. Briggs, *Phys. Status Solidi A* **194**, 536 (2002).
- Ohk98 M. Ohkubo, T. Ijichi, K. Iketani, T. Kikuta. *IEEE J Quantum Electron.* **30**, 408 (1998).
- Ohk00 M. Ohkubo and O. Takai, *Proceedings of the International Workshop on Nitride Semiconductors (IWN' 2000)*, Nagoya, Japan, September 24-27, 2000, IPAP conference series 1, p. 770.
- Oku91 H. Okumura, S. Yoshida, and E. Sakuma, *J. Cryst. Growth* **120**, 114 (1991).
- Oku98a H. Okumara, H. Hamaguchi, T. Koizumi, K. Balakrihnan, Y. Ishida, M. Arita, S. Chichubu, H. Nakanishi, T. Nagamoto, and S. Yoshida, *J. Cryst. Growth* **189/190**, 390 (1998).
- Oku98b S. Okubo, N. Shibata, T. Saito, and Y. Ikuhara, *J. Cryst. Growth* **189/190**, 452 (1998).

- Ono99 T. Onozu, I. Gunji, R. Miura, S. S. C. Ammal, M. Kubo, K. Teraishi, A. Miyamoto, Y. Iyechika, and T. Maeda, *Jpn. J. Appl. Phys.*, Part 1 **38**, 2544 (1999).
- Osa72 K. Osamura, K. Nakajima, Y. Murakami, H. P. Shingu, and A. Ohtsuki, *Solid State Commun.* **11**, 617 (1972).
- Osa75 K. Osamura, S. Naka, and Y. Murakami, *J. Appl. Phys.* **46**, 3432 (1975).
- Qia02 Z. G. Qian, W. Z. Shen, H. Ogawa, and Q. X. Guo, *J. Appl. Phys.* **92**, 3683 (2002).
- Qian02b Z. G. Qian, W. Z. Shen, H. Ogawa, and Q. X. Guo, *Physica B.* **318**, 180 (2002).
- Qin02 Z. Qin, Z. Chen, Y. Tong, S. Lu, and G. Zang, *Appl. Phys. A* **74** 655 (2002).
- Ou98 J. Ou, W. Chen, H. Lin, Y. Pan, and M. Lee: *Jpn. J. Appl. Phys.* **37**, L633 (1998).
- Pan96 J. S. Pan, A. T. S. Wee, C. H. A. Hual, H. S. Tan, and K. L. Tan, *J. Phys. D* **29**, 2997 (1996).
- Pan98 J. I. Pankove, *Gallium Nitride (GaN) I*, Academic Press (1998).
- Pan99 Y. C. Pan, W. H. Lee, C. K. Shu, H. C. Lin, C. I. Chjang, H. Chang, D. S. Lin, M. C. Lee, and W. K. Chen, *Jpn. J. Appl. Phys.*, Part 1 **38**, 645 (1999).
- Par02 Park, C., W.-S. Jung, Z. Huang and T.J. Anderson, *J. Mater. Chem.*, 12, 356 (2002).
- Pas63 J. Pastrnak and L. Souckova, *Phys. Status Solidi* **3**, K71 (1963).
- Pea67 W. B. Pearson, *A Handbook of Lattice Spacing and Structures of Metals and Alloys*, Pergamon Press, Oxford (1967) .
- Pin98 E. L. Piner, N. A. El-Mastry, S. X. Liu, and S. M. Bedair, *Materials Research Society Proceedings*, Vol. **482** (1998), *Appl. Phys. Lett.* **72**, 40 (1998).
- Pos02 M. Poschenrieder, F. Schulze, J. Blasing, A. Dadgar, A. Diez, J. Christen, and A. Krost, *Appl. Phys. Lett.* **81**, 1591 (2002).
- Pow93 R. C. Powell, N. E. Lee, Y. W. Kim, and J. E. Greene, *J. Appl. Phys.* **73**, 189 (1993).
- Put86 N. Putz, H. Heinecke, M. Heyen, P. Balk, M. Wayers, H. Luth., *J. Crystal Growth* **74**, 292 (1986).
- Puy76 N. Puychevricr and M. Mcnoret, *Thin Solid Films* **36**, 141 (1976).

- Qia02 Z.G. Qian, W. Z. Shen, H. Ogawa, and Q.X. Guo, *J. Appl. Phys.* **92.**, 3683 (2002).
- Pea93 S. J. Pcarton, C. R. Abemathy, F. Ren, J. R. Lothian, P. W. Wisk, and A. Katz, *J. Vac. Sci. Technol. A* **11**, 1772 (1993).
- Rai98 Raina N. Smith, Virginia Commonwealth University, May 5 (1998)  
[http://www. Geocities.com/Capecanaverl/5702/Fe\\_Si.html](http://www.Geocities.com/Capecanaverl/5702/Fe_Si.html).
- Ree02 Mike Reed Dissertation 2002, University of Florida.
- Ren58 T. Renner, *Z. Anorg. Allg. Chem.* **298**, 28 (1958).
- Rom05 Electronic Materials, <http://electronicmaterials.rohmhaas.com/>, June 2, 2005.
- Ros97 S. J. Rosner, E. C. Carr, M. J. Ludowise, G. Girolami, and H. I. Erikson, *Appl. Phys. Lett.* **70**, 420 (1997).
- Rus96 S. A. Rushworth, J. R. Brown, D. J. Houlton, A. C. Jones, J. S. Roberts, and G. W. Critchlow, *Advanced Materials for Optics and Electronics* **6**, 119 (1996).
- Sai01 Y. Saito, Y. Tanabe, T. Yamaguchi, N. Teraguchi, A. Suzuki, T. Araki, and J Y. Nanishi, *Phys. Status Solidi B* **228**, 13 (2001).
- Sai02a Y. Saito, H. Harima, E. Kurimoto, T. Yamaguchi, N. Teraguchi. A. Suzuki, T. Araki, and Y. Nanishi, *Phys. Status Solidi B* **234**, 796 (2002).
- Sai02b Y. Saito, T. Yamaguchi, H. Kanazawa, K. Kano, T. Araki, Y. Nanishi, A. Suzuki, and N. Teraguchi, *J. Cryst. Growth* **237-239**, 1017 (2002).
- Sam69 G.V. Samsonov. *Nitridy Kiev*, 1969.
- San92 C. Sant, P. Gibart, P. Genou, C. Verie, *J Cryst Growth* 124, 690 (1992).
- Sat89 Y. Sato and S. Sato, *Jpn. J. Appl. Phys. Part* **228**, L1641 (1989).
- Sat94a Y. Sato and S. Sato, *J. Cryst. Growth* **144**, 15 (1994).
- Sat94b Y. Sato, S. Kakinuma, and S. Sato, *Jpn. J. Appl. Phys.*, Part 1 **33**, 4377 (1994).
- Sat95 Y. Sato and S. Sato, *J. Cryst. Growth* **146**, 262 (1995).
- Sat96 H. Sato, H. Takahashi, A. Watanabe, and H. Ota, *Appl. Phys. Lett.* **68**, 3617 (1996).
- Sat97a M, Sato, *Jpn. J. Appl. Phys.*, Part 2 **36**, L595 (1997).
- Sat97b M. Sato, *Jpn. J. Appl. Phys.*, Part 2 **36**, L658 (1997).

- Sat98 H. Sato, T. Sugahara, Y. Naoi, and S. Sakai: *Jpn. J. Appl. Phys.* **37**, 2013 (1998).
- Sch91 M.C. Schabel and J. L. Martins: *Phys. Rev. B* **43**, 11873 (1991).
- Sch00 W. J. Schaff, H. Lu, J. Hwang, and H. Wu, *Proceedings of the Seventeenth Biennial IEEE/Cornell Conference on Advanced Concepts in High Performance Devices*, August 7-9, 2000, p. 225.
- See97 M. Seelmann-Eggebert, J. L. Weher, H. Obloh, H. Zimmermann, A. Rar, and S. Porowski, *Appl. Phys. Lett.* **71**, 2635 (1997).
- She79 A. U. Sheleg and V. A. Savastenko, *Inorg. Mater. Transl. of Neorg. Mater.* **15**, 1257 (1979).
- She91 M. E. Sherwin, and T. J. Drummond, *J. Appl. Phys.* **69**, 8423 (1991).
- She02 Jianyun Shen, Steven Johnston, Shunli Shang, Timothy Anderson, *J. Cryst. Growth* **240**, 6 (2002).
- Shi94 M. Shimizu, K. Hiramatsu, and N. Sawaki, *J. Crystal Growth*, **145**, 209 (1994).
- Shu98 R. J. Shul, C. G. Willison, M. M. Bridges, J. Han, J. W. Lec, S. J. Pearton, C. R. Abemathy, J. D. Mackenzie, and S. M. Donovan, *Solid-State Electron.* **42**, 2269 (1998).
- Shu00 Shuji Nakamura: *IEICE Trans. Electrons.* **E83-C**, 529 (2000).
- Sin97 R. Singh, D. Doppalapudi, T. D. Moustakas, L. T. Romano, *Appl. Phys. Lett.* **70**, 1089 (1997).
- Sla98 G. A. Slack, *Mater. Res. Soc. Symp. Proc.* **512**, 35 (1998).
- Smi98 Raina N. Smith, Virginia Commonwealth University, May 5, 1998  
[http://www.geocities.com/CapeCanaveral/5702/Fe\\_Si.html](http://www.geocities.com/CapeCanaveral/5702/Fe_Si.html).
- Sta92 R. A. Stall, E. Wolak, P. Zawadski. *Mat Res Soc Symp Proc.* **282**, 115 (1992).
- Sta00 C. Stampfl, C. G. Van de Walle, D. Vogel, P. Kruger, and J. Pollmann, *Phys. Rev. B* **61**, R7846 (2000).
- Str92 S. Strite and H. Morkoc, *J. Vac. Sci. Technol. B* **10**, 1237 (1992).
- Str93 S. Strite, D. Chandrasekhar, D. J. Smith, J. Sariel, H. Chen, N. Teraguchi, and H. Morkoc, *J. Cryst. Growth* **127**, 204 (1993).
- Str97 W. Van der Stricht, I. Moerman, P. Demeester, L. Considine, E. J. Thrush, and J.A. Crawley, *MRS Internet J. Ntride Semicond. Res.* **2**, 16 (1997).

- Str98 A. Strittmatter, A. Krost, K. Schatke, D. Bimberg, J. Blasing, and J. Christen, *Proceedings of the Seventh International Conference on SiC, III-Nitrides and Related Material, Trans Tech Publ., Part 2*, 1145 (1998).
- Str99 G. B. Stringfellow, *Organometallic Vapor-Phase Epitaxy*, Academic Press, New York (1999).
- Sug91 T. Sugimoto, M. Yoshida, K. Yamaguchi, Y. Yamada, K. Sugawara, Y. Shirohara, *J Crystal Growth* **107**, 692 (1991).
- Sul88 B. T. Sullivan, R. R. Parsons, K. L. Westra, and M. J. Brett, *J. Appl. Phys.* **64**, 4144 (1988).
- Sun89 T. Suntola. *Mat. Sci. Rep.* **4**, 261 (1989).
- Sun94 C. J. Sun, P. Kung, A. Saxier, H. Ohsato, K. Haritos, and M. Razeghi, *J. Appl. Phys.*, **75**, 3964 (1994).
- Sun96 H. Sunakawa, A. Yamaguchi, A. Kimura, and A. Usui, *Jpn. J. Appl. Phys.*, Part 2 **35**, L 1395 (1996).
- Tab99 A. Tabata, A. P. Lima, L. K. Teles, L. M. R. Scolfaro, J. R. Leite, *Appl. Phys. Lett.* **74**, 362 (1999).
- Tak97a N. Takahashi, J. Ogasawara, and A. Koukitu, *J. Cryst. Growth* **172**, 298 (1997).
- Tak97b N. Takahashi, R. Matsumoto, A. Koukitu, and H. Seki, *Jpn. J. Appl. Phys.*, Part 2 **36**, L743 (1997).
- Tak99 Takashi Mukai and Shuji Nakamura, *Jpn. J. Appl. Phys.* **38**, 5735 (1999).
- Tan84a T. L. Tansley and C. P. Foley, *Electro. Lett.* **20**, 1066 (1984).
- Tan84b T. L. Tansley and C. P. Foley, in *Proceedings of the 3rd International Conference on Semi-Insulating III-V Materials*, Warm Springs, Oregon, 1984, p. 497.
- Tan86a T. L. Tansley, C.P. Foley, *J. Appl. Phys.* **59**, 3241 (1986).
- Tan86b T. L. Tansley and C. P. Foley, *J. Appl. Phys.* **60**, 2092 (1986).
- Tan88 T. L. Tansley, R. J. Egan, and E. C. Horrigan, *Thin Solid Films.* **164**. 441 (1988).
- Tan92a T. L. Tansley and R. J. Egan, *Phys. Rev. B* **45**, 10942 (1992).
- Tan92b T. L. Tansley and R. J. Egan, *Mater. Res. Soc. Symp. Proc.* **242**, 395 (1992).

- Tod95 A. Toda, T. Kawasaki, D. Zmaniski, A. Ishibashi. *Electron. Lett.* **31**, 235 (1995).
- Tom92 G. S. Tompa, E. Wolak, R. A. Stall, M. A. George, M. Lippitt, Norman JAT. *Mat. Res. Soc. Symp. Proc.* **282**, 323 (1992).
- Tom94 K. Tominaga, Y. Sakashita, H. Nakashima, M. Ada, *J Cryst Growth.* **145**, 219 (1994).
- Tra74 J. W. Trainor and K. Rose, *J. Electron. Mater.* **3**, 821 (1974).
- Tra78 N. N. Travkin, P. K. Stachov, I. G. Tonoyan, and B. I. Kozykin, *J. Gen. Chem. USSR* **48**, 2428 (1978).
- Tra99 C. A. Tran, A. Osinski, and R. F. Kalicek, Jr., *Appl. Phys. Lett.* **75**, 1494 (1999).
- Tra00 A. Trampert and K. H. Ploog, *Cryst. Res. Technol.*, **35**, 793 (2000).
- Tsu99 T. Tsuchiya, H. Yamano, O. Miki, A. Wakahara, and A. Yoshida, *Jpn. J. Appl. Phys.*, Part 1 **38**, 1884 (1999).
- Tsu00a T. Tsuchiya, O. Miki, K. Shimada, M. Ohnishi, A. Wakahara, and A. Yoshida, *J. Cryst. Growth* **220**, 185 (2000).
- Tsu00b T. Tsuchiya, M. Ohnishi, A. Wakahara, and A. Yoshida, *J. Cryst. Growth* **220**, 191 (2000).
- Tu92 King Ning Tu, James W. Mayer, Leonard C. Feldman, *Electronic Thin Film Science*, Macmillian Publishing Company, (1992).
- Uch96 K. Uchida, A. Watanabe, F. Yano, M. Kouguchi, T. Tanka and S. Hinakawa, *J. Appl. Phys.* **79** (1996) 3487.
- Utr99 M. Utriainen, C. Kovacs, J. M. Campbell, L. Niinistö, F. Reti. *J. Electrochem. Soc.* **146**, 189 (1999).
- Utr00 M. Utriainen, Kroeger, M. Laukkanen, L. S. Johansson, L. Niinistö, *Appl. Surf. Sci.* **157**, 151 (2000).
- Vis95a R.D. Vispute, J. Narayan, H. Wu, and K. Jagannadham, *J. Appl. Phys.* **77**, 4724(1995).
- Vis95b R. D. Vispute, H. Wu, and J. Narayan, *Appl. Phys. Lett.* **67**, 1549 (1995).
- Wak89 A. Wakahara and A. Yoshida, *Appl. Phys. Lett.* **54**, 709 (1989).
- Wak90 A. Wakahara, T. Tsuchiya, and A. Yoshida, *J. Cryst. Growth* **99**, 385 (1990).
- Wak97 A. Wakahara, T. Tokuda, X. Dang, S. Noda, and A. Sasaki, *Appl. Phys. Lett.* **71**, 906 (1997).

- Wan01 K. Wang and R. R. Reeber, *Appl. Phys. Lett.* **79**, 1602 (2001).
- Wat93 A. Watanabe, T. Takeuchi, K. Hirose, H. Amano, K. Hiramatsu, I. Akasaki, *J. Crystal Growth*, **128**, 391 (1993).
- Wes88 K. L. Westra, R. P. W. Lawson, and M. J. Brett, *J. Vac. Sci. Technol. A* **6**, 1730 (1988).
- Wri97 A. F. Wright, *J. Appl. Phys.* **82**, 2883 (1997).
- Wu02 J. Wu, W. Walukiewicz, K.M. Yu, J. W. Ager III, E.E. Haller, H.Lu, W.J. Schaff, Y. Saito, and Y. Nanishi, *Appl. Phys. Lett.* **80**, 3967 (2002).
- Xu02 K. Xu, W. Terashima, T. Hata, N. Hashimoto, Y. Ishitani, and A. Yoshikawa, *Phys. Status Solidi C* **0**, 377 (2002).
- Yam94a A. Yamamoto, M. Tsujino, M. Ohkubo, and A. Hashimoto, *Sol. Energy. Mater. Sol. Cells* **35**, 53 (1994).
- Yam94b A. Yamamoto, M. Tsujino, M. Ohkubo, and A. Hashimoto, *J. Cryst. Growth* **137**, 415 (1994).
- Yam96 A. Yamamoto, Y. Yamauchi, T. Ogawa, M. Ohkubo, and A. Hashimoto, *Inst. Phys. Conf. Ser.* **142**, 879 (1996).
- Yam97a A. Yamamoto, Y. Yamauchi, M. Ohkubo, A. Hashimoto, and T. Saitoh, *Solid-State Electron.* **41**, 149 (1997).
- Yam97b A. Yamamoto, Y. Yamauchi, M. Ohkubo, and A. Hashimoto, *J. Cryst. Growth* **174**, 641 (1997).
- Yam98a A. Yamamoto, T. Shin-ya, T. Sugiura, and A. Hashimoto, *J. Cryst. Growth* **189/190**, 461 (1998).
- Yam98b A. Yamamoto, T. Shin-ya, T. Sugiura, M. Ohkubo, and A. Hashimoto, *J. Cryst. Growth* **189/190**, 476 (1998).
- Yam99a S. Yamaguchi, M. Kariya, S. Nitta, T. Takuchi, C. Wetzel, H. Amano, I. Akasaki, *J. Appl. Phys.* **85**, 7682 (1999).
- Yam99b A. Yamamoto, M. Adachi, T. Arita, T. Sugiura, and A. Hashimoto, *Phys. Status Solidi A* **176**, 595 (1999).
- Yam01a A. Yamamoto, Y. Murakami, K. Koide, M. Adachi, and A. Hashimoto, *Phys. Status Solidi B* **228**, 5 (2001).
- Yam01b A. Yamamoto, M. Adachi, and A. Hashimoto, *J. Cryst. Growth* **230**, 351 (2001).

- Yam01c T. Yamaguchi, Y. Saito, K. Kano, T. Araki, N. Teraguchi, A. Suzuki, and Y. Nanishi, *Phys. Status Solidi B* **228**, 17 (2001).
- Yam02 A. Yamamoto, T. Tanaka, K. Koide, and A. Hashimoto, *Phys. Status Solidi A* **194**, 510 (2002).
- Yam03 A. Yamamoto, T. Tanaka, A. G. Bhuiyan, K. Sugita, K. Kasashima, Y. Kimura, A. Hashimoto, and V. Yu. Davydov, *5th International Conference on Nitride Semiconductors (ICNS-5)*, Nara, Japan, May 25-30, 2003.
- Yam04a A. Yamamoto, N. Imai, K. Sugita, and A. Hashimoto, *J. Cryst. Growth* **261**, 271 (2004).
- Yam04b A. Yamamoto, K. Sugita, H. Takatsuka, Y. Hamano, N. Imai, and A. Hashimoto, *Proceedings of the International Workshop on Nitride Semiconductors (IWN' 2004)*, Pittsburgh, USA, July 19-23, p113 (2004).
- Yan95 Z. Yang, L. K. Li, and W. I. Wang, *Appl. Phys. Lett.* **67**, 1686 (1995).
- Yan96 J.W. Yang, C. J. Sun, Q. Chen, M.Z. Anwar, M. A. Khan, S. A. Nikishin, G. A. Seryogin, A. V. Osinsky, L. Chernyak, H. Temkin, C. Hu, and S. Mahajan, *Appl. Phys. Lett.* **69**, 3566 (1996).
- Yan99 C.C. Yang, G.C. Chi, C.K. Huang, and M.C. Wu, *J. Cryst. Growth* **200**, 32 (1999).
- Yan00 J. W. Yang, A. Lunev, G. Simin, A. Chitnis, M. Shatalov, and M. Asif Khan, Joseph E. Van Notrand, and R. Gaska, *Appl. Phys. Lett.* **76**, 273 (2000).
- Yan02a F. H. Yang, J.S. Hwang, Y.J. Yang, K.H. Chen, and J.H. Wang, *Jpn. J. Appl. Phys.*, Part 2 **41**, L1321 (2002).
- Yan02b H. F. Yang, W. Z. Shen, Z. G. Qian, Q. J. Pan, H. Ogawa, and Q. X. Guo, *J. Appl. Phys.* **91**, 9803 (2002).
- Yan02c F.H. Yang, J.S. Hwang, K. H. Chen, Y. J. Yang, T. H. Lee, L. G. Hwa, and L. C. Chen, *Thin Solid Films* **405**, 194 (2002).
- Yaw99 C. L. Yaws, *Chemical Properties Handbooks*, McGraw-Hill, 475 (1999).
- Yod01 T. Yodo, H. Ando, D. Nosei, and Y. Harada, *Phys. Status Solidi B* **228**, 21 (2001).
- Yod02 T. Yodo, H. Yona, H. Ando, D. Nosei, and Y. Harada, *Appl. Phys. Lett.* **80**, 968 (2002).
- Yos83 S. Yoshida, S. Misawa and S. Gonda, *Appl. Phys. Lett.* **42** 427 (1983).

- Yos91 N Yoshimoto, T. Matsuoka, T. Sasaki, and A. Katsui, *Appl. Phys. Lett.* **59** 2251 (1991).
- Zim01 S. Zimmer, B. Meyler, and J. Salzman: *Appl. Phys. Lett.* **78**, 288 (2001).
- Zun94 A. Z. Zunger and S. Mahajan, in *Handbook on Semiconductors*, ed. T. S. Moss, Elsevier Science, Amsterdam, (1994) p.1402.

## BIOGRAPHICAL SKETCH

Taewoong Kim was born to Doohoi Kim and Byungrae Yoo on July 31, 1968, in Seoul, Korea. He grew up in Seoul, Korea. He graduated from Youngil High School in 1986. He then went on to Inha University in Incheon City, where he graduated in 1993 with a Bachelor of Science in polymer science and engineering. He went on to graduate school in Inha University where he graduated in 1995 with a Master of Science in polymer science and engineering. In graduate school, he studied the ER-fluid (electrorheological fluid). After graduating, he worked for LG Chemical Company from 1995 to 1999, where he performed research on polymer processing.

He changed his major and joined the Chemical Engineering Department at University of Florida in August of 1999. There he researched semiconductor epitaxial InN film growth in Dr. Timothy Anderson's group.